UNIVERSITY OF Southampton

University of Southampton Research Repository

Copyright © and Moral Rights for this thesis and, where applicable, any accompanying data are retained by the author and/or other copyright owners. A copy can be downloaded for personal non-commercial research or study, without prior permission or charge. This thesis and the accompanying data cannot be reproduced or quoted extensively from without first obtaining permission in writing from the copyright holder/s. The content of the thesis and accompanying research data (where applicable) must not be changed in any way or sold commercially in any format or medium without the formal permission of the copyright holder/s.

When referring to this thesis and any accompanying data, full bibliographic details must be given, e.g.

Thesis: Author (Year of Submission) “Full thesis title”, University of Southampton, name of the University Faculty or School or Department, PhD Thesis, pagination.

Data: Author (Year) Title. URI [dataset]

University of Southampton

Faculty of Engineering and Physical Sciences

School of Electronics and Computer Science

Polypropylene-Based Nanodielectrics for HVDC Cables

by

Xinyu Wang

ORCID ID: 0000-0001-9434-2906

Thesis for the degree of Doctor of Philosophy

March 2021

University of Southampton

Abstract

Faculty of Engineering and Physical Sciences

School of Electronics and Computer Science

Thesis for the degree of Doctor of Philosophy

Polypropylene-Based Nanodielectrics for HVDC Cables

By

Xinyu Wang

Due to the limited recyclability and operating temperature of the cross-linked polyethylene (XLPE) insulation for high voltage direct current (HVDC) cables, renewable next-generation insulation materials have drawn great attention during recent years, especially polypropylene-based nanodielectrics. The filler-matrix interphase within nanodielectrics is believed to be the determining factor in bringing unique features, which show great potential in tailoring the dielectric and thermal properties of the insulations. However, it is still unsatisfactory in understanding how interphase works.

In this study, polypropylene (PP) and aluminium nitride (AlN) nanocomposites have been investigated regarding their potential application for HVDC cable insulation. A conceptional model (two-side model) is proposed to explain the behaviours of PP nanocomposites contains the silane coupling agents (SCA) treated fillers. The novelty of this model is to divide the surface chemistry of fillers into two sides (the near- and far-particles sides) at the molecular level, which differs from the conventional theory that the interphase properties are dominated by the interaction between the organofunctional tails (far-particle side) of SCA and polymer matrix. The bonding structure between

SCA and particle surface (near-particle side) also executes a strong influence on the filer-matrix interaction by modifying the polarity of the particle surface, e.g., the monolayer of SCA on nanoparticles surface can maintain the polarity of the AlN then provide an inter-spherulites-boundary-free structure, thus giving a higher dielectric break down strength compared to systems contains AlN with a multilayer of SCA. Four SCA were used to analyse the effect of the AlN surface chemistry that differ in the near- and far-particle structures on the morphology, thermal, and dielectric properties of nanocomposites. The introduction of AlN shows a nucleating and hindrance effect, increasing the nuclei density but maintaining the crystallinity of the nanocomposites. AlN with higher surface polarity presents a higher nucleating effect and can induce an inter-spherulite-boundary-free structure where the AC breakdown strength is improved. Such so-called surface polarity is positively related to both the near- and far-particles sides.

A water absorption analysis was used to investigate the interphase properties of the nanocomposites, as the absorbed water molecules will mainly be located at the interfacial region. The AlN filled PP was found to reduce the hydrophobicity of PP, result in an increased permittivity and dielectric loss. This issue can be mitigated by using tri-alkoxy silanes to form a silane network that repels water molecules; meanwhile, the mono-alkoxy silane cannot increase the hydrophobicity of the nanocomposites.

Despite the AlN dispersion can be improved by SCA treatment, large agglomerations (> 20 μm) can still be observed in silane treated samples caused by the hydrolysis of AlN. The removal rather than dispersing of those large agglomerations by a centrifugal separation method gives us an excellent opportunity to investigate the relationship between bulk properties and the degree of AlN agglomeration. It is found that the AC breakdown strength is significantly improved after the separation process compared to the PP with non-separated AlN. The improved nanoparticle dispersion reduced the defects and cavities within nanocomposites; benefit from that, the samples still exhibit an excellent hydrophobicity even the interfacial area is increased.

The addition of SCA increases the thermal conductivity of the PP/AlN nanocomposites, where 10 % of the increase can be achieved. Although the total interfacial thermal resistance increases with the increased AlN dispersion after the centrifugal separation processes, there is a higher chance for the fillers to percolate, thus showing a comparable bulk conductivity.

Overall, this study investigated the influence of the material interphase on the morphology, thermal, and electrical properties of nanocomposites using a proposed two-side model (near- and far-particle side), which is expected to serve as a valuable tool in the future design and application of nanodielectrics.

Table of Contents

Table of Tables

Table of Figures

Research Thesis: Declaration of Authorship

Print name: Xinyu Wang

Title of thesis: Polypropylene-Based Nanodielectrics for HVDC Cables

I declare that this thesis and the work presented in it are my own and has been generated by me as the result of my own original research.

I confirm that:

1. This work was done wholly or mainly while in candidature for a research degree at this University;
2. Where any part of this thesis has previously been submitted for a degree or any other qualification at this University or any other institution, this has been clearly stated;
3. Where I have consulted the published work of others, this is always clearly attributed;
4. Where I have quoted from the work of others, the source is always given. With the exception of such quotations, this thesis is entirely my own work;
5. I have acknowledged all main sources of help;
6. Where the thesis is based on work done by myself jointly with others, I have made clear exactly what was done by others and what I have contributed myself;
7. Part of this work has been published.

Signature: ..... Date:.....

Acknowledgements

I would like to thank my supervisor Dr Thomas Andritsch and Professor George Chen for their inspiration, support, and invaluable discussions.

Big thanks to everyone who helped me during this journey, especially those who have supported me during the pandemic.

Thank you, my family, friends, and colleagues.

List of Abbreviation

Abbreviation	Description
AlN	Aluminium nitride
ATR	Attenuated total reflection
CNT	Carbon nanotube
CS	Centrifugal separation
XLPE	Cross-linked polyethylene
EVA	Ethylene vinyl acetate
EPR	Ethylene-propylene rubber
FTIR	Fourier-transform infrared spectroscopy
GO	Graphene oxide
HN	Havriliak-Negami
HVAC	High voltage alternating current
HVDC	High voltage direct current
HDPE	High-density polyethylene
ITR	Interfacial thermal resistance
iPP	Isotactic polypropylene
LDPE	Low-density polyethylene
MI	Mass impregnated
MAS	Mono-alkoxy silane
OF	Oil-filled
OHL	Overhead lines
PE	Polyethylene

PP	Polypropylene
QDC	Quasi-dc
SEM	Scanning electron microscope
SCA	Silane coupling agents
TGA	Thermogravimetric analysis
TEM	Transmission electron microscopy
TAS	Tri-alkoxy silane
XRD	X-Ray Diffraction

List of Publication

- Wang, Xinyu, Luming, Zhou, Andritsch, Thomas and Chen, George Introduction of Centrifugal Separation in Processing Polypropylene/AlN Nanodielectrics. (In draft)
- Wang, Xinyu, Andritsch, Thomas and Chen, George Influence of mono-alkoxy and tri-alkoxy silane on the water absorption and dielectric response of polypropylene/AlN nanodielectrics. (In draft)
- Lei, Zhipeng, Fabiani, Davide, Bray, Tommaso, Li, Chuanyang, Wang, Xinyu, Andritsch, Thomas, Credi, Alberto and La Rosa, Marcello (2021) Space charge behavior of quantum dot-doped polystyrene polymers. IEEE Transactions on Dielectrics & Electrical Insulation. (In press)
- Bai, Yu, Qiang, Dayuan, Zhang, Yanru, Wang, Xinyu, Zhuang, Xu, Chen, George and Yan, Wang (2020) Recognition of Nanocomposites Agglomeration in Scanning Electron Microscopy Image with Semantic Segmentation Algorithm. In 2020 Conference on Electrical Insulation and Dielectric Phenomena (CEIDP). IEEE. (In press)
- Suraci, Simone Vincenzo, He, Xiaozhen, Chaudhary, Sunny, Wang, Xinyu, Anyszka, Rafal, Mahtabani, Amirhossein, Fabiani, Davide, Andritsch, Thomas and Vaughan, Alun (2020) Assessment of the chemical and electrical properties of nano structured polyethylene with antioxidant-grafted nanosilica. In 2020 International Conference on Dielectrics (ICD). IEEE. (doi: 10.1109/ICD46958.2020.9341980)
- Wang, Xinyu, Qiang, Dayuan, Hosier, Ian, Zhu, Yanqiu, Chen, George and Andritsch, Thomas (2020) Effect of water on the breakdown and dielectric response of polypropylene/nano aluminium nitride composites. Journal of Materials Science, 55 (21), 8900-8916. (doi:10.1007/s10853-020-04635-1).
- Qiang, Dayuan, Wang, Xinyu, Wang, Yan, Andritsch, Thomas and Chen, George (2020) Experimental study and numerical estimation of moisture effect on charge transport in polymer nanocomposites. Journal of Physics D: Applied Physics, 53 (34), [345304]. (doi:10.1088/1361-6463/ab8cee).
- Wang, Xinyu, Qiang, Dayuan, Andritsch, Thomas, Chen, George and Vaughan, Alun (2020) Influence of monoalkoxy silane on the dielectric response of polypropylene aluminium nitride nanocomposites. In 2020 International Conference on Dielectrics (ICD). IEEE. (doi: 10.1109/ICD46958.2020.9341871)
- Wang, Xinyu, Andritsch, Thomas and Chen, George (2020) Influence of the amount of silane coupling agent on the dielectric properties of AlN/polypropylene nanocomposites. In 2019 Conference on Electrical Insulation and Dielectric Phenomena (CEIDP). IEEE. 356-359. (doi:10.1109/CEIDP47102.2019.9009642).

- Lian, Zheng, Wang, Xinyu and Andritsch, Thomas (2019) Dielectric and mechanical properties evaluation of polypropylene containing nitride-based nanoparticles. In 2019 International Conference on Electrical Materials and Power Equipment (ICEMPE). IEEE. 250-253. (doi:10.1109/ICEMPE.2019.8727368).
- Wei, Min, Wang, Xinyu and Andritsch, Thomas (2019) Space charge and breakdown strength behaviour of PP/POE/MgO nanocomposites. In 2019 International Conference on Electrical Materials and Power Equipment (ICEMPE). IEEE. 260-263. (doi:10.1109/ICEMPE.2019.8727367).
- Qiang, Dayuan, Wang, Yan, Wang, Xinyu, Chen, George and Andritsch, Thomas (2019) The effect of filler loading ratios and moisture on DC conductivity and space charge behaviour of SiO2 and hBN filled epoxy nanocomposites. Journal of Physics D: Applied Physics, 52 (39), 1-16. (doi:10.1088/1361-6463/ab2d5b).
- Wang, Xinyu, Andritsch, Thomas and Chen, George (2019) The effect of water on the dielectric properties of polypropylene/aluminium nitride nanocomposites. In 2019 Universities High Voltage Network Colloquium (UHVnet).
- Wang, Xinyu, Andritsch, Thomas, Chen, George and Virtanen, Suvi (2019) The role of the filler surface chemistry on the dielectric and thermal properties of polypropylene aluminium nitride nanocomposites. IEEE Transactions on Dielectrics & Electrical Insulation, 26 (3), 1009-1017. (doi:10.1109/TDEI.2019.007773).
- Qiang, Dayuan, Wang, Xinyu, Wang, Yan, Andritsch, Thomas and Chen, Guanghui (2019) Thermal stability of epoxy nanocomposites: surface treatment and morphology impact based on nano SiO2 and hBN fillers. Materials Research Express, 6 (10), 1-18. (doi:10.1088/2053-1591/ab3f8f).
- Wang, Xinyu, Andritsch, Thomas and Chen, George (2018) Effect of surface functionalization on the dielectric properties of polypropylene aluminium nitride nanocomposites. In 2018 International Conference on Dielectrics (ICD). IEEE. (doi:10.1109/ICD.2018.8514621).
- Wang, Xinyu, Andritsch, Thomas and Chen, George (2018) The effect of surface modification on the dielectric properties of polypropylene/aluminum nitride nanocomposites. In 2018 Universities High Voltage Network Colloquium (UHVnet).

Chapter 1 Introduction

The development of human society is inseparable from the use of energy. In recent decades, more and more extreme weather phenomena have made us continue to reflect on the existing fossil energy-dominated energy structure and focus on developing and utilising renewable and sustainable energy. In a future dominated by renewable distributed power, high-performance and reliable transmission lines are of critical importance. HVDC cable technology has a wide range of needs and potential among them [1]. However, the development of HVDC cables is limited by the insulation material, which reaches a maximum voltage level of 600 kV nowadays, much lower than the overhead line technology that has achieved an 1100 kV HVDC power transmission [2, 3].

PP is considered a potential next-generation high-voltage cable insulation material by many researchers due to its potential to permit higher cable operating temperatures than traditional XLPE [4-7]. Owing to its thermoplastic nature and the elimination of a cross-linking step, its environmental impact is significantly reduced compared to XLPE over the full life cycle of a cable [8]. However, PP cable insulation suffers from a number of drawbacks regarding thermo-mechanical properties; one of them is having a low thermal conductivity, which is 0.14 $W \cdot m^{-1} \cdot K^{-1}$ [9]. Such an issue can lead to localised regions of higher conductivity/higher dielectric loss, which can shorten the lifetime of the cable. This drawback can be overcome by adding fillers with high thermal conductivity, which can also help alleviate high thermal gradients between the inner and outer of the cable insulation [10-12]. In addition to the thermal properties, improved dielectric properties by incorporating nanoparticles into polymer insulation have been reported widely. The large interfacial area associated with nanoparticles means that a relatively small filler loading ($\leqslant$ 5 wt%) can significantly influence the dielectric performance of the composites [13-15]. Indeed, when discussing the main factor that can dominate the property changes caused by adding nanoparticles into the polymer dielectrics, the notion of the large interfacial region between nanoparticles and the base polymer, giving rise to the interphase volume, plays a significant role. However, while the potential benefits of nanodielectrics have been exploited over the last twenty years, there are plenty of inconsistent or contradictory results that impede the thorough understanding of how nanoparticle interacts with the base polymer and then affecting the bulk properties.

1.1 Research Aims and Scopes

The proposed work will focus on PP-based nanocomposites and their potential for next-generation HVDC cable. The interfacial region and the potential interactions between nanoparticles and the PP

matrix will be the main focus. The silane coupling agents (SCA) are used to obtain nanoparticles with varied surface chemistry then provide different interactions with the PP matrix. As they will bond to the nanoparticle surface before the blending step, the bonding mechanism could also impact the bulk properties due to the large interfacial area. Therefore, the proposed work will dedicate to the following aspects (aim 1 to 5 are in the order of novelty of the completed research, the thesis structure can be found in section 1.2):

- Aim 1: to understand the interactions between nanoparticles and polymer matrix and the role of the surface chemistry on the "far-particle" side (see Figure 1.1, the definition of terms) of the nanoparticles on the thermal and dielectric properties of nanocomposites.

Nano-AlN was selected as the filler in this work, and the surface chemistry was varied with the help of two different silane coupling agents with different organofunctional groups. SCA with octyl and methacrylate groups were used. This allows us to investigate the influence of the nanoparticles surface chemistry at the far-particle side and its induced filler-matrix interactions on the morphology, thermal conductivity, dielectric permittivity, losses, and the breakdown strength of the nanocomposites.

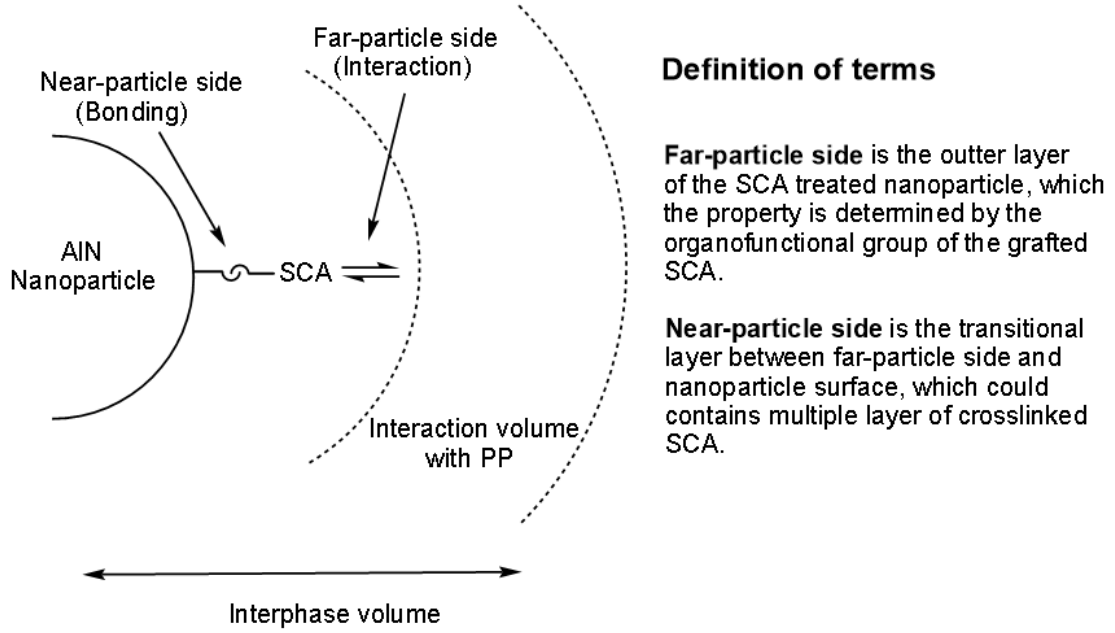

Figure 1.1 The general idea of near- and far-particle side and their role in the filler-matrix interphase volume (not to scale).

- Aim 2: to investigate the influence of the “near-particle” side (see Figure 1.1, the definition of terms) structure on the bulk properties of the nanocomposites.

Apart from the interactions between the surface chemistry of fillers and the PP matrix (far-particles side), the interphase properties of the “near-particle” side were also investigated. This was achieved by using silane coupling agents that can provide different grafting mechanisms onto nanoparticles, namely methoxy silane vs ethoxy silane and tri-alkoxy silane (TAS, conventional SCA) vs mono-alkoxy silane (MAS) (see Figure 1.2).

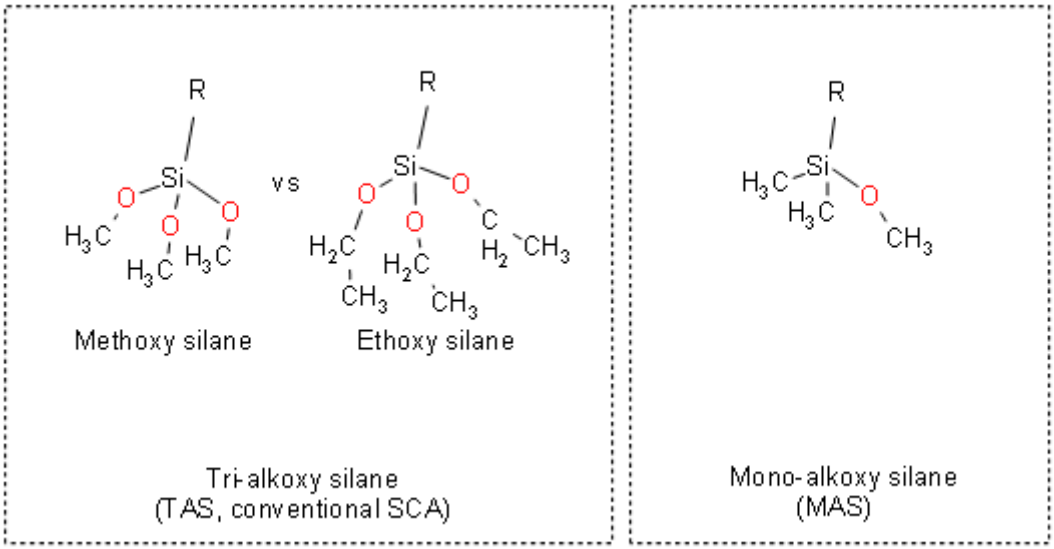

Figure 1.2 The illustration of different SCA used that differs from the hydrolysable side (not to scale).

- Aim 3: to investigate the influence of nanoparticle dispersion and the interphase volume on the thermal and dielectric properties of nanocomposites.

The interphase volume is positively related to the dispersion of the nanoparticles, but changing the filler dispersion without changing the nanoparticles surface chemistry (and the interphase properties resulting from the nanoparticles surface chemistry) is quite challenging during material processing. Therefore, a centrifugal separation (CS) method was used (see Figure 1.3), which allows us to solely investigate the influence of nanoparticle dispersion and the interphase volume on the morphology, thermal conductivity, dielectric permittivity, losses, and breakdown strength of the nanocomposites.

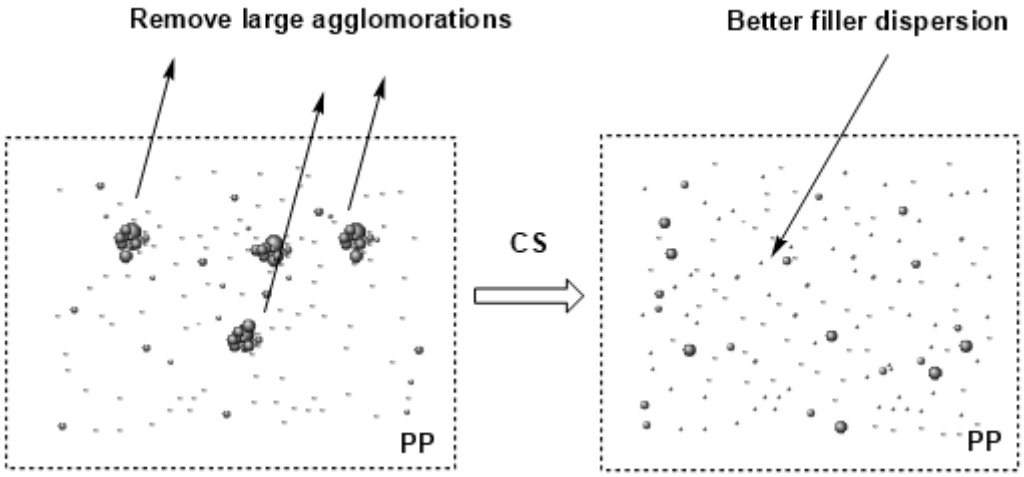

Figure 1.3 Illustrates removing the large agglomerations through centrifugal separation rather than changing the filler surface chemistry (not to scale).

- Aim 4: to obtain a better understanding of interphase properties by using water absorption analysis and formulate an approach to avoid the water absorption issues of the nanocomposites.

A water absorption analysis was used as a probe to study the interphase properties of the nanocomposites since the water molecules are prone to interact with the nanoparticle surface rather than the hydrophobic PP matrix (see Figure 1.4). By applying a proper surface treatment of the nanoparticles, the water absorption issues are expected to be minimised.

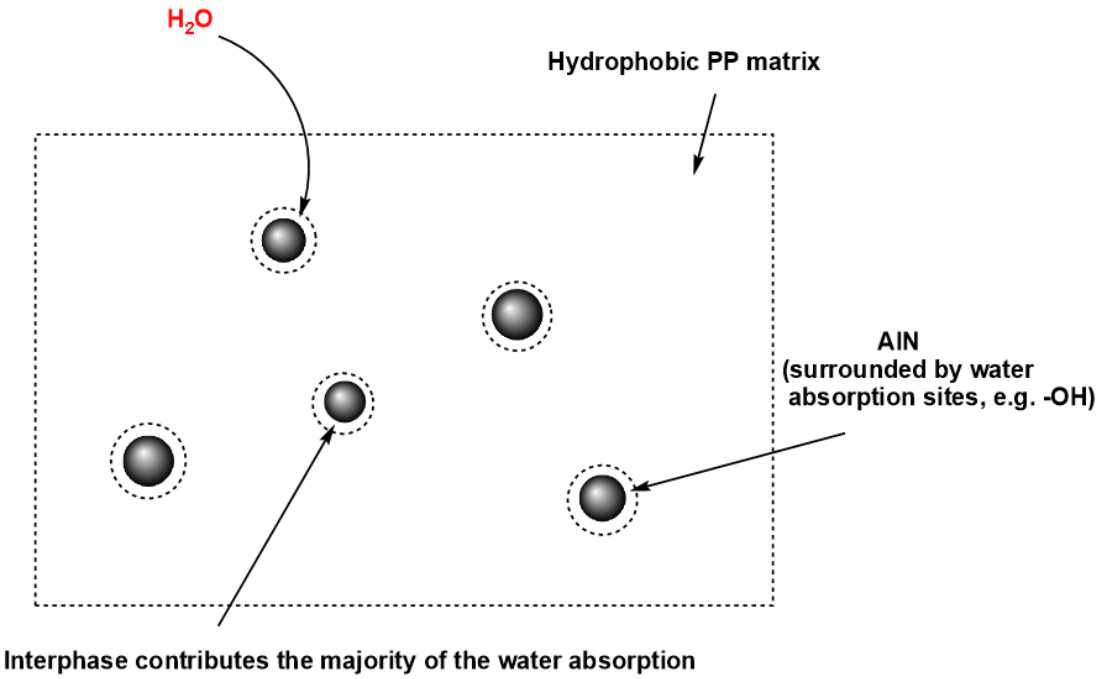

Figure 1.4 The idea of using water as a probe to investigate the interphase properties (not to scale).

- Aim 5: to investigate the potential sources that may cause the inconsistency of the experiment results regarding nanocomposites.

To avoid the inconsistent experiment results, a thorough characterisation of the AlN nano-filler, PP and their nanocomposites was conducted regarding filler surface chemistry, filler dispersion and the morphology of the nanocomposites. Upon this, the possible reason which may cause inconsistent results was discussed. In order to minimise the intrinsic limitation and error from a characterisation technique, multiple characterisation techniques/settings and repeat testing were adopted, and the related results were proved to be consistent, e.g., Thermogravimetric analysis (TGA), Fourier-transform infrared spectroscopy (FTIR), and water absorption analysis were used to characterise the surface chemistry of the AlN nanoparticles used in this work.

1.2 Thesis Structure

Chapter 1 introduce the research aims and scopes of this work.

Chapter 2 introduce the potential application of PP-based insulation and the promising properties of PP-based nanodielectric, for HVDC cable. The challenges of its application are discussed, which define the research scopes and aims of this work.

Chapter 3 consists of four parts. Part 1 explains why AlN is used in this work according to the aims discussed in Chapter 2. Part 2 introduced the hydrolysis issue of the AlN and the possible influence on the further research of this work. Parts 3 provides a thorough investigation of the hydrolysis and the surface chemistry of the as-received AlN, eliminating the inconsistent results from the hydrolysis of AlN. In part 4, the idea of changing AlN surface chemistry by silane functionalisation with different conventional SCA is introduced, followed by a proposed nanoparticle two sides model including both “far-particle” and “near-particle” sides.

Chapter 4 introduced an improved solution blending method. The morphology (crystalline structure and particle dispersion) and thermal properties (melting and crystallisation behaviours, thermal degradation, and thermal conductivity) of the nanocomposites treated with different conventional SCA were studied in this chapter.

Chapter 5 focuses on the electrical properties (dielectric permittivity, loss, and AC breakdown strength) of the nanocomposites treated with different conventional SCA with the help of the water absorption analysis.

Chapter 6 applied a unique SCA, which is MAS. It can provide a strict monolayer of silane on the AlN surface, which significantly changes the near-particle side. The morphology (crystalline structure and particle dispersion), thermal (melting and crystallisation behaviours and thermal degradation) and electrical properties (dielectric permittivity, loss, and AC breakdown strength) of the resulting nanocomposites were studied with the help of the water absorption analysis.

Chapter 7 introduced a novel centrifugal separation technique in preparing the PP/AlN nanocomposites with a solution blending method. This allows the controlling of the AlN dispersion states within the PP matrix. The morphology (crystalline structure and particle dispersion), thermal (melting and crystallisation behaviours and thermal degradation) and electrical properties (dielectric permittivity, loss, and AC breakdown strength) of the nanocomposites with better AlN dispersion states were studied with the help of the water absorption analysis.

Chapter 8 presents the general conclusion of this work and the aims raised in Chapter 1. Future works are suggested regarding the limitation of this work.

Chapter 2 Research Background and Motivation

2.1 HVDC Cable Insulation

2.1.1 HVDC Transmission

Compared to conventional high voltage alternating current (HVAC) power transmission, HVDC technology provides a power transmission with lower loss. Still, the requirement of the AC-DC and DC-AC conversion leads to higher initial investments. This cost will be balanced at a "break-even distance", shown in Figure 2.1, which is usually 600 km for overhead lines (OHL) and 50 km for submarine cable systems [16-18]. This makes the HVDC systems a strong competitor in long-distance power transmission and undersea power transmission to HVAC [19].

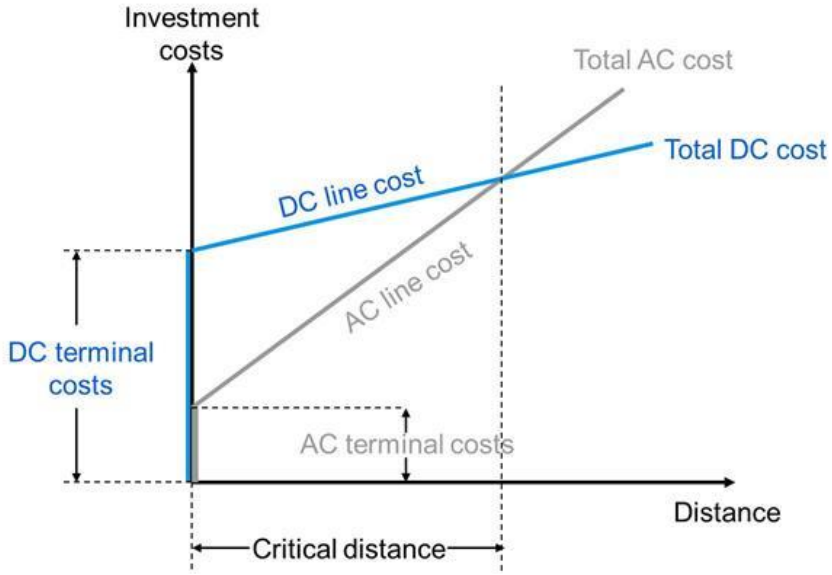

Figure 2.1 HVDC system becomes more cost-effective if a transmission line is over a break-even or critical distance, and the critical distance is typically 600 km for OHL and 50 km for submarine cable [16, 18].

Over the last decades, HVDC cable technology has been playing a crucial role in undersea power transmission [1]; The increasing trend of offshore renewable energy integration and regional submarine interconnections makes developing the high-capacity HVDC cables an urgent demand [1, 20]. Such is also true for land-based power transmission since land-based (underground) cable system benefits from intrinsic advantages over OHL, such as conquering terrain that is not suitable

for building OHL towers, avoiding occupying expensive land resources in urban areas, and ease the public concerns over the environmental, visual and health impact of OHL [1, 19, 21].

A thick insulation layer is required for power cables, e.g., the HVDC submarine cable of the NorNed link (450 kV) has an insulation layer of 20 mm, Figure 2.2, which is a critical factor in cable design. The first HVDC cable project launched in 1906, Lyon, has a 4 km underground cable with an 18 mm mass impregnated (MI) insulation operated under 125 kV [1]. Since then, efforts on cable insulation material have been made to meet the financial requirement, reliability and the increasing of the transmission distance as well as the operational voltage [1, 22]. This figure reached 600 kV (e.g., Prysmian, XLPE cable) nowadays. However, there is still a gap compared to OHL regarding the operating voltage level, which is now 1,100 kV (Changji-Guquan project). The lack of reliable insulation is the main reason for the cable system that stays behind [2, 3].

Figure 2.2 A section of the HVDC submarine cable in NorNed project with a 20 mm MI insulation [1].

2.1.2 Development of Cable Insulation Materials

Different types of insulations for the HVDC cable have been developed to obtain a higher capacity and a longer transmission distance [1, 23]; a detailed review can be found in [1]: The operational voltage of oil-filled (OF) cables can reach 600 kV and even 1400 kV in the early 1980 s [24], but drawbacks like the limited length, oil leakage, and requirement of oil feed equipment constrained the development of the OF cable. Thus, it was gradually replaced by MI and extruded cable techniques [25]. Despite the MI cable technique is considered a proven HVDC cable technology with reliable performance, the significant advantages of extruded cable make itself become the most popular technology during recent years, namely, no oil leakage concern like OF and MI cable, a higher operational temperature (up to 90 °C), a better mechanical performance, more convenient installation, and the feasibility of using recyclable materials [1, 26].

[1] https://deepresource.wordpress.com/2013/06/15/norned/

2.1.3 XLPE Cable

Nowadays, state of the art insulation material used for extruded cables is XLPE. The base material, low-density polyethylene (LDPE), is chemically cross-linked, where a macromolecule with a 3-dimensional polymer chain network is formed. It can successfully maintain appropriate thermomechanical integrity at 100 °C if a sufficient ratio of the LDPE is cross-linked (above 60 %) [8]. By contrast, LDPE will suffer from the issues related to phase transition at this temperature as the melting point is close, which is generally in a range of 90 to 115 °C [27].

However, the drawbacks below are limiting the future development of XLPE insulation:

- XLPE is not ready for recycling due to cross-linking, which will lead to disposal issues at the end of the cable life cycle.
- The cross-linking process will introduce by-products, which will lead to undesired dielectric properties, such as increased space charge accumulation [28].
- During cable manufacturing, large catenary cable manufacture facilities and a long degassing period (typically more than 7 days) are required [29].
- Large thermal expansion of XLPE negatively impacts dielectric properties and cable components [8, 30]. An early work from Eichhorn shows that XLPE will expand up to 10 % when increase temperature from room temperature to 100 °C; In comparison, the ethylene-propylene rubber (EPR) can expand less than 4 % at the same conditions and be accompanied by a lower reduction in thermal conductivity than XLPE insulation [31].
- Significantly reduced Young's modulus at high temperature is a potential risk of mechanical damage. A reduction in Young's modulus from 100 MPa to less than 1 MPa is observed when increasing the temperature from 20 to 100 °C [32].

2.2 After XLPE Era (PP-Based Insulation)

A number of attempts were made to improve the feasibility of XLPE for future generation extruded HVDC cables, such as super clean XLPE with a minimised level of by-products and doping inorganic nano-fillers into XLPE [1, 33]. However, due to the nature of chemical cross-linking, and the thermomechanical and manufacturing drawbacks listed above, it is prone to have diminishing rewards from the efforts on the further development of XLPE [8].

2.2.1 Potential of Polypropylene

Studies on recyclable or environmentally friendly extruded cable have drawn a great deal of attention in recent years, especially for PP and its polymer blends, copolymer, and nanocomposites [4-8, 22, 34-36].

The research and application of polypropylene-based material are motivated by the following facts:

- PP usually has excellent dielectric performances suitable for cable insulation, such as high breakdown strength, low dielectric permittivity and loss, high electrical resistivity, etc. [5].
- The melting point of the commonly available isotactic polypropylene (iPP) is typically 160 °C, which could significantly improve the cable rating. This allows a potential higher operation temperature than its competitors—XLPE and polyethylene (PE) based system [37].
- PP is one of the most commonly used thermoplastics with full recyclable nature, low price and is widely used in packaging, domestic appliance, the car industry, etc. [37, 38]. No cross-linking and degassing are required, shortening the production time of cable, and making PP cable free from cross-linking by-product-related issues.
- PP has a non-polar structure with excellent hydrophobicity. PP cable insulation will tend to have a consistent performance under different humidity, especially for submarine cable [38].

The interest in PP based power cable material is also seen in the industry. Prysmian announced to upgrade their high-performance thermoplastic elastomer (HPTE), one of the key points of P-laser, from medium voltage power cable application to HV cable with 600 kV since 2016 [39][1]. This patented material is a PP based insulation and claimed to have full recyclability and better mechanical performance than the base PP [40]. Another representative example is a patent issued by Dow Chemical, a "soft PP" insulation for power cables [41].

2.2.2 Polypropylene/Elastomer Blend

Despite the potentials listed above, the undesirable high brittleness limited the application of PP for HVDC cable, which drives the theme of the research on softening the material [7, 34, 37]. This is in line with the patents described above. PP homopolymer plus elastomer blend and "softer" PP-based copolymer have been developed to mitigate the mechanical issue of PP [4, 42-44]. An overall trend of a negative impact on dielectric properties is clear if a uniform or well-designed microstructure is not acquired. Zhou et al. found that by adding polyolefin elastomer (POE) into PP, a dramatic improvement in mechanical performance can be achieved [42]. But the reduced DC breakdown strength and increased hetero-charge accumulation are evident. The authors suggest that the phase separation of PP and POE (Figure 2.3) is the main reason. Phase separation easily occurs in the polymer blend. The microstructure or morphology of said material can be affected by a number of factors, namely the selection of polymers, loading of elastomers, thermal history, and additives.

[1] https://uk.prysmiangroup.com/node/9973

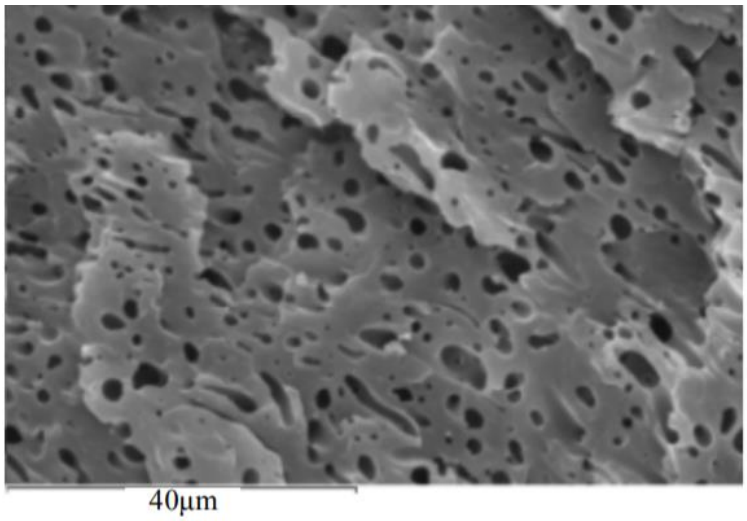

Figure 2.3 Phase separation can be observed in PP with 30 % of POE blend, and hollow structures are formed from the removal of POE during acid etching, reproduced from [42].

2.2.3 Crystalline Structure of Polypropylene and Blend

Studies found that the crystalline structure will significantly impact the mechanical and dielectric properties of PP-based material [44, 45]. The crystalline growth of the commonly available iPP is shown in Figure 2.4. The growth of the crystalline structure of PP normally starts from the melted states above the melting temperature of PP, where the polymers chains are tangled. With the temperature reduced below the melting point, chains begin to align and fold in an ordered form as crystalline lamella. Then more lamellas formed and gradually extended from a dense lamellar structure (nuclei), becoming a spherulite structure, as shown in Figure 2.4a[1]. The spherulite will keep growing until it collides with the adjacent spherulites; see Figure 2.4b [46]. Figure 2.4c shows a final structure of an iPP structure produced by injection moulding, and the inter-spherulite boundaries are clearly evident [47]. An early study by Kolesov et al. reported that the crystalline spherulite region of PP shows higher DC breakdown strength than the inter-spherulite boundaries region. Therefore, these regions are considered a “weak spot” under the electrical field and are found to become “weaker” with the increase of the spherulite diameter. This leads to a monotonic decrease in bulk breakdown strength with the increasing spherulite diameter [48].

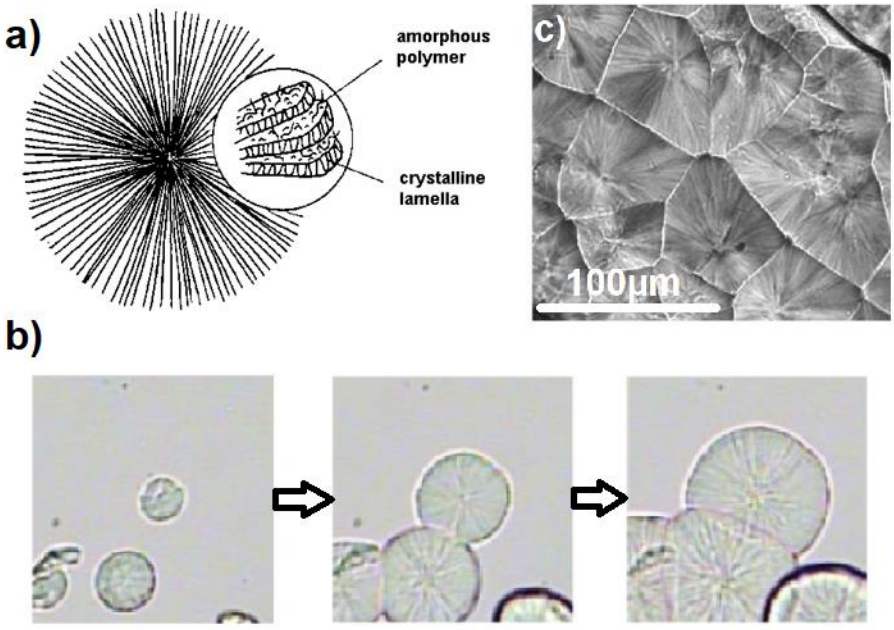

Figure 2.4 a) an illustration of spherulite crystal of PP[1], b) the growth of PP crystal at 135 °C [46], and c) the final structure of an iPP structure produced by injection moulding with inter-spherulite boundary [47].

The morphology of PP based material is sensitive to the thermal history of the sample processing. Hosier et al. proposed a PP and ethylene-propylene rubber (EPR) blend (50 % of PP with 50 % of PE40) for cable application [44]. The quenched sample shows promising mechanical, thermal, and electrical properties for high voltage cable insulation. However, the isothermal crystallisation at 120 °C is leading to a brittle fracture feature and a decreased breakdown strength of the same composition. Figure 2.5 shows the microstructure of iPP and EPR blend with different thermal histories. The larger spherulite size and clear inter-spherulite boundary in the isothermal crystallised sample are suggested to have a negative impact on the mechanical properties and breakdown strength.

[1] https://www.doitpoms.ac.uk/tlplib/polymers/spherulites.php

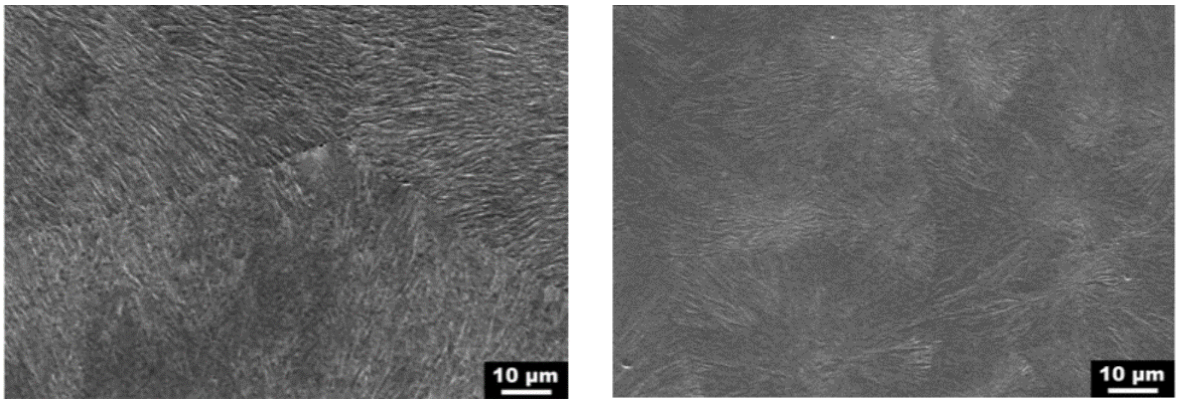

Figure 2.5 SEM images show the Microstructure of iPP with 50 % of PE40, larger spherulite size, and clear inter-spherulite boundary can be found in samples isothermal crystallised at 120 °C (left), no clear inter-spherulite boundary can be found in quenched samples (right) [44].

The PP samples prepared with different thermal histories are usually leading to a different crystallinity. The isothermal crystallisation or low cooling rate from the melt phase trend produce samples with higher crystallinity [49, 50]. This indicated the reduced breakdown strength could also result from the increased crystallinity reported in [44]. However, many studies have reported the breakdown strength of PP show a low correlation with the crystallinity of samples [51-53]. Researchers could only speculate the mechanism as the breakdown trend to occur in the amorphous region of the PP, and the reduced fraction of this region is supposed to have a higher breakdown strength [54]. Krishnakumar *et al*. suggest that the independent breakdown strength to the crystallinity could result from the unchanged crystal-amorphous boundaries [52]. Although the changing crystallinity of PP samples is hard to be independent of other morphological properties, further study on the breakdown mechanism on PP is still needed to understand the influence of crystallinity.

2.2.4 Thermal Conductivity of Polypropylene and Issues

Polymer materials are usually considered thermal insulators with low thermal conductivity, usually less than 0.5 $W \cdot m^{-1} \cdot K^{-1}$ (Table 2.1); it is also true for PP [9]. Joule heat produced from the conductor leads to the increased temperature of the inner layer of the insulation. Insulation with poor ability to dissipate heat generated will limit the current rating of the cable. Therefore, how to increase the thermal conductivity of PP based insulation material is essential in its development in next-generation power cables.

Table 2.1 Thermal conductivity of different materials [9, 55].

Material	Thermal conductivity ($W \cdot m^{-1} \cdot K^{-1}$)
LDPE	0.33
HDPE	0.45-0.52
XLPE	0.4
PP	0.14
Epoxy	0.17-0.21
Copper	401
Diamond	2,000

2.2.5 Summary

PP based insulation material shows great potential in the next-generation HVDC cable application due to its promising properties, such as high melting point and recyclability. However, issues related to the high brittleness, morphological weak spots, and low thermal conductivity have limited its application so far.

2.3 Why Nanodielectrics?

Nanodielectrics are the polymer nanocomposites used for the dielectric insulation within which nano-sized fillers are dispersed and have a loading ratio of typically a few weight percentage (<10 wt%). The concept of “nanodielectrics” was first introduced as “nanometric dielectrics” by Lewis in 1994 [56]. Nevertheless, the research on nanodielectrics did not receive much attention until promising performances, such as the suppressed space charge accumulation, was delivered by the pioneering experimental work of Nelson and Fothergill in 2002 [14]. Since then, many studies have reported the remarkable performance of nanodielectric [57-64]. Although there is no consensus on the mechanism by which nanoparticles can change the bulk properties of composites, it is undeniable that the introduction of nanoparticles provides higher flexibility in adjusting the properties of the composites by tailoring the material at a nanometric level. In this section, why nanodielectric is gaining significant interest in the future HVDC cable insulation will be discussed in the dielectric and thermal aspects.

2.3.1 Dielectric Properties of Nanodielectrics

Many studies have reported that adding nanofillers can bring enhanced dielectric properties to polymeric insulation. Notably, PP based nanocomposites with superior dielectric properties in terms of electrical breakdown strength, space charge distribution, electrical tree propagation, etc., have increased their potential for the future HVDC cable [57-63].

The breakdown strength is a primary indicator for selecting the material for HVDC cable insulation, and a material with high breakdown strength can potentially reduce the thickness of the insulation. The AC/DC breakdown strength was founded improved in nanodielectrics [57-59]. For example, Takala et al. reported that both the AC and DC breakdown strength were improved when comparing the PP with hydrophobic fumed silica nanocomposites with the reference PP [59].

Space charge accumulation is a critical issue for DC applications, and the charges accumulated inside the insulation bulk will distort the electric field distribution. This can lead to problems related to the enhanced local electric field, such as the partial discharge and accelerated ageing of cable insulation. A reduced space charge accumulation has been widely reported in PP based nanocomposites [57, 60-63]. Representative work for Zhou et al. compared PP filled with four different inorganic fillers, MgO, TiO_2, ZnO and Al_2O_3. All nanocomposites show a suppressed space charge accumulation to the non-filled PP [57].

Properties related to the growth of the electrical tree is highly associated with the life-long reliability of the cable insulation. Not many studies have investigated the tree growth in PP nanocomposites, but nanofillers in LDPE and epoxy show a suppressing effect on the electrical tree propagation. As the microstructure of electrical trees in LDPE and its nanocomposites are shown in Figure 2.6, slower tree growth can be observed in LDPE with 3 wt% of nanosilica [64].

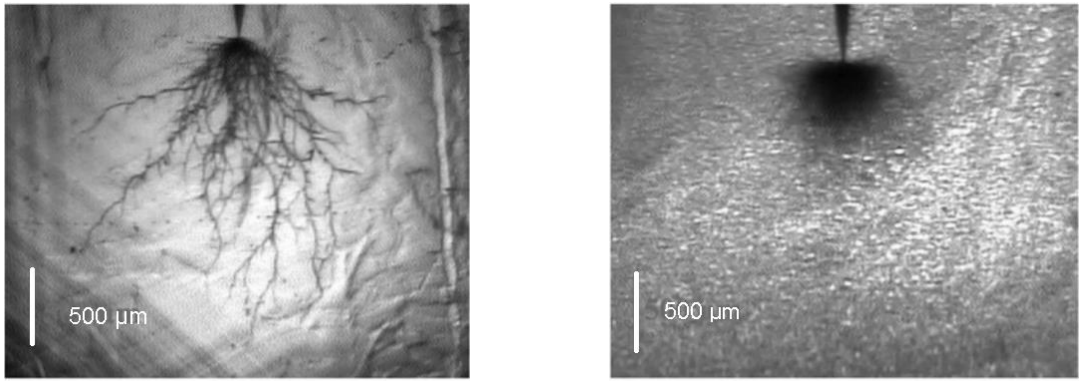

Figure 2.6 Electrical trees in LDPE (left) and LDPE with 3wt% of silica nanocomposites (right). A suppressed tree growth is evident in nanocomposites, reproduced from [64].

The enhanced dielectric properties usually tend to only show the best performance at a low loading ratio. Zhou et al. reported the best space charge profile is obtained by adding 1 wt% of TiO_2, and the degree of the electric field distortion is then getting worse when increasing the filler loading [57]. The DC breakdown strength of epoxy nanocomposites as a function of filler loading ratio has been studied; as shown in Figure 2.7, the highest breakdown strength is acquired by adding 0.5 wt% of fillers in most cases [65]. Although the low filler loading is not favourable regarding increasing the thermal conductivity of the nanocomposites, it will ease the total cost of the cable. It is because the fillers are usually more expensive than the polymer matrix.

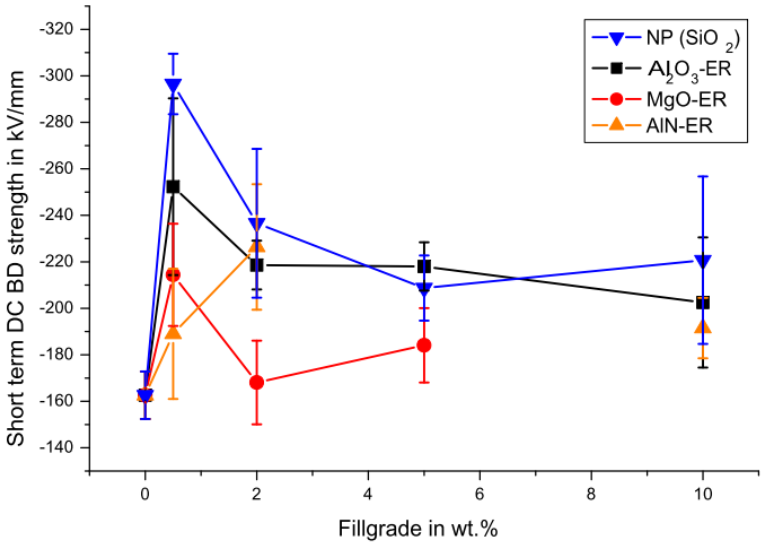

Figure 2.7 DC breakdown results of silica, alumina, magnesium oxide and aluminium nitride filled epoxy nanocomposites as a function of the fill grade [65].

2.3.2 Polypropylene/elastomer Nanodielectrics

As mentioned in Section 2.2.2, the addition of polymeric elastomers can reduce the brittleness of PP, but the simultaneous weakened dielectric performance is hard to avoid. Therefore, the idea of balancing the dielectric and mechanical properties by blending polypropylene, elastomer and nanoparticles have been proposed by many researchers [5, 58, 63, 66]. Zhou et al. investigated the dielectric properties of PP/POE/MgO nanocomposites, and they found the DC breakdown strength of PP/POE can be improved from 323 kV/mm to 370 kV/mm by adding 3 phr (parts per hundred rubber) of nano-MgO [58]. Recent work from Shaw et al. reported that adding ethylene vinyl acetate (EVA) elastomer into iPP and increased space charge accumulation and DC conductivity can be found [66]. Fortunately, such issues can be mitigated by adding 0.5 wt% of nano clay. The authors also highlighted the ability of nano clay to reduce the phase separation of iPP and EVA, shown in Figure 2.8. It should be noted the phase separation in Figure 2.8a is not obvious as the examples

shown in Figure 2.3, which could be related to the insufficient acid etching during sample preparation.

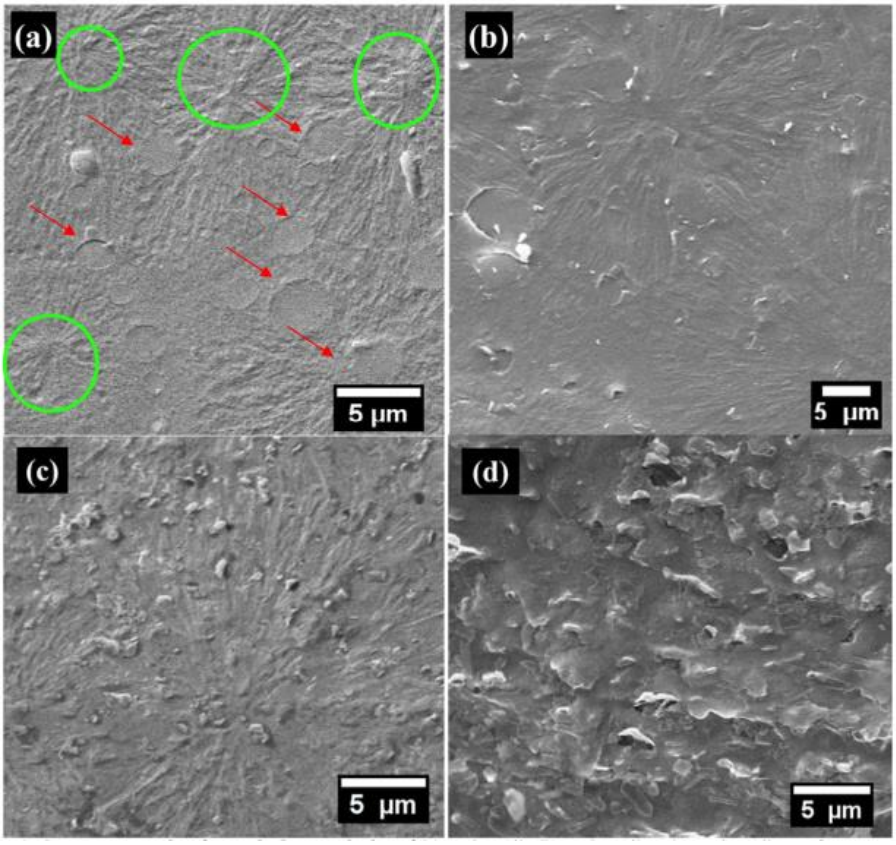

Figure 2.8 SEM micrograph of PP/EVA blend with nano clay, a) PP/EVA, b) PP/EVA/0.5wt% clay, c) PP/EVA/2.5wt% clay, d) PP/EVA/5wt% clay. Phase separation can be seen from PP/EVA (red arrow) but eliminated with the addition of nano clay [66].

2.3.3 Crystalline Structure of Polypropylene Nanodielectrics

Not many studies have attributed the change of morphology as a major influencer of the electrical properties since the presence of the nanoparticle itself is usually more noticeable. But it is evident that the crystal structure of the PP can be significantly altered by adding nanoparticles. Primarily due to the nucleating effect of nanoparticles, which is related to the shape, surface chemistry, and loading ratios of nanoparticles, e.g., Palza et al. studied the spherulite growth of the PP/silica nanocomposites, both spherulites quantity and density in PP are increased by adding nanosilica (Figure 2.9) [67]. As a result, a final product with a more uniform structure is formed. From this, we can see the potential to minimise the weak spot issue mentioned in Section 2.2.3 with the help of nanoparticles.

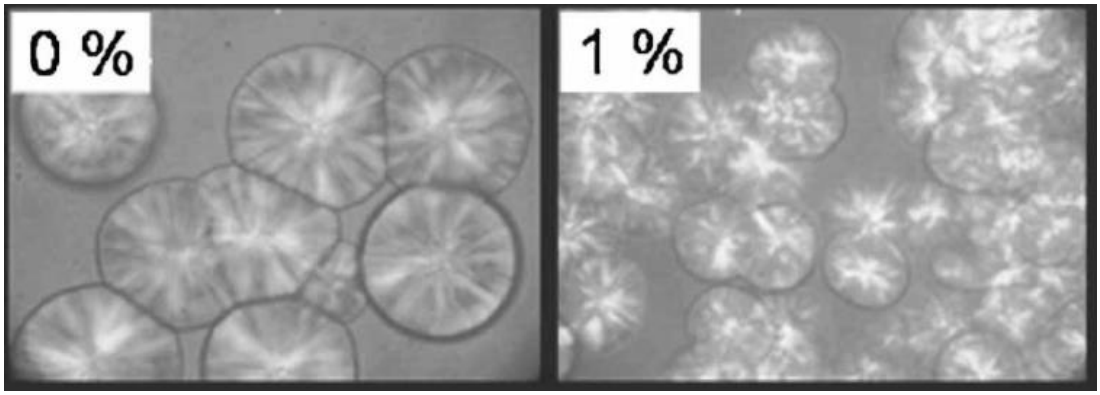

Figure 2.9 The morphology change of PP by adding 1 % of nanosilica, reproduced from [67], the same scale applied for both images.

2.3.4 Thermal Conductivity of Nanocomposites

When considering the potential of PP-based materials in the HVDC cable application, other than the mechanical performance such as the high brittleness at low temperature, the thermal conductivity, about 0.14 $W \cdot m^{-1} \cdot K^{-1}$, is another main weakness of PP, which is around half that of PE (0.33 to 0.52 $W \cdot m^{-1} \cdot K^{-1}$ [9]. That means the heat generated during the cable operation from the conductor cannot dissipate efficiently to the out layer of the polymeric insulation, and the consequence is detrimental to cable rating and the life expenditure of the insulation.

One approach to increase the thermal conductivity of the polymers is to add fillers with high intrinsic thermal conductivity, and it is widely reported [12, 68-73]. Some carbon and metal-based fillers, such as carbon nanotube (CNT), graphene oxide (GO) and silver particles, are generally favourable candidates. But an accompanying increase in the electrical conductivity is a trend, which can be fatal to electrical insulation. Therefore, metal oxide/nitride and other non-conductive inorganic fillers are more prevalent in high voltage equipment.

The thermal conductivity of polymer composites is related to several factors, such as the type, size and distribution of fillers, polymer type and its morphology, the filler-polymer interaction, etc. An integrated approach is strictly required to address a better understanding of these factors [74]. Regarding the effect of filler size, composites containing filler with smaller sizes will have a larger interface area between filler and polymer if the particles are in a homogeneous dispersion. This can lead to a reduced thermal conductivity result from the increased interfacial scattering of the heat conduction. The modelling of the thermal conductivity of composite materials can date back to Maxwell's study in 1904 [75], and many models have been proposed since then, e.g. Fricke's model extended Maxwell's model in 1953 and the effect of shapes of fillers was included [76]. But not until Hasselman and Johnson (H-J) modified Maxwell's model by adding the effect of interfacial resistance and filler size in 1987 [77], most of the models assumed the "perfect contact" between

filler and matrix [78]. From Figure 2.10, in the H-J model, if the product of spherical filler radius (a) and the boundary conductance (h_c) is lower than a critical value, a lower thermal conductivity to the matrix will be obtained. Smaller filler size means lower thermal conductivity of the composites when assuming h_c, and the thermal conductivity of filler (K_d) is independent of the filler size.

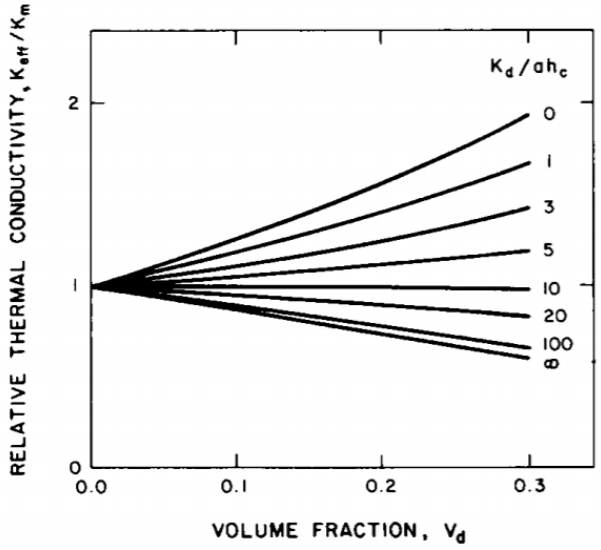

Figure 2.10 Thermal conductivity of matrix with spherical fillers based on the H-J model, K_d is the thermal conductivity of filler, a is the filler radius, and h_c is the boundary conductance between two materials [77].

However, findings are sometimes contradictory and show a high relevance to the shape and the distribution of the filler, especially when it goes to nanometric [79-81]. For example, Zhang et al. compared the effect of filler size on the thermal conductivity of alumina and high-density polyethylene (HDPE) composites, and they got the opposite trend. The observed thermal conductivity continuously increases with the decrease of filler size. The authors suggest the thermally conductive percolation pathways are easier to be formed in composites with nanofillers than micro-fillers [80]. A notable work from Pashayi et al. shows that by adding 25 % of sliver nanoparticle, epoxy nanocomposites can have a thermal conductivity of 10 W/(m·K); The results of its counterpart with micro-size fillers is only 0.3 W/(m·K), which is lower than two orders of magnitude versus the conventional mixing rule where the interfacial thermal resistance is not considered [81]. The authors suggest that it is related to a high conductive network formed by the sintering of the silver nanoparticle during the high temperature (150 °C) curing process. The results indicate a network structure formed by nanoparticles shows the potential to compensate for the loss of thermal conductivity related to the interfacial thermal resistance between filler and matrix (Figure 2.11).

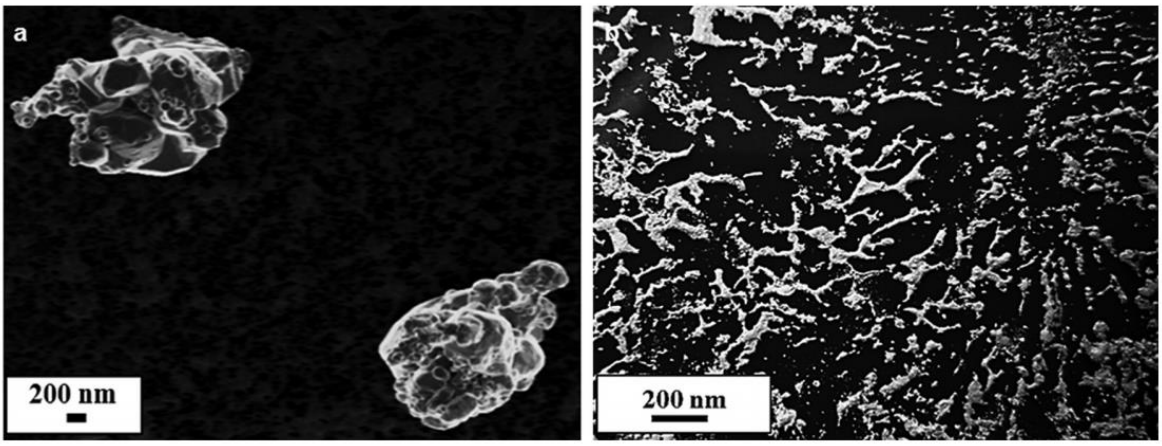

Figure 2.11 SEM image of (a) the micro composite and (b) the nanocomposite. While the silver fillers are not connected in the micro composite, a network structure is revealed in the nanocomposite [81].

They also show the nanoparticles themselves can have a property change compared to micro-particles; the melting point of the silver particle is reduced when it is in nano-size, thus a better sintering performance.

The formation of the thermal conductive pathway is closely related to the nanofiller dispersion states. The uniformly dispersed nanoparticles create a huge interfacial area within the composites, and the improvement in thermal conductivity will be restricted by the large total interfacial thermal resistance. A proper degree of filler agglomeration could form thermal conduction paths, further increasing thermal conductivity [74]. But in most cases, the thermal conduction path or network can only be formed at a high filler loading ratio. The samples usually have a significantly reduced electrical performance [65]. A contradictory trend has been reported for nanocomposites with a low loading ratio [82-84], e.g., Tessema et al. studied the Poly(2-vinyl pyridine)/SiO_2 nanocomposites where the filler dispersion can be controlled by the casting solvent selection. The authors suggest non-uniform heat flow results from the local high thermal conductive region (agglomerations), and the longer inter-particle distance could limit phonon propagation through samples with large agglomerations [83]. However, the improved filler dispersion is usually a result of the filler surface treatment (discussed in section 2.4.3), where the interfacial thermal resistance is reduced; thus, the effect of filler dispersion is obscured [84].

Although the potential of nanofillers in increasing the thermal conductivity of polymer materials have been widely introduced, extra concerns should be given for nanocomposites with a low filler concentration, where the thermal conduction network is unlikely to form, regarding the filler size, dispersion, and surface treatment; Low filler concentration is vital for polymer nanodielectrics, since enhanced dielectric properties by adding nanofillers, e.g., an increased breakdown strength

and suppressed space charge accumulation, are usually obtained in a low filler loading (<5 wt%), as discussed in section 2.3.1.

2.3.5 Nanodielectrics with Functionalised Nanoparticles

The surface of nanoparticles can usually be functionalised and providing the required functions for the insulation material. Small molecular additives, e.g., voltage stabiliser and antioxidant, may suffer from problems related to their migration to the outside of the polymer insulation. To overcome this, they can be grafted onto the surface of nanoparticles [35, 85]. It can increase the stability of additives, lower the surface energy, and increase the dispersion of nanofillers. Gao et al. found that by grafting voltage stabiliser onto the nanosilica surface, enhanced dielectric properties of PP can be achieved in terms of breakdown strength, DC conductivity and space charge [35]. But it is a shame that the long-term stability of the voltage stabiliser is not analysed. The filler functionalisation with SCA is the most common approach, and it will be introduced in Section 3.4.

2.3.6 Summary

Promising properties can be offered by adding nanoparticles into insulation materials, such as increased electrical performance, reduced phase separation between PP and elastomer, and the increased thermal conductivity of the base polymer. For HVDC cable application, the insulation material needs to consider both electrical performance and thermal conductivity. A balanced filler loading must be achieved as the best electrical performance is usually accomplished with a low filler loading; in contrast, the thermal conductivity is usually proportional to the loading of nanoparticles.

2.4 Challenge of Nanodielectric in HVDC Cable

Based on the promising results mentioned in Section 2.3, it is expected that the dielectric properties of polymers could be improved, or more specifically, “tailored” by adding nano-sized fillers. Despite those promising performances, there are many contradicting results in the literature, and some studies indicate that nano-fillers will introduce unwanted side effects into polymer dielectrics. Power cables are usually designed for a service life of more than 20 years [86]; extra efforts and time are needed to locate and repair if a fault occurs. As a major component of the HVDC cable, the insulation material is expected to have high reliability and consistent performance throughout its service life. Therefore, to investigate the feasibility and the future application of PP based nanodielectrics in HVDC cable insulations, the following questions will need to be answered:

- How do nanoparticles work (theory)?
- What are the side effects brought by nanoparticles, and how we can control them?
- What is the origin of the inconsistency reported in the literature?

2.4.1 Interface or Interphase?

As aforementioned, numerous studies have been published regarding the improvement of the electrical, thermal, and mechanical properties of base polymers when introducing various nano-fillers into polymer matrixes within the last two decades. However, the structure-property relations are still not fully understood. Theoretical models have been proposed, but most of these models tend to focus on specific sets of experimental results and show limited ability to thoroughly understand the micro-mechanism about how nanoparticle work in nanodielectrics [65, 87-91]. Even so, the notion that the large interface between nano-fillers and the base polymer plays a significant role is acknowledged by most researchers; as shown in Figure 2.12, the interface area increases exponentially with the decrease of the filler size.

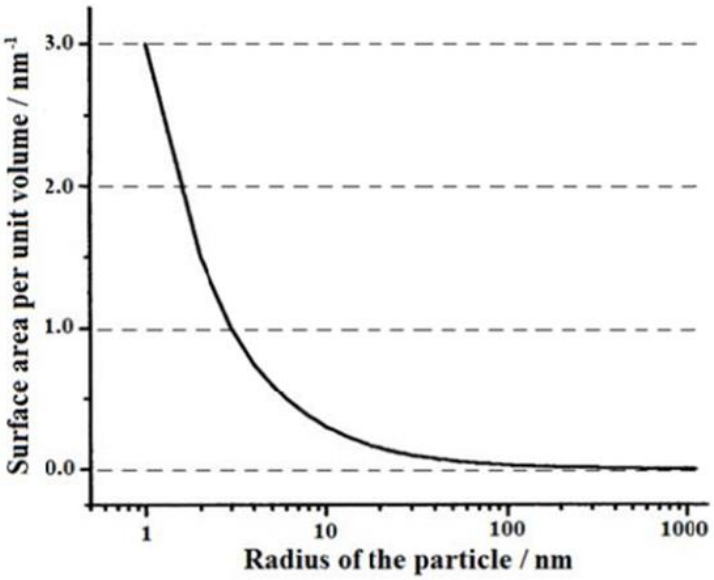

Figure 2.12 The Interfacial area within nanocomposites as a function of the filler size [92, 93].

Instead of “interface”, “interphase” could be a better term—the latter point out the volume between filler and matrix with distinct properties to neither materials. The interphase is considered an interaction volume between two materials, and its fraction can be extremely large in nanocomposites, even with low filler percentages. Rätzke and Kindersberger calculated the volume fraction of the interphase of nanocomposites by assuming interphase with a certain thickness [91]. The relationships between interphase volume fraction, interphase thickness, filler size and filler fraction are shown in Figure 2.13. If there are interphase with only 5 nm, the volume fraction of total interphase within nanocomposites can take up to 70% by adding just 10% of 10 nm filler.

However, it is challenging to prove and identify the interphase properties as most of the works focus on the macroscopic properties, and the interphase volume will significantly reduce when particles agglomerate. Therefore, further work on interphase properties is required to obtain a better understanding of nanodielectrics.

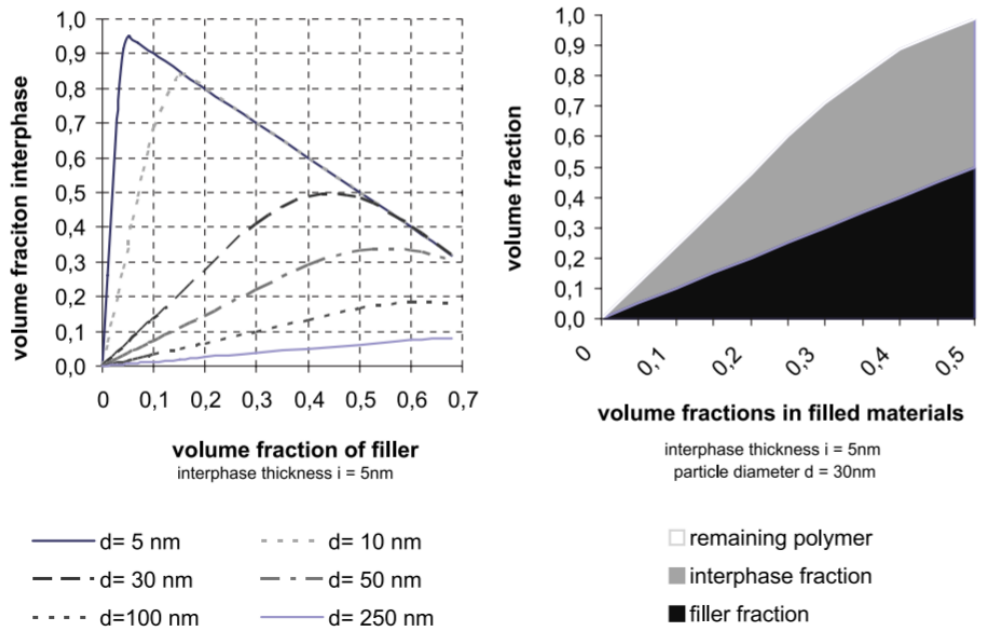

Figure 2.13 The relationship between interphase volume fraction, interphase thickness, filler size and filler fraction by assuming the existence of filler-polymer interphase with a certain thickness [91]. Notably, the volume fraction of interphase starts to decrease when the filler loading is higher than a critical point, where the interphase of each particle starts overlapping.

2.4.2 Water Absorption Issue of Nanodielectrics

One of the biggest problems of nanodielectrics for use in cable systems is continuously shown to be the water absorption issue [87, 94-97]. Nanocomposites with hydrophilic fillers tend to absorb water from the ambient environment. The hydroxyl groups on the surface of commonly used nanofillers, such as SiO_2 and Al_2O_3, are favourable water absorption sites. A large surface area of fillers will make the bulk properties of nanocomposites to be very sensitive to moisture. Zou et al. investigated the dielectric response of epoxy/silica nanocomposites stored under different humidity, and a quasi-dc (QDC) behaviour was observed at low frequencies [87]. The authors suggest that the QDC behaviour is related to water shells formed surround nanosilica, Figure 2.14. Hosier et al. compared the dielectric properties of PE nanocomposites with silicon-based fillers stored at different humidity [97]. When comparing nanocomposites immersed in water and dried in a vacuum oven, a weight difference of up to 1.3 % of the total weight can be observed. The DC

conductivity of nanocomposites shows orders of increase after the sample was immersed in water for 14 days, whilst reference PE is independent of the storage condition. Percolation of the water shells is suggested to be formed, which increases the bulk electrical conductivity. Chi et al. studied the effect of water on PP/SiO_2 nanocomposites, and they found that the DC breakdown strength of PP can be improved from 345.6 kV/mm to 413.9 kV/mm by adding 0.5 phr nanosilica [94]. But after samples were stored at 98 %HR and 80 °C, it dropped drastically to 157.4 kV/mm, while the reference PP had a breakdown strength of 255.8 kV/mm after the same treatment.

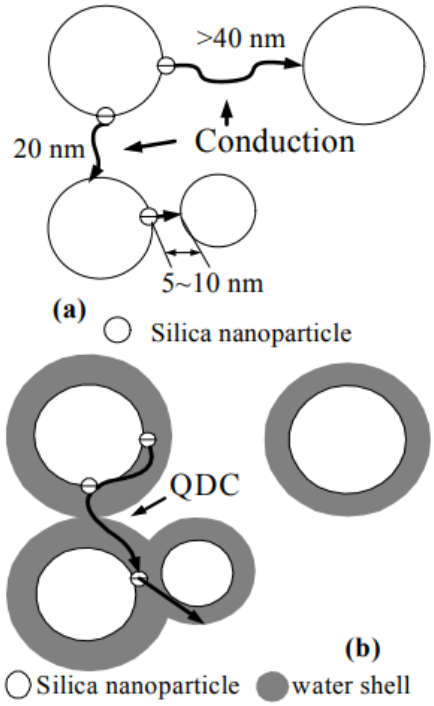

Figure 2.14 The formation of water shells surround nanoparticles resulting in different conduction mechanisms of nanocomposites [87].

2.4.3 Interfacial Thermal Resistance

The total interfacial resistance within the material is significantly enlarged when using nanofillers as the increased interface area. This can cause a reduction in thermal conductivity of composites in some specific cases due to the interfacial thermal resistance, albeit filler have higher thermal conductivity than matrix [98]. This results from the surface roughness and the phonon scattering during the heat conduction between two phases, and a temperature drop at the interface can occur (see Figure 2.15) [99]. Kochetov et al. compared the thermal conductivity of epoxy and silica composites. Samples with micro-silica show a higher thermal conductivity to samples with nanosilica at all filler loading ratios, from 5 to 15 wt%, even though a coupling agent is applied to increase the compatibility between matrix and fillers [100]. Proper surface treatment can improve

the bulk thermal conductivity of nanocomposites [101]. Still, it is challenging to understand its effect on the interfacial thermal resistance because the surface treatment will also lead to other property changes that can influence the bulk thermal conductivity, such as filler dispersion and structure of the matrix.

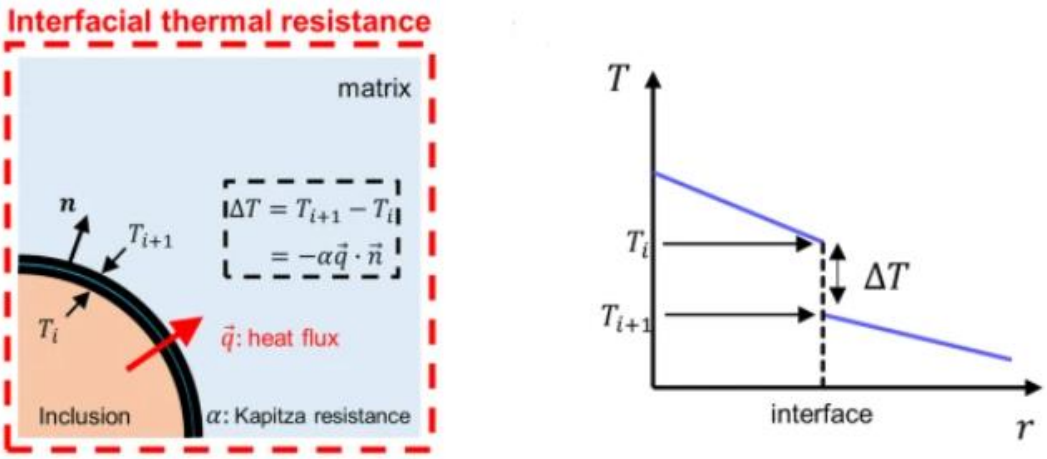

Figure 2.15 The temperature drop at the interface results from the interfacial thermal resistance [99].

2.4.4 Inconsistent Results in Nanodielectrics

When studying nanodielectrics, one cannot ignore the inconsistent results reported in the literature, restricting the understanding and development of nanodielectrics. For example, DC breakdown strength was improved by adding MgO nanoparticles into PP [58, 61]. But contradictory results are also reported where the DC breakdown strength monotonically decreases with the increase of the MgO loading [60]. Similarly, it is said the introduction of MgO will restrict the chain movement of PP, leading to a reduced dielectric permittivity [102, 103], but this may not be true as the increased dielectric permittivity due to the adding of MgO is also reported elsewhere [57]. Calebrese et al. pointed out that the different dispersion states resulting from the different samples preparation method are among the major reasons for inconsistency [104]. Other than that, the dielectric performances of nanocomposites are also sensitive to moisture content, material morphology, and degradation. Therefore, the following aspect should be considered for polypropylene/AlN nanocomposites regarding the consistency of the testing results:

- Due to the water absorption issue discussed in section 2.4.2, samples with different moisture content should be tested to understand the inconsistent results from samples where the effect of moisture have been neglected.
- The morphology and filler distribution should be identified through proper microscopic techniques. Many works use the cross-section images from the cracked samples to identify the nanofiller dispersions. The drawback of this method is the morphology properties of semi-crystalline polymers can be destroyed. An acid etching method was proved to be able to reveal the morphological structure of polyethylene.
- AlN used in this work suffers from the hydrolytic degradation issue, which could cause inconsistent results from the status of the raw material during the material preparation (this unique feature of AlN is discussed in Chapter 3). The raw material, especially nanoparticles, should be characterised with multiple characterizing techniques regarding its surface chemistry, crystal structure, and degradation features.

2.5 Summary

In this chapter, the background and motivation of this work have been discussed. The reason why PP was selected in this work is listed mainly related to its excellent electrical performance, potential higher operation temperature to other candidates, and recyclability. However, the low thermal conductivity could restrict the further application of PP-based insulations. The addition of nanofillers is reported to have a great potential in enhancing the thermal conductivity of the PP while maintaining or even improve the electrical performance. However, the understanding of how nanofillers work and the future development of nanodielectrics are limited by the following research topics, and below topics are the main concerns of this thesis: the understanding of the interaction between nanofiller and matrix material (studied in Chapter 4, 6 & 7), the water absorption issue of nanodielectrics (Chapter 5, 6 & 7), the interfacial thermal resistance between filler and matrix material (Chapter 4 & 7), and the inconsistent results reported in the literature (studied in Chapter 3, 4, 5 & 7).

Chapter 3 AlN Properties, Issues, and Silane Functionalisation

When studying nanodielectrics, the selection of filler is crucial. Fillers are different in types, size, shapes, surface chemistry, etc., which will lead to distinct properties of nanodielectrics. In this chapter, the reason why aluminium nitride is selected in this work is clarified—followed by the as-received AlN characterisation, an investigation of the hydrolysis issue of the aluminium nitride and the details of SCA functionalisation in this study.

Part of the results presented below are published in**:**

Wang, Xinyu, Qiang, Dayuan, Hosier, Ian, Zhu, Yanqiu, Chen, George and Andritsch, Thomas (2020) Effect of water on the breakdown and dielectric response of polypropylene/nano aluminium nitride composites. Journal of Materials Science, 55 (21), 8900-8916. (doi:10.1007/s10853-020-04635-1).

Wang, Xinyu, Andritsch, Thomas, Chen, George and Virtanen, Suvi (2019) The role of the filler surface chemistry on the dielectric and thermal properties of polypropylene aluminium nitride nanocomposites. IEEE Transactions on Dielectrics & Electrical Insulation, 26 (3), 1009-1017. (doi:10.1109/TDEI.2019.007773).

The experimental details can be found in Appendix A.

3.1 Why Aluminium Nitride?

3.1.1 Water Absorption Issue

As discussed in Chapter 2, many published works have indicated that the introduction of nanofiller can bring enhanced electrical and thermal properties [65, 105, 106]. However, a number of them are related to the addition of oxide-based filler, such as Al_2O_3, MgO and SiO_2, which will introduce a considerable number of hydrophilic sites into the bulk insulation. These hydrophilic sites, such as hydroxyl groups, are favourable for water molecules and make the material and dielectric properties sensitive to ambient humidity [96, 97]. The water absorption issue for nanodielectric is fatal, as the absorbed water can be the origin of increased losses and conduction pathways in the bulk insulation. The conduction pathways formed by the percolation of water shells can dramatically increase electrical conductivity and decrease the electrical breakdown strength of nanocomposites [87, 97]. Although some studies proving that the amount of water absorbed by nanocomposites could be reduced with proper surface treatment of the filler, the resulting nanocomposites still show significantly diminished dielectric properties under wet conditions [92].

Therefore, alternative fillers have been studied regarding the water absorption issue. Hosier et al. reported that nitride-based filler, such as AlN, shows minimal ability to introduce water absorption sites into polyethlyene compared to its oxide counterpart, Al_2O_3 [96]. Figure 3.1 shows the weight change of PE filled with different aluminium-based filler stored under dry and wet conditions. Al_2O_3 nanocomposites can absorb more than 6 times the water than the AlN nanocomposites at the same filler loading ratio.

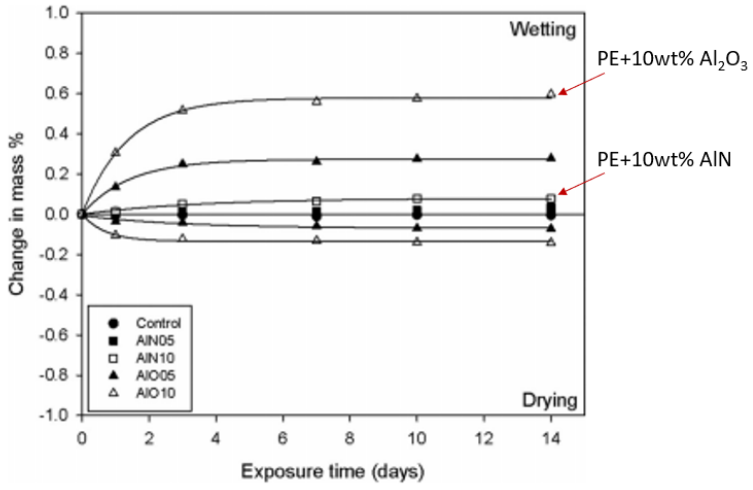

Figure 3.1 Mass change of PE nanocomposites filled with different aluminium-based fillers after immersed in water or drying in an oven for 14 days [96].

Elsewhere, similar results were highlighted by Ayoob et al. in which the polyethlyene nanocomposites with 10 wt.% of hexagonal boron nitride can only gain about 0.05 % of weight after being immersed in water for 15 days [107]—the polyethlyene nanocomposites with 10 wt.% of SiO_2, by contrast, can gain up to about 1.5 % of weight after the same pre-conditioning process [95]. These results indicate that the water absorption behaviour of nanocomposites is directly linked to the types (or surface chemistry) of nano-fillers. For example, silica is fully covered with hydroxyl groups, while those groups can only be found on the edge of hexagonal boron nitride platelets [108].

3.1.2 Thermal Conductivity Consideration

Besides the water absorption issue and the related electrical properties mentioned above, the intrinsic low thermal conductivity of polymer insulation is another critical factor for us to make the decision when selecting nanofiller [9]. The thermal conductivities of commonly used nanofillers for nanodielectrics are listed in Table 3.1.

Table 3.1 Thermal conductivity of filler materials, reproduced from [9].

Material	Thermal conductivity ($W \cdot m^{-1} \cdot K^{-1}$)
Al_2O_3	38-42
Crystalline SiO_2	3
Fumed SiO2	1.5-1.6
ZnO	60
BN	**29-300**
Crystalline AlN	**150-220**
Si_4N_3	86-120
$BaTiO_3$	6.2

As the thermal conductivity of pp is less than 0.2 $W \cdot m^{-1} \cdot K^{-1}$, two potential filler materials with high thermal conductivity are initially selected in the proposed research, namely, BN and AlN. As discussed, these two metal-nitrides provide better hydrophobicity to their nanocomposites than many metal oxide fillers under humid conditions, making them ideal choices to meet our aim to increase the thermal conductivity of PP while maintain or improving electrical properties.

3.1.3 Surface Functionalisation Consideration

The most common and stable crystalline of BN is in its hexagonal phase, which has a honeycomb laminate structure with a functional-group-free plane on both sides. Hydroxyl and amino groups can only be found on the edge of the "plate", as illustrated in Figure 3.2. This means most surface areas are not covered by any surface group, which is not ideal for silane functionalisation [109]. In this study, alter the surface chemistry of nanoparticles with the help of the SCA is the proposed method in investigating the interphase properties. The unique feature of BN will limit the change of its surface chemistry by silane functionalisation. The high aspect ratio of commercially available h-BN will also hide the relationship between bulk properties and interfacial region behind the property changes caused by the aspect ratio itself.

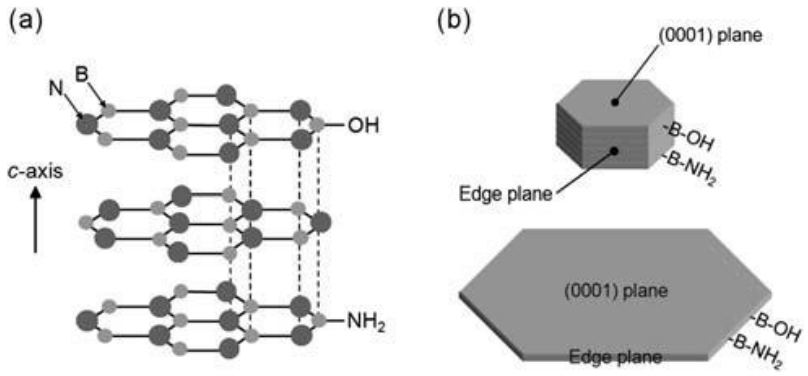

Figure 3.2 a) Crystalline structure, b) Honeycomb "plate" structure of the hBN nano-particle [108].

Unlike hexagonal BN mentioned, nano-AlN particles usually have an irregular structure and a uniform surface group distribution. Baraton and Gonsalves have studied the surface chemistry of nanostructured AlN powder; hydroxyl and amine groups were found on the surface of AlN, as shown in Figure 3.3 [110, 111]. The presence of hydroxyl groups is usually related to the hydrolysed layer with $Al(OH)_3$ formed surround AlN when reacting with H_2O in air. Although the hydrolysis of the AlN is often considered an undesired feature, the pendent hydroxyl groups from $Al(OH)_3$ layer provide a vital capability for silane functionalisation in this work. Therefore, nano-AlN is finally selected for this work.

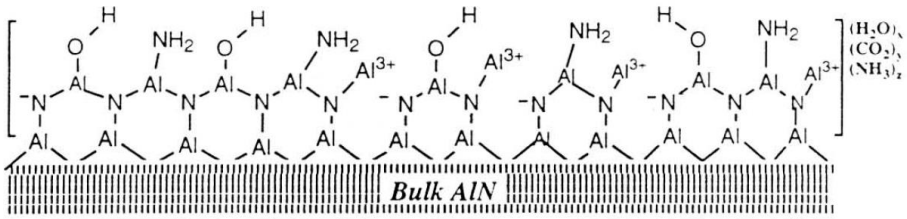

Figure 3.3 Surface chemistry of nanostructured AlN [110].

3.1.4 Summary

Upon discussion, the reason why AlN is selected In this work can be concluded as follow,

- Nitride-based fillers are reported to have reduced water absorption in nanodielectrics.
- Relatively high thermal conductivity among commonly used fillers shows a great potential to enhance the polymer insulation's thermal conductivity.
- The hydrolysed layer on the surface of AlN allows it to be functionalised with silane coupling agents. This will help investigate the role of filler surface chemistry on the interphase properties of the nanodielectrics.

3.2 Hydrolysis of AlN

3.2.1 Introduction

AlN is chemically sensitive to moisture. It can degrade thoroughly into aluminium trihydroxide from the surface to bulk, unique in metal nitride [112]. The degradation routine of AlN in moist air is shown in Equations 3.1 and 3.2 [113].

$$AlN + 3H_2O \rightarrow AlOOH_{amorph} + NH_3 \quad (3.1)$$

$$AlOOH_{amorph} + H_2O \rightarrow Al(OH)3 \quad (3.2)$$

Although the AlN blended in the polymer is reported to have a negligible weight increase after immersing in water over 300 hours, studies revealed the AlN powder would start to degrade after only 50 h (incubation period) exposed to the moist air (80 RH%) [96, 113]. The incubation period is reported to be related to the synthesis method, e.g. the AlN prepared by carbothermal-nitridation method shows a significantly longer incubation period than the AlN prepared by direct nitridation from aluminium [113]. The authors claim that the AlN prepared with carbothermal-nitridation method have a "ϑ-alumina-like and/or thicker surface layer", which is more stable and retard the further reaction. In contrast, a "Υ-alumina-like or boehmite-like surface layer" formed surrounding the AlN prepared with the direct nitridation and CVD method show limited ability to prevent water diffusion [113]. Unfortunately, the data of synthesis details for most commercial-available nano-AlN are usually not provided by manufacturers. Therefore, a comprehensive study of the surface chemistry of the as-received AlN must be taken, and the degree of hydrolysis must be understood.

3.2.2 Inconsistent Particle Size Distribution

It is worth mentioning that many inconsistent particle size distributions between lab observations and the data provided by suppliers have been reported for AlN particles [96, 114, 115], e.g. the size distribution of AlN in [96] was observed to vary from nano to micro size. The lower water uptake of its nanocomposites could result from the small particle surface area due to the varied particle size distribution rather than the surface properties. Here we suggested that the various particles size distribution could be related to the hydrolytic instability of AlN powders. Li et al. reported that the morphology and particle size distribution of the AlN microparticles are significantly changed after exposure AlN to moist air (80 RH%) for 400 h; see Figure.3.4 [113, 116].

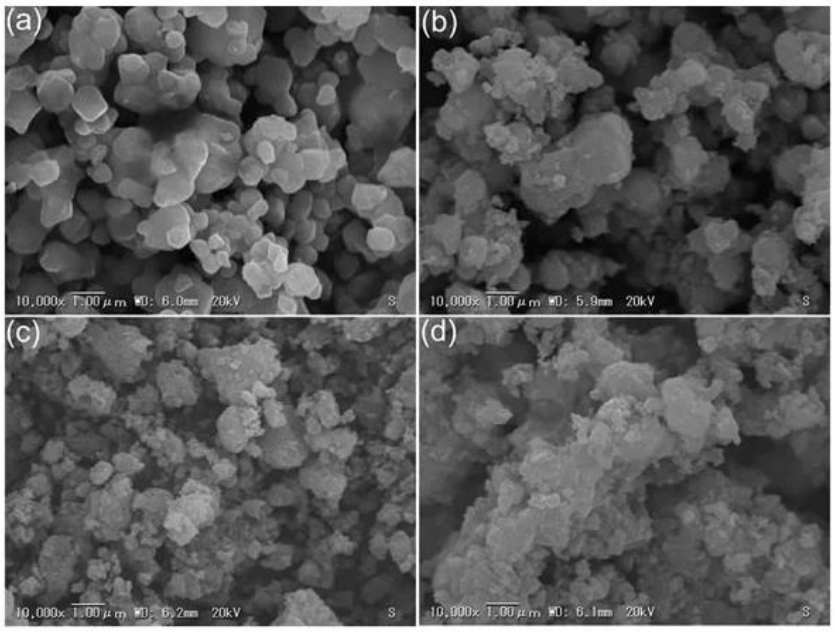

Figure 3.4 SEM of as-received AlN and AlN under 80 RH% for 400 h, a) 0 h, b) 50 h, c) 150 h, and d) 400 h (approx.), reproduced from [116].

This unique feature of AlN is challenging for us to keep the consistency of the sample making. Although the particles size can be identified via microscopic technique, issues related still need to be solved, which are,

- How to prevent the hydrolysis of the as-received AlN during storage and avoid the morphology change?
- How to confirm the effectiveness of the prevention method applied?
- How to prevent the hydrolysis of AlN during the sample preparation?

3.2.3 Hydrolysis in Aqueous Solution

The hydrolysis of AlN is usually more active in aqueous solutions. Kocjan et al. proposed a reaction course of AlN powder in aqueous suspension, shown in Figure. 3.5, where various products can form under different temperatures and times [117]. The authors also claimed in a different work that the controlled hydrolysis of AlN could be a powerful tool in advanced materials engineering, e.g., "an extremely facile synthesis strategy for fabrication of hierarchically‐assembled, mesoporous alumina powders" can be achieved with the help of the self-driven hydrolysis of the AlN, see Figure 3.6 [112, 118]. But in this work, this feature is considered a nuisance. The potential sample preparation method is limited due to this, and additional efforts are needed to maintain the consistency and the reproducibility of the samples making.

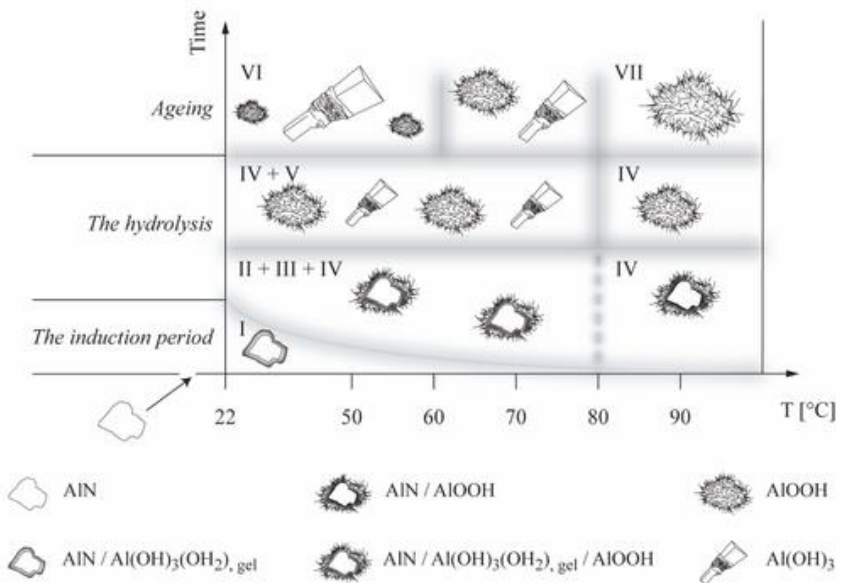

Figure 3.5 Mechanistic model for the degradation of the AlN powder in dilute aqueous suspensions [112, 117].

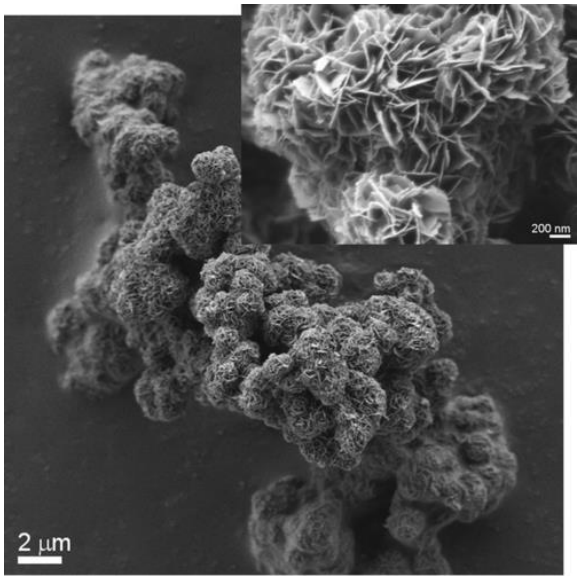

Figure 3.6 SEM micrograph mesoporous alumina powder, which is a product of the hydrolysed AlN [118].

3.2.4 Hydrolysis Prevention and Characterisation Strategy

The hydrolysis of the AlN can be prevented. Carboxylic acid treatment on the surface of AlN is one the most commonly used method to prevent or hinder the hydrolysis of the AlN [112]. The presence of organic tails on the AlN surface can prevent the approach of the water molecule to the AlN surface. Besides organic coating, inorganic treatment uses are reported to form a protection layer in various ways. For example, the formation of a phosphate-based surface layer can prevent the

hydrolysis of AlN when dispersing it in a phosphoric acid aqueous solution [112, 119, 120]. In this study, the as-received AlN is expected to have no additional treatment since these treatments may introduce uncertainties during surface functionalisation with SCA. However, it cannot be ruled out that the as-received AlN has been treated for preventing hydrolysis by the manufacturer without noticing.

Assuming an AlN with a non-degraded surface is impractical, since the water molecule can be found everywhere during production, packaging, delivering, etc., the as-received nano-AlN can have a varied range of morphology and surface chemistry, which may differ from the manufacturer's data and depends on the synthesis process and the degree of its degradation. To avoid the inconsistency result from the AlN hydrolysis, a hydrolysis prevention & characterisation strategy is delivered in this chapter, along with a thorough study of as-received nano-AlN,

- To avoid the uncertainties from the hydrolytic instability of AlN, the as-received AlN is stored in a glass bottle and protected by nitrogen gas. Further, the bottled nano-AlN is placed in a vacuum desiccator with vacuum checking regularly to minimise the hydrolysing degradation.
- The handling, such as weighing and mixing, is executed in a dry nitrogen atmosphere inside a glove bag.
- An anhydrous silane functionalisation method is selected to avoid the hydrolysis of AlN during the surface treatment, where dry toluene is used as the solvent, see section 3.4.
- The solvent used for dispersing AlN and mixing with PP is dried xylene due to its non-polar feature and low water content.
- Scanning electron microscope (SEM) & Transmission electron microscopy (TEM) is applied to identify the morphological characteristics of the as-received AlN used in this work, namely size and shape.
- Fourier-transform infrared spectroscopy (FTIR) is used to examine the surface chemistry of the AlN. It is a powerful tool that can provide distinct features related to the surface groups of the AlN.
- Thermogravimetric analysis (TGA) can show the degree of the hydrolysis degradation of the as-received AlN following Equation 3.3. For silane functionalised AlN, TGA can also identify the amount of the silane couple agent grafted on the AlN surface.

$$Al(OH)_3 \; or \; AlOOH \xrightarrow{calcination} Al_2O_3 + H_2O \tag{3.3}$$

- X-Ray Diffraction (XRD) analysis can provide the crystallographic structure of the as-received AlN. The AlN hydrolysis products can differ, and the combination of this technic with TGA and FTIR can give a more comprehensive picture of the as-received AlN.

- Hydrolysis degradation analysis of AlN in the water at 20 and 80 °C will help to understand the possible product of the hydrolysed AlN and the potential source that provide inconsistency.
- A hydrolysis degradation analysis of AlN in air last 26 months is delivered. This will help to verify the effectiveness of the prevention methods adopted.

The details of the experimental conditions listing above (SEM, TEM, FTIR, TGA, and XRD) can be found in Appendix A.

3.3 Investigation of the As-received AlN

The AlN used in this work is obtained from Aladdin Industrial Corporation Shanghai, China, with a quoted average of 50 nm and a metal-based purity of 99.9%.

3.3.1 Morphology (SEM & TEM)

Sample for SEM was prepared by brushing as-received powder onto a conductive tape attached to a pin-type SEM mount. It was then coated with gold by a sputter coater. TEM sample was prepared by dispersing as-received AlN in isopropyl alcohol in a water sonication bath for 20 min before being transferred onto a standard carbon film-coated Cu TEM grid.

The SEM image of the as-received AlN is shown in Figure 3.7. Particles and "clumps" from nano-size to up to 20-30 μm can be observed. It is common for AlN nanoparticles to have a wide range of particles size distribution. Similar results were also reported where the AlN are obtained from different manufactures [96, 115]. However, it would be opinionated to claim that it contains a large number of microparticles because those large entities could be agglomerations of nano-AlN as no sharp edges and clear crystal structure can be observed. Nanoparticles are favoured to form agglomeration, which makes morphology, and the size of single particles cannot be unambiguously identified from SEM. When considering the hydrolysis of the AlN, the presence of the large clumps can also be related to the formation of the hydrolysed product of the AlN. Therefore, further analysis is necessary until any conclusion is made.

Unlike the SEM technique is showing the surface of the samples, TEM offers images created by the transmitted electrons that give more details about the "inner" morphology of the samples. The TEM micrograph of the as-received AlN is shown in Figure 3.8. The shapes of the nanoparticles vary from rods to plates, with the size is within 20 to 60 nm. Lamellar structure on plate particles can be found in the zoom-in image (Figure 3.8b). The above results are in line with the literature where the nano-AlN from the same manufacturer was used [121]. The diverse synthesised morphological structures are usual for AlN, related to the synthesis process [122]. Both rod-like and plate structures of AlN have been reported elsewhere [122-124]. However, as mentioned in Section 3.2.1, various

hydrolysis products of AlN can exist, such as AlOOH and Al_2O_3, and similar structures (a combination of rod and plate) can also be found in γ-Al_2O_3 [125].

With the combination of SEM and TEM, the morphology structure of the as-received AlN is clarified. The results suggested that the micro-sized clumps observed on SEM are more likely to be the agglomerations or aggregations of the nanoparticles. But the composition of these nanoparticles needs further study.

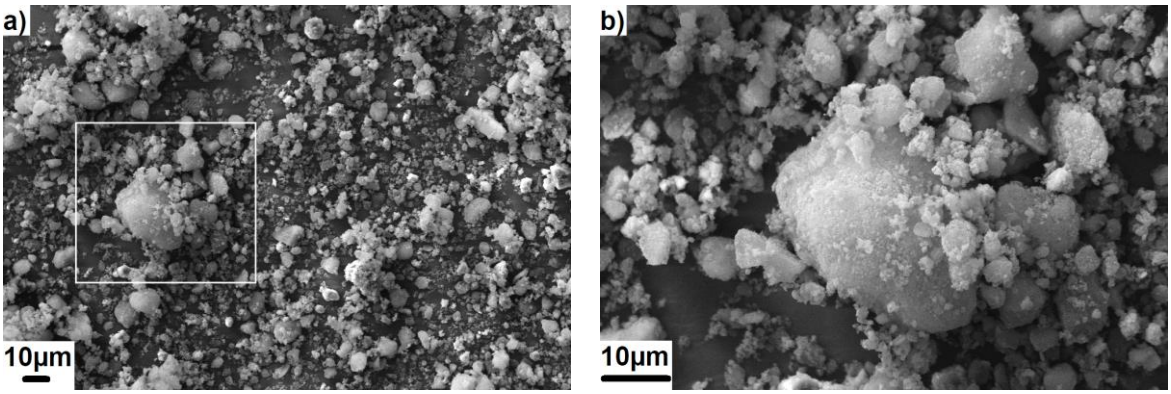

Figure 3.7 SEM micrograph of (a) as-received AlN, (b) selected area of (a).

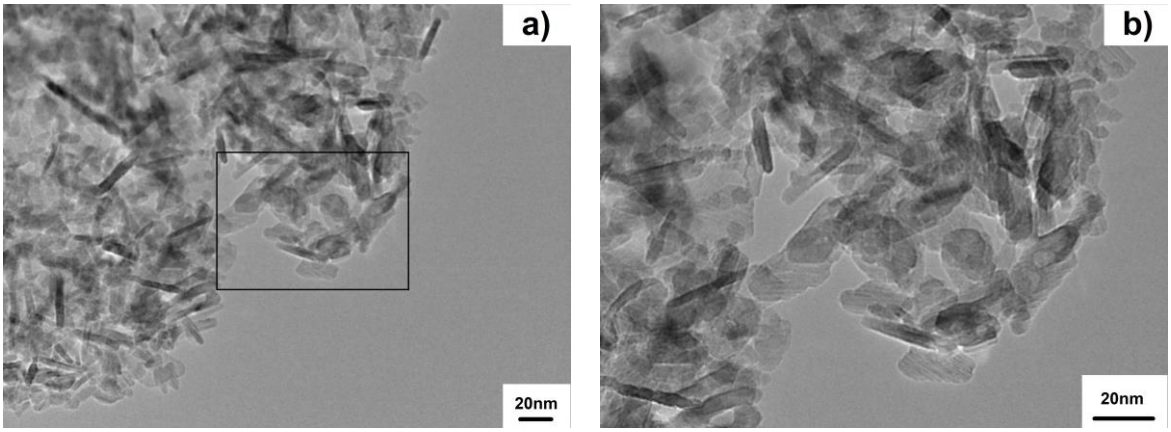

Figure 3.8 TEM micrograph, (a) as-received AlN, (b) selected area of (a).

3.3.2 FTIR

The FTIR spectrum of the as-received nano-AlN is shown in Figure 3.9 (the detailed conditions of the FTIR experiment can be found in Appendix A). No apparent features of the organic coating can be seen, which indicates the as-receive AlN is less likely to be treated with organic modifiers to prevent the hydrolysis of the AlN. The FTIR spectrum shows two prominent absorption peaks in the

wavenumber range from 4000 to 425 cm^{-1}. The most substantial absorption peak at 483 cm^{-1} corresponds to the stretching vibration of the aluminium-oxygen bond (δ_{as} Al-O) [126, 127]. However, the peak corresponds to the Al-N vibration range of 780 to 650 cm^{-1} cannot be clearly identified [128-130]. This feature might be related to the attenuated total reflection (ATR) mode used in FTIR analysis. The data from ATR mode will emphasise the feature of the particle surface rather than the material in bulk. Therefore, the feature of Al-N vibration is hidden behind the broad peak from 1000 to 483 cm^{-1}, which confirms the existence of the hydrolysed surface layer of AlN particles.

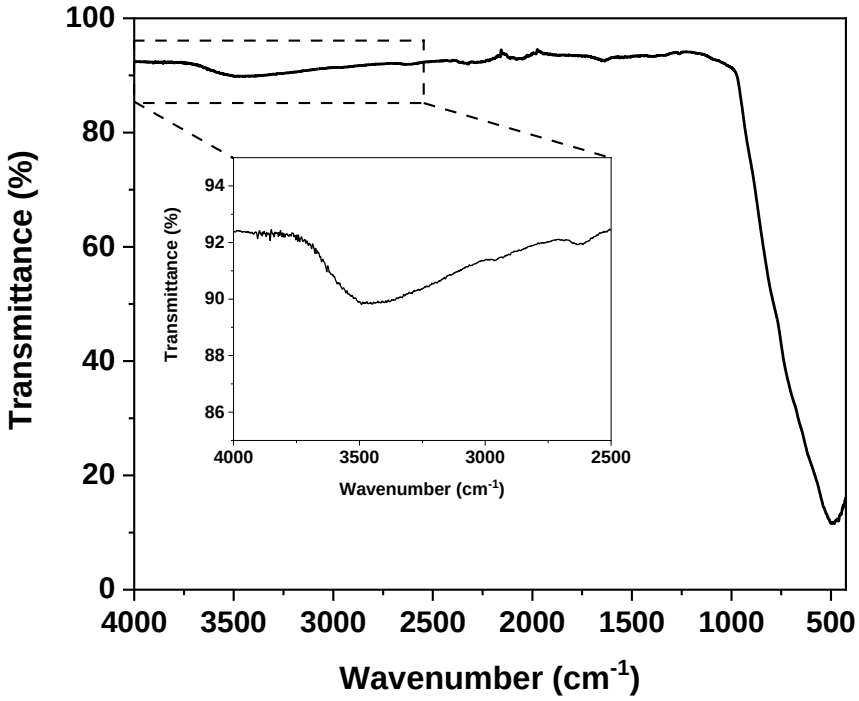

Figure 3.9 IR spectrum of as-received AlN.

The broad peak centred at 3465 cm^{-1} is a characteristic absorption peak of the hydroxyl group and the H-bonded water [131]. The presence -OH is consistent with the analysis given above; an oxidised layer surrounding the AlN core is evident. It is common to see water molecules bonded onto the surface of metal oxides and nitrides with an oxidised layer. They can come from any process during production, packing and delivery. It is worth mentioning that ammonia (NH_3) can also bond to particle surface through NH···O or hydrogen bond. Thus, it is reasonable to believe there are also absorbed ammonia on the particle surface since it can originate from the hydrolysis of AlN, see Equation 3.1 & 3.2. Both the stretching vibration of NH from ammonia and -OH from H-bonded water fall in the range of 3300-3200 cm^{-1} [110]. However, ammonia has strong characteristic peaks at ~950 and 1650 cm^{-1} (NIST Chemistry WebBook, SRD 69), and the related

features cannot be found at the IR spectrum of as-received AlN. This indicates the assumption of absorbed ammonia on the AlN surface is not valid in this case, and the broad peak centred at 3465 cm^{-1} is solely related to the -OH and H-bonded water.

3.3.3 TGA

The TGA of as-received AlN powder is performed in a dry nitrogen gas flow. This gas flow might introduce a risk of nanoparticle contamination of the furnace chamber if the powder is placed directly on the testing balance. Thus, the powder was first dispersed in toluene before being dropped onto a weighing balance. The isothermal solvent evaporation process at 110.60 °C for 30 to 60 min was applied to evaporate the solvent. After this, particles will form a stable pellet structure with hydrogen bonding. A temperature scan starts from 120 to 900 °C is performed on the resulting pellet with a temperature increasing rate of 10 °C/min. The TGA and derivative TGA of the temperature scan is shown in Figure 3.10.

After being heated to 900 °C, AlN has 96.4 % of the weight remained. The 3.6 % of the mass loss can be ascribed to removing 1. absorbed molecules, such as water, ammonia and carbon dioxide; 2. dehydration of AlOOH and $Al(OH)_3$ to alumina (Equation 3.3); 3. loss of hydroxyl and amino groups on the particle surface. The temperature range of the above processes can overlap, and the derivative curve is plotted to get a better understanding. From the derivative curve shown in Figure 3.10b, a sharp peak at 128 °C is related to the absorbed molecules, such as toluene residue and water bonded on the particle surface. The results indicate the drying temperature at 110.60 °C is insufficient for removing the solvent residues. A broad peak from 140 to 300 °C is evident, assigned to the dehydration process of AlOOH and $Al(OH)_3$, where a peak on the derivative curve usually centred around 200 to 300 °C [113].

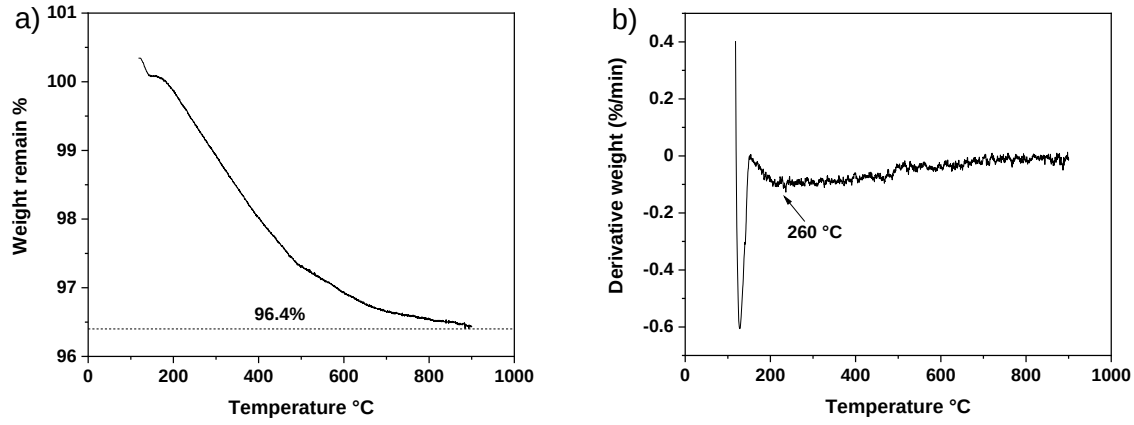

Figure 3.10 a)TGA, and b)Derivative TGA plot of AlN from 120 to 900 °C.

3.3.4 XRD

The XRD pattern of as-received AlN is shown in Figure 3.11 (The detailed condition of the XRD experiment can be found in Appendix A). The typical different diffraction peaks assigned to (100), (002), (101), (102), (110), (103), and (112) crystal planes of hexagonal AlN could be found at 2ϑ value of 33.2°, 35.8°, 37.7°, 51.7°, 59.3°, 66.1°, and 71.0°, respectively. However, there is a peak observed at 2ϑ =46.2°, and another merged one at ca. 2ϑ=67.2, which represent the (400) and (440) peaks of γ-Al_2O_3 [132]. The existence of this kind of γ-Al_2O_3, which can be a calcinated product of hydrogenated boehmite as expressed in Equation 3.4, suggests that the as-received AlN was partially hydrolysed before a calcination process during the manufacturing process. The presence of γ-Al_2O_3 can be related to the synthesis techniques of AlN. The dehydration process (calcination) of the surface hydrolysed AlN is reported to form an alumina shell and hinder further hydrolysis [133, 134]. A similar calcination process can be found in many AlN synthesis methods as the last step, e. g. the carbon residue will need to be burnt off at 700 °C in a carbothermal synthesis method [135].

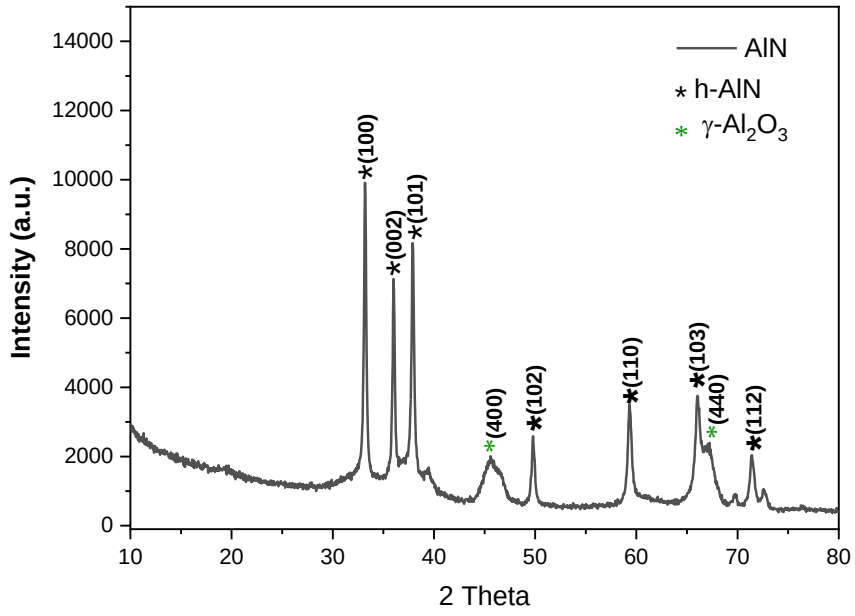

Figure 3.11 XRD pattern of as-received AlN.

$$boehmite\ or\ amorph\ Al_2O_3 \xrightarrow{calcination} \gamma - Al_2O_3 \tag{3.4}$$

No noticeable features of AlOOH and $Al(OH)_3$ crystal structure can be found in XRD patterns, which means the hydrolysis product of AlN is mostly amorphous AlOOH. When combining TGA and XRD

results, it is evident that the as-received AlN contains hexagonal AlN, amorphous AlOOH, and *γ*-Al_2O_3. However, due to the presence of the *γ*-Al_2O_3, the ratio of the AlN and amorphous AlOOH (the degree of the hydrolysis of AlN) cannot be deduced from the TGA results directly. A hydrolysis degradation analysis is conducted in the next section to investigate the hydrolysis behaviour of the as-received AlN. The results can be helpful to understand the hydrolysis degree of the as-received AlN.

3.3.5 Hydrolysis of AlN in Water

0.2 g of the as-received AlN was dispersed in 10 ml of deionised water for 24 h with two storage temperatures were selected, 20 °C and 80 °C. After that, the hydrolysed AlN was separated from water with a filter. After drying in a vacuum oven for another 24 h, SEM, TGA and XRD were conducted to characterise the hydrolysed AlN.

The SEM image of the AlN hydrolysed at different temperatures are shown in Figure 3.12. Both AlN hydrolysed at 20 & 80 °C shows a significant change in the morphology compared to the results of the as-received AlN shown in Figure 3.7. In Figure 3.12a, triangle-shaped crystals can be observed, a similar structure was observed [136], and the authors suggest it could be related to the formation of $Al(OH)_3$ polymorph bayerite. Kocjan et al. have studied the hydrolysis of AlN powder in dilute aqueous suspensions at different temperatures. The formation of bayerite is reported to be the last stage of an amorphous aluminium hydroxide gel – boehmite – bayerite reaction course of the AlN with water at 22 °C [137]. However, at a high temperature (90 °C), where only boehmite can be observed, and the authors explain that boiling of the suspension is restricting the formation of bayerite. In this study, prismatic and chamfered faces crystals can be observed when AlN hydrolysed at 80 °C (Figure 3.12b), which is one of the typical structures of gibbsite ($Al(OH)_3$) [136, 138, 139].

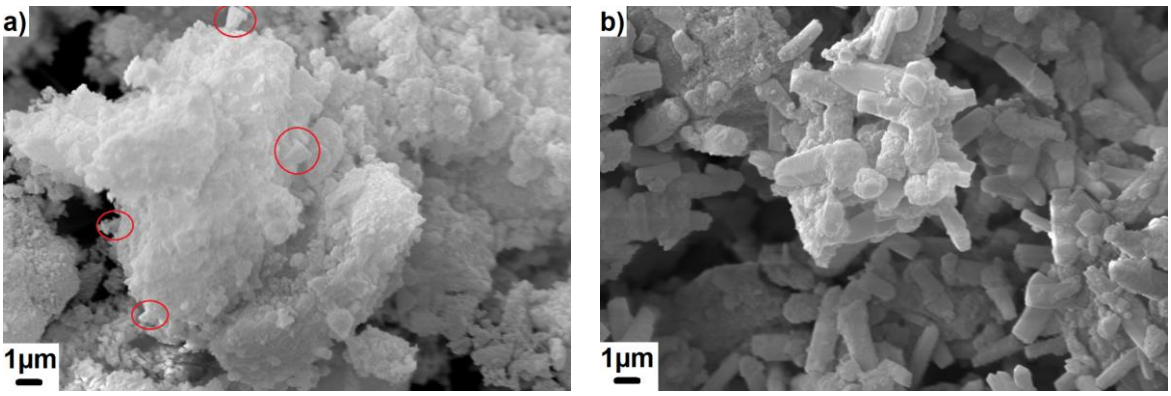

Figure 3.12 SEM micrograph of AlN hydrolysed at a) 20°C, and b) 80°C.

The TGA results of the AlN powder hydrolysed at 20 & 80 °C is shown in Figure 3.13. A temperature scan starts from 50 to 600 °C is performed on the hydrolysed AlN with a temperature increasing rate of 20 °C/min (in order to better compare with [113], the same experimental set-up was adopted). The hydrolysed AlN have a significant weight decrease from 200 °C to 350°C. This is assigned to the degradation of Al_2O_3/AlOOH [113]; see Equation 3.5 & 3.6. For AlN hydrolysed at 80 °C, the weight loss between 200 °C to 350°C is 17.2 %. If assuming AlN was hydrolysed entirely into $Al(OH)_3$ at 80°C, according to Equation 3.5 and the amount of water loss (17.2 %), the AlN content in the as-received powders is 50 %. Due to the possible existence of AlOOH, this value should be higher than 50 %. Therefore, we may conclude that at least 50% of AlN is not hydrolysed in the as-received AlN.

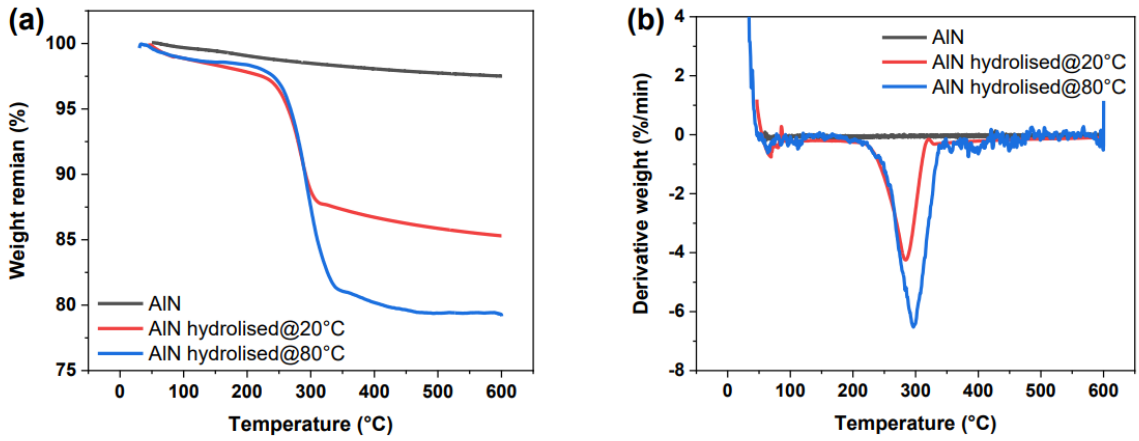

Figure 3.13 a)TGA, and b)Derivative TGA plot of hydrolysed AlN from 50 to 600 °C.

$$2Al(OH)_3 \triangleq Al_2O_3 + 3H_2O \quad (3.5)$$

$$2AlOOH \triangleq Al_2O_3 + H_2O \quad (3.6)$$

The XRD pattern of the hydrolysed AlN is shown in Figure 3.14. The presence of $Al(OH)_3$ is evident for hydrolysed AlN. The typical features of $Al(OH)_3$ can be found in both samples, but the intensity of these features is more significant in AlN hydrolysed at 80 °C, which suggests more AlN transferred to $Al(OH)_3$ at 80 °C when reacted with water [140, 141]. In contrast, the XRD pattern of AlN hydrolysed at 20 °C shows stronger diffraction features of h-AlN, and these features are can be barely seen in the 80 °C samples. We may conclude that most of the AlN are hydrolysed in the water at 80 °C within 24 h, and the transfer from h-AlN to $Al(OH)_3$ has a lower reaction rate at 20 °C in an

aqueous solution. It should be noted that in both spectra, the peaks correspond to γ-Al_2O_3 are identical in samples hydrolysed at different temperatures. It is because the γ-Al_2O_3 from the as-received AlN does not react with water.

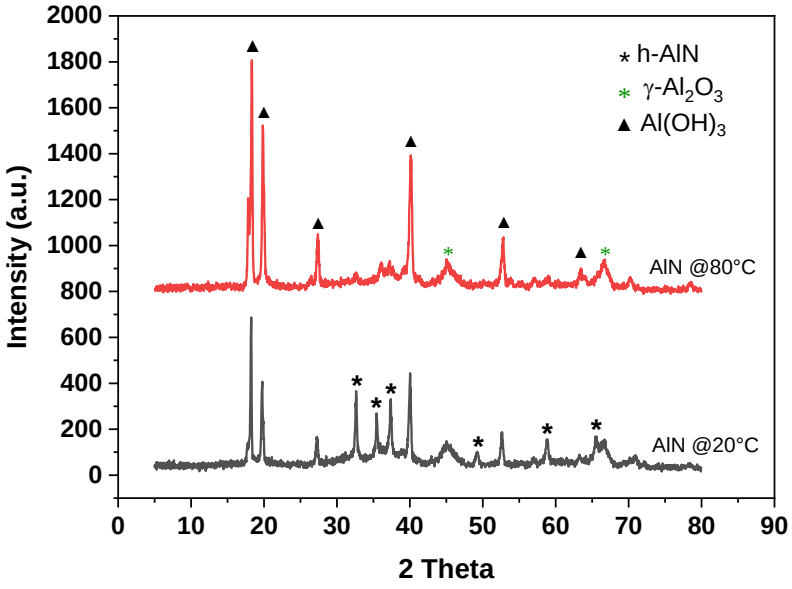

Figure 3.14 XRD spectra of AlN hydrolysed at different temperatures.

3.3.6 Hydrolysis of AlN in Moist Air

The hydrolysis degradation analysis of AlN in the air is important to this work. The length of this project will last for more than two years, and the AlN received from the manufacture will be used for making samples during this long period. Therefore, to ensure the consistency of the material, the AlN stored with and without the protection method have been studied. For AlN stored in a desiccator and protected with nitrogen gas after 26 months, no significant change from the as-received AlN can be identified from the SEM and TGA results in Figure 3.15. In contrast, AlN stored in a lab storage room with humidity ranges from 20 to 80 %RH shows changes in various aspects. The first thing that can be observed is the colour shifted from grey to white (Figure 3.15a), which is related to the presence of the hydrolysed layer. From SEM results in Figure 3.15 b & c, the size of the particle agglomerations is reduced after AlN is exposed to moist air, but no clear crystal structure of the hydrolysed product such as $Al(OH)_3$ and AlOOH can be found.

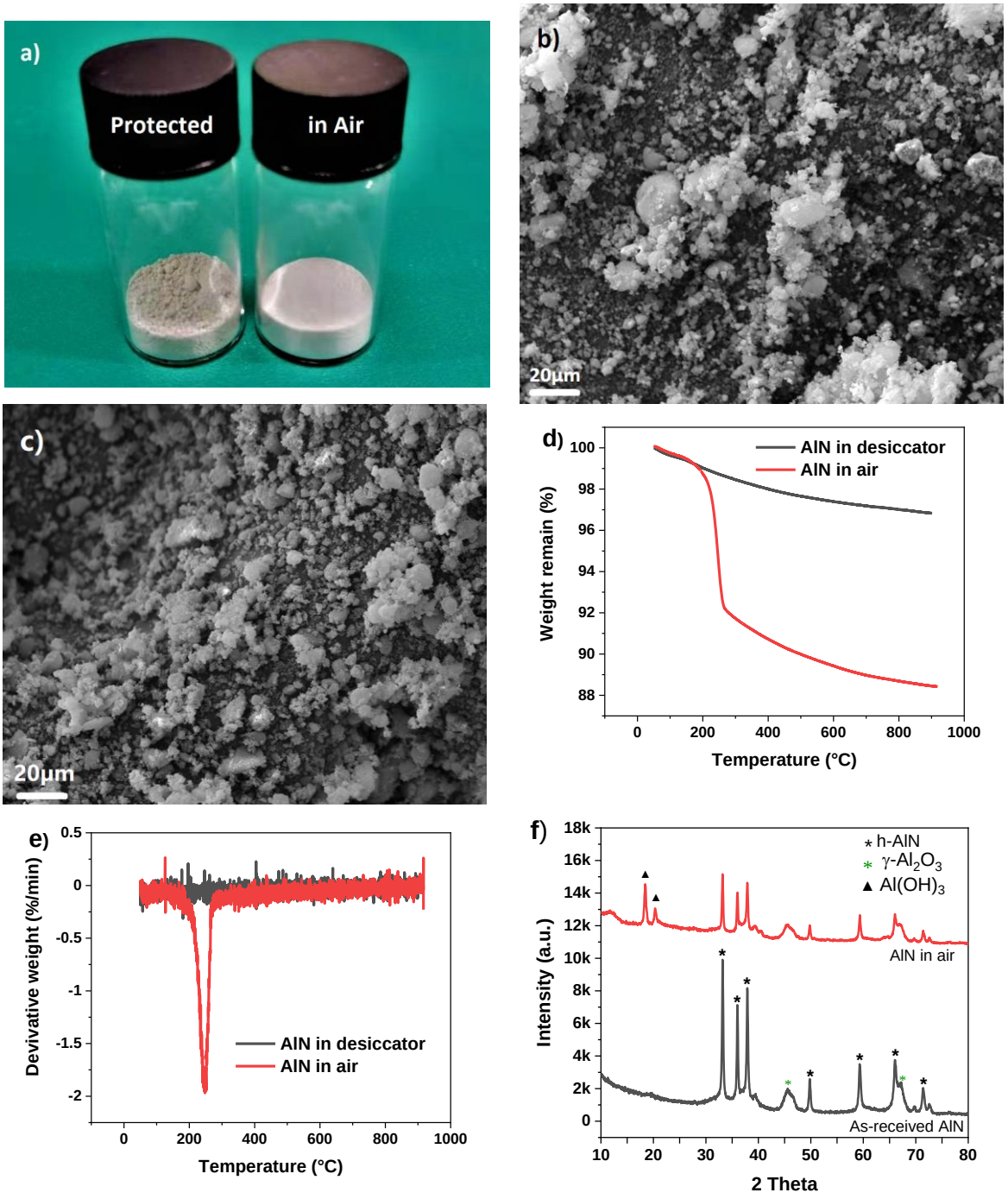

Figure 3.15 A combination results of a) the colour change of AlN with different storage conditions, SEM image of AlN b) with, and c) without protection method, d & e) TGA results of AlN with different storage conditions, and f) XRD results of AlN without protection method.

From Figure 3.15 d & e, the sharp weight loss on TGA results of AlN in the air from 200 to 300 °C is the degradation of the $Al(OH)_3$ and AlOOH, which contribute an additional 8 % of the weight loss. From the XRD result of the hydrolysed in the air in Figure 3.15f, the presence of the $Al(OH)_3$ is clear, and the features related to h-AlN show a reduced intensity, which proved the transition from h-AlN

to $Al(OH)_3$ after exposure to moist air during 26 months. The above features related to hydrolysed AlN cannot be found in the AlN when the protection method was applied, which indicates that the adopted method can successfully prevent the hydrolysis of the AlN.

3.3.7 Summary

Upon analysis, we can summarize that,

- The As-received AlN vary from rods to plates, with the size is within 20-60 nm, but large agglomerations up to 20-30 μm can be observed.
- Slight hydrolysis occurred, and a layer of *γ*-Al_2O_3 and amorphous AlOOH formed around as-received AlN. *γ*-Al_2O_3 could come from the calcination process during manufacturing.
- The hydrolysis analysis in the water proved that there are at least 50 % of AlN is not hydrolysed in the as-received AlN.
- The hydrolysis analysis in air confirmed the hydrolysis prevention methods could successfully restrict the hydrolysis of as-received AlN for a long period (26 months), ensuring the consistency of the sample making.

3.4 Silane Functionalisation

3.4.1 Introduction

Inorganic nano-fillers usually have a polar structure and inherently low compatibility with organic polymers. SCA is usually used to increase the adhesion between organic and inorganic materials. The surface chemistry of inorganic fillers can be altered dramatically after grafting such molecules onto the surface [142-145]. The general chemical formula of SCA is shown in Figure 3.16. The organofunctional group R may form a durable bond, such as a covalent bond, with the organic polymer material, e.g., the epoxide group could bonding with the epoxy matrix during the curing process [65]. In contrast, the hydrolysable group can form a covalent bond by displacing a hydroxyl group on the inorganic surface in two different ways, namely the hydrolytic and anhydrous methods [146].

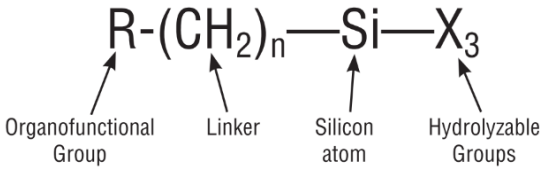

Figure 3.16 A general chemical formula of SCA [144].

The selection of SCA is usually based on the compatibility between its organofunctional group and the polymer matrix, e.g., the epoxide silanes are widely used in epoxy nanocomposites, since the formation of the covalent bond can bring many valuable properties, like the increased AC breakdown strength [142, 147, 148]. Although some studies believe methacrylic silanes can form covalent bonds with PP [142, 149], there is still a lack of convincing evidence that shows that any SCA can form covalent bonds with PP in the same way as observed in epoxy. Zhao et al. demonstrated that methacrylate silane could enhance interfacial interaction between inorganic filler and PP host [149]. The mechanical properties, such as the tensile strength, are noticeably improved. Still, in our case, the introduction of polar groups like methacrylate might result in little or no change in terms of the hydrophobicity of the nanocomposites. Alkyl silanes are considered a good choice since the repeating $(CH_2)_n$ structure of its organofunctional group can provide compatibility with PP. Their non-polar nature is also expected to confer favourable degrees of hydrophobicity. Upon discussion, two different organofunctional groups are selected in this work, listed in Table 3.2. They are expected to provide different interactions between nanoparticles and the PP matrix.

Table 3.2 The options of the organofunctional group for SCA [142, 149].

Name	2D Structure	Reason	Polarity
Octyl group	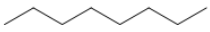	Octyl groups are intended to aid the dispersion and do not chemically interact with PP.	Non-polar
Methacryl group	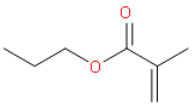	It is believed that the unsaturated double bond in methacrylic silanes could react with hydrocarbon matrices of PP, improving the interfacial interaction between the polymer and inorganic fillers.	Polar

Apart from the organofunctional groups, the grafting layer's microstructure can also lead to a change in bulk properties. Yeung et al. reported that the AC breakdown strength and the complex permittivity of silica-epoxy nanocomposites were related to the thickness of the silane layer [148].

This allows us to think the interactions between SCA and nanoparticle surfaces can also lead to a change in bulk properties. Such interaction is provided by the hydroxyl group on the nanoparticle surface with the hydrolysable groups of SCA.

The hydrolysable group is usually alkoxy, chlorine or amine groups. Silanes with alkoxy groups are the most common, generally with one or two carbons in length, namely methoxy ($-CH_3O$) and ethoxy group ($-C_2H_5O$). The most commonly used silanes have 3 hydrolysable groups. They can bond onto the inorganic substrate and provide some degree of self-condensation depending on the reaction environment. The hydrolytic method (Figure 3.17) is the most commonly used method for silane functionalisation. During the hydrolytic process, active silanol groups are formed after the hydrolysis with water. It can condense (crosslink) and form oligomers that will form the hydrogen bond with the hydroxyl group on the inorganic surface, accompanied by the loss of water during a drying process [146].

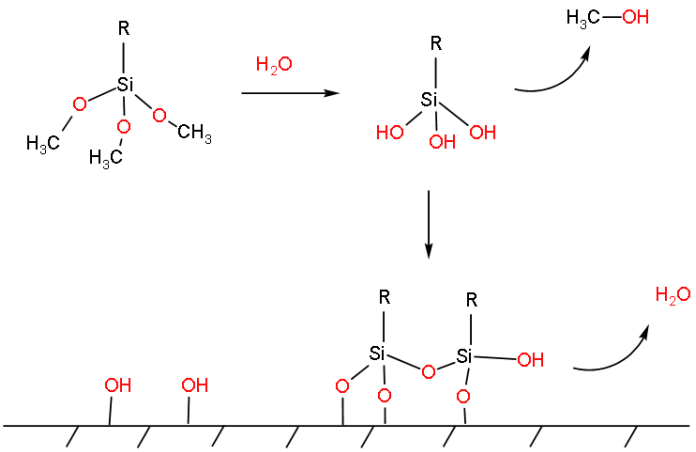

Figure 3.17 Illustration of the hydrolysis method for silane functionalisation (not to scale).

However, the hydrolytic method is not suitable for AlN. The addition of water during the surface treatment will lead to the degradation of the AlN. The condensation of SCA will also result in the formation of a thick SCA layer. In contrast, no water is needed during the anhydrous method (Figure 3.18). The crosslinking of silanes will be restricted [146]. In this work, the anhydrous method was selected for the proposed research as it can provide a more controlled manner regarding the thickness of the silane layer. Most importantly, the inconsistency related to the hydrolysis of AlN powder can be avoided [150].

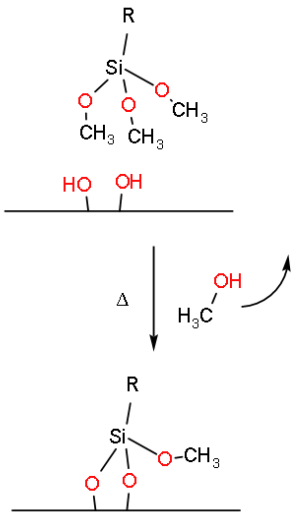

Figure 3.18 Illustration of the anhydrous method for silane functionalisation (not to scale).

The hydrolysable group is a critical factor determining the hydrolysis rate in the hydrolytic method and the grafting rate in the anhydrous method. As shown in Figure 3.19, methoxy silane can have a 7 times hydrolysis rate to the ethoxy silane [151]. Different grafting rates will lead to a distinct microstructure at the near-particle side during the silane treatment (Figure 3.20). Therefore, SCA with different hydrolysable groups were selected in this work. They are expected to provide a different near-particle structure towards the silane treatment.

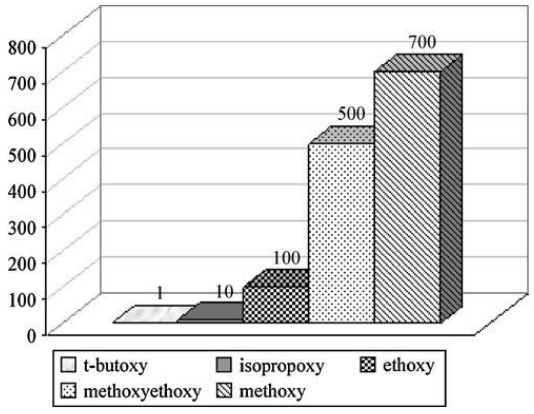

Figure 3.19 Relative rates of hydrolysis of hydrolysable groups of silanes [151]. The numbers on the y-axis are the relative ratios of the hydrolysis rate.

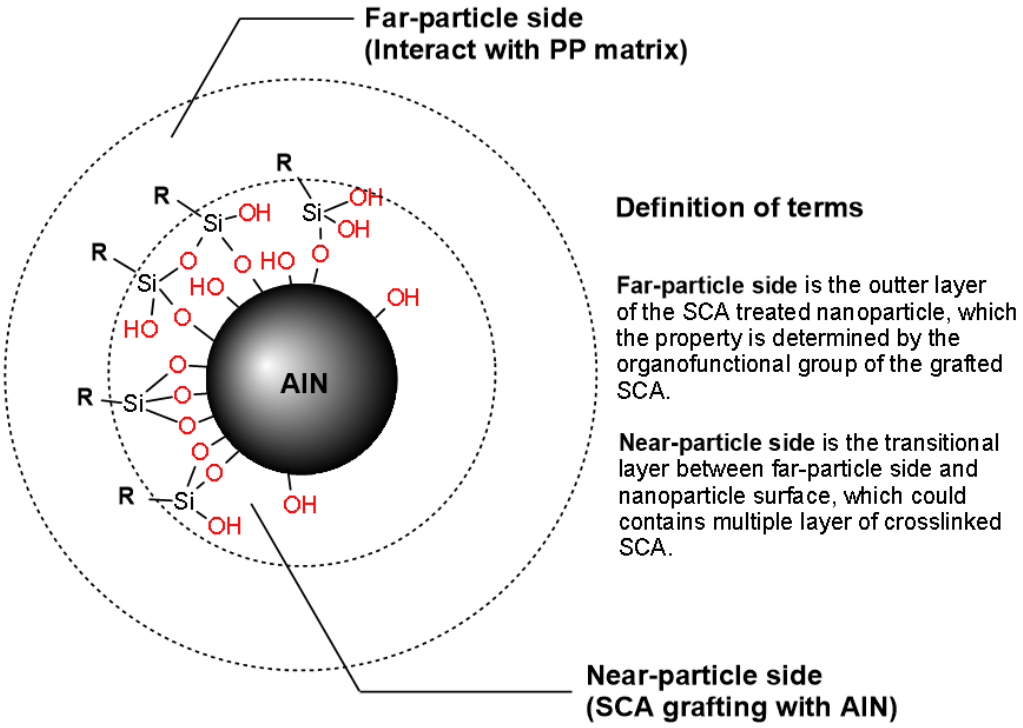

Figure 3.20 The proposed surface structure of the SCA functionalised nanoparticle (two-side model, not to scale).

The details of the SCA used in the proposed research can be found in Table 3.3. The triethoxy (octyl) silane (C8E) with quoted ⩾ 97.5 % purity and the 3-(trimethoxysilyl) propyl methacrylate (MPS) with 98 % quoted purity were purchased from Sigma-Aldrich; The trimethoxy (octyl) silane (C8M) with 97 % quoted purity was obtained from Aladdin Industrial Inc; Within them, C8M and MPS have different organo-functional group, provides different far-particle surface chemistry; C8M and C8E with different hydrolysable groups could leading to the different near-particle structure.

The work related to the Mono-alkoxy silane (MAS) is not included in this chapter; the related work can be found in Chapter 6 and Appendix B.

Table 3.3 Details of the SCA used in this work.

SCA	2D Structure	Hydroly-sable group	Organo-functional group	Density (g/ml)	M_{SCA} (g/mol)
MPS	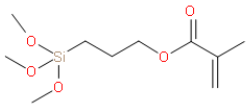	-OCH_3	Methacrylate group	1.045	248.35
C8M	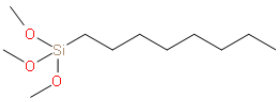	-OCH_3	Octyl group	0.907	234.41
C8E	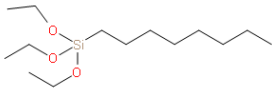	-OC_2H_5	Octyl group	0.88	276.49

3.4.2 Processing

Before the silane functionalisation, the quantity of the silane coupling agent adopted in the reaction was needed. The proposed research aims to have as much as the surface area can be functionalised. However, if an overly abundant amount of SCA were added, the superfluous SCA would tend to react with each other and form gel-like oligomers [145]. The appropriate amount was then determined by an estimation method used in [65].

It is expected that SCA can displace all hydroxyl groups on the AlN surface. Thus, the amount of SCA used can be roughly estimated by the hydroxyl group density on the particle surface. The hydroxyl groups will start to lose around 446.85 °C and cannot be entirely removed up to 700 °C but with a very low density [65, 152]. From the TGA result shown in Figure 3.10, the weight decreased by about 0.7 % in a temperature range from 446.75 to 700 °C. That means 1 g of AlN contains about 7 mg of hydroxyl groups. How many hydroxyl groups in 1 g of AlN powder can be calculated using Equation 3.10, where N_A is Avogadro number, $m_{\text{-}OH}$ is the mass of the hydroxyl groups, and $M_{\text{-}OH}$ is the molar mass of the hydroxyl group.

$$N_{-OH} = N_A \cdot v_{-OH} \tag{3.7}$$

$$v_{-OH} = \frac{m_{-OH}}{M_{-OH}} \tag{3.8}$$

$$N_{-OH} = N_A \cdot \frac{m_{-OH}}{M_{-OH}} \tag{3.9}$$

$$N_{-OH} = 6.02 \cdot 10^{23} \cdot \frac{7 \cdot 10^{-3}}{17} = 2.5 \cdot 10^{20} \quad (3.10)$$

If one SCA can displace 3 hydroxyl groups, then N_{SCA}=8.3×10^{19} of SCA molecules is required for 1 g of AlN. Therefore, the volume of SCA used, V_{SCA}, can be calculated by Equation 3.13. However, the condensation of SCA and the loss of SCA on the equipment make the actual amount needed to be more than the estimated value. So, the obtained value is often multiplied by a multiplication factor n, n=7 was applied in this work as it is an empiric value obtained by plenty of attempts (See Appendix C). Thus, the volume of SCA required can be obtained by Equation 3.14, where ρ_{SCA} is the density of SCA and M_{SCA} is the molecular weight of SCA. Equation 3.15 is an example of MPS. That means 0.23 ml of MPS will be used in silane functionalisation for 1 g of AlN powders. The calculated result for different SCA is listed in Table 3.4.

$$m_{SCA} = M_{SCA} \cdot \frac{N_{SCA}}{N_A} \quad (3.11)$$

$$V_{SCA} = \frac{m_{SCA}}{\rho_{SCA}} \quad (3.12)$$

$$V_{SCA} = \frac{M_{SCA}}{\rho_{SCA}} \cdot \frac{N_{SCA}}{N_A} \quad (3.13)$$

$$V_{SCA,E\text{empiric}} = n \cdot V_{SCA} = n \cdot \frac{M_{SCA}}{\rho_{SCA}} \cdot \frac{N_{SCA}}{N_A} \quad (3.14)$$

$$V_{SCA,E\text{empiric}} = 7 \cdot \frac{248.35}{1.045} \cdot \frac{8.3 \cdot 10^{19}}{6.02 \cdot 10^{23}} = 0.23\ ml \quad (3.15)$$

The processing route of the silane functionalisation is shown in Figure 3.21. The AlN/toluene solution was sonicated for 30 min with a Hielscher UPS200S probe sonicator at 60 % magnitude and 0.5 s pulse in a 1.0 s cycle, then stirred and sonicated for another 30 min. After that, the mixture was poured into a 100 ml evaporation flask. Simultaneously, a desired amount of SCA was dissolved in 20 ml of dry toluene and added to the same flask. The AlN/SCA/toluene mixture was then stirred by a magnetic stirrer with a heater and heated to reflux at the boiling point of toluene for 4 hours. The resulting slurry was washed with 300 ml of toluene 3 times. The centrifuging at 8000 rpm was used here to recover the nano-AlN during the washing operation. After that, the treated AlN was dried in a vacuum oven at 80 °C.

Table 3.4 The amount of SCA used in this work.

SCA	2D Structure	$V_{SCA,E\text{empiric}}\ (ml/g)$
MPS	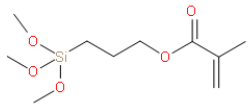	0.23
C8M	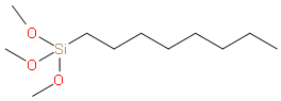	0.25
C8E	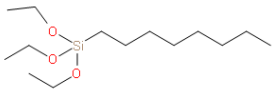	0.3

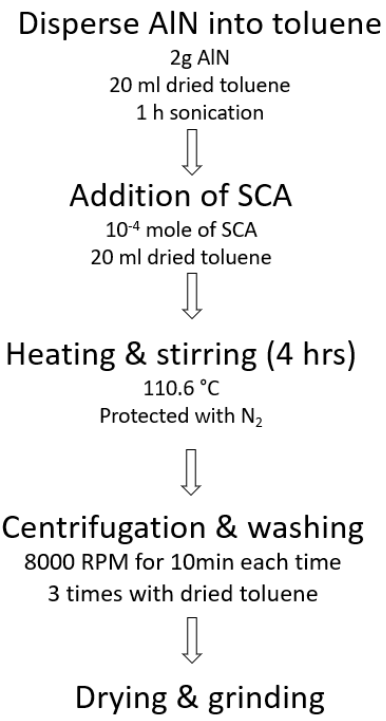

Figure 3.21 Processing route of the silane functionalisation.

3.4.3 Verification

A clear difference can be observed after the particles were surface functionalised, as shown in Figure 3.22. Due to the low compatibility between toluene and AlN with polar surface groups, phase separation is clear. In contrast, SCA functionalised AlN shows better compatibility with toluene because the surface groups have been displaced by the non-polar tails from SCA. Before the silane functionalised AlN was solvent blended with PP, the silane functionalisation was verified by TGA and FTIR. The powder/toluene mixture was first placed at the boiling point of toluene for 30 to 60

min to remove the solvent residues. Then it was heated to 900 °C at the scan rate of 10 °C/min. The TGA result of MPS functionalised AlN is shown in Figure 3.23. Compared to the non-functionalised AlN, MPS treated AlN has about 4.8 % more weight loss at the temperature range from 250 to 500 °C, which was assigned to the de-grafting of the SCA on the AlN surface. The TGA results of the non-washed AlN have a sharp weight loss that peaked at 213 °C, but not appears on the washed AlN samples. This indicates the washing process can effectively remove the non-grafted SCA. The peak at 133 °C is assigned to the loss of bonded water, where a decreased intensity can be observed after surface treatment. It is because the grafted SCA reduced the amount of water absorbed on the AlN surface.

Figure 3.22 The non-functionalised (left) and C8M functionalised (right) AlN/toluene mixture.

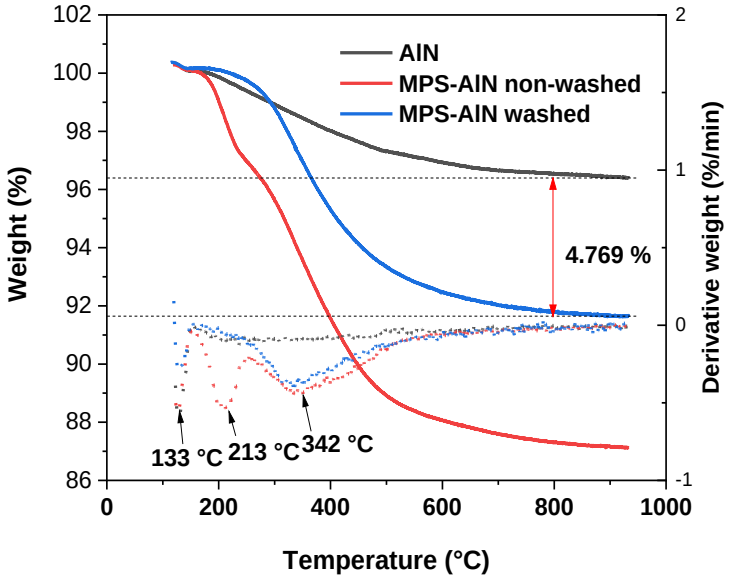

Figure 3.23 The TGA result of as-received AlN, unwashed slurry and washed mixture after silane functionalised by MPS.

A study related to the amount of SCA applied during the silane treatment is presented in Appendix C. The condensation of SCA is restricted due to the application of the anhydrous method. Therefore, the amount of grafted SCA on the AlN reaches saturation when n≥7 in Equation 3.14.

The FTIR results of MPS, C8M and C8E treated AlN are shown in Figure 3.24. These traces have been vertically offset for clarity of presentation. From the spectra of MPS treated AlN, the absorption band at 1718 and 1637 cm^{-1} associated with the stretching vibration of C=O and C=C groups [153, 154] and the two peaks at 1297 and 1170 cm^{-1} are then subjected to C-O-C from the organofunctional group of MPS [154]. From the spectra of C8M and C8E, three adjacent peaks are found at 2959, 2922 and 2853 cm^{-1}. They correspond to the asymmetric C-CH_3, asymmetric CH_2, symmetric CH_2 stretching vibrations from the C8 tail, and the peak at 1458 cm^{-1} is related to the bending vibration of -CH_3 [155]. All spectra show a distinct broad peak from 968 to 1142 cm^{-1}, related to the presence of Si-O-Si, Si-O-C and Si-OH [153]. Upon above, and combined with the TGA results in Figure 3.23, there is little doubt that all three SCA have successfully bonded to the surface of AlN and the changes of the surface chemistry by SCA treatment are significant. However, the SCA with different hydrolysable groups shows comparable results on the FTIR spectra. The hydrolysable group is expected to provide different grafting mechanisms of SCA onto the particle surface. Still, the feature of the near-particle side (Figure 3.20), Si-O-Si, Si-O-C, and Si-OH, falls into broadband (from 968 to 1142 cm^{-1}), which is difficult to differentiate.

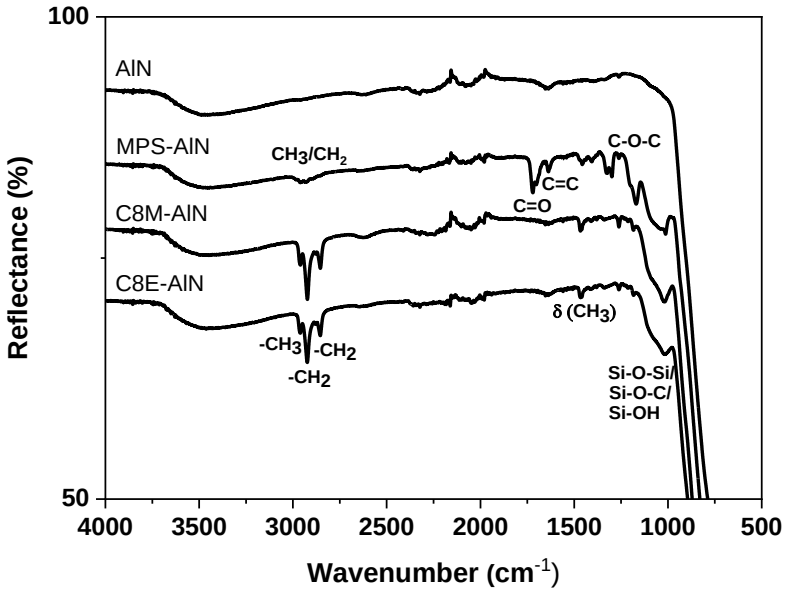

Figure 3.24 FTIR spectra of MPS, C8M and C8E treated AlN.

3.4.4 Summary

Three different SCA has been selected for the silane functionalisation, and successful grafting of these SCA on the AlN surface are confirmed by TGA and FTIR analysis. A surface structure of the SCA functionalised nanoparticle that highlight the chemical structure of the “far-particle side” and “near-particle side” has been proposed (Figure 3.20). It is confirmed by FTIR that C8M and MPS with different organofunctional groups give a distinct AlN surface chemistry on the far-particle side. C8M and C8E with different hydrolysable groups are expected to provide a different AlN surface chemistry on the near-particle side. However, the related features show no difference through the above identification methods. Therefore, further study is conducted in the following chapters to identify the structure of the near-particles side after silane functionalisation.

Chapter 4 Material Preparation, Morphology, and Thermal Properties of PP/AlN Nanocomposites

This Chapter introduce a modified solution blending method for making PP/AlN nanocomposites, and their crystal structure, filler dispersion and thermal properties are investigated.

Part of the results presented below are published in:

Wang, Xinyu, Qiang, Dayuan, Hosier, Ian, Zhu, Yanqiu, Chen, George and Andritsch, Thomas (2020) Effect of water on the breakdown and dielectric response of polypropylene/nano aluminium nitride composites. Journal of Materials Science, 55 (21), 8900-8916. (doi:10.1007/s10853-020-04635-1).

Wang, Xinyu, Andritsch, Thomas, Chen, George and Virtanen, Suvi (2019) The role of the filler surface chemistry on the dielectric and thermal properties of polypropylene aluminium nitride nanocomposites. IEEE Transactions on Dielectrics & Electrical Insulation, 26 (3), 1009-1017. (doi:10.1109/TDEI.2019.007773).

The experimental details can be found in Appendix A.

4.1 Material Preparation

4.1.1 Procedure

Solution blending is a commonly used method to produce polymers on the lab scale. When applying the solvent blending method, polymers will be dissolved in an organic solvent while nano-fillers will be dispersed in the same or another solvent. Then the solvent/polymer mixture and the nano-filler/solvent mixture can be mixed. After drying the master mixture by evaporating the solvent, the resulting blend then can be pressed into samples with desired shapes and thicknesses for different tests. In the proposed work, xylene is selected as the solvent for polypropylene since studies have proved that xylene is a suitable solvent for PP [156].

When considering the solvent that dissolves nano-AlN, xylene was selected, although the preliminary study indicated that ethanol is the best solvent for nano-AlN among 5 different commonly used solvents for nano-fillers (toluene, chlorobenzene, dichloromethane, isopropyl alcohol, and ethanol). Due to the non-polar nature and low water content of xylene can prevent the hydrolysis of AlN, the uncertainty related to the moisture content of the solvent can be eliminated. A modified form of solution blending was applied in this work, which is expected to give

a more consistent dispersion state than the method used previously [10], where a hand mixing step was included. The processing route of the solution blending method is shown in Figure 4.1.

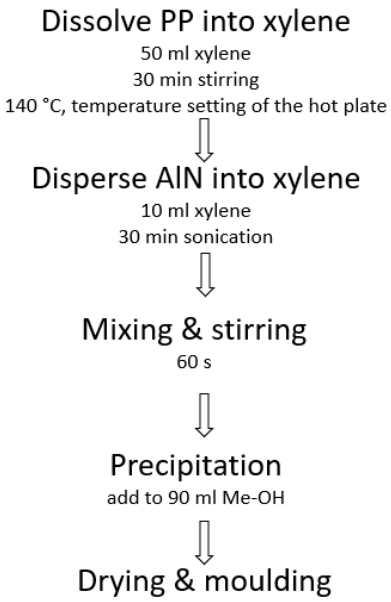

Figure 4.1 Processing route of the solution blending method.

Initially, 4.5 to 4.95 g of PP was added to 50 ml of xylene and heated at 140 °C for 30 min whilst stirring. The required amount of treated and non-treated AlN (0.05 to 0.5 g) was dispersed in 10 ml of xylene and sonicated for 30 mins. This was then poured into the PP/xylene mixture and magnetically stirred for another 60 s to avoid re-agglomeration. The PP/xylene/AlN was then removed from the heat and poured into 90 ml of methanol, inducing precipitation. The resulting mixture was dried at room temperature for 1 day after filtration. It was then put in a vacuum oven at 80 °C for 3 days to remove any trace of the solvent. The obtained composites were pressed at 180 °C into sheets, then further processed and pressed into film samples (quenched in water, 20 °C) suitable for different tests.

4.1.2 Sample Names

Samples are denoted as X-Y in this chapter, where X represents the surface states of AlN fillers, either C8M, C8E, MPS, and N or Non (non-treated AlN); Y is the loading ratio by wt. % either 1, 2.5, 5 or 10, e.g. C8M-5 is PP filled with 5 wt.% of C8-M treated AlN. Reference PP without AlN is referred to PP. Details can be found in Table 4.1.

Table 4.1 Processing route of the solution blending method.

Sample	Treatment	Loading (wt%)	Sample	Treatment	Loading (wt%)
PP	-	0	-	-	-
N-1 or Non-1	-	1	C8M-1	C8M	1
N-2.5 or Non-2.5	-	2.5	C8M-2.5	C8M	2.5
N-5 or Non-5	-	5	C8M-5	C8M	5
N-10 or Non-10	-	10	C8M-10	C8M	10
C8E-1	C8E	1	MPS-1	MPS	1
C8E-2.5	C8E	2.5	MPS-2.5	MPS	2.5
C8E-5	C8E	5	MPS-5	MPS	5
C8E-10	C8E	10	MPS-10	MPS	10

4.1.3 Loading Ratio Verification

TGA is usually used to verify the actual loading concentration of nanoparticles in nanocomposites. Most PP will decompose after being heated to 600 °C, and the actual AlN loading ratio can be derived from the weight remain after heat samples to 600 °C. The weight remains (%) of each sample after heated to 600 °C are listed in Table 4.2.

Table 4.2 The weight remain (%) of each sample after heated to 600 °C

Sample	Weight remains (%)	Sample	Weight remains (%)
PP	-0.2	-	-
N-1	0.4	C8M-1	1.1
N-2.5	2.8	C8M-2.5	2.1
N-5	4.7	C8M-5	4.7
N-10	9.9	C8M-10	9.5
C8E-1	0.9	MPS-1	1.5
C8E-2.5	2.3	MPS-2.5	2.5
C8E-5	5.2	MPS-5	5.2
C8E-10	9.1	MPS-10	8.7

4.2 Morphology Characterisation

4.2.1 Crystalline Structure

SEM images taken from the etched surface of PP samples are shown in Figure 4.2. The samples use for examining were etched in an acid mixture for 15 h. The composition of the acid mixture (5 parts of sulfuric acid & 2 parts of phosphoric acid & 1 part of water) was proven to be suitable for PP in [157]. The spherulites structure with an average size of 11.1 μm can be found clearly, which is a typical α-phase crystalline structure of isotactic PP. The growth of α crystals of PP starts from the formation of the nucleus, then grown larger until colliding with neighbour spherulites. Boundaries between spherulites are evident in Figure 4.2b. However, regions with no crystal structure can also be found. This is related to the quenching process during sample making restricts the growth of the spherulites; thus, distinct amorphous regions between spherulites are formed.

SEM image of PP filled with 1 wt% of non-treated AlN is presented in Figure 4.3. Nanocomposites samples with high loading ratios, such as 5 and 10wt%, are usually not ideal for crystal structure investigation, as the particles and agglomeration will cover the polymer structure. Therefore, the SEM image of PP with high AlN loading ratios is not presented in this section. The crystal structures of N-1 are inconspicuous compared to non-filled PP. No clear boundaries between spherulites can be observed. SEM images can only reveal the surface structure, and it would be difficult to identify the spherulite size in this case. Gómez et al. studied the crystallisation behaviours of PP filled with different nanoparticles [158]. The results show that layered silica and clay nanoparticles can initiate the formation of the PP nucleus and accelerate the growth of the spherulites. A similar nucleating effect of nanoparticles can also be observed here; the accompanied reduction in spherulites size in the N-1 sample can be the reason for the inconspicuous crystal structures.

SEM images of PP filled with 2.5 wt% of SCA treated AlN (C8M-2.5 and MPS-2.5) are presented in Figure 4.4 as an example. The addition of MPS treated AlN results in a similar crystal structure with N-1 (Figure 4.3), reduced spherulites size and obscure boundaries between spherulites. In contrast, in C8M-2.5, the boundaries between spherulites are apparent, although the crystal structure is unclear to the reference PP shown in Figure 4.2. After AlN was added into PP, the surface of the nanoparticle is the first contact with the PP matrix. The alteration of the nanoparticles surface chemistry can drastically affect their nucleating performance. Lin et al. have studied PP/$CaCO_3$ nanocomposites and the effect of stearic acid coating thickness, and the thinner coating leads to an increased number of the nucleus and reduced spherulites size [159]. The authors claim that the surface rigidity of coating plays a significant role. In this work, AlN coated with C8 groups show a weak nucleating effect to non-treated and MPS-treated AlN. The DSC results in Section 4.3.1 further confirm this conclusion.

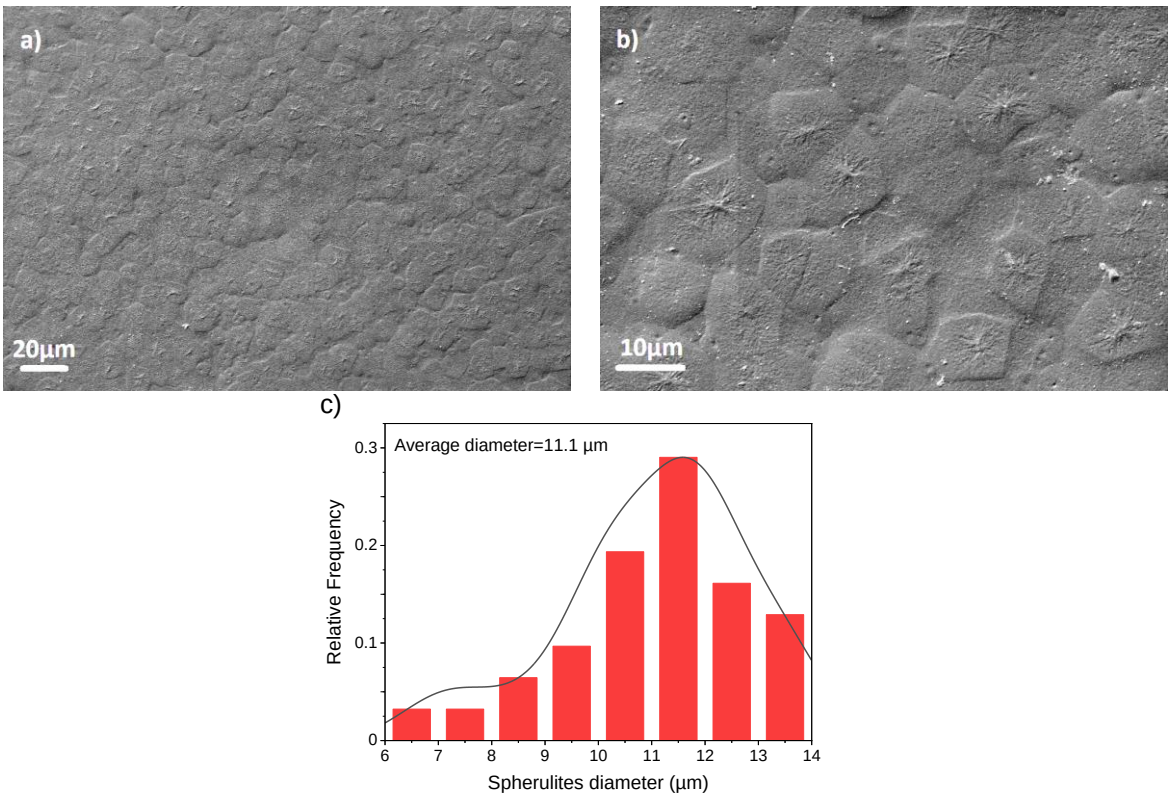

Figure 4.2 SEM image of PP with a) 1,000 magnification, b) 3,000 magnification; c) the spherulites distribution obtained from (b); average spherulites diameter=11.1.

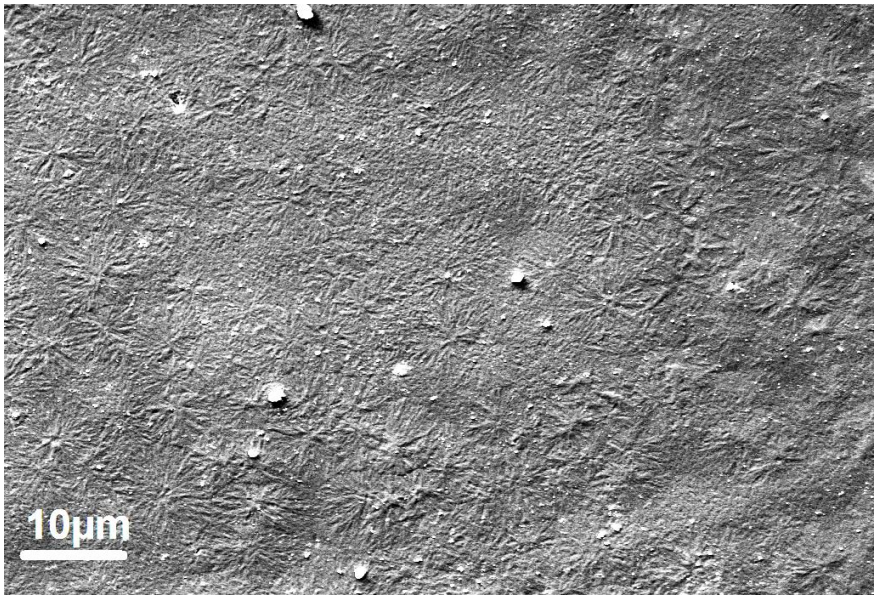

Figure 4.3 SEM image of N-1.

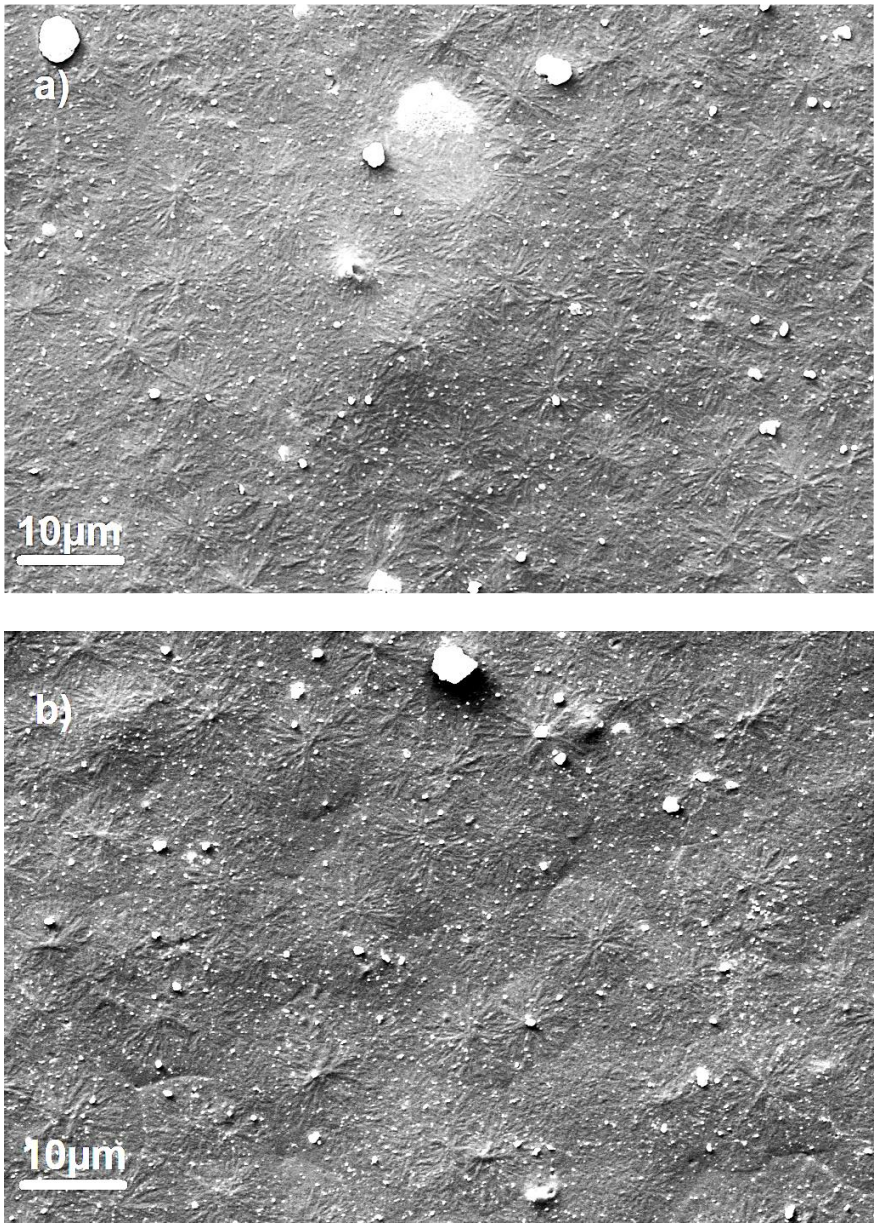

Figure 4.4 SEM image of a) MPS-2.5, where no inter-spherulite boundaries can be found, and b) C8M-2.5, the inter-spherulite boundaries are obscured but still can be identified.

4.2.2 Particle Dispersion

Figure 4.5 shows the SEM micrograph of PP filled with 5 wt% of non-treated AlN (N-5) at different magnifications, as an example. This will allow us to investigate the dispersion of nanoparticles at different scales.

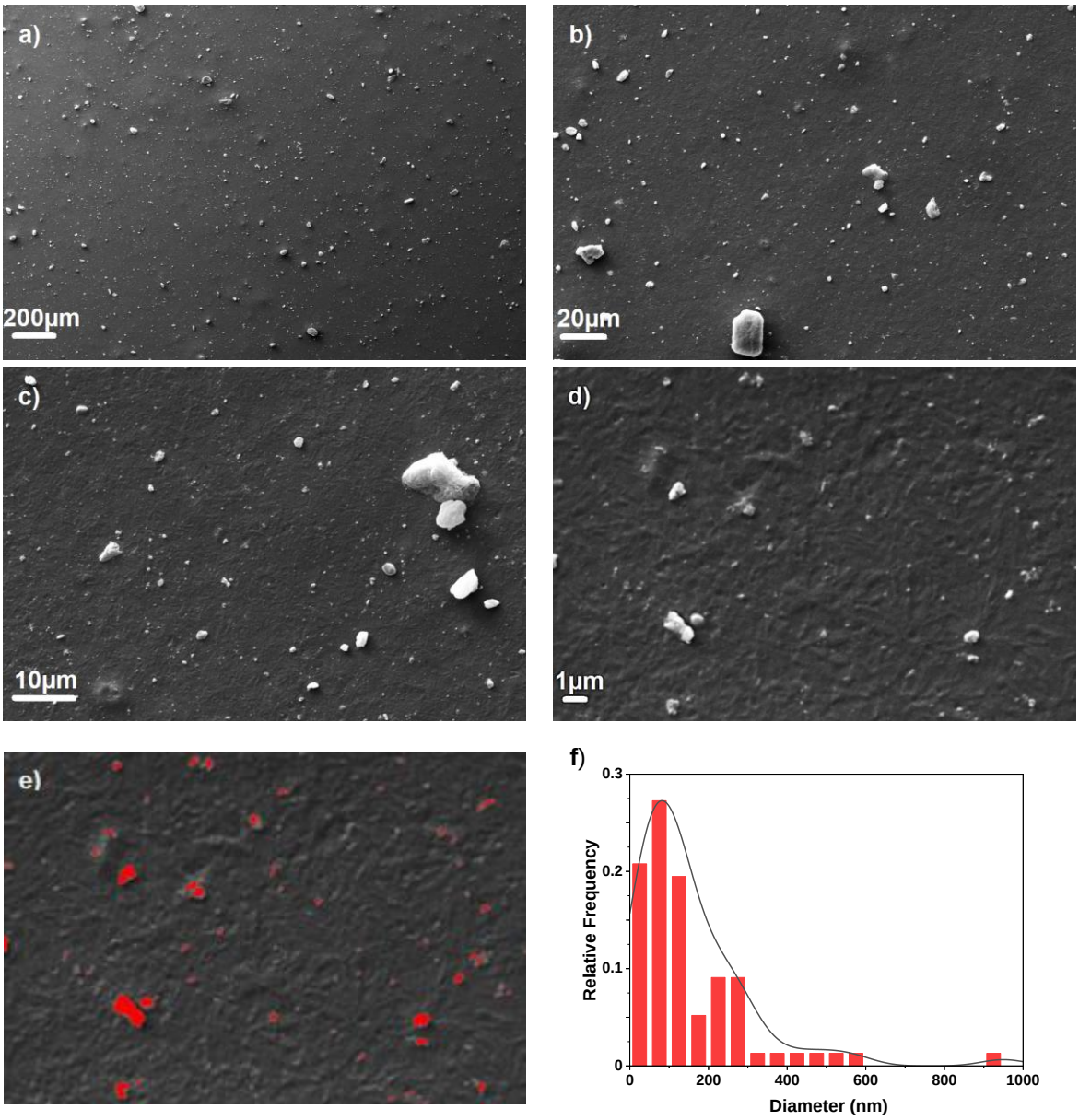

Figure 4.5 SEM images of N-5 with a) 100 magnification, b) 1,000 magnification, c) 3,000 magnification, and d) 10,000 magnification; e) identified AlN from (d), and f) the particle size distribution obtained from (d).

It is apparent that the size of the agglomerations is varied from nanometres up to 30 μm since nanoparticles with large surface area tend to form agglomerations spontaneously to reduce the surface free energy. Larger entities with the decreased surface area are created by weak force between particle surfaces. In nanodielectrics, agglomeration of nanoparticles has been widely reported, and it is particularly true for PP nanocomposites. Nano-fillers usually have a surface with polar groups, high surface energy, and low compatibility with non-polar material like PP. However, considering large agglomerations can also be found in the as-received powder (see Chapter 3, Figure 3.7), the agglomerations in PP nanocomposites is more likely to be formed before the blending procedure. This indicates the sonication applied on AlN and xylene suspension during the sample preparation process have a very limited ability to separate particle agglomerations.

SCA used in this work are expected to reduce the degree of agglomeration by decreasing the surface energy of AlN. The SEM analysis of PP filled with 10 wt% of silanes functionalised AlN is presented here as an example. Figures 4.6 and 4.7 show the SEM micrograph of samples filled with AlN with different treatments (N-10, C8M-10, C8E-10, and MPS-10) at 100 and 10,000 magnifications. In Figure 4.6, large agglomerations can be found in N-10. The size of large aggregations is reduced with the help of surface treatment, where the grafted organic groups can increase the compatibility between AlN and PP. But agglomerations up to 30 µm still exist in silane treated samples, even for low loading of AlN like 1 wt%. Due to the unique hydrolysis properties of AlN, only the anhydrous silane treatment method was applied here. The presence of these large agglomerations could be related to the toluene used as the solvent for dispersing AlN, but it is not the best solvent for breaking agglomerations due to its non-polar nature. It should be noted the large entities could also be formed by the re-agglomeration of adjacent particles during the etching procedure. After the surrounding PP was removed, the possible movement of the particles makes the SEM images shown here unable to present the true filler dispersion. When comparing samples treated with different SCA, it seems that different SCA presents comparable ability to break the large agglomerations as no clear difference can be found in Figure 4.6 b to d. However, from the SEM images with higher magnification shown in Figure 4.7, MPS seems to have a weaker ability to obtain a good AlN dispersion in nanoscales like C8M and C8E. It is because the organofunctional end of C8 silanes has lower polarity than the methacryl groups from MPS, hence presenting better compatibility with PP.

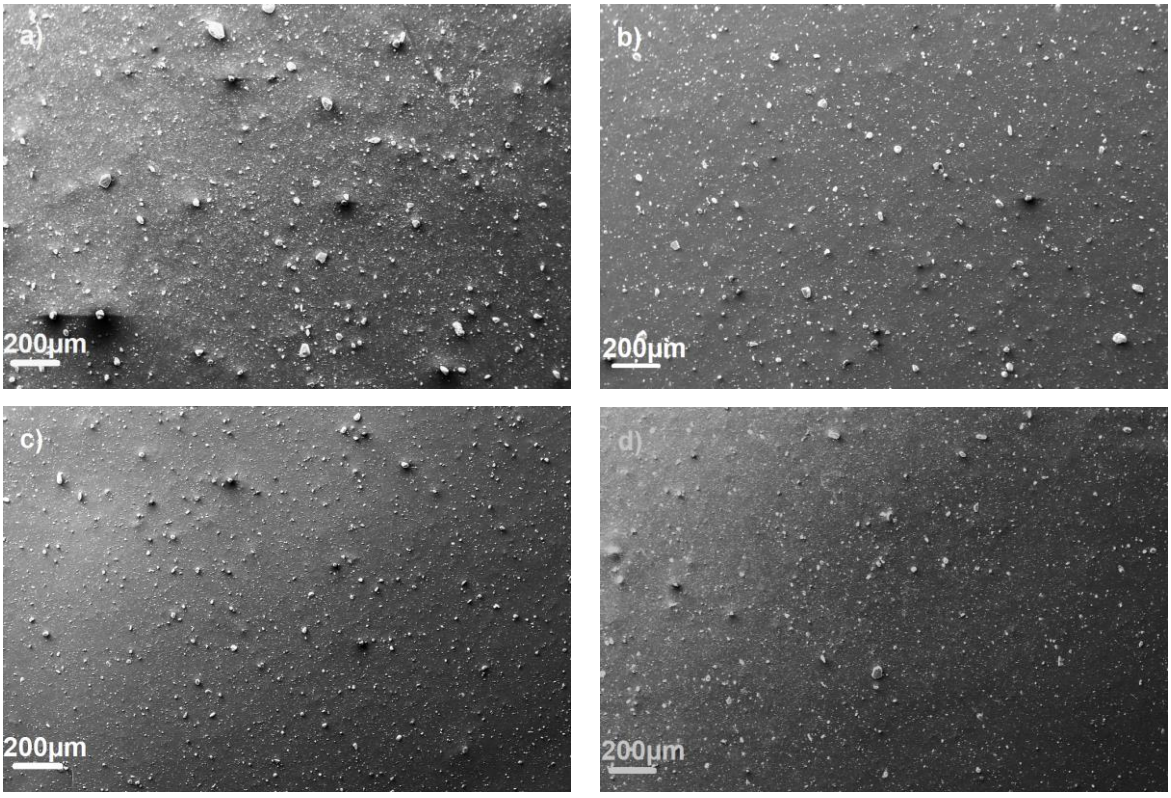

Figure 4.6 SEM images of samples filled with AlN with different treatments at 100 magnification, a) N-10, b) C8M-10, c) C8E-10, and d) MPS-10.

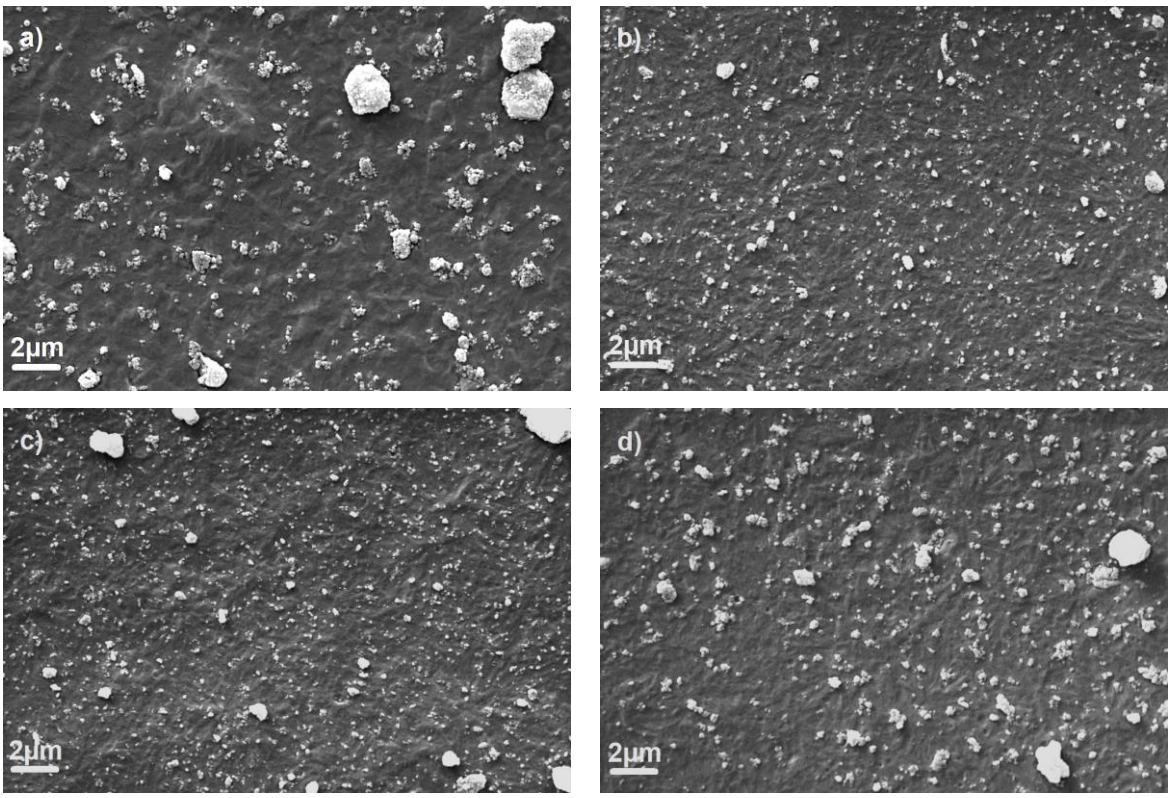

Figure 4.7 SEM images of samples filled with AlN with different treatments at 10,000 magnification, a) N-10, b) C8M-10, c) C8E-10, and d) MPS-10.

4.2.3 XRD

The XRD patterns of neat PP and a selection of PP/AlN nanocomposites are shown in Figure 4.8. C8M and MPS treated samples are selected here as they are different from their organofunctional group, providing different interactions with PP.

The diffraction pattern of the neat PP shows typical peaks at 14.2°, 16.6°, 18.5°, 21.0°, 21.8°, 25.5° and 28.5° correspond to the (110), (040), (130), (111), (131) + (041), (060) and (220) crystal planes of the α-crystals (monoclinic), and the same peaks are also shown in PP/nano-AlN composites; besides, MPS-10 samples present the β-crystal (trigonal) peaks at 2ϑ of 16.0° and 21.0° corresponding to the planes of (300) and (301), respectively. The different results of MPS from others may be due to its methacrylate groups on the nanoparticle surface. It is because polar groups like methacrylate could facilitate more nucleating effects than non-polar ones, e.g., octyl (C8), as discussed in Section 4.2.1. This may also be the reason why (111) + (301) and (131 + 041) planes of MPS-10 show independent peaks from each other, whereas those of C8M-10 are merged because smaller nucleating ability could limit the dimension of microcrystals during the quenching process and broadens the corresponding peaks. Moreover, as N-10 contains non-treated AlN, which has the worst filler dispersion, it could provide more space for the growth of crystallites, resulting in narrower peaks and similarly as observed in C8M with lower filler loadings (C8M-2.5). The

broadened peaks in the quenched neat PP could be attributed to the lack of the nucleating effect and resultant smaller size of microcrystals during quenching. Besides, the intensity of peaks assigned to AlN increases while the filler loading concentration rises in the composites. A peak between 40° and 45° is evident in all samples, including the as-received PP. This is consistent with other works [160, 161], but few attempted to explain the source of this peak. It is suggested that this peak can be related to the (100) and (101) planes of carbon-based impurity in the as-received PP.

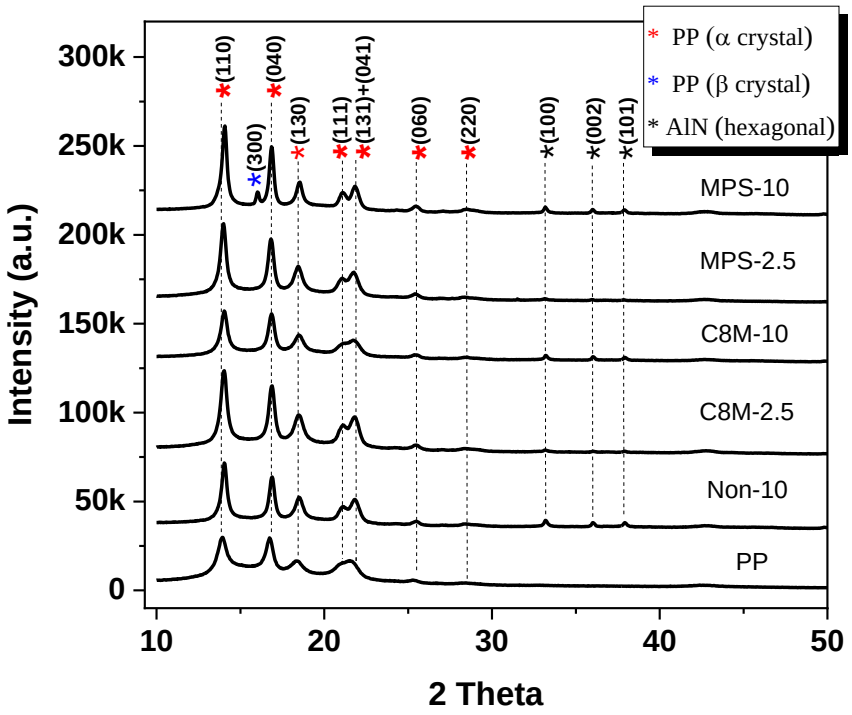

Figure 4.8 XRD spectra of neat PP and a selection of PP/AlN nanocomposites.

4.3 Thermal Analysis

4.3.1 DSC

The details of DSC experimental conditions are given in Appendix A. Figure 4.9 shows the DSC heating and crystallisation curve of the selected dielectric systems. Key parameters obtained from DSC curves are listed in Table 4.3. C8M and MPS treated samples are chosen here as they are different from their organofunctional group, providing different interactions with PP. From heating curves, although some nanocomposites show a slight decrease up to 2 °C, the melting point of each system seems unaffected by the presence of AlN, indicating the introduction of AlN does not seem to influence the melting behaviours of PP.

All samples show an increased crystallisation temperature (T_c) from crystallisation traces than the reference PP, and the T_c increase with the increasing AlN loading ratio. It is because nanoparticles can act as the nucleating agent, thus elevate the crystallisation temperature. The PP filled with non-treated AlN has the highest crystallisation temperature, followed by the PP with MPS treated AlN, and C8M treated AlN has the least ability to increase the T_c. These results are in line with the crystalline structure from SEM images; the nucleating effect regarding the AlN surface chemistry decreases in the following order: non-treated > MPS > C8.

For the crystallinity of each system, no significant differences can be found by adding AlN compared to the neat PP, except the N-10 has a marginal increase (2.1 %); see Table 4.3. This is due to the quenching process that restricts the growth of the crystalline structure, and the effect of the AlN nucleating behaviours on the crystallinity of the composites is limited. Apart from the nucleating effect, the hindrance effect of the nanoparticles on the growth of the crystalline structure is also reported [162]. The increased density of the nucleus accelerates the inter-spherulites collision within the system. Meanwhile, particles and agglomerations that occupy the free spaces during the cooling processes can act as barriers and hinder the growth of the crystalline structure. In PP/AlN nanocomposites reported in this work, we suggest the introduction of AlN with different surface chemistry bring both nucleating and hindrance effects; the balanced co-effect led to the comparable crystallinity of each system.

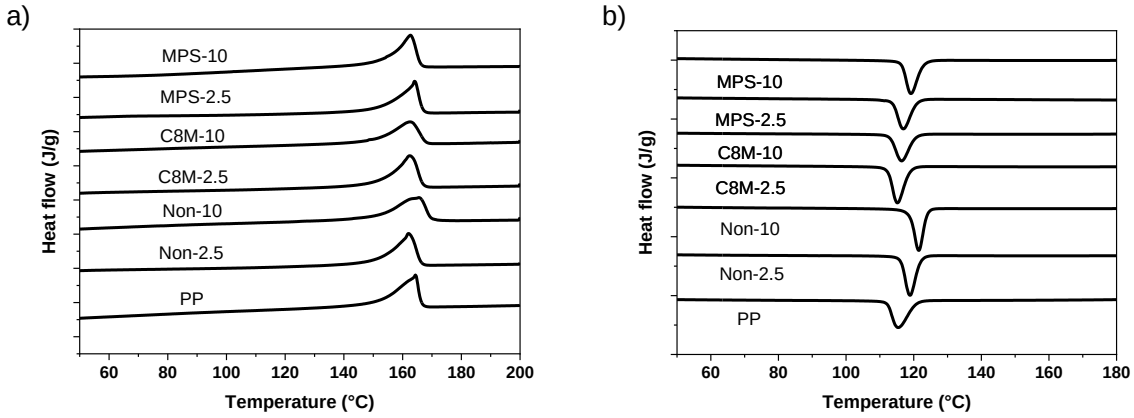

Figure 4.9 DSC a) heating, and b) crystallisation curve of the selected dielectric systems.

Table 4.3 Thermal properties of the selected dielectric systems, *ΔH (J/g)* is the melting enthalpy obtained from the melting peak area, T_m and T_c is the melting and cooling peak temperature, respectively, and χ is the calculated crystallinity when ΔH=100% for neat PP is 208 J/g.

	ΔH (J/g)	T_m (°C)	T_c (°C)	χ (%)
PP	49.7	164.3	115.2	23.9
N-2.5	49.9	162.0	119.0	24.6
N-10	48.7	165.5	121.5	26.0
C8M-2.5	47.9	162.5	115.3	23.6
C8M-10	44.4	162.5	116.5	23.7
C8E-2.5	47.1	163.5	116.0	23.2
C8E-10	45.4	162.8	118.0	24.3
MPS-2.5	47.4	164.2	117.0	23.4
MPS-10	46.2	162.7	119.2	24.7

4.3.2 Thermal Degradation

The TGA results of PP and PP/AlN nanocomposites obtained by heating samples from 50 to 600 °C at 10 °C/min are shown in Figure 4.10. The temperature at 5 % (onset) and 50 % (half) of weight remain are also plotted. The PP start to decompose at the temperature of 290.7 °C. All nanocomposites show an increased onset temperature, and it increases with an increased loading ratio. In order to eliminate the misunderstanding caused by the TGA data based on the mass of composite, part of the measured data was processed according to the mass of PP in the composite system (Appendix D, Figure D.1), where similar behaviours regarding the thermal stability of PP/AlN nanocomposites can be observed.

The TGA results indicate the addition of AlN can prevent the thermal degradation of PP. The increased thermal resistance to polymer degradation has been widely reported [163-166]. This behaviour was commonly interpreted with barriers formed by nanofillers and the chars, restricting the volatility of free radicals and heat transfer to the inner materials. However, the barrier theory is more convincible to fillers with layered structure and low thermal conductivity, such as montmorillonite (MMT) and nano clay, as they are more favourable to form a percolated layered structure with low thermal conductivity [164].

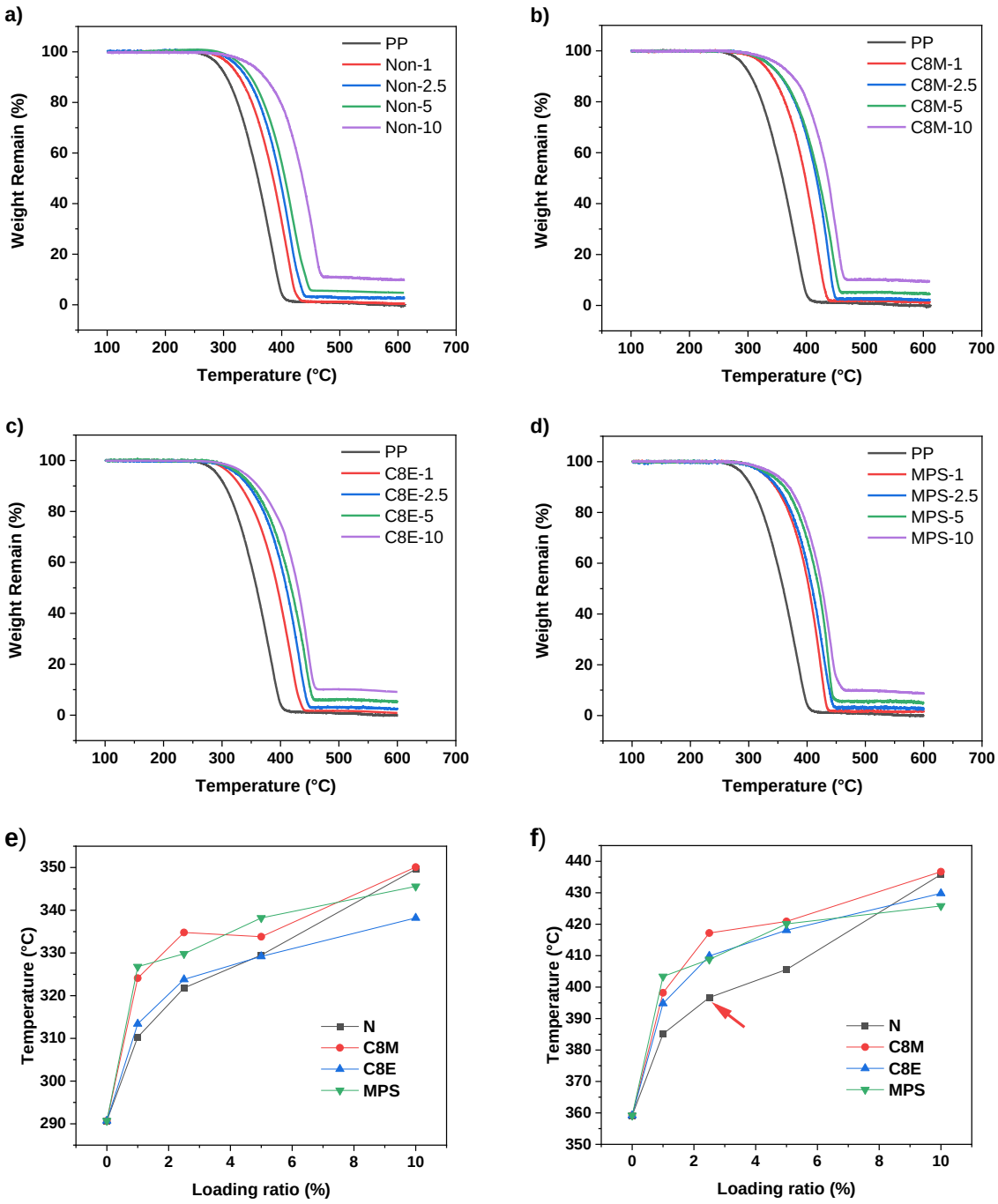

Figure 4.10 TGA curves of PP and PP/AlN nanocomposites, a) to d) Non-treated, C8M-treated, C8E-treated, and MPS treated; The temperature at e) 5 %, and f) 50 % of weight loss of each sample.

The AlN usually has a thermal conductivity much higher than PP, and the shape of the as-received AlN is confirmed to be plate and rod with a low aspect ratio, which is unlikely to form a protective barrier as MMT. Franco-Urquiza et al. have studied the thermal degradation kinetics of ZnO/polyester nanocomposites; the increased thermal resistance was observed by adding ZnO nanoparticles. By analysing the “minimum amount of energy required to initiate the degradation process, " the author suggests the added ZnO provide a catalytic effect that can reduce the amount

of energy needed to initiate the degradation process [163]. The added AlN may also produce such a catalytic effect and improved the thermal stability of PP. However, the forming of protective barriers can not be ruled out in this case.

The temperature around 300 °C reaches the de-drafting temperature of the SCA on the AlN surface; thus, it is not difficult to explain why no significant difference can be found between samples with different surface chemistry regarding the onset temperature. However, from Figure 4.10f, SCA treated samples shows higher stability than the PP with non-treated AlN samples. It could be related to the batter dispersed AlN has a larger contacting area with PP, thus giving a better catalytic effect and/or forming a denser barrier due to the better dispersion.

4.3.3 Thermal Conductivity

The thermal conductivity of a selection of samples is shown in Figure 4.11. It is clear that: (1) the nano-AlN filled PP shows higher thermal conductivity than the non-filled PP, and all nanocomposites have monotonically increased thermal conductivity as a function of the loading ratio; (2) in functionalised systems, the increased thermal conductivity compared to untreated systems can be observed. Different surface treatment seems to result in a similar ability of the bulk to conduct the heat flow; (3) it is noticeable that PP filled with 10 wt. % MPS treated nano-AlN can have about 15 % improvement over the unfilled PP, which is consistent with the work that blended 10 wt. % of nano-AlN with HDPE [167] and epoxy [168], where 10.2 % and 17.9 % of thermal conductivity enhancement were achieved.

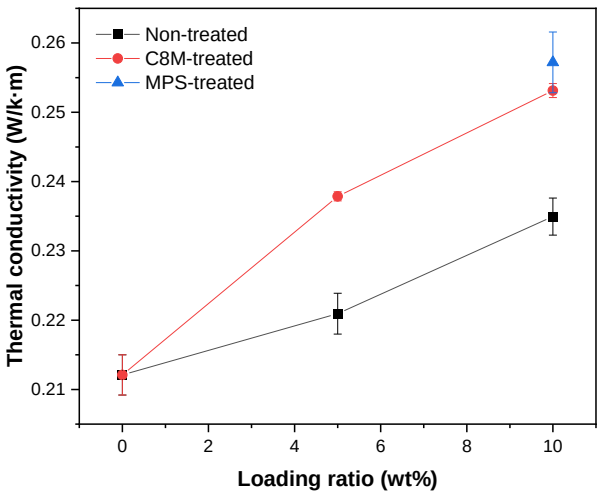

Figure 4.11 The thermal conductivity of a selection of samples.

When incorporating the non-metallic material into a polymer, the interfacial barrier between nanoparticles and polymer matrix is the main contribution to phonon scattering [169]. The surface treatment can improve the compatibility between the nanoparticles and matrix material. When comparing the thermal conductivity related to the AlN surface chemistry, the surface-treated systems can be observed to have a significant improvement compared to the non-treated systems. Without surfactant acting as a compatibilizer, the phase separation between nanoparticle and polymer can result in a strong phonon scattering phenomenon during the heat flow transmission. It is consistent with the SEM results in Figures 4.6 and 4.7, where the surface functionalisation can improve the compatibility between nanoparticles and PP, and an improved dispersion can be observed.

One interpretation of these results is that the organic layers on the particle surface weaken the scattering phenomenon and decrease the heat resistance of the interphase [170]. The thermal conductivity results here also show less dependence on the dispersion of nanoparticles. Thus, the results show the significant role surface chemistry plays regarding the thermal conductivity of nanocomposites.

4.4 Summary

This chapter introduced an improved solution blending method, and the true loading ratios of the prepared nanocomposites were confirmed via TGA. The morphology and thermal properties of the nanocomposites treated with different silane coupling agents were studied. It is evident that the addition of AlN can reduce the size of the spherulites of PP due to its nucleating effect, and the nucleating effect decreases in the following order: non-treated > MPS > C8, regarding the AlN surface chemistry. Although significant morphological differences can be observed from SEM, all samples show a comparable crystallinity. It is suggesting the introduction of AlN with different surface chemistry bring both nucleating and hindrance effect, and the balanced co-effect led to the similar crystallinity of each system. Notably, the structure features related to the inter-spherulite boundaries in PP are eliminated by adding non-treated and MPS treated AlN, but these features can still be found on the PP with C8 treated samples.

From the TGA results, AlN shows a strong ability to increase the thermal stability of PP, and this ability seems independent of the AlN surface chemistry. We suggest that the increased thermal degradation stability is mainly because of the catalytic effect or the formation of a protecting barrier by AlN. Meanwhile, the inclusion of AlN can increase the thermal conductivity of PP, which is a promising result for cable insulation material. Upon surface treatment, the grafted SCA on the AlN surface can effectively increase the compatibility between fillers and the PP matrix and provide a higher bulk thermal conductivity.

Chapter 5 Effect of Water on Dielectric Properties of PP/AlN Nanocomposites

Samples investigated in this chapter are named X-Y-Z, where X represents the surface states of AlN fillers, either C8M, C8E, MPS, and N (non-treated AlN); Y is the loading ratio by wt. % either 1, 2.5, 5 or 10; Z is the condition of the samples, either D (dry) or W (immerse in water for 9 days).

Part of the results presented below are published in**:**

Wang, Xinyu, Qiang, Dayuan, Hosier, Ian, Zhu, Yanqiu, Chen, George and Andritsch, Thomas (2020) Effect of water on the breakdown and dielectric response of polypropylene/nano aluminium nitride composites. Journal of Materials Science, 55 (21), 8900-8916. (doi:10.1007/s10853-020-04635-1).

The experimental details can be found in Appendix A.

5.1 Introduction

The presence of inorganic filler in nanodielectrics will introduce hydrophilic sites like hydroxyl groups that are prone to absorb water from the surrounding environment. As a result, the dielectric properties of nanodielectrics are reported to have a considerable difference between samples with different water content. Since little published work has clearly identified the influence of moisture on the dielectric properties of nanocomposites, it is reasonable to believe that at least some of the inconsistency reported in the literature on nanodielectrics is related to the unknown water content in tested samples, which results from, e.g., the different sample storage techniques and testing environments.

For PP nanocomposites, the absorbed water is preferred to distribute on the surface of the filler rather than the hydrophobic PP matrix. Investigating samples treated under different environments is considered an effective method that can identify the properties of the nanoparticles surface and their impact on the composite material. SCA with non-polar organofunctional groups, such as octyl silanes, can displace the surface hydroxyl groups and increase the hydrophobicity of the nanocomposites. It is believed that the octyl tail on the nanoparticle surface can reduce the amount of water absorbed on the nanoparticle surface [171, 172]. As discussed in Chapter 3, SCA selection is mainly determined by the interaction between its organofunctional groups and matrix material. The potential options that can provide capable interactions with PP are usually polar, such as methacrylate group, which are questioned to deliver favourable results regarding hydrophobicity like octyl silanes [144]. Thus, AlN/PP nanocomposites with different surface treatments (octyl silane

and methacrylate silane) on nano-filler and the effect of the water absorption have been studied in this chapter.

In Chapter 3, a surface structure of an SCA functionalised nanoparticle that highlights the chemical structure of the “far-particle side” and “near-particle side” was proposed (Figure 3.20). However, it is challenging to characterise the near-particle structure of the surface-treated AlN. The water absorption analysis could help identify the hydrophobicity of the near-particle structure, such as the density of the Si-OH group and the condensation rate of the grafted SCA, which could draw a better picture of the near-particle structure of the SCA treated AlN. To understand the influence of the AlN surface chemistry on the interphase and bulk properties of the PP nanocomposites, dielectric properties including AC breakdown strength, dielectric spectroscopy have been obtained by testing samples under different water content. A better understanding of the correlation between water content, nanoparticle surface chemistry, and its interaction with the PP matrix is expected.

5.2 Water Absorption Behaviour

Water absorption analysis was conducted by immersing film samples into de-ionised water, and the weight of the samples was monitored at regular intervals up to 9 days. In Figure 5.1, the weight increase of PP and nanocomposites samples after immersion in water for 9 days is presented. It can be observed that the weight increase of all samples reaches near saturation in 6 days or less. The weight of pure PP as reference shows, as expected, no dependence on water immersion due to its non-polar carbon chain structure, which has a very weak ability to absorb water. This and the increase in water uptake with increased AlN loading (Figure 5.1 a to d) suggest that the weight increase of nanocomposites is solely related to the incorporation of nano-AlN and water absorption onto its surfaces. Although all nanocomposites have an increase in mass after immersing in water, silane functionalisation shows a significant effect on altering the issue of water absorption. Figure 5.1e shows the weight increase of PP/AlN nanocomposites on day 9 in de-ionised water. Surprisingly, there is no significant difference between samples treated with different SCA, especially for samples treated with polar (MPS) and non-polar (C8M, C8E) silanes. This indicates that the methacrylate group has less ability to absorb water than the -OH groups left on the surfaces of the non-treated AlN or that the interaction with PP somehow alters the ability of the methacrylate group to interact with water. When compared to PE/AlN nanocomposites as reported in [96], where PE with 10 wt.% of AlN only has an uptake of water less than 0.1 % of the total weight after immersing in water for 14 days, the higher weight increase for the non-treated samples (0.25 %, Figure 5.1a) in this work is likely related to the smaller particle size and the thus increased surface area. It is worth noting that the weight increase of most nanocomposites reaches almost

saturation after only one day, with no further significant increase in weight after 24 hours. This might be related to the thickness of the water shell around nanoparticles. As Lau et al. suggested, a thick shell can gradually be formed surrounding a nanosilica particle during a long period (more than 10 days) after the water immersion. Dielectric loss peaks were found to move to a high-frequency range while moisture uptake increases [173], which has also been numerically proved by Qiang et al. [171]. The above results indicate a thick water shell are less likely formed in PP/AlN nanocomposites. The water shell thickness and the related dielectric loss behaviours will be explained in the dielectric spectroscopy section results in this chapter.

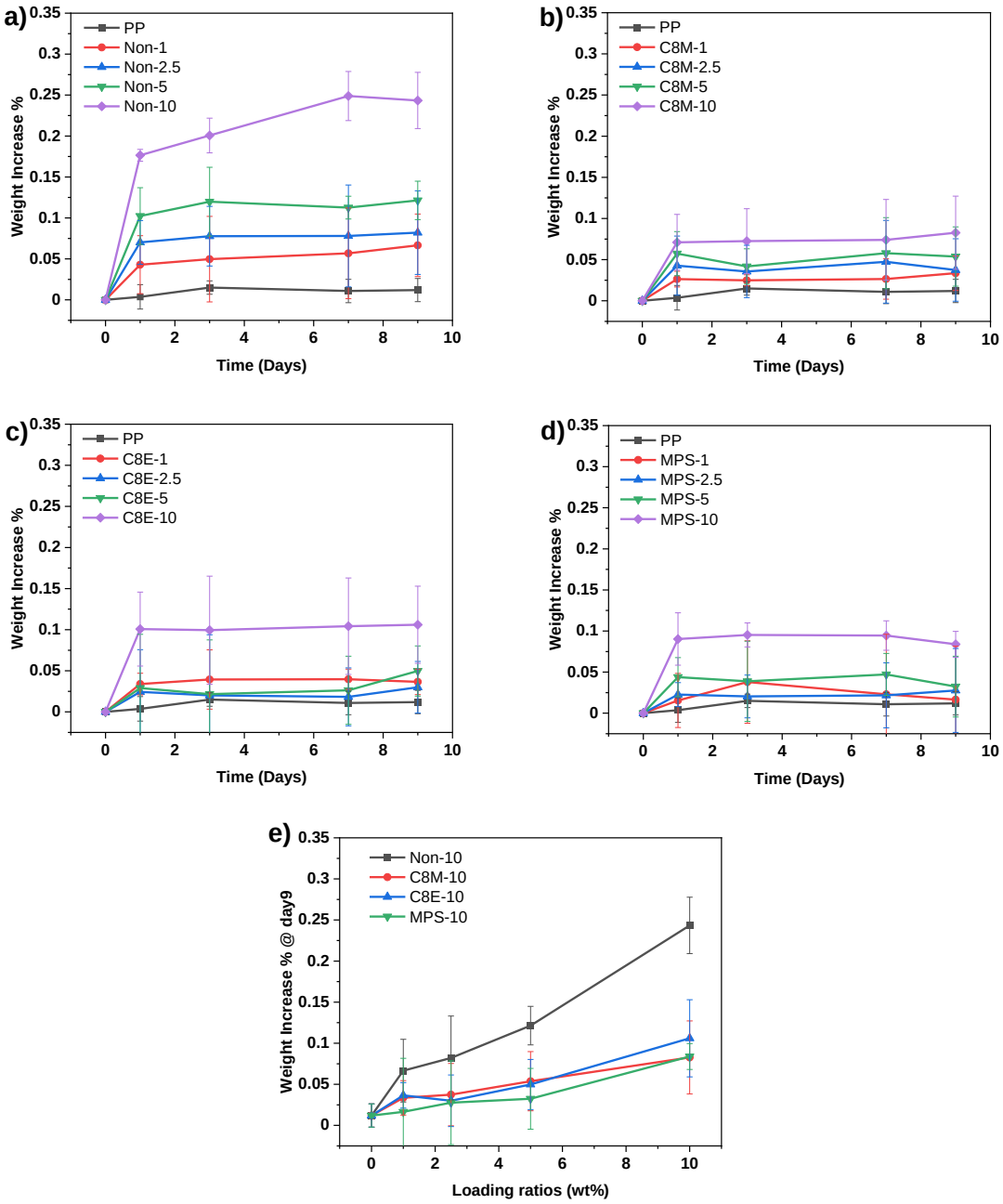

Figure 5.1 Weight increase of PP and nanocomposites after immersion in de-ionised water with a) non-treated, b) C8M-treated, c) C8E-treated, and d) MPS treated AlN; e) weight increase of PP with 10 wt% of AlN at day 9 in de-ionised water.

5.3 Dielectric Spectroscopy

The real (ε') and imaginary (ε'') permittivities of PP and its nanocomposites in dry conditions are plotted in Figure 5.2. The experimental details can be found in Appendix A. The real permittivity shows an increase with the AlN loading ratio growth (Figure 5.2 a to d). When considering the measurement uncertainties that arise from the sample thickness measurement, which can have up to ± 0.02 (ε') from multiple tests, nanocomposites with different nanoparticle surface chemistry have little effect on the real permittivity.

The real permittivity of each sample is a flat line throughout the tested frequency range at room temperature due to the non-polar nature of PP. This also results in neat PP having a very low imaginary permittivity under an AC electric field, which results in data fluctuation as the value of the imaginary permittivity falls near the minimum sensitivity of the instrument (10^{-4}). The imaginary permittivity of PP with non-treated AlN increases with the decreasing frequency (Figure 5.2 e to h). This trend shows a monotonic increase with the increasing of the filler loading ratio. The increased losses at low frequency for polyolefin nanocomposites were widely reported, which is likely caused by the interfacial polarization and/or the polarisation effect due to surface group on the nanoparticle surface [96, 173, 174]. A reduced imaginary permittivity can be observed in SCA treated samples since the number of hydroxyl groups has reduced with surface treatment. However, the results seem independent of the types of SCA applied.

The real and imaginary permittivities of samples immersed in water for 9 days are shown in Figure 5.3. From the real permittivity results in Figures 5.3 a to d, all nanocomposites show an increase in the value of ε' compared to the dry samples, and obvious upturns at low frequency can be observed in samples with 5 and 10 wt. % non-treated AlN (Figure 5.3a). When considering the magnitude of the upturns of N-10-W, it is evident that it shows higher values than 10 wt.% AlN/PE composites in [96], where N-10-W gain more water (0.25 %) than 10 wt.% AlN/PE (0.1 %). Although similar trends at low frequencies can also be seen in samples with silane treated AlN (Figure 5.3 b to d), the magnitudes are significantly reduced with the help of the silane treatment, especially for samples treated with non-polar silanes, C8M and C8E, where the water content is less than 3 times to the non-treated samples. It is not surprising that notably higher values of ε' are observed in MPS-10-W (Figure 5.3d) than in any of its C8M and C8E functionalised counterparts; the polar surface functional groups are the main reason. From above, it can be found that the real permittivity results for wet samples are related to the water content of the sample. A better understanding of the influence of absorbed water can be achieved by combining ε' with the imaginary permittivity results.

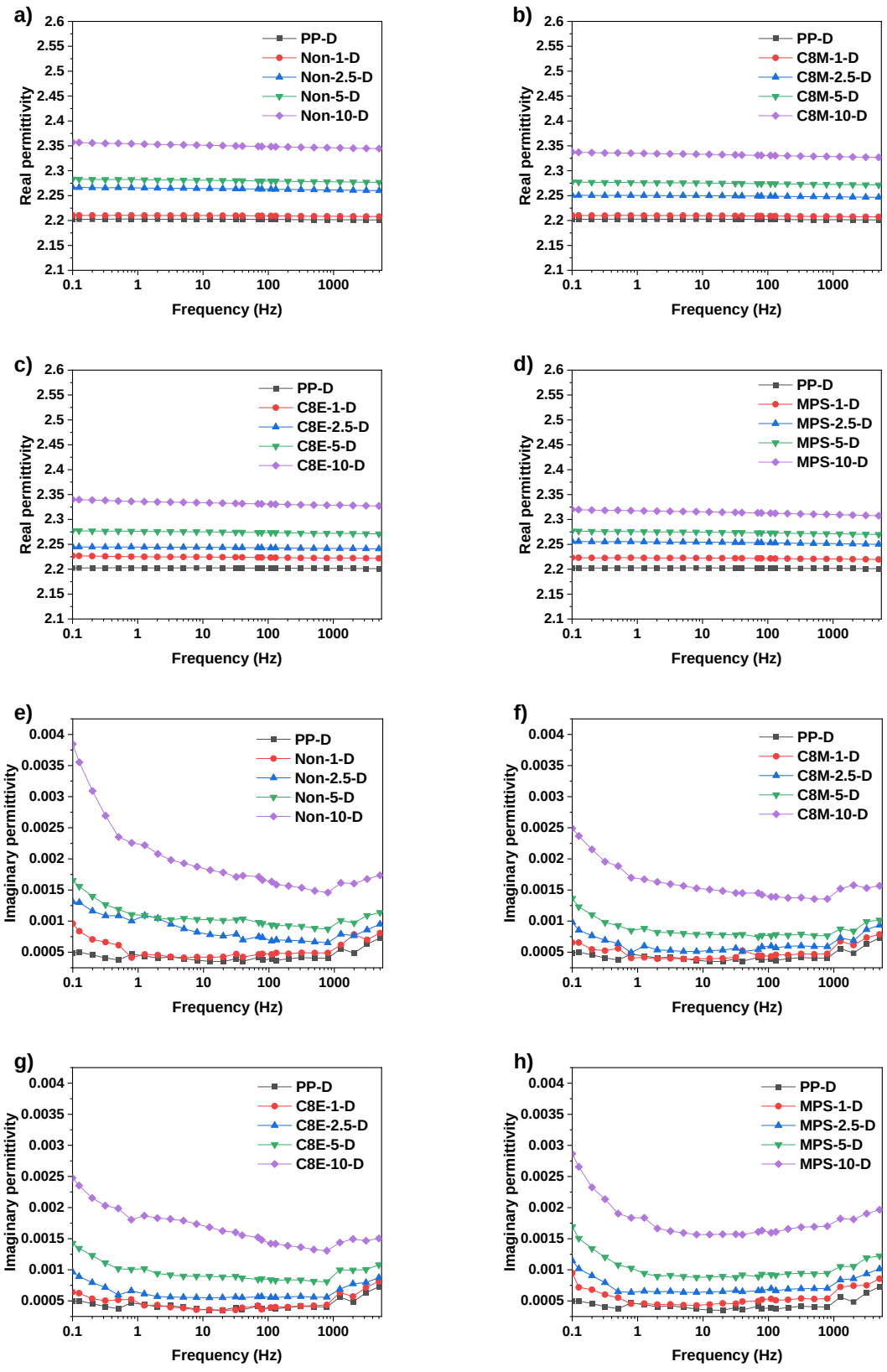

Figure 5.2 Complex permittivity of PP and its nanocomposites at dry condition, a) to d) are the real part, and e) to h) are the imaginary part.

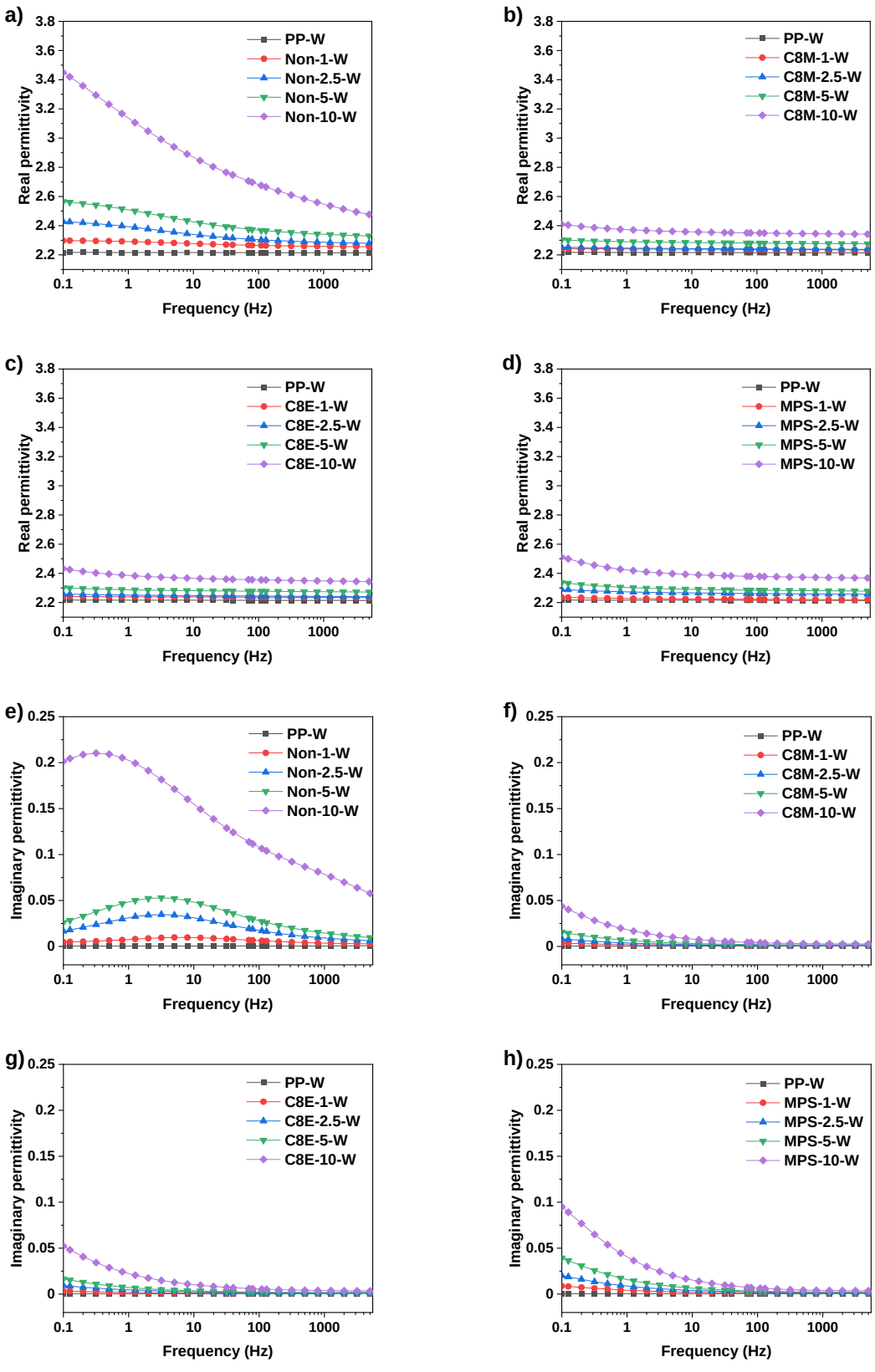

Figure 5.3 Complex permittivity of PP and its nanocomposites at wet condition, a) to d) are the real part, and e) to h) are the imaginary part.

From Figure 5.3e, unlike the clearly visible loss peaks at high frequencies (10^3-10^5 Hz) in imaginary permittivity, which result from water uptake according to the literature [96, 97, 175], the relaxation features for PP with non-treated AlN are located in the low-frequency range (< 50 Hz). The relaxation frequency is reported to be related to the thickness of the water shell and the mobility of the resulting water clusters [96, 97, 171]; the relaxation features at low frequency are consistent with the water absorption results in section 5.2, where the AlN/PP nanocomposites show a low water absorption ability when comparing to literature using different filler selections, e.g. N-10-W can only gain 0.25 % of the total weight. In comparison, a 10 wt.% nanosilica/PE composite shows more than 1.5 % weight increase, and relaxation peaks at 10^3-10^5 can be observed [173].

As proven by the water absorption results in section 5.2, the absorbed water is more likely to surround the nanofillers than within the hydrophobic PP. Therefore, the relaxation behaviours of wet samples could be explained by an interlayer model proposed by Steeman and Maurer, where the complex permittivity ε^* of composites with interlayers between particulate fillers and polymer matrix can be expressed as [171, 176]:

$$\varepsilon^*(\omega) = \frac{\varepsilon_f^*(\omega)\varphi_f + \varepsilon_l^*(\omega)\varphi_l R^* + \varepsilon_m^*(\omega)\varphi_m S^*}{\varphi_f + \varphi_l R^* + \varphi_m S^*} \tag{5.1}$$

with

$$R^* = \frac{2\varepsilon_l^* + \varepsilon_f^*}{3\varepsilon_l^*} \tag{5.2}$$

$$S^* = \frac{(2\varepsilon_m^* + n\varepsilon_l^*)(2\varepsilon_l^* + n\varepsilon_f^*) - 2d(\varepsilon_l^* - \varepsilon_m^*)(\varepsilon_f^* - \varepsilon_l^*)}{9\varepsilon_l^*\varepsilon_m^*} \tag{5.3}$$

$$d = \frac{\varphi_f}{\varphi_f + \varphi_l} \tag{5.4}$$

In the above equations:

- $\varepsilon^*(m, f, l)$ and $\varphi(m, f, l)$ are the complex permittivity of the matrix, filler, and interlayer.

Equation 5.1 can be reduced to a derby-type expression if φ_l is small enough:

$$\varepsilon^*(\omega) = \varepsilon_\infty + \frac{\varepsilon_0 - \varepsilon_\infty}{1 + j\omega\tau'} \tag{5.5}$$

in which

$$\varepsilon_\infty = \varepsilon_m\left(\frac{1 + 2\varphi_f}{1 - \varphi_f}\right) \tag{5.6}$$

$$S^* = \varepsilon_m \frac{(\varepsilon_f + 2\varepsilon_m) + 2(\varepsilon_f - \varepsilon_m)\varphi_f}{(\varepsilon_f + 2\varepsilon_m) - (\varepsilon_f - \varepsilon_m)\varphi_f} \quad (5.7)$$

and

$$\tau = \left(\frac{\varphi_f}{1-\varphi_f}\right)\left(\frac{3\varepsilon_{vac}}{2\sigma_l\varphi_l}\right)\left[(\varepsilon_f + 2\varepsilon_m) - (\varepsilon_f - \varepsilon_m)\varphi_f\right] \quad (5.8)$$

In the above equations:

- ε_{vac} is the vacuum permittivity.
- σ_l is the conductivity of the interlayer.
- τ is the relaxation time where the frequency of maximum dielectric loss appears, f_{max_loss}=1/ τ.

It can be found in Equation 5.8, and the relaxation time is Inversely proportional to the volume fraction of the interlayer, which means the lower peak loss frequency is related to a thinner water shell surrounding the nanofillers. Therefore, we suggest that the absorbed water forms a thinner water shell compared to the samples reported in [96, 97, 173].

As the loading ratio increases to 10 wt%, the relaxation peak moved from 2 Hz to 0.6 Hz, it is because the average thickness of the water shells will be restricted by its overlapping at high filler loading (as shown in Figure 4.7a), which will result in the relaxation peak shift to a lower frequency, similar behaviours can be found in [107, 177], where the relaxation peak shifted to a lower frequency as the loading ratio increase.

Consistent with the real permittivity, C8M and C8E treated samples show identical results in the imaginary part (Figure 5.3 f & g). An increase of the magnitude of ε" with the AlN loading can be seen, but the relaxation peaks are now expected to exist at much lower frequencies <0.1 Hz than the non-treated systems. The C8 silane treatment can displace a significant amount -OH on the AlN surface. Therefore, less is available to trap water on the nanoparticle surfaces; this can be confirmed by the water absorption analysis shown in Figure 5.1. The associated relaxations shift to lower frequencies due to the reduced water shell thickness. Nevertheless, the water absorption results clearly show that the octyl silanes treated PP/AlN nanocomposites can still absorb some water. One possible explanation for this is the displacement of -OH is incomplete by C8 silane treatment. Alternatively, in addition to the hydroxyl group from the Al-OH on the AlN surface, polar sites other than the Al-OH, e. g. the Si-OH from the silane treatment and surface Al-NH_2, can also contribute to the weight gain of samples during water immersion [10, 178]. Besides, identical results provided by C8M and C8E treated nanocomposites indicate that the assumption of the thick

SCA layer could introduce more hydrophilic sites (Figure 3.20, outstretched Si-OH) is not the determining factor in the change of the dielectric response in [10].

MPS treated samples show higher imaginary permittivity than the C8 treated samples with the same loading ratios (Figure 5.3h), which is related to the presence of the methacrylate group. The increase in the slope of the imaginary curves of MPS-10-W indicates a relaxation feature at lower frequencies. While these might be revealed by performing measurements at elevated temperatures, this was not performed in current work. It would result in loss of absorbed water, therefore negating comparability with results at lower temperatures. Nevertheless, a similar relaxation feature can be observed in [10], where dry samples were tested at 90 °C.

5.4 AC Breakdown Strength

The experimental set-up and details of samples used in AC breakdown strength tests can be found in Appendix A. AC breakdown strength of dry and wet (immersed for 9 days) samples with 5 and 10 wt.% of filler loading are shown in Figure 5.4, 2-parameter Weibull scale and shape parameters of samples with low loading ratios are listed in Table 5.1.

The breakdown strength of non-filled PP (Figure 5.4a) is not dependent on water immersion due to its non-polar structure; consistent with this is the parallel observation of no weight gain after water immersion (see Figure 5.1). No noticeable increase in AC breakdown strength can be achieved after incorporating nano-AlN into PP under any sample condition or surface treatment. Instead, all nanocomposites, regardless of surface treatment method, show a monotonic decreasing trend with increased AlN loading, but a marginal increase for MPS treated samples at low filler loading. Consistent results were also reported where both non-treated and C8E treated AlN were added into PE and PP, respectively [96, 131]. Different silane treatments can slightly enhance the AC breakdown strength for dry samples relative to counterparts employing non-treated AlN. MPS treated samples show the highest AC breakdown strength among all samples with the same AlN loading ratio under dry conditions. This can be related to the crystalline structure with eliminated inter-spherulite-boundaries (Figure 4.4) and the presence of β crystal in MPS treated samples (Figure 4.8) [179].

After 9 days of water immersion, a significant (~35 kV/mm) reduction of the AC breakdown of non-treated systems can be observed (Figure 5.4a), while C8M and C8E (Figures 5.4 b &c) exhibit much less of a decrease (~20 kV/mm) when compared to the non-filled PP. Ayoob et al. reported that a 30 wt.% BN/PE sample did not show a pronounced reduction in AC breakdown strength after 14 days of water immersion (0.08 % weight gain) which is similar to both sets of C8 treated samples here where C8E-10-W shows the most reduction when compared to C8E-10-D, 5.9 kV/mm [177].

Although wet MPS treated samples show a higher reduction in AC breakdown strength (e.g., Δα=15.4 kV/mm for MPS-5) relative to their dry counterparts C8 treated samples, they still offer a value close to the wet C8 treated samples. This could be related to the same level of water uptake, as shown in Figure 5.1.

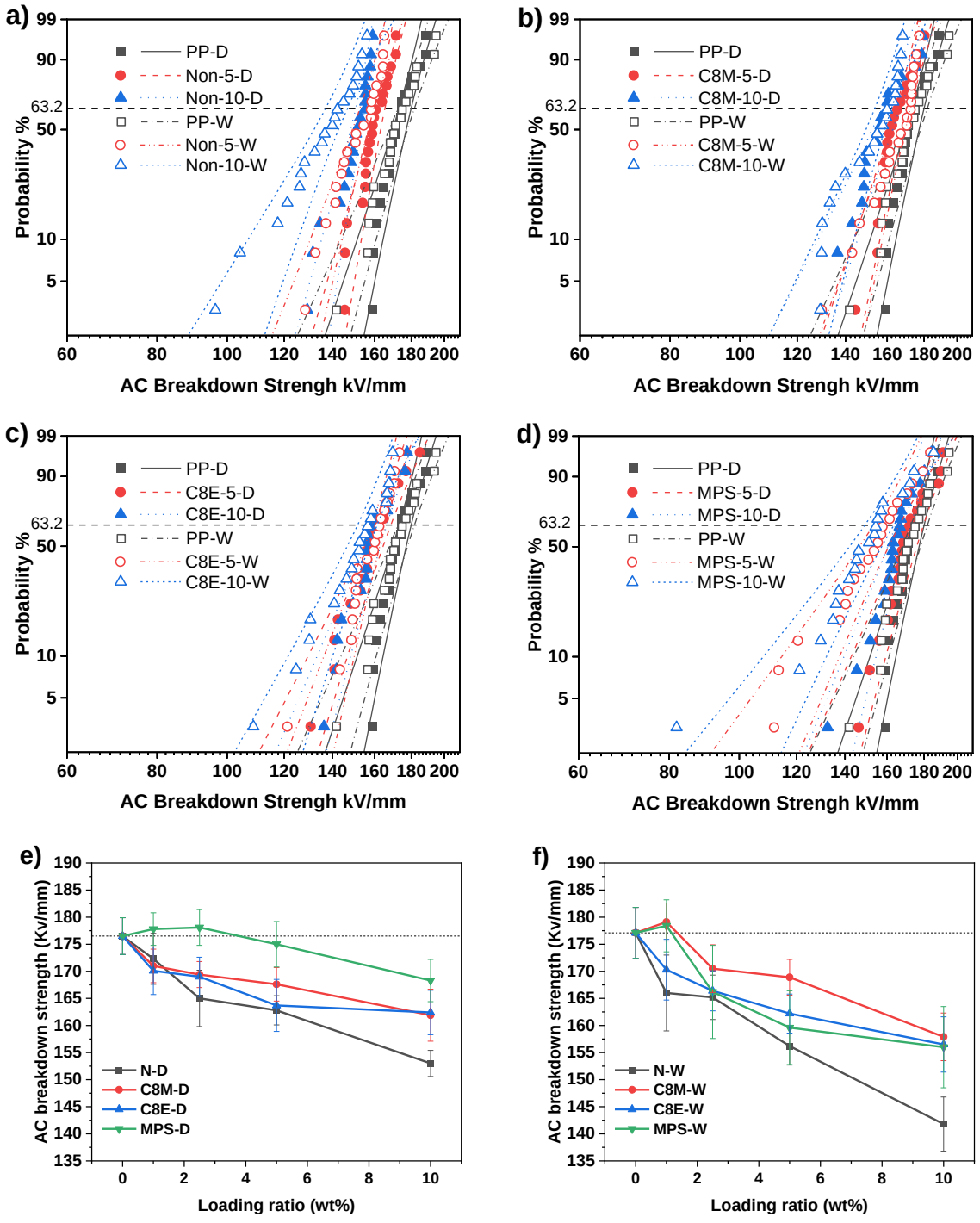

Figure 5.4 AC breakdown strength of dry and wet samples (0, 5 and 10 wt. %) tested at 20 °C and 50 Hz, a) PP and non-treated samples, b) PP and C8M treated samples, c) PP and C8E treated samples, d) PP and MPS treated samples; the Weibull scale parameter of samples at e) dry and f) wet condition.

Table 5.1 AC breakdown strength of dry and wet samples, where β value is obtained when the confidence level is 90 %.

Filler	Filler Loading	α, kV/mm, Dry	β Dry	α, kV/mm, Wet	β Wet
Non-filled	0	176.5	20.2	177.1	14.8
Non-treated	1	172.3	14.4	166.0	9.2
	2.5	165.0	12.4	165.2	15.8
	5	162.8	23.9	156.2	17.4
	10	153.0	25.3	141.8	11.1
C8M	1	171.0	20.6	179.1	18.3
	2.5	169.4	27.2	170.5	14.4
	5	167.6	20.3	168.9	19.6
	10	161.9	13.3	157.9	14.5
C8E	1	170.1	14.3	170.3	11.4
	2.5	169.0	17.8	166.4	17.1
	5	163.7	13.1	162.2	17.9
	10	162.4	15.7	156.5	12.4
MPS	1	177.8	21.3	178.4	13.2
	2.5	178.1	19.5	166.2	7.3
	5	175.0	15.1	159.6	9.3
	10	168.3	16.4	156.0	8.4

5.5 Summary

The silane treated samples benefit from the improved hydrophobicity and show a better ability to retain permittivity and AC breakdown strength than their non-treated counterparts following water immersion. These prove that silane functionalisation is a practical approach to mitigate the water absorption issue, especially for samples treated with octyl silanes. From the AC breakdown strength of the dry samples, it is suggested the higher values of the MPS treated samples compared to nanocomposites with non-treated or C8 treated AlN are related to eliminated inter-spherulite boundaries and the presence of the β crystal, which is the evidence of an interaction region is formed close to nanoparticles. Although MPS treated samples show an almost identical hydrophobicity to the samples treated by octyl silanes, it would be reasonable to believe that a significant reduction of AC breakdown strength and a notable higher dielectric loss at low frequency

after exposure to water is coming from the presence of the polar methacrylate groups in MPS treated samples.

As the dielectric properties of polymeric insulating materials are susceptible to the presence of water, the benefit of introducing and the resulting interaction between the functional groups and the PP matrix, such as MPS induced β crystals, and the hence increased AC breakdown strength, can be quickly undone by absorbed water from a humid environment settling on said functional groups. Thus, a balance must be found between the additional functionality required by an additive and the hydrophobicity of said additives, especially for insulating materials that will be subjected to high humidity environments during operation.

Chapter 6 Effect of Mono-alkoxy Silane on the Dielectric Properties of PP/AlN Nanocomposites

Part of the results presented below is planned to be submitted for publication as:

Wang, Xinyu, Andritsch, Thomas and Chen, George Influence of mono-alkoxy and tri-alkoxy silane on the water absorption and dielectric response of polypropylene/AlN nanodielectrics. (In draft)

Part of the results in Chapters 4 & 5 is re-presented in this chapter for better comparison. The experimental details can be found in Appendix A.

6.1 Introduction

Organic and inorganic materials usually have low compatibility with each other. SCA has been used widely to form a chemical bonding or enhance the compatibility between materials interface within the compound [144, 145]. In nanodielectrics, the addition of SCA is reported not only to increase the dispersion of nanofillers [173] and minimise the water absorption issue but also can bring promising properties for high voltage dielectric application, e.g., increased breakdown strength [146], decreased dielectric permittivity and losses [180, 181], and enhanced space charge suppression ability [182].

A commonly used SCA is TAS (tri-alkoxy silane). The general structure of a TAS is a silicon atom surround by an organofunctional group (octyl, epoxy, amino, etc.) and three hydrolysable groups (methoxy or ethoxy) [144]. The organofunctional group will form bonding or interaction with the organic part. The hydrolysable groups allow TAS to develop bonding with the -OH group on the inorganic surface (oxane bond) and, at the same time, condense with each other leading to the formation of a polysiloxane structure [144]. In the case of nanoparticles, a disordered crosslinking layer of TAS with various properties, such as thickness and condensation rate, can be formed around (as illustrated in Figure 6.1a).

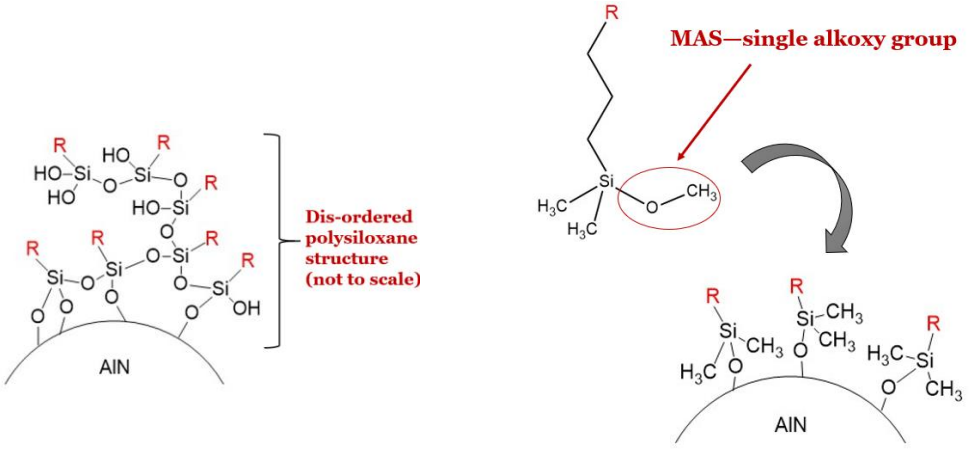

a b

Figure 6.1 Illustration of the AlN surface structure treated with a) TAS and b) MAS; R is the organofunctional group (not to scale).

Due to the large interfacial area within nanocomposites, the variation of this polysiloxane structure on the nanoparticle surface can significantly change the bulk properties of nanocomposites. Yeung et al. reported that the increased amount of TAS applied during silane treatment generates a silane layer with increased thickness. A thick silane layer can result in a decreased breakdown strength of epoxy/silica nanocomposites [146]. Zhang et al. applied different amounts of TAS to BST/PVDF composites [181]. The results suggest the crosslinking of TAS is forming a thicker oligomer layer that can result in the aggregation of the particles and introduce higher dielectric losses of the composite. Similar behaviours were reported when different amounts of TAS are applied in preparing $BaTiO_3$/VC91 nanocomposites by Tong *et al.*; TAS brings the interaction between fillers and induces aggregations with the increase of the TAS loading. Still, the authors suggested the increased dielectric losses are related to the free (non-bonded) or de-bonded TAS when a higher amount of TAS is applied [180].

An anhydrous method is adopted to control the thickness of the TAS layer and reduce the variability from the amount of the TAS applied during silane functionalisation. It can restrict the hydrolysis and condensation of the TAS [146]. However, the results still show an increased amount of TAS grafted on the nanosilica surface with an increased amount of TAS added [146]. Although an improved anhydrous method reported can reach saturation of the layer thickness when an excess amount of TAS is used, see Appendix C, the continuous study suggested the polysiloxane structure formed by TAS can act as water absorption sites that lead to the increased hydrophilicity and dielectric losses of the composites. In Chapter 4, three different TAS are used for surface treatment, and they were studied with the help of a water absorption analysis. Although TAS treatment

reduces the water absorption compared to the non-treated nanocomposites, they still show a higher water absorption to the neat PP.

Alternatively, MAS (mono-alkoxy Silane) with a single alkoxy group (while other two alkoxy groups replaced by methyl) can provide a strict monolayer of silane with an isolated silane structure (Figure 6.1b), which is considered as a "frequently used alternative" for nanostructured material [144]. Although not many studies have revealed the application of MAS in nanodielectrics for high voltage insulation, its unique feature shows a great potential to limit the influence of the polysiloxane structure formed by TAS and the disadvantages from the "inappropriate" amount of silane used during silane treatment.

In this chapter, MAS-treated AlN nanoparticles were prepared with an anhydrous method then blended with PP. The structure of the silane layer on the treated AlN surface is characterised; A significant difference in the “near-particle” side structure is expected. This approach could help us better understand the said region, as the SCA with different hydrolysable groups has a limited ability to alter the near-particle structure, which is restricted by the anhydrous method used. The water absorption analysis usually uses water as a probe that can investigate the interface properties of the nanocomposites, especially for polyolefin composites where the hydrophobic matrix contributes to few amounts of water compared to the interfacial region [97, 183]. Therefore, the water absorption behaviours and dielectric response of composite samples are studied to reveal the influence of the different structures of the “near-particle” side on the dielectric properties of AlN/PP nanocomposites treated with TAS and MAS.

6.2 Material Characterisation

MAS, named n-octyldimethylmethoxy silane (C8Mono), was purchased from Gelest. It has the same organofunctional group as C8M, allowing us to eliminate the effect of far-particles side surface chemistry. AlN was treated with C8Mono using the same method in Chapter 3, except the SCA are different. It was then blended with PP via the solution blending method used in Chapter 4. Samples involved in this chapter are listed in Table 6.1. It should be noted that part of the results related to the PP filled with non-treated and C8M treated AlN are re-presented in this chapter for a better comparison.

Table 6.1 Details of samples involved in this chapter.

Sample	Treatment	Loading (wt%)	Sample	Treatment	Loading (wt%)
PP	-	0	-	-	-
N-1	-	1	-	-	-
N-2.5	-	2.5	-	-	-
N-5	-	5	-	-	-
N-10	-	10	-	-	-
C8Mono-1	C8Mono	1	C8M-1	C8M	1
C8Mono-2.5	C8Mono	2.5	C8M-2.5	C8M	2.5
C8Mono-5	C8Mono	5	C8M-5	C8M	5
C8Mono-10	C8Mono	10	C8M-10	C8M	10

6.2.1 TGA

The TGA results of the AlN and composite samples are shown in Figure 6.2. In Figure 6.2a, C8M treated AlN shows a 4.1% additional weight decrease to the non-treated AlN, assigned to the grafted C8M on the AlN surface. Meanwhile, 1.7% of the additional weight decrease to the non-treated is observed for C8Mono treated AlN. This indicates less C8Mono is bonded to the AlN surface than C8M. This suggests that the surface coverage of C8Mono is lower than that of C8M on the AlN surface or that C8Mono is generating a thinner layer of SCA, while C8M forms a multilayer.

As the derivative curves are shown in Figure 6.2b, broad peaks from 150 to 600 °C can be observed on the C8M and C8Mono treated AlN, which is related to the thermal decomposition of grafted SCA layer on the AlN surface. The highest decomposition rate of the C8M layer is located at 409 °C, which gives a significantly higher thermal stability than the SCA layer formed by C8Mono (decomposition peak centred at 289 °C). A C8M molecule can form three covalent bonds with the surface -OH group or adjacent C8M; this will result in a polysiloxane structure with higher thermal stability. For C8Mono, only a single bonding is available, giving a higher probability of being removed from the AlN surface at an increased temperature [144].

Figure 6.2c shows the TGA results of the AlN treated with increased amounts of C8Mono added during the surface treatment. The corresponding results of C8M treated AlN can be found in

Appendix C. The additional weight decrease compared to the non-treated AlN reaches saturation when the C8Mono loading amount is higher than 0.26 ml/g. After most of the surface -OH are displaced by C8Mono, the excess of C8Mono is removed from the system through the washing process. The results suggest that 0.26ml/g is sufficient for replacing available -OH on the AlN surface. This means the C8Mono is more likely to form a thinner silane layer than provide a lower -OH displacement rate than C8M.

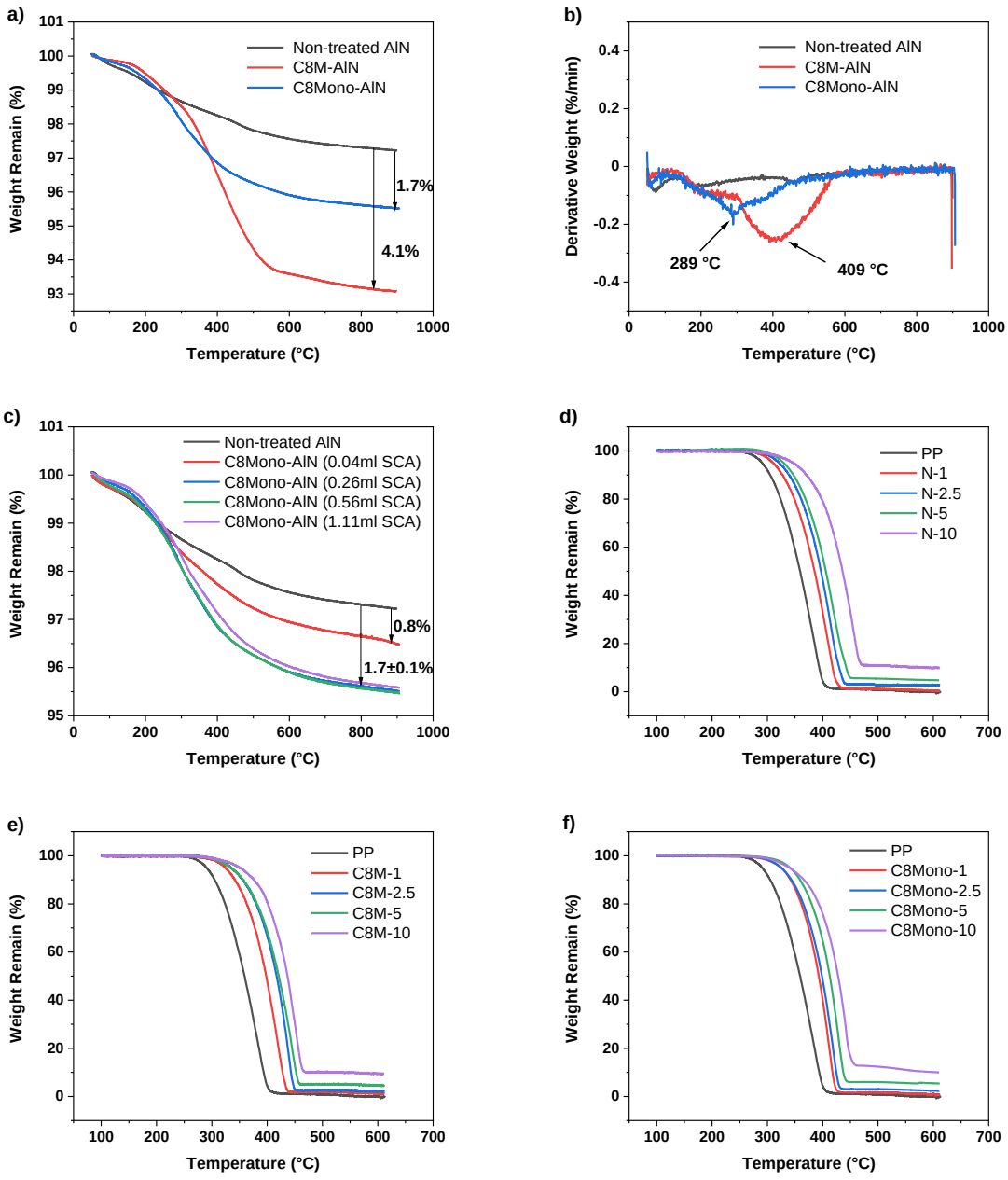

Figure 6.2 TGA results of the reference AlN and silane treated AlN, a) to c) TGA and derivative TGA curves of AlN; d) to f) TGA data of nanocomposites.

From figure 6.2 d to f, the actual loading ratio of nanocomposites can be confirmed. PP is decomposed at a temperature range from 250 to 500 °C, and the AlN filler will remain intact at 600 °C. All samples are confirmed to match the designed filler loading ratio, but a variation of ± 0.5 % could be observed, e.g., the N-1 sample has a weight remain of 0.51 % of weight remain (designed to be 1 %). This is acceptable considering the instrumental error is about 1 % acknowledged from multiple tests. Notably, the onset of the PP decomposition is moving to a higher temperature when an increased amount of AlN is blended. It may suggest that the addition of AlN is increasing the thermal stability of PP. Carvalho et al. proposed a "diffusion barrier" formed by fillers will physically impede the decomposition of the polymer matrix [184]. Wang et al. suggest that the addition of filler with higher thermal conductivity will enhance the bulk thermal conductivity and lead to higher thermal stability [185]. Regarding the samples with different filler surface chemistry, the thermal decomposition behaviours present an independent trend consistent with the TGA results of different TAS treated samples reported in Chapter 4.

6.2.2 FTIR

The detailed condition of the FTIR experiment can be found in Appendix A. The FTIR spectra of non-treated, C8M-treated, and C8Mono-treated AlN are presented in Figure 6.3, and an offset y-axis is applied for better illustration. Peaks located at 2959, 2922 and 2853 cm^{-1} from the C8M and C8Mono treated AlN correspond to the asymmetric C-CH_3, asymmetric CH_2, and symmetric CH2 stretching vibrations, contributed by the octyl group on C8M and C8Mono [155]. The peak of -CH_3 (2959 cm^{-1}) shows a significantly higher intensity on C8Mono treated AlN than the C8M treated AlN, which could be related to two additional methyl groups on the C8Mono molecules. The presence of Si-CH_3 bonding on the C8Mono treated AlN surface can also be confirmed by the absorption peaks at 1408 and 1257 cm^{-1}, assigned to the scissoring vibration and symmetric bending vibration of Si-CH_3 on grafted C8Mono [155]. It is notable that free -OH is distinct on the spectra of C8Mono treated AlN. This suggested the de-bonding process occurs, which can be related to the nature of C8Mono, having only one bonding site than C8M for three. The de-bonding process is more likely to happen for MAS treated AlN before the FTIR test, which the TGA confirmed results in Figure 6.2 where C8Mono shows less stability than grafted C8M on the AlN surface. The spectra of C8M treated AlN have broadband from 968 to 1142 cm^{-1}, it is originating from the overlapped band of Si-O-Si, Si-O-C and Si-OH of the polysiloxane structure formed by C8M [153]. In contrast, C8Mono treated AlN show a sharp peak at 1067 cm^{-1}, corresponding to the presence of Si-O-Si; this could be a result of the condensation of the de-grafted C8Mono.

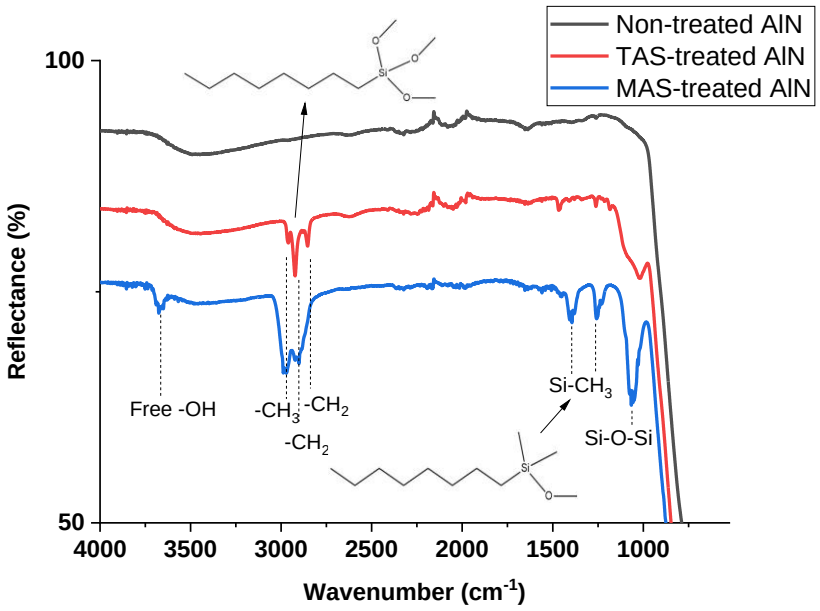

Figure 6.3 FTIR spectra of Non-, C8M-, and C8Mono-treated AlN.

6.2.3 SEM

SEM images of nanocomposites are shown in Figure 6.4. Only those images obtained from samples with 10 wt% of AlN are included since they are the most representative showing the AlN dispersion varied from the silane treatment.

Figures 6.4 a, c, and e show an overall dispersion through 100 magnification. Both C8M and C8Mono can improve the dispersion of the nanoparticles. The octyl groups at the outer layer of the treated AlN provide enhanced compatibility with the PP matrix. Figures 6.4 b, d, and f present a nanoscale dispersion with a 10,000 magnification. Agglomerated nanoparticles can be found in non-treated and C8Mono treated samples. Fewer agglomerations are visible from the C8M treated samples. Hosier et al. studied the effect of organofunctional chain length on the dispersion of nanoparticles. Particles with a longer chain length (higher SCA thickness) shows a higher ability to separate the particles in nanoscale [95]. This suggesting that the nanoscale dispersion could be strongly related to the thickness of the SCA layer.

The morphological properties of PP filled with C8Mono treated AlN is shown in Appendix B for better presentation (larger images). SEM and DSC results of C8M and C8Mono treated samples are presented.

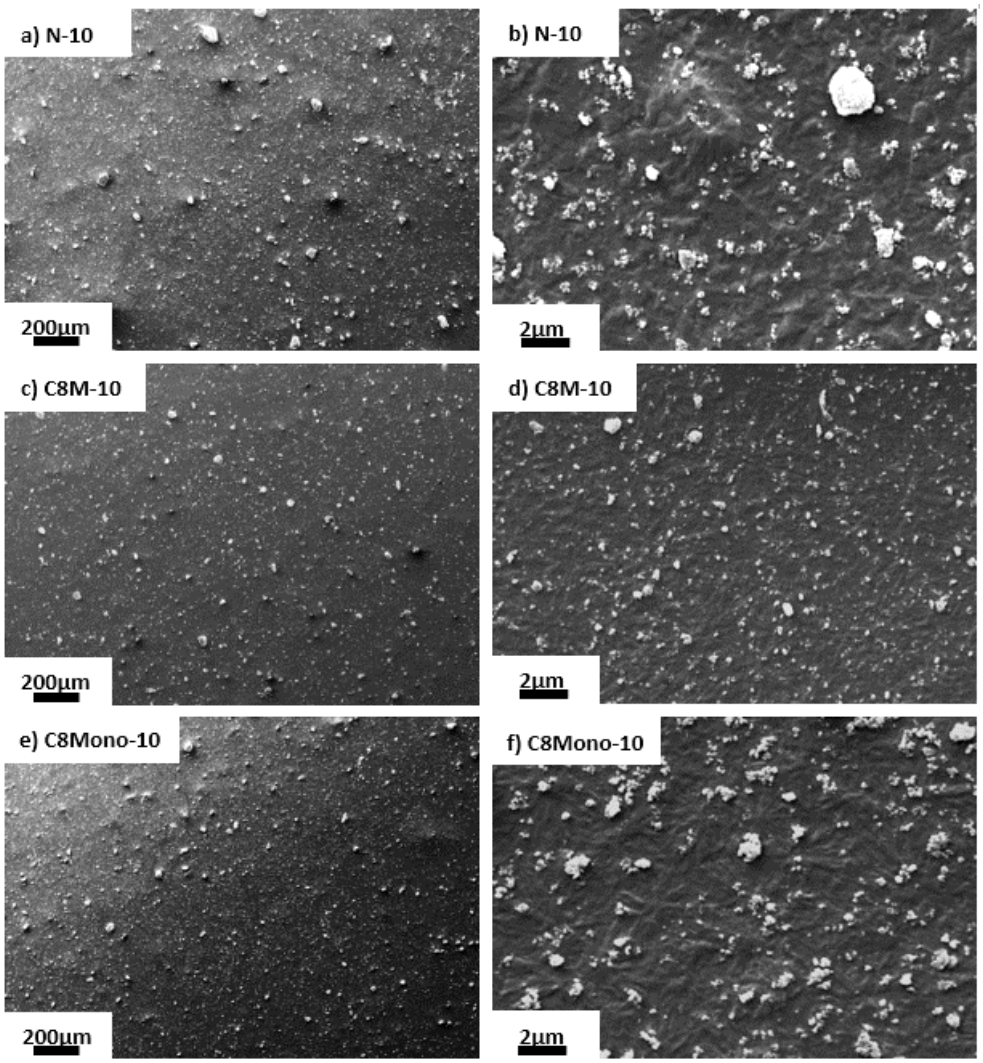

Figure 6.4 SEM images of nanocomposites with 10 wt% AlN with a), c), and e) 100 magnification, and b), d), and f) 10,000 magnification.

6.2.4 Water Absorption

The weight increases in film samples over 9 days of water immersion are shown in Figure 6.5. PP sample shows almost no weight increase after water immersion. The hydrocarbons backbone and polar group free structure allow PP to have excellent hydrophobicity. This also indicates the increased weight of nanocomposites after water immersion are solely related to the addition of AlN. It has been proposed that the absorbed water is more likely to be located on the surface of nanofillers, as the presence of -OH groups is a favourite site for water molecules, hydrogen bonds are built [97, 173]. This can explain the C8M treated samples have significantly eased water

absorption issues to the samples filled with non-treated AlN (Figures 6.5a & b) because SCA has displaced the -OH groups with a hydrophobic tail (octyl group). However, it is surprising that the C8Mono treated samples are taking a comparable amount of water than the non-treated samples (Figures 6.5a & c), although TGA and FTIR results suggest that the C8Mono is grafted onto the AlN surface via displacing -OH groups. The results show that the crosslinking layer formed with C8M has a better repelling ability to water molecules or a higher silane coverage when C8M is used. Marcinko and Fadeev have studied the hydrolytic stability of trifunctional and monofunctional silane on the TiO_2 and ZrO_2 substrates; most monofunctional silane de-grafted within 50 h in an aqueous solution at pH~7, and the de-grafting process is even faster in both acidic and alkaline solutions at other pH levels. In contrast, more than 75% of trifunctional silanes can remain grafted after 200 h [186]. There is reason to believe that the grafted C8Mono has de-grafted through a hydrolysis process even particles are enclosed within a hydrophobic matrix (PP). Thus, contributing to the increased water absorption from the re-exposed -OH groups and the hydrolysis process itself. The dispersion of nanoparticles determines the interfacial area between filler and matrix. The high interfacial area by adding C8Mono (see SEM results in Figure 6.4) can also increase water absorption.

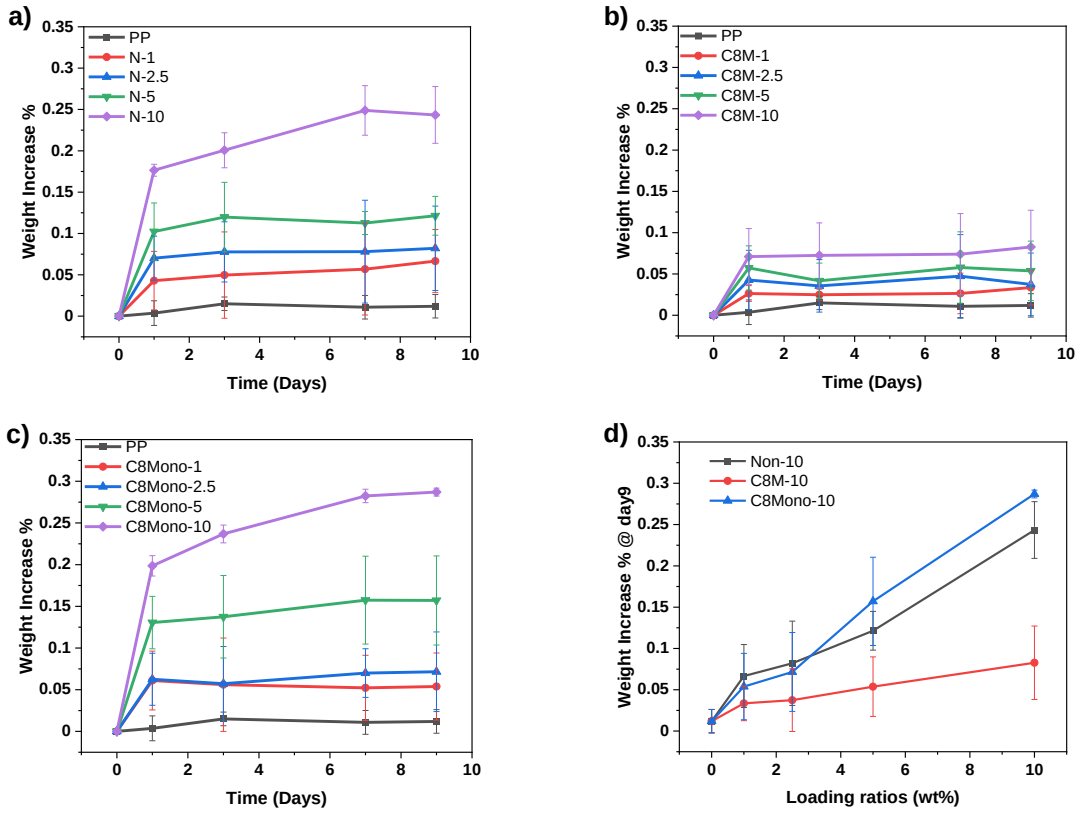

Figure 6.5 The weight increase of each sample during the water immersion up to 9 days.

6.3 Dielectric Properties

6.3.1 Dielectric Spectroscopy

The dielectric spectroscopy of dry samples is shown in Figure 6.6; only samples with 10 wt% AlN under dry conditions are presented for brevity, as filler with different loading ratios offers the same trend. Compared to the PP sample, all nanocomposites show increased real and imaginary permittivity. Upturns at low frequency can be found on imaginary permittivity, but there are no features related to the relaxation process. The introduced AlN has a higher permittivity than the PP matrix, and the polar surface groups of AlN are also contributing to the increased permittivity. This explains the C8M- and C8Mono-treated samples show a lower permittivity to the non-treated samples. For samples treated with C8M and C8Mono, on significant difference can be found.

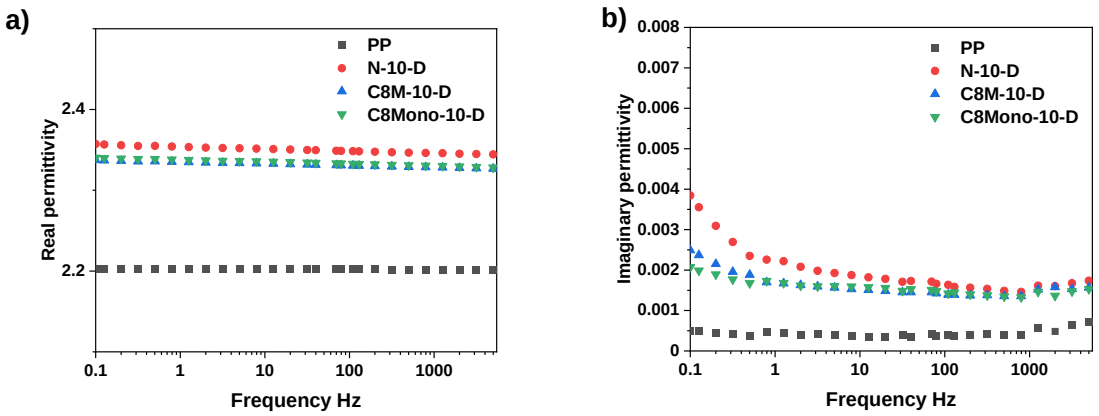

Figure 6.6 a) real, and b) imaginary permittivity of PP with 10 wt% of AlN under dry condition.

However, we need to note that dry samples can also absorb moisture from the ambient environment. The difference between samples with different surface treatments is insignificant, which can easily be affected by the testing environment [97]. Therefore, samples immersed in water for 9 days are investigated. This approach is suggested can magnify the dielectric response that originated from the surface structure of AlN through its interaction with water molecules. In Figure 6.7 a & b, relaxation processes can be observed for non-treated samples. They are related to the absorbed water around AlN. The peak moves to a lower frequency with the sample having 10 wt% of AlN similar shift can also be found in C8Mono treated samples (Figure 6.7f). The peak location is suggested to be related to the thickness of the absorbed water shell surrounding the filler. A thicker water shell induces a relaxation peak at a higher frequency as the outer layer is more loosely bonded on the filler surface. For composites with higher loading ratios, the probability of filler aggregation is increased. The water shell thickness between adjacent particles is then reduced,

thus, moving the relaxation peak to a lower frequency. Similar behaviour is also reported elsewhere [177].

For C8M treated samples in Figures 6c and d, the results are consistent with the water absorption behaviour in Figure 6.5. C8M samples absorb the least amount of water. The relaxation feature is assumed to be located at a low frequency that is not within the testing range due to the limited water shell thickness, according to Equation 5.8.

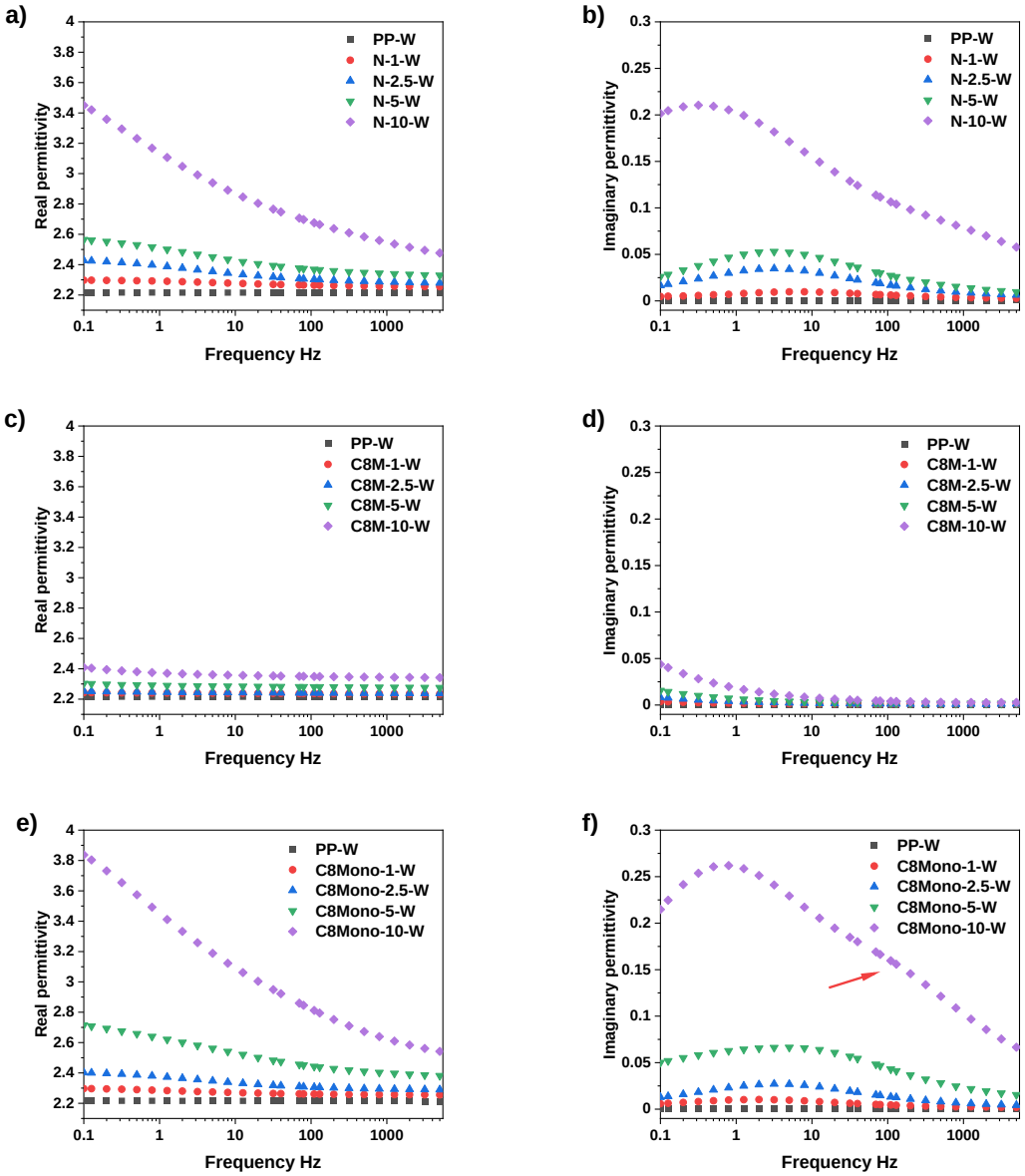

Figure 6.7 Complex permittivity of PP and its nanocomposites at wet condition, a), c), and e) are the real part, and b), d), and f) are the imaginary part.

C8Mono treated samples with 1 to 5 wt % of filler loadings give an identical relaxation feature after water immersion with the non-treated samples, which is consistent with the water absorption behaviour. However, as shown in Figure 6.7f, additional relaxation processes can be observed on C8Mono-10-W treated samples, which are not negligible. To further investigate this behaviour, the data was analysed via the Havriliak-Negami (HN) relaxation model, where the real and imaginary permittivity can be described as [187]:

$$\varepsilon' = \varepsilon_{\infty} + \Delta\varepsilon \times \frac{cos(\beta\theta)}{\left[1 + 2\left(\frac{f}{f_0}\right)^{\alpha} cos\left(\frac{\alpha\pi}{2}\right) + \left(\frac{f}{f_0}\right)^{2\alpha}\right]^{\frac{\beta}{2}}} \quad (6.1)$$

$$\varepsilon'' = \Delta\varepsilon \times \frac{sin(\beta\theta)}{\left[1 + 2\left(\frac{f}{f_0}\right)^{\alpha} cos\left(\frac{\alpha\pi}{2}\right) + \left(\frac{f}{f_0}\right)^{2\alpha}\right]^{\frac{\beta}{2}}} \quad (6.2)$$

Where

$$\theta = tan^{-1}\frac{\left(\frac{f}{f_0}\right)^{\alpha} sin\left(\frac{\alpha\pi}{2}\right)}{1 + \left(\frac{f}{f_0}\right)^{\alpha} cos\left(\frac{\alpha\pi}{2}\right)} \quad (6.3)$$

In the above equations:

- *α and β* are the shape parameters of the relaxation features where $0 < \alpha,\beta \leq 1$.
- f_0 *is* the frequency related to the maximal loss peak location of the relaxation processes.
- $\Delta\varepsilon$ is the difference between the static dielectric permittivity and the high-frequency permittivity, which is related to the temperature-dependent intensity of the relaxation processes.

A numerical fitting was performed with Origin software with the above equations, shown in Figure 6.8. Two individual relaxation processes can be separated from the fitted curve, a significant peak with $f_{0\ (peak1)}$ = 0.2 Hz and a minor peak with $f_{0\ (peak\ 2)}$ = 83.2 Hz. Due to the asymmetry of the relaxation peak, the peak location f_{max} can be calculated by:

$$f_{max} = f_0 \left[\frac{\sin\left(\frac{\alpha\pi}{2(\beta+1)}\right)}{\sin\left(\frac{\alpha\beta\pi}{2(\beta+1)}\right)} \right]^{\frac{1}{\alpha}} \quad (6.4)$$

The calculated peak frequency from Equation (6.4), $f_{max\ (peak\ 1)}$ = 0.7 Hz and $f_{max\ (peak\ 2)}$ = 191.2 Hz, match with the relaxation features are observed from the experimental data. The phenomenon of two relaxation processes related to water from the water immersed nanocomposites is widely reported with inorganic fillers, such as Al_2O_3 and SiO_2 with polyethylene nanocomposites [96, 97, 173]. Water molecules with different bonding states result in a relaxation feature centred at a different frequency. The peak centred at a higher frequency originated from the water at the outer layer of the water shell. They are considered "loosely bonded" [173]. In this work, AlN filler is believed to have a surface with lower hydroxyl groups concentration compared to oxides fillers used in [96, 97, 173]. Therefore, the loosely bonded water layer is less likely to form after water immersion; two relaxation processes cannot be observed from the non-treated AlN/PP nanocomposites in Figure 6.7b. After C8Mono is grafted onto the AlN surface, the water shell structures are altered with the presence of the C8Mono, resulting in a small portion of water bonded at a distinct state. Alternatively, this can be related to the presence of the de-bonded C8Mono within the immersed samples.

Besides, from the SEM images shown in Figure 6.4, the increased AlN dispersion with the help of the C8Mono is leading to an increased interfacial area. This could result in more water being absorbed (Figure 6.5) then gives rise to the formation of the loosely bonded water layer.

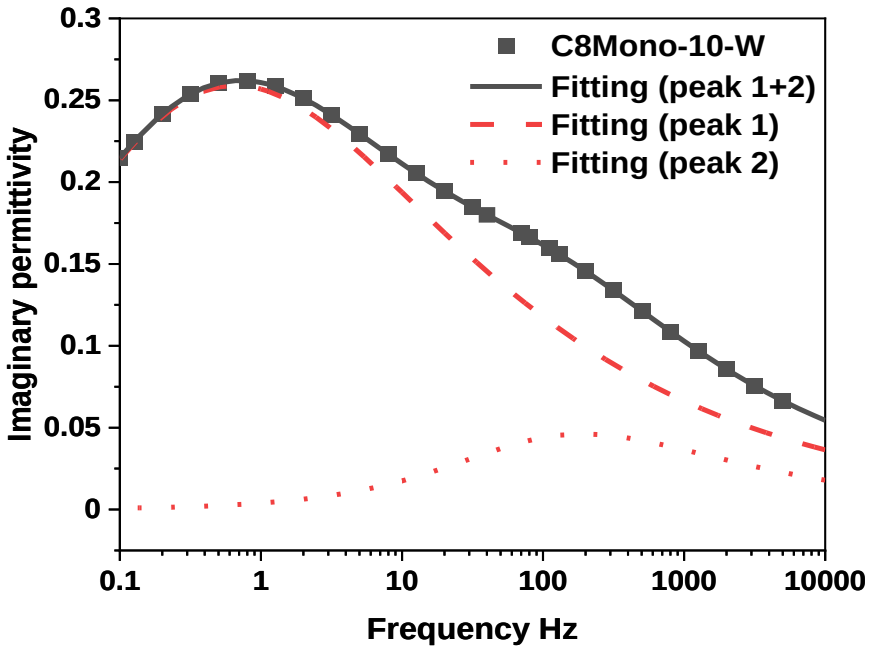

Figure 6.8 Numerical fitting of the Imaginary permittivity of 10 wt% of C8Mono-treated samples after 9 day's water immersion.

6.3.2 AC Breakdown Strength

The AC breakdown strength of the non-, C8M-, and C8Mono-treated PP/AlN nanocomposites are shown in Figure 6.9. A reduction (5.6 %) in AC breakdown strength can be found by adding 10 wt% of C8Mono-treated AlN in PP under the dry conditions; and Lower loading (1, 2.5, and 5 wt%) of the C8Mono-AlN provide comparable results to the neat PP. In contrast, PP/C8M-AlN shows a lower breakdown throughout each loading ratio under dry conditions. This could relate to the thinner silane layer formed by C8Mono. Alternatively, the better breakdown performance offered by C8Mono treated AlN can result from its different crystal structures. As shown in Appendix B, the PP/C8Mono-AlN samples show a similar inter-spherulites-free structure like MPS- and non-treated nanocomposites. The single C8Mono layer without interconnections is too thin to minimise the polarity of the AlN surface, which offers a stronger nucleating effect to the C8M treated AlN. This is unique from the common conception that the interactions between filler and polymer matrix are mainly related to far-particles chemistry. The application of C8Mono in this chapter proved that the near-particle structure could also play an essential role in the interactions between filler and matrix.

After immersing the sample in water for 9 days, C8Mono treated samples show a higher decrease in the breakdown strength, which is in line with the water absorption behaviours, where C8Mono treated can absorb more water than the C8M treated samples.

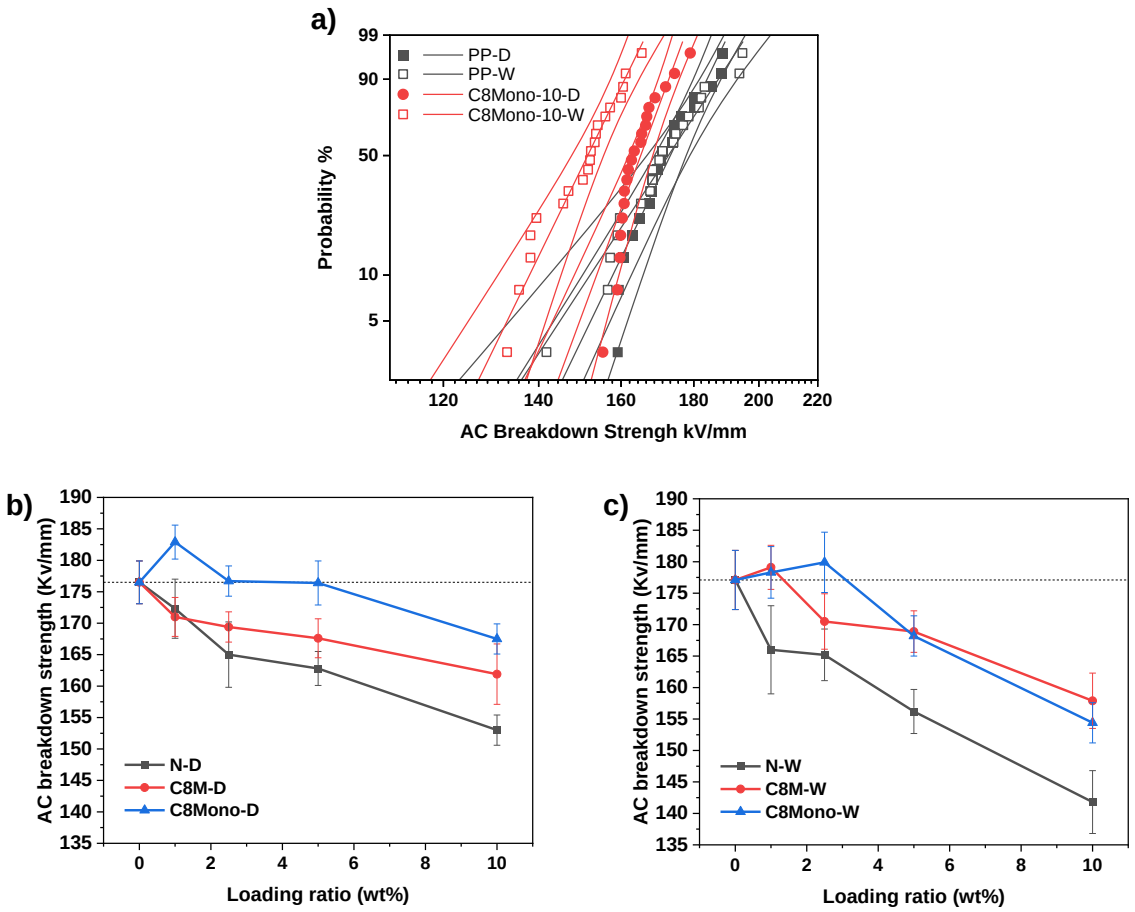

Figure 6.9 AC breakdown strength of a) C8Mono-10 at dry and wet conditions; the Weibull scale parameter of Non-, C8M-, and C8Mono- treated samples at b) dry, and c) wet condition.

6.4 Summary

The effect of a mono-alkoxy silane, C8Mono, on the morphology, thermal and dielectric properties of PP/AlN have been studied in this chapter. One notable finding is the C8Mono treated samples have a higher AC breakdown strength than the C8M treated samples, which can result from a thinner near-particle structure within the interphase or the inter-spherulites free system by applying C8Mono. However, the surface hydrophobicity is significantly reduced and leading to deteriorated dielectric properties under wet conditions. This proved that the near-particle properties could also play a vital role to determine the bulk properties, which can be related to the

thin layer or the limited surface coverage of C8Mono shows a weak ability to reduce the surface polarity. Thus, it offers a higher nucleating effect. (see Figure 6.10).

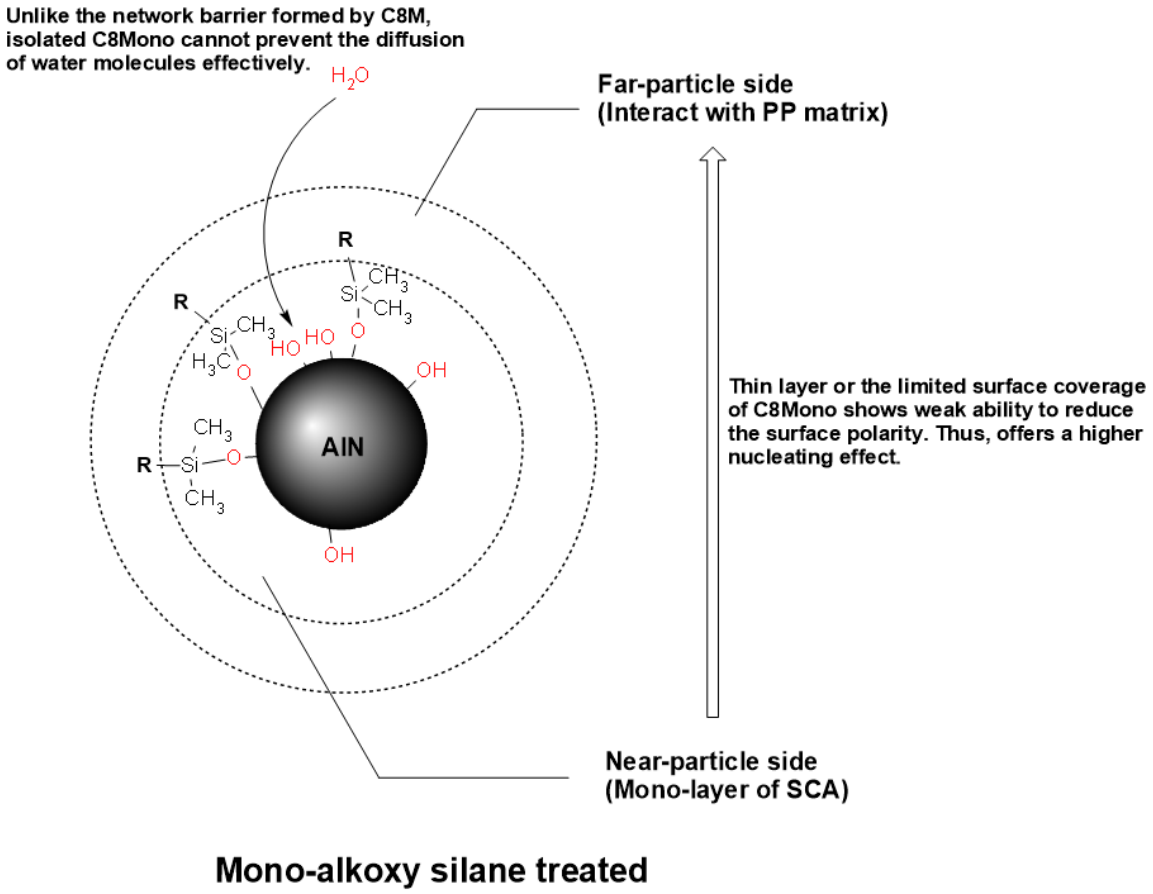

Figure 6.10 The proposed surface structure of the MAS functionalised nanoparticle (not to scale).

We learn from the water absorption results that C8M can form polysiloxane networks that prevent water absorption of the nanoparticle surfaces. Meanwhile, the silane structure formed by C8Mono cannot prevent water absorption of the composite samples effectively and shows less stability (Figure 6.10). Better nanoparticle dispersions can be achieved by applying both C8M and C8Mono compared to the samples with non-treated AlN. However, the C8Mono treatment offers a low ability to improve the AlN dispersion within nanoscale (from SEM results of high magnification), although the SEM results of low magnification are identical with the sample treated with C8M. The dielectric spectroscopy results show a high consistency with the water absorption data. Relaxation features related to the absorbed water are evident from the non-treated and MAS treated samples after water immersion. MAS treatment will result in the water molecules forming a loosely bonded water layer around AlN nanoparticles. In contrast, only a slight increase in imaginary permittivity can be observed from TAS samples at low frequencies.

C8Mono treated samples have a higher breakdown strength than the C8M treated samples. But this superiority quickly vanished under the wet condition. Water molecules play an important role throughout this work regarding the interfacial properties of the AlN/PP nanocomposites resulting from different silane coupling agents, C8M and C8Mono. With the help of that, one of the major disadvantages of the mono-alkoxy silane (low hydrophobicity) in the dielectric insulation application is revealed, especially for insulation devices operating under humid conditions.

Chapter 7 Introduction of Centrifugal Separation Techniques in Processing PP/AN Nanodielectrics

Part of the results presented below is planned to be submitted for publication as:

Wang, Xinyu, Luming, Zhou, Andritsch, Thomas and Chen, George Introduction of Centrifugal Separation in Processing Polypropylene/AlN Nanodielectrics. (In draft)

Part of the results in Chapters 4 & 5 is re-presented in this chapter for better comparison. The experimental details can be found in Appendix A.

7.1 Introduction

AlN is susceptible to hydrolysis, and control methods were applied during the sample preparation process, using xylene for dispersing AlN and dried toluene for silane functionalisation. However, due to the polar nature of the surface groups -OH and -NH_2, large particle agglomerations that exist in the as-received AlN cannot be separated effectively in a non-polar solvent, even with the help of ultrasonication and silane treatment (illustrated in Figure 7.1).

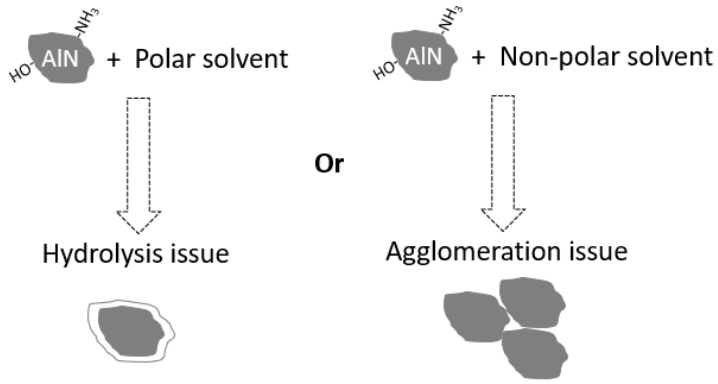

Figure 7.1 Effect of solvent during material processing.

Many studies have pursued the aqueous solution processing of AlN, but most of them propose a pre-treatment procedure that usually provides a protective layer surround AlN, e.g., Ganesh et al. found the AlN particle coated with a phosphoric-acid protective layer can prevent the AlN from reacting with water for more than 72 h [188]. However, the formation of such layers is not in line with the aims of this study, since they will significantly alter the surface chemistry of AlN and might not be suitable for SCA treatment. Therefore, we employ the anhydrous silane treatment (Chapter

3) and non-polar solvent blending procedure, which provides better consistency regarding the status (surface chemistry and morphology) of the AlN.

As a result, a number of large-size agglomerations in the nanocomposites reported in previous chapters and the particle size distribution are varied from nanometres up to 30 μm. These agglomerations can bring side effects to polymer nanocomposites as discussed,

- SCA coatings are formed surrounding the large agglomerations. The space enclosed can be a water absorption site which leads to a reduced hydrophobicity of the samples.
- The possibility of forming a thermal conduction pathway is reduced due to the agglomeration of the nanoparticles, which restrict the thermal conductivity performance of the nanocomposites.
- Large agglomerations can introduce defects into nanocomposites, leading to increased dielectric losses and reduced AC breakdown strength.

Typically, the change of dispersion state (agglomeration rate) results from significant changes in the filler's surface chemistry or the samples preparation procedure. The transition of the bulk properties cannot be solely related to the change of the dispersion state of the filler. In this chapter, a centrifugal separation technique was used during the sample preparation procedure, and the agglomeration is excluded before mixing AlN with PP. This allows investigating the isolated influence of agglomerations on the water absorption, thermal, and electrical performance of PP/AlN nanocomposites in a straightforward manner.

7.2 Processing

An additional centrifugal separation process was added during the silane functionalisation procedure described in Chapter 3. During the centrifuging process, larger particles and agglomerations are expected to move towards the bottom of the centrifuging tube, as shown in Figure 7.2. Therefore, the well-dispersed particles or smaller agglomerations are suspending in the supernatant at the top of the centrifuging tube. Keys steps are listed below. 10g of AlN was dispersed in 300 ml of dried toluene with the help of a probe sonicator of 1 h. The desired amount of SCA was added to the suspension and heated at 110 °C for 24 hrs. After the resulting slurry was washed with fresh toluene 3 times, the treated AlN was re-dispersed in 300 ml of xylene with sonication for 5 min. The AlN/xylene suspension was then added into centrifugation tubes and treated at 2000 rpm for 5 min. After that, the suspension at the top supernatant of the centrifugation tube was separated and ready to blend with PP.

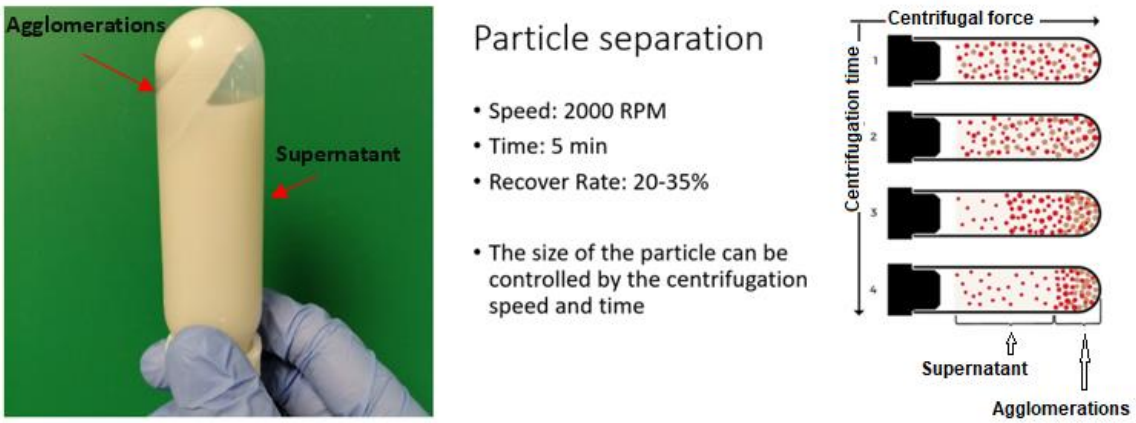

Figure 7.2 The centrifugal separation process, the image on the right reproduced from[1].

It is important to note that the drying procedure applied in Chapter 3 is not used here; thus, the re-agglomeration of the nanoparticles during drying is restricted. However, this approach would be challenging for weighing the desired amount of nanoparticles during the blending step with PP. 1 ml of the top supernatant was used to estimate the AlN concentration of the suspension by weighing the solid residue after dried in a vacuum oven at 100 °C for 24 hrs to overcome this issue.

7.3 Filler Properties

7.3.1 SEM

SEM images of the AlN separated with and without centrifugal separation are shown in Figure 7.3; AlN treated with MPS are presented as an example. SEM samples were prepared by dropping 0.5ml of AlN/xylene suspension on a glass slide. The protrusions observed in the non-separated AlN are assigned to the large agglomerations, and none of these features can be found in the separated AlN. Instead, a uniform structure with a flat surface can be found. Cracks are formed due to the surface absorption force between particles during the drying process. The existence of more cracks in the separated AlN revealed smaller entities with more surface area. This demonstrated that the large agglomerations in the non-separated AlN are formed before the drying process, suggesting that the SCA treatment cannot break those agglomerations; the centrifugal separation process can successfully remove them.

[1] https://www.beckman.co.il/resources/fundamentals/principles-of-centrifugation/particle-separation

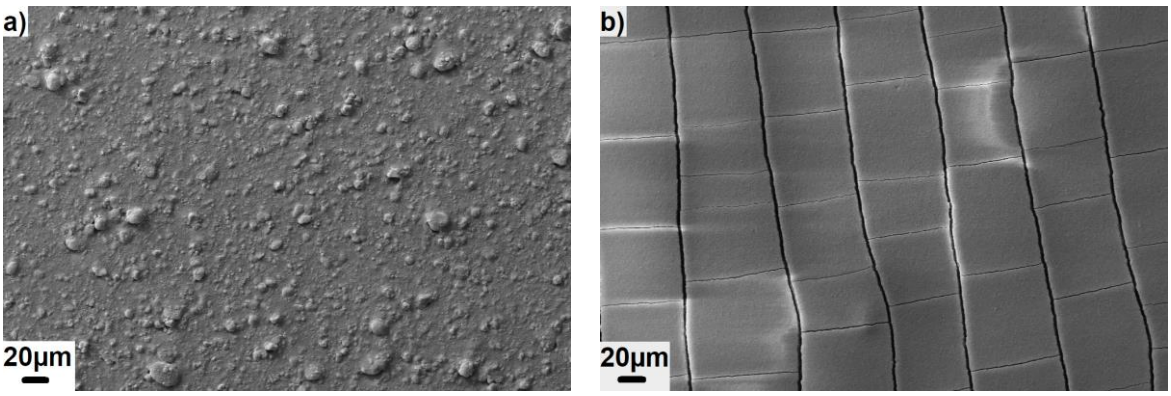

Figure 7.3 SEM images of the AlN separated a) with and b) without centrifugal separation.

7.3.2 TGA

TGA and the derivative TGA results of the AlN separated with and without centrifugal separation are shown in Figure 7.4; AlN treated with C8M are presented as an example. The additional weight decreases compared to the reference AlN from 300 °C to 600 °C are related to the degradation of the grafted SCA on the AlN surface. It is evident the separated AlN shows more weight loss at this temperature range. An additional weight loss of 3.6 % to the non-separated AlN can be found due to the increased surface area covered with SCA. The results confirmed the number of large agglomerations in SCA treated AlN can be successfully reduced with the help of centrifugal separation.

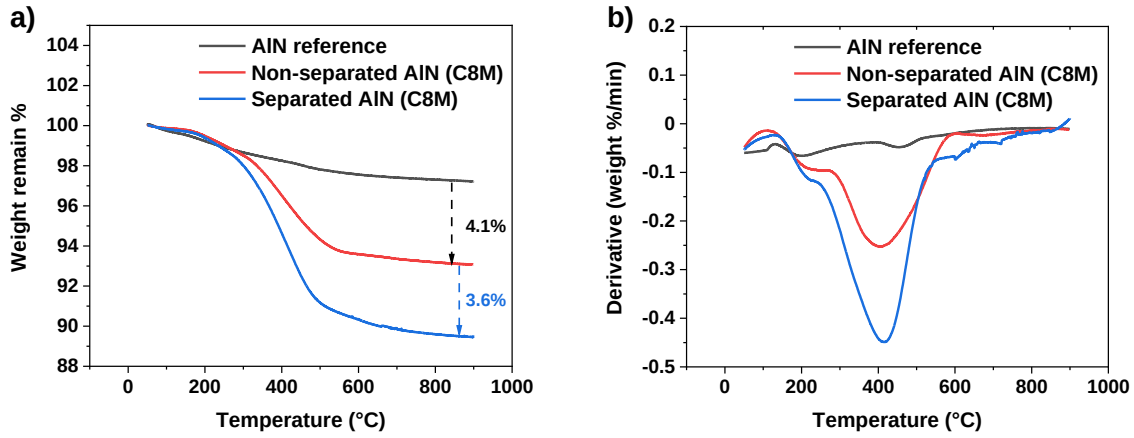

Figure 7.4 a) TGA and b) derivative TGA results of the AlN treated with and without centrifugal separation.

7.3.3 FTIR

FTIR results of AlN treated with different SCA after centrifugal separation are shown in Figure 7.5. A broadband absorption from 3800 cm^{-1} to 3000 cm^{-1} can be found in all samples, corresponding to the surface -OH groups and the absorbed water molecules. Sharp bands at 3675 cm^{-1} could be related to the isolated Si-OH from SCA or the Free -OH from ethanol or methanol, which is more noticeable on the C8E treated AlN. Three adjacent peaks from C8M and C8E treated AlN found at 2988, 2925, and 2853 cm^{-1} correspond to the asymmetric C-CH_3, asymmetric CH_2, symmetric CH_2 stretching vibrations, related to the grafted C8 functional group on the AlN surface [155]. For C8E, the enhanced absorption band at 2988 cm^{-1} (asymmetric stretching C-CH_3) and 2925 cm^{-1} (asymmetric stretching CH_2) could result from ethanol, and the presence of C-O (1394 cm^{-1} and 1250 cm^{-1}) also proved the ethanol content in C8E treated AlN (NIST Chemistry WebBook, SRD 69). Ethoxy silane, like C8E, usually have a much lower grafting rate during silane treatment than methoxy silane (C8M and MPS), see Figure 3.19. The C8E treated AlN can still have a number of Si-O-C_2H_5 on the AlN surface. These ethoxy groups will release ethanol and become Si-OH when in contact with moist air before the FTIR test (Figure 7.5b). It should be noted the absorption band related to ethanol or methanol cannot be found in the FTIR results of non-separated AlN shown in Chapter 3. It is due to the separated AlN prepared here were stored in dried xylene, which has less chance to react with water compared to the non-separated AlN stored in glass bottles in powder form where less Si-O-C_2H_5 and Si-O-CH_3 remained on the AlN surface after a short period of storage time. On the MPS treated AlN, two bands at 1718 and 1637 cm^{-1} are associated with the stretching vibration of C=O and C=C groups, resulting from grafted methacrylate groups from MPS. All spectra have a distinct band at 1064 cm^{-1}, related to the presence of the condensation of SCA, Si-O-Si [189-191].

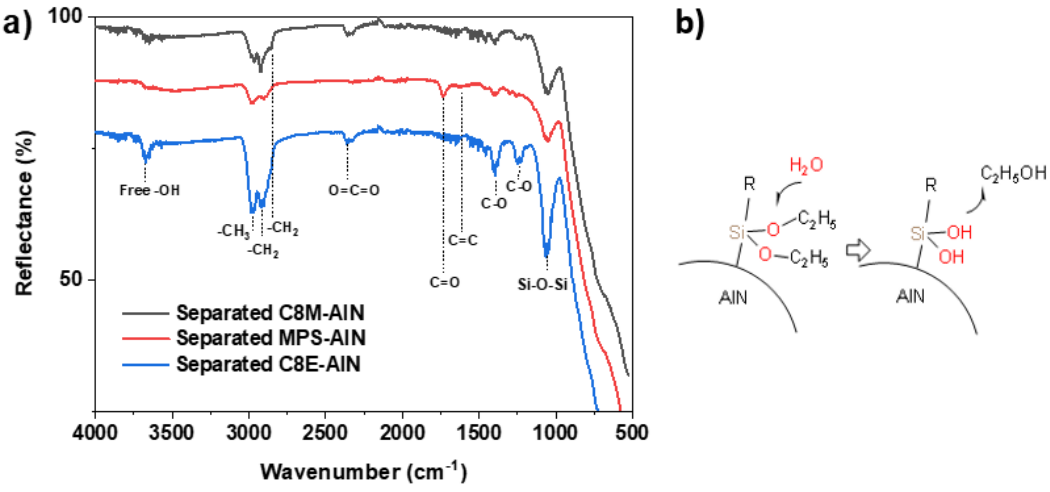

Figure 7.5 a) FTIR spectra of AlN separated with centrifugal separation; b) an illustration of the generation of ethanol on the surface of C8E-S treated AlN.

7.4 Nanocomposites Characterisation

The nanocomposites contain centrifugal separated AlN was named as [SCA]-S-[loading ratio]-[conditioning]. For example, C8M-S-10-W is the PP blended with 10 wt% of C8M treated AlN after the separation procedure after being Immersed in water for 9 days.

7.4.1 SEM

SEM micrograph of PP/AlN nanocomposites prepared with centrifugal separation method is shown in Figure 7.6. SEM images of PP filled with non-separated AlN are also included for comparison; C8M-10 and C8M-S-10 are presented here as an example.

It is evident that a significant improvement of the AlN dispersion and distribution can be observed after the centrifugal separation method was applied. For 100 magnification, no trace of fillers can be seen for SEM images of the PP filled with 10 wt% of separated AlN. In contrast, even silane treatment was applied, large entities are evident from the sample prepared with the conventional solution blending method (non-separated). This underlines the assumption in Chapter 4 that the SCA by itself cannot break the agglomerations, and in samples filled with non-separated AlN, silane layers surrounding agglomerations are being formed.

When comparing samples prepared with two methods at high magnifications (Figure7.6 g & h), more fillers can be seen at these scales in C8M-S-10, and the visible space without fillers are reduced. No agglomerations larger than 2 µm can be found in the sample prepared with an additional centrifugal separation process. The above results suggest that the centrifugal separation process can effectively remove the agglomerations in PP/AlN nanocomposites.

The SEM images of separated samples treated with different silanes are shown in Figure 7.7. Only samples with 5 wt% are presented as all samples offer a similar trend regarding filler loading. It is apparent that the MPS treated samples have a slightly better dispersion than C8M and C8E treated samples, where fewer agglomerations about 1 µm are visible. This is because MPS treated samples have lower compatibility with xylene; thus, fewer agglomerations can stay in the supernatant if the centrifugal separation is performed at the same speed and time duration. But overall, no significant difference regarding the filler dispersion can be seen when different SCA was applied.

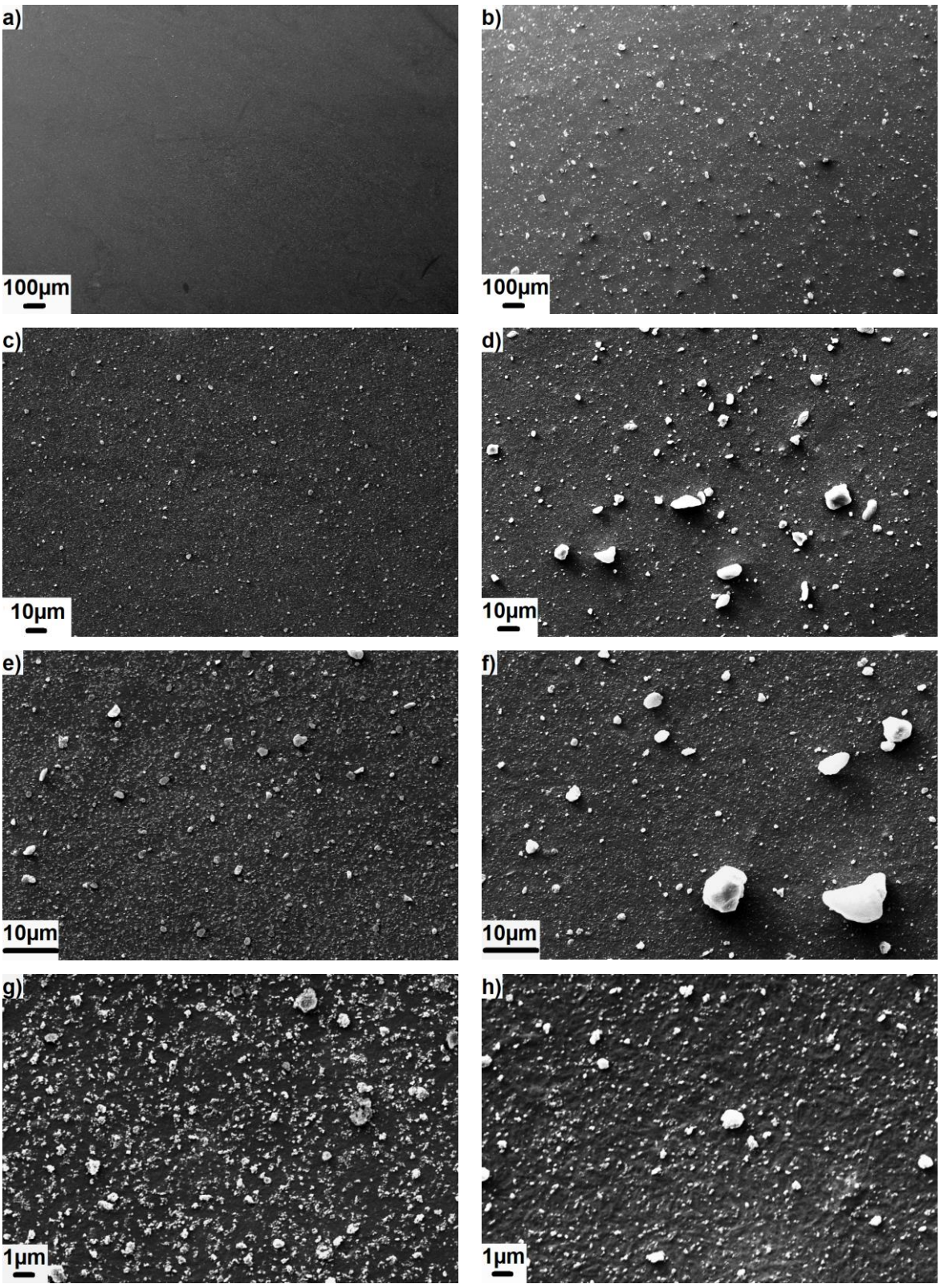

Figure 7.6 SEM images of C8M-S-10 at a) x100, c) x1,000, e) x3,000, and g) x10,000, and C8M-10 at b) x100, d) x1,000, f) x3,000 and h) x10,000 magnification.

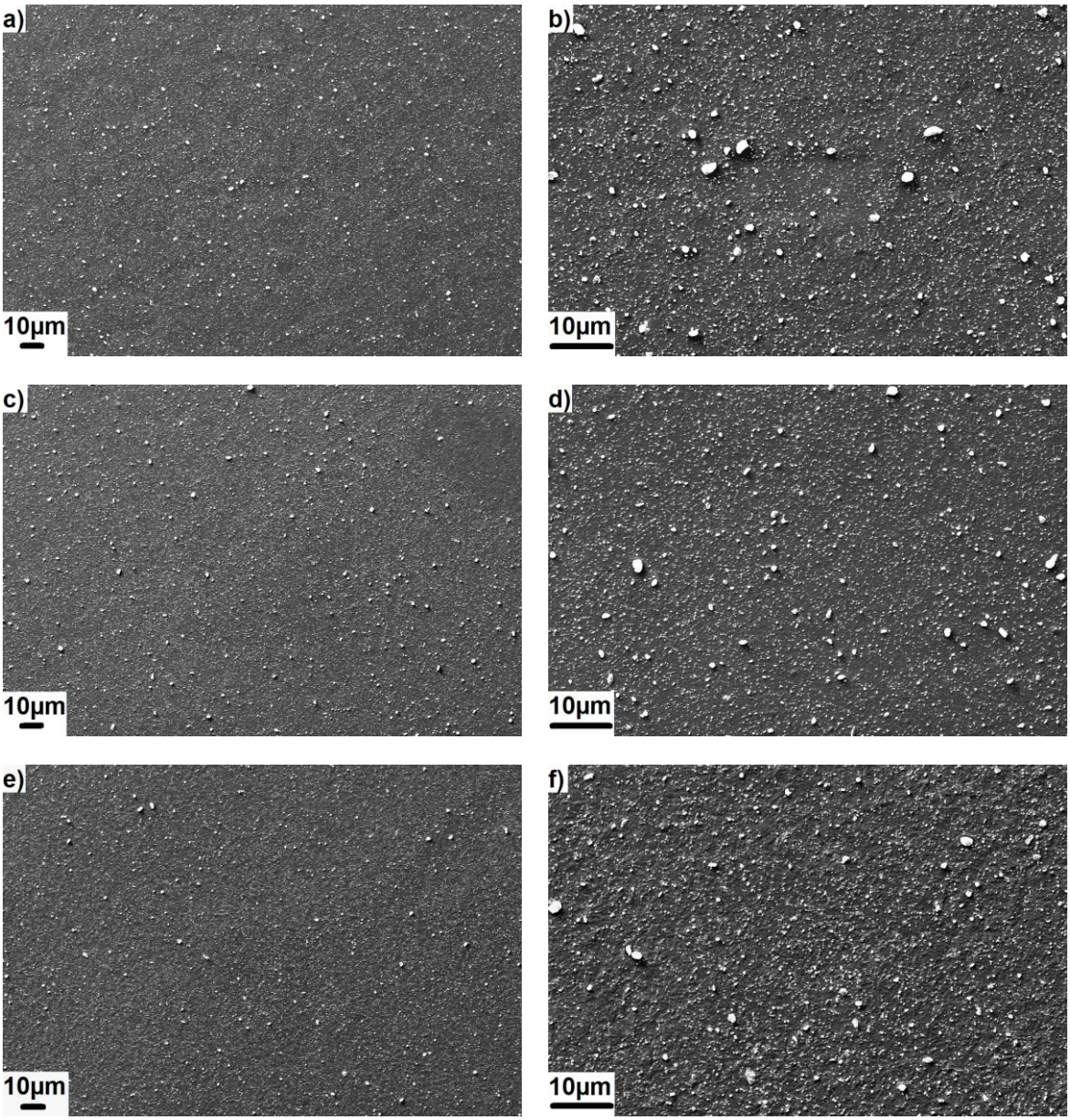

Figure 7.7 SEM image of a) C8M-S-5, c) C8E-S-5, and e) MPS-S-5 at x1,000 magnification, and b) C8M-S-5, d) C8E-S-5, and f) MPS-S-5 at 3,000 magnification.

Nanocomposites filled with separated AlN treated by C8M and MPS are presented in Figure 7.8. C8E treated sample is omitted as it shows the same trend with the C8M treated sample. Samples with 2.5 wt% are presented to highlight the crystal structure of the nanocomposites. The resulting morphological structures are consistent with samples prepared by the conventional solution blending method (non-separated); see Figure 4.4 in Chapter 4. The inter-spherulite boundaries are evident in the C8M-S-2.5 due to the low nucleating effect of the grafted C8 group. In contrast, MPS

treated samples offer a homogeneous structure where no inter-spherulite boundaries can be seen. The results indicate that the crystallisation structures of the PP nanocomposites are more dependent on the surface chemistry of the fillers rather than their dispersion states.

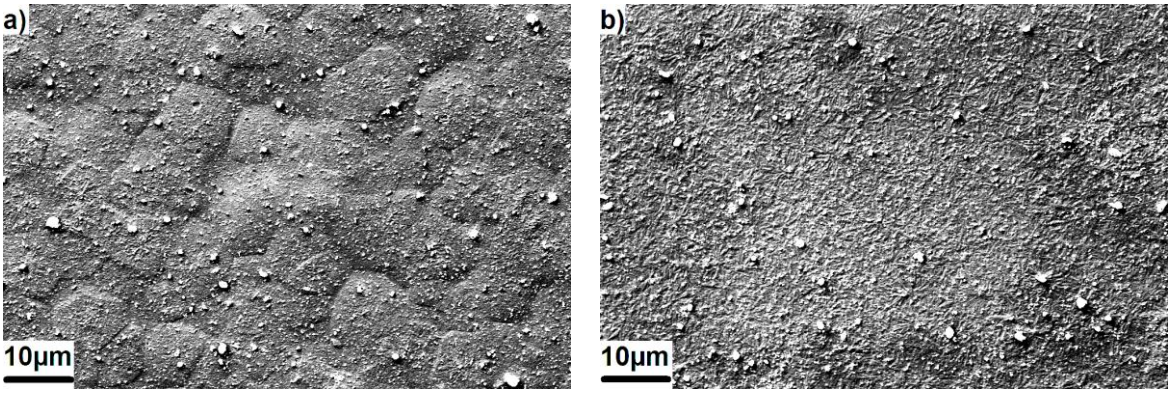

Figure 7.8 SEM image of a) C8M-S-2.5, b) MPS-S-2.5 at x3000 magnification.

7.4.2 DSC

Figure 7.9 compares the melting and crystallisation curve of non-filled PP and nanocomposites with centrifugal separated AlN. Table 7.1 provides the crystallinity, along with the melting and crystallisation peak temperature of each sample; within the table, the data of the PP with non-separated AlN are presented in the followed bracket for better comparison. C8M and MPS treated systems are presented here as the potential interactions brought by their different organofunctional groups are the key feature to be instigated.

At first glance, the DSC results of PP with centrifugal separated AlN show a high degree of similarity with the PP filled non-separated AlN in Chapter 4. To be specific, all samples show a melting endotherm with a similar shape and peak location, indicating the introduction of centrifugal separated AlN does not seem to influence the melting behaviours of PP. Regarding the cooling trace, all samples exhibit an increased crystallisation temperature than the non-filled PP and increase with the increasing loading ratio of the AlN. These results are related to the nucleating effect of the nanoparticles on the PP matrix where the AlN induce the formation of the nuclei, thus shifting the crystallisation endotherms to a higher temperature. Regarding the surface chemistry of the AlN fillers, the grafted methacrylate groups from MPS present a stronger nucleating effect than the C8 group from C8M, which result in samples with MPS treated AlN show a higher crystallisation peak temperature at all filler loadings.

Despite the similar trend described above, two minor differences can be observed compared to nanocomposites prepared without centrifugal separation process in Chapter 4: 1. a marginally decreased crystallinity is evident after centrifugal separation was applied; 2. The T_c of C8 treated samples become less dependent on the filler loading ratio.

The decreased crystallinity is due to the increased filler dispersion resulting in a reduced volume of neat PP without filler. Then the growth of the PP crystals has a higher chance of being restricted by interference with nanoparticles. Meanwhile, better dispersion leads to an increased density of the spherulites, and the growth of crystals are more likely to be hindered due to the collision at the boundaries. This is in line with our hypothesis in Chapter 4 that the nanofillers will offer both nucleating and hindrance effects throughout the crystallisation process. When the temperature is approaching the T_c during the cooling from the melt, fillers serve as nucleating agents inducing the formation of the nucleus, then acting as impurities that hinder the growth of the crystal structure. As discussed earlier, the nucleating effect will reach saturation with the increased filler loading or increased particles-matrix interfacial area. Still, the hindrance effect contributes more when better dispersion is achieved, leading to a decreased crystallinity.

As for the second minor change, no increase on the T_c can be observed when increasing the loading of C8 treated from 2.5 to 10. C8 treated AlN shows a very weak nucleating effect, and the increased filler loading behoves to see a minimum increase on the T_c. However, we should not rule out that the size of the nanoparticles (or agglomerates) can also influence the nucleating behaviours of PP [192]. This suggests the large agglomerations in non-treated samples could contribute more nucleating effect than the better dispersed AlN.

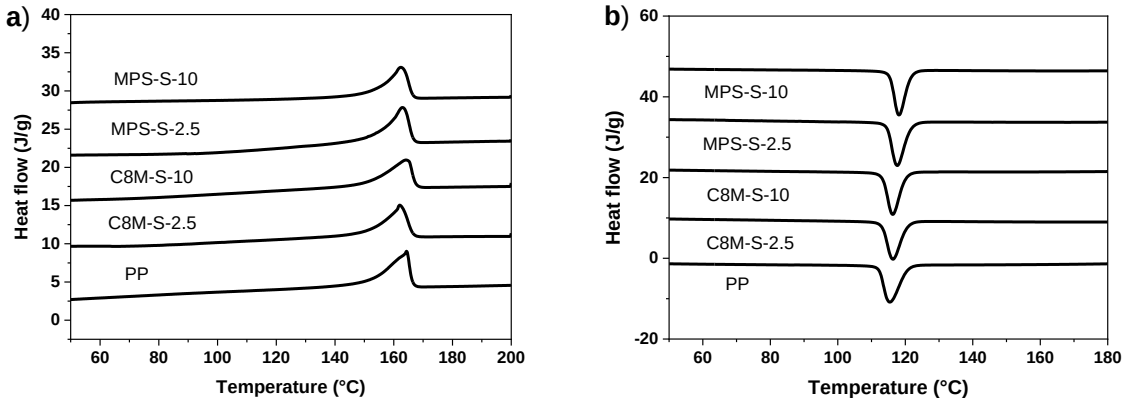

Figure 7.9 DSC a) heating, and b) crystallisation curve of the selected dielectric systems.

Table 7.1 Thermal properties of the selected dielectric systems, $\Delta H_{100\%}$ for neat PP is 208 J/g; the data of the PP with non-separated AlN are presented in the followed bracket for better comparison.

	ΔH (J/g)	T_m (°C)	T_c (°C)	χ (%)
PP	49.7	164.3	115.2	23.9
C8M-S-2.5	42.9 (47.9)	162 (162.5)	116.3 (115.3)	21.2 (23.6)
C8M-S-10	41.8 (44.4)	164.2 (162.5)	116.3 (116.5)	22.3 (23.7)
C8E-S-2.5	43.2 (47.1)	162 (163.5)	115.7 (116.0)	21.3 (23.2)
C8E-S-10	42.7 (45.4)	162.2 (162.8)	115.7 (118.0)	22.8 (24.3)
MPS-S-2.5	44.5 (47.4)	162.8 (164.2)	117.5 (117.0)	21.9 (23.4)
MPS-S-10	44.7 (46.2)	162.3 (162.7)	118.2 (119.2)	23.9 (24.7)

7.4.3 TGA

The TGA results of the PP and nanocomposites with centrifugal separated AlN are shown in Figure 7.10. The number within the bracket following the sample name in Figure 7.10 a to c is the weight remaining at 600 °C, which is related to the actual loading ratio of the filler. No significant difference between the actual and intended loading ratio can be found, considering the equipment's error can be up to ± 1 % obtained from multiple tests. This indicates that the concentration estimation method used for blending separated AlN with PP is successful in controlling the loading ratio.

The temperature at 5 % (onset) and 50 % (half) of weight loss are shown in Figure 7.10 d & e. similar to PP filled with non-separated AlN, the thermal stability of PP/AlN nanocomposites exhibiting an increasing trend with the increase in filler loading, and no significant difference can be observed when different SCA was applied. It is attributed to the barriers formed by AlN surrounding samples that prevent oxygen diffusion to the inner material or the catalytic effect discussed in Chapter 4. The dashed lines in Figure 7.10 d & e are the average value of the PP filled with 10 wt% of non-separated AlN. It is evident the PP with separated AlN achieved higher thermal stability than the PP with non-separated AlN. This suggests that the increased dispersion of AlN by the centrifugal separation within PP will form a denser AlN shell or better interfacial effect discussed in Chapter 4 during the sample's degradation, thus bring higher thermal stability to the composites.

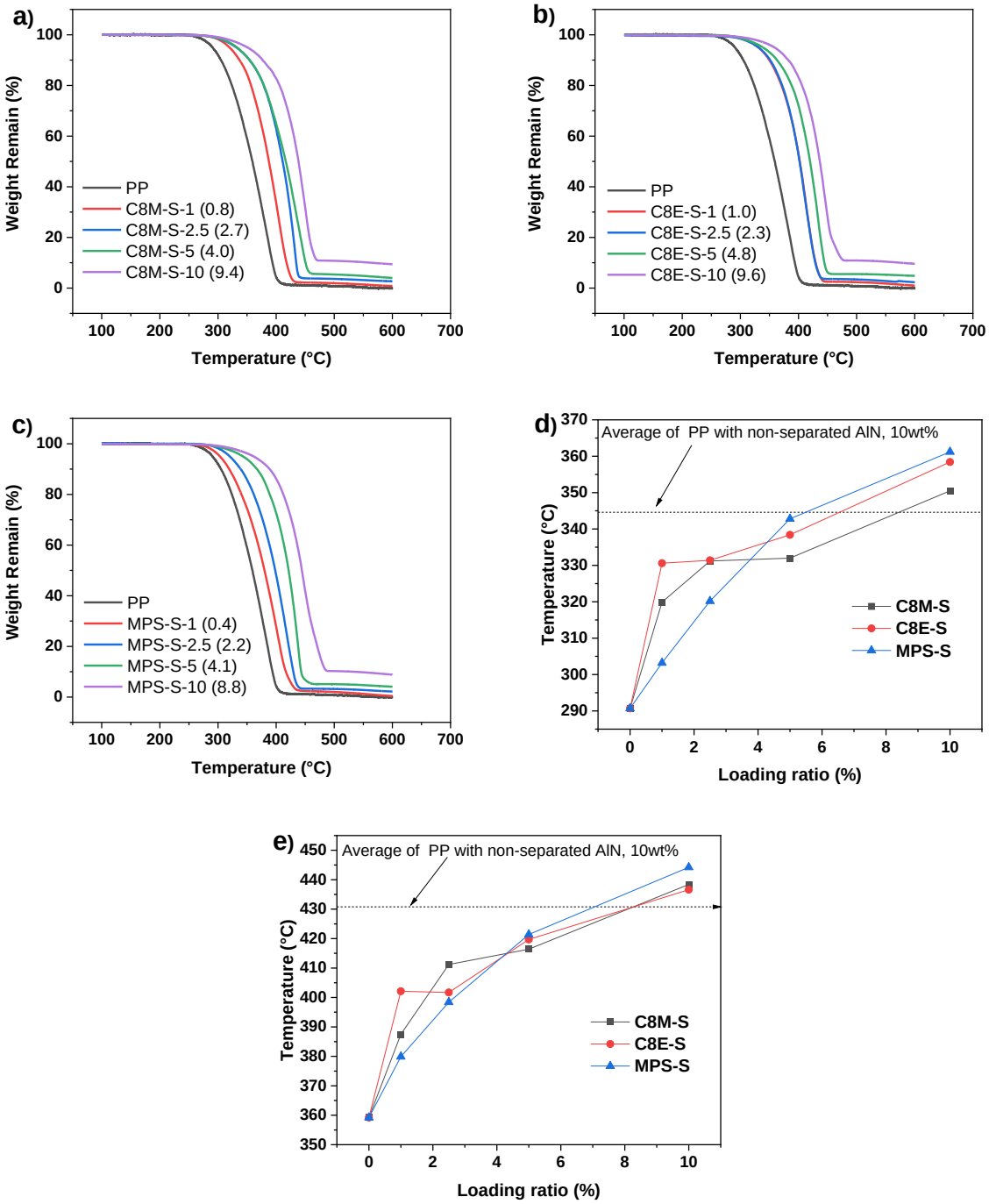

Figure 7.10 TGA curves of PP and PP/AlN nanocomposites a) C8M-S, b) C8E-S, and c) MPS-S; The temperature at d) 5 %, and e) 50 % of weight loss of each sample.

7.4.4 XRD

The XRD patterns of neat PP and a selection of PP/AlN nanocomposites are shown in Figure 7.11. Only samples with 10 wt% of loading are presented for brevity. A similar trend can be observed with different filler loadings.

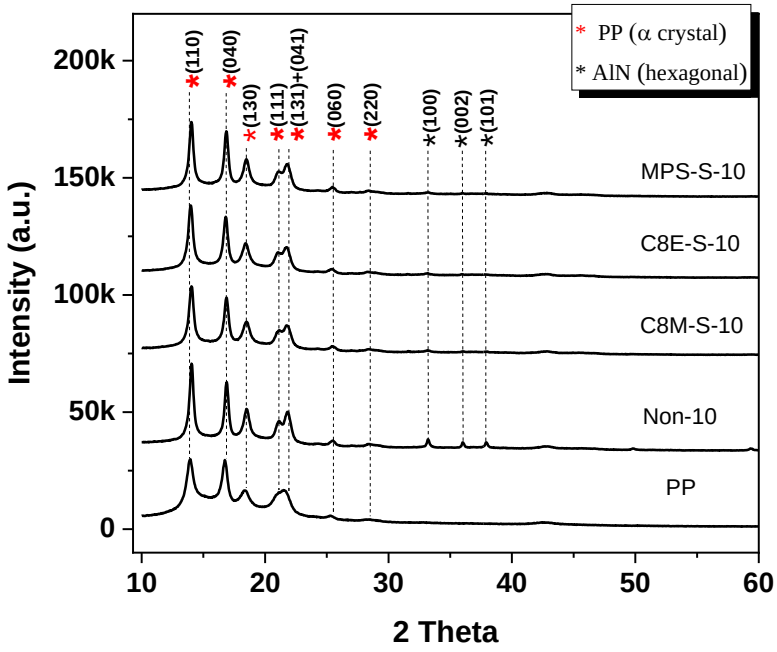

Figure 7.11 XRD spectra of neat PP and a selection of PP/AlN nanocomposites.

The diffraction pattern of the neat PP shows typical peaks at 14.2°, 16.6°, 18.5°, 21.0°, 21.8°, 25.5° and 28.5° correspond to the (110), (040), (130), (111), (131) + (041), (060) and (220) crystal planes of the α-crystals (monoclinic), and the same peaks are also shown in PP/AlN nanocomposites. It is worth noting that the MPS-S-10 here shows no feature that related to the presence of β-crystal, but peaks at 2θ of 16.0° and 21.0° corresponding to the (300) and (301) planes of β-crystal can be found on XRD spectra of MPS-10 (see Figure 4.8 in chapter 4). It suggests the formation of β-crystal can be related to the MPS treated agglomerations and the internal tension within PP [193]. The broadened peaks in the quenched neat PP could be attributed to the lack of the nucleating effect and resultant smaller size of microcrystals during quenching. By contrast, all nanocomposites show sharper peaks corresponding to the larger microcrystals. Besides, the intensity of peaks assigned to AlN decreases when compared to samples with non-treated AlN. It is because the agglomerations protect the AlN inside it from hydrolysis. The separated AlN with the larger surface area have a higher ratio of the surface hydrolysed layer, showing a weaker peak related to the AlN.

7.4.5 Thermal Conductivity

The thermal conductivity of a selection of samples is shown in Figure 7.12.

PP filled with separated AlN has higher thermal conductivity than the non-filled PP. All nanocomposites have monotonically increased thermal conductivity as a function of the loading ratio. Compared to the PP with as-received AlN, an increased thermal conductivity can be observed for all samples with separated AlN.

As the regions filled with slash lines show the thermal conductivity of PP with 10wt% non-separated AlN, no significant difference between PP with separated and non-separated fillers can be found. However, a slight reduction is evident for samples with C8M treatment. The reduced thermal conductivity is mainly related to the increased dispersion of the AlN that introduce more interfacial area, leading to an increased total interfacial thermal resistance within nanocomposites. For MPS-S-10, it shows comparable results to its non-separated counterparts, MPS-10. This suggests the increased percolation effect has compensated for the potentially reduced thermal conductivity related to the increased interfacial area. Better dispersion of AlN in samples MPS-S-10 can be observed than C8M-S-10 (Figure 7.7), which indicates that AlN filler has a higher chance to percolate and creating a thermal conduction pathway that can increase the thermal conductivity of the nanocomposites. Besides, the interfacial thermal resistance is positively related to the compatibility between two contacting materials. The less-affected thermal conductivity by the increased interfacial area can also be related to the higher thermal compatibility provide by MPS than C8M.

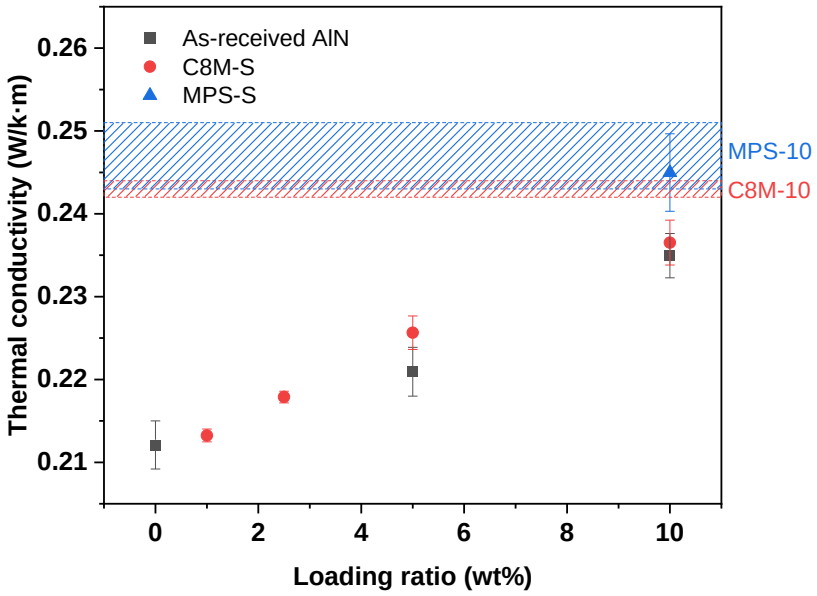

Figure 7.12 The thermal conductivity of a selection of samples; the regions filled with slash lines are the thermal conductivity of PP with 10wt% non-separated AlN.

7.4.6 Water Absorption

Figure 7.13 shows the weight increase of PP and nanocomposites samples with separated AlN after immersion in water for 9 days. It can be observed that the weight increases in all samples show an increase after immersion. The nanocomposites with better dispersion and the high interfacial area produced in this chapter with the help of centrifugal separation allow us to have an enhanced understanding of the interphase properties on both near- and far-particle sides. Similar to the PP filled with non-separated AlN, samples processed with different surface treatments show comparable ability to absorb water. Although the organofunctional group of MPS has a higher polarity than the C8 group, they are both hydrophobic and present a limited ability to absorb water molecules. The error from the weight measuring can easily obscure the slight difference in the water absorption ability between C8 and MPS treated samples.

The comparable results provided by C8M and C8E treated samples can be explained as two-fold. The application of the SCA with the different hydrolysable group is preferred to offer a similar chemical structure, such as Si-OH density, on the near-particle side and show less influence on the hydrophobicity of the nanocomposites; or the formation of SCA crosslinking network prevent the diffusion of water molecules from reaching the near-particles side of the SCA treated AlN, thus show independent results to the change of SCA hydrolysable group.

Figure 7.13d shows the weight increase of PP and nanocomposites at day 9 of water immersion, the data of PP filled with non-separated AlN are also included for better comparison. Surprisingly, the PP filled with centrifugal separated AlN shows a comparable result with the PP filled with non-separated AlN. A significantly higher water absorption ability of the PP filled with separated AlN is expected since an improvement in the filler dispersion and a hugely increased interfacial area is achieved by centrifugal separation. This indicates there is a water absorption contributor within the PP filled with non-separated AlN other than the surface of SCA treated AlN. One possible explanation is the large agglomerations results in more defects and cavities at the interface where more water can be absorbed (See Appendix E). Alternatively, the agglomerations contribute to additional water absorptions if the water molecules can migrate inside those agglomerations.

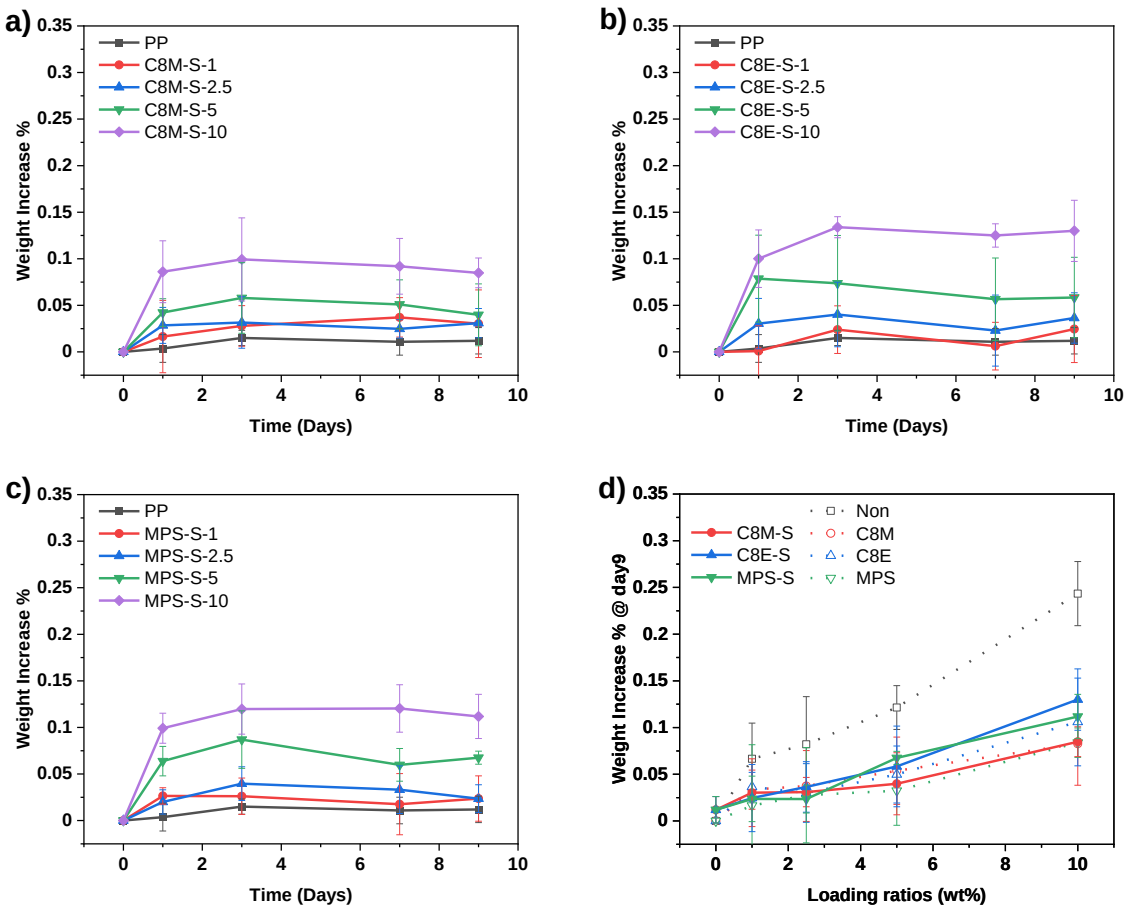

Figure 7.13 Weight increase of PP and nanocomposites after immersion in de-ionised water with, a) C8M-treated, b) C8E-treated, and c) MPS treated AlN; d) weight increase of PP/AlN nanocomposites at day 9 in de-ionised water, the data of PP filled with non-separated AlN are plotted in dash line.

7.5 Dielectric Properties

7.5.1 Dielectric Spectroscopy

The real and imaginary permittivities of PP and its nanocomposites filled with centrifugal separated AlN in dry condition are plotted in Figure 7.14 a to f. Figure 7.14 g & h presents the real and imaginary permittivity of each sample at 0.1 Hz, respectively; the data of PP with non-separated

AlN are shown in the dashed line for better comparison. The real permittivity shows a monotonic increase with the AlN loading ratio, and the results seem independent of the filler surface chemistry. A similar trend can be seen for imaginary permittivity, but an increasing trend towards the low frequencies is evident. Compared to the PP filled with non-separated AlN, their dielectric response at dry condition is very alike, except for a slight increased imaginary permittivity. It is a result of the increased interfacial area, thus an increased interfacial polarization effect.

The real and imaginary permittivities of samples immersed in water for 9 days are shown in Figure 7.15 a to f. Figure 7.15 g & h presents the real and imaginary permittivity of each sample at 0.1 Hz, respectively; the data of PP with non-separated AlN are shown in the dashed line. For real permittivity results, all nanocomposites show an increase in the value of ε' compared to the dry samples, and clear upturns at low frequency can be observed for samples with 5 and 10 wt. % AlN. This suggests that, in this case, these upturns are caused by the interfacial polarization and/or the enhanced polarisation effect due to water molecules.

It is noted that MPS treated systems show a higher imaginary permittivity in the samples treated with C8M and C8E, where the C8 groups are less polar than the methacrylate group from MPS and may contribute less to the water absorption and interfacial polarization. As discussed in Chapter 5, the relaxation features related to the interfacial polarisation or the reorientation of absorbed water should be located at frequencies lower than the testing range.

Compared to the PP with non-separated AlN, an increasing trend can be found in both real and imaginary permittivity. It is consistent with the SEM results, where an improved AlN dispersion introduces more interfacial area that increase the interfacial polarization and the water absorptions. After centrifugal separation, the estimated interfacial area improvement for PP with MPS treated AlN is larger than 2 folds (estimated from SEM images). However, only an insignificant increase (less than 2 folds) in the imaginary permittivity can be measured. This indicates the large agglomerations in PP filled with non-separated AlN could introduce more defects and cavities (See Appendix E), contributing more to the interfacial polarization and water absorption.

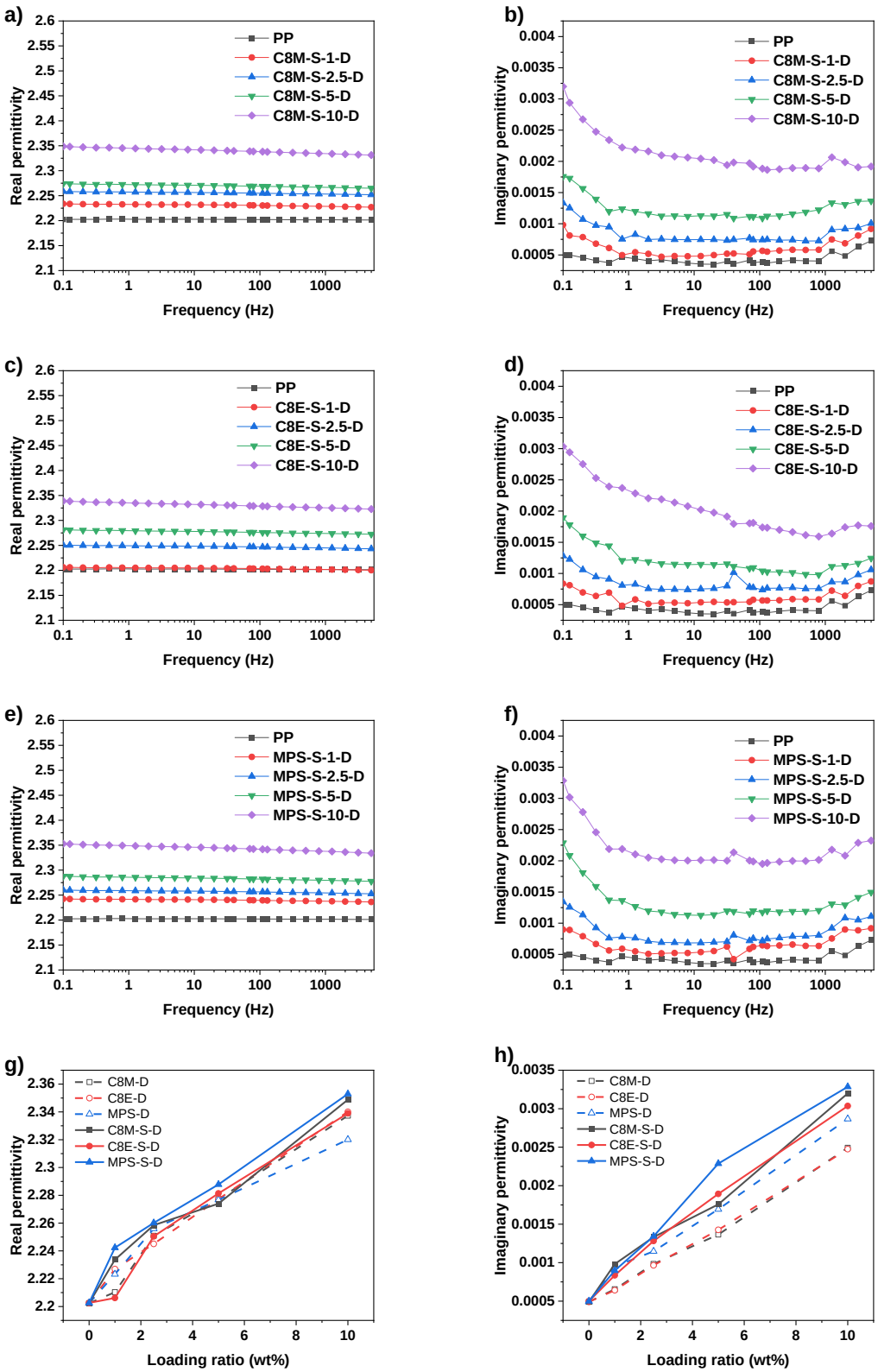

Figure 7.14 Complex permittivity of PP and its nanocomposites filled with separated AlN at dry condition, a), c), and e) are the real part, and b), d), and f) are the imaginary part; g) and h) are the real and imaginary permittivity of each sample at 0.1 Hz.

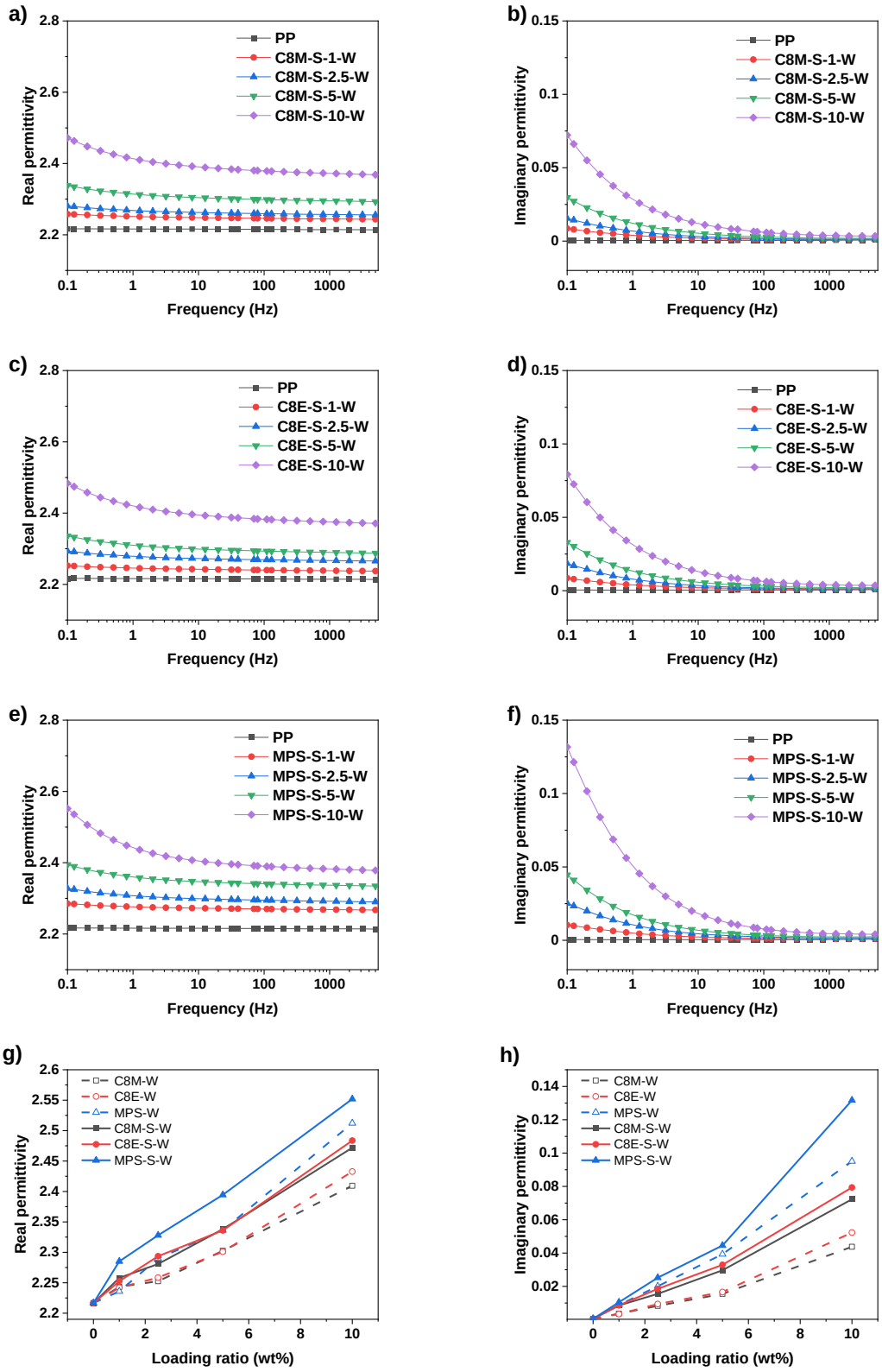

Figure 7.15 Complex permittivity of PP and its nanocomposites filled with separated AlN at wet condition, a), c), and e) are the real part, and b), d), and f) are the imaginary part; g) and h) are the real and imaginary permittivity of each sample at 0.1 Hz.

7.5.2 AC breakdown Strength

The AC breakdown strength of PP filled with centrifugal separated AlN under dry and wet conditions are shown in Figure 7.16 a to c. Only filler loading of 10 wt% is presented for clear presentation. Figure 7.16 d & e shows the scale parameter of each sample with separated AlN under dry and wet conditions, respectively, along with the scale parameter of samples with non-treated AlN under dry and wet conditions presented in Figure 7.16 f for comparison.

From Figure 7.16 a & b, the AC breakdown strength of the PP filled with C8M and C8E treated AlN after centrifugal separation shows comparable results and a slight increase compared to neat PP under dry conditions. Although this increase is negligible when considering the uncertainty of the Weibull plot, the trend is evident. It is surprising that the water immersion shows no influence on their breakdown strength, which could be related to the transient breakdown tested here and are more related to the structural properties of the samples; the increased dielectric loss from absorbed water shows a negligible effect.

Similar behaviour can also be found on MPS-S-10, as shown in Figure 7.16c. The results are independent of pre-conditioning, but a higher breakdown strength than C8M-S-10 and C8E-S-10 samples can be achieved. This could be related to the reduced inter-spherulite boundary structure within PP samples, and an evenly distributed crystal structure is formed with added filler. In contrast, nanoparticles coated with C8 groups show a weak ability to reduce inter-spherulite boundary structures (see Figure 7.8).

Figure 7.16 d & e shows the breakdown strength (Weibull scale parameter) of PP with separated AlN as a function of loading ratio. Though a few exceptions appear, a general trend of breakdown strength following a tendency that the highest values are located around the filler loading of 2.5 wt%. The improved breakdown strength at low loading levels (<2.5 %) is related to the enhanced morphology or the barrier effect of fillers. The increased agglomerations then offset these benefits brought by the addition of AlN at a high loading level (>2.5 wt%), thus providing a lower breakdown strength. The agglomerations within nanocomposites are usually fatal for AC breakdown strength, since the related defects and cavities will distort the local electric field distribution and lead to a lower breakdown strength (the evidence of defects and cavities can be found in Appendix E). This is proven when comparing the AC breakdown strength of PP filled with AlN before and after centrifugal separation (Figure 7.16 d to f). Before the large agglomerations were removed by centrifugal separation, all systems except MPS samples showed a monotonic decrease in the breakdown strength by adding AlN, which indicates these decreases are positively related to the presence of large agglomerations. The increased filler loading introducing more large agglomerations, thus lead to a decreased breakdown strength.

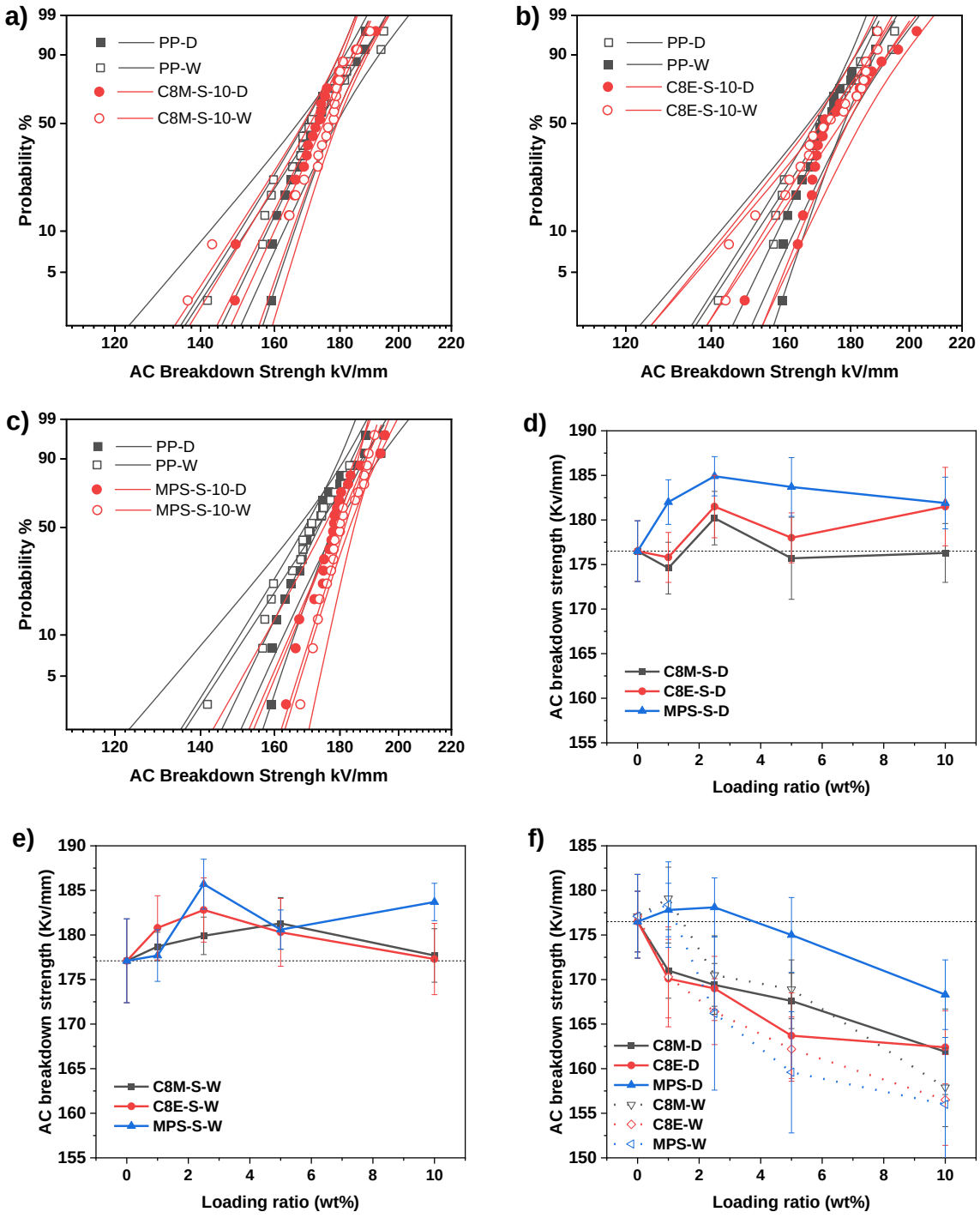

Figure 7.16 AC breakdown strength of PP with separated AlN (10 wt%) at dry and wet condition, a) PP and C8M treated samples, b) PP and C8E treated samples, and c) PP and MPS treated samples; d) and e) the Weibull scale parameter PP with separated AlN at dry and wet condition, respectively, f) the Weibull scale parameter of PP with non-separated AlN at the dry and wet conditions for comparison.

7.6 Summary

In this chapter, a novel centrifugal separation method has been applied during the nanocomposites processing procedure. Key findings are listed as follow,

- A significantly increased AlN dispersion can be achieved after centrifugal separation was used. The large agglomerations were removed before being blended with PP.
- The large agglomerations are the primary issue that causes the reduction of the AC breakdown of the PP filled with non-separated AlN. The increased AC breakdown strength is evident for PP filled with separated AlN, where the highest outcome can be found at an intermediate loading ratio (2.5 wt%).
- After separation, PP with MPS treated AlN shows the highest AC breakdown among all SCA treated samples; Reduced inter-spherulite structures are the main reason.
- The use of SCA with ethoxy can bring impurities (ethanol) into the system but seems to have a limited influence on the bulk properties, such as AC breakdown strength and dielectric response.
- An increased imaginary permittivity compared to the PP with non-separated AlN is evident, related to the increased interfacial due to the better AlN dispersion.
- The water absorption ability of PP filled with centrifugal separated AlN is comparable to the PP with non-separated AlN. This means the large agglomerations will lead to more water absorbed surrounding or inside them due to defects and cavities, or water molecules can migrate into these large agglomerations.
- PP with separated AlN shows higher thermal stability than PP with non-separated AlN. The better dispersed AlN could form a denser barrier or increased the catalytic effect during thermal degradation.
- PP with separated AlN shows a comparable thermal conductivity to PP with non-separated AlN. The increased dispersion will lead to a higher chance of forming thermal conduction pathways, thus compensating for the increased total interfacial thermal resistance due to the enlarged interfacial area.

Chapter 8 Conclusions and Future Work

8.1 Summary of Findings

In this work, AlN with different surface chemistry and agglomeration status were prepared. They were added as fillers to PP nanocomposites, to investigate the effect of the interphase on the structural, thermal, and electrical properties of these composites. To be specific, 8 types of AlN were used, the related purpose and a proposed two-side (near- and far-particles side) model are illustrated in Figure 8.1 for clarity.

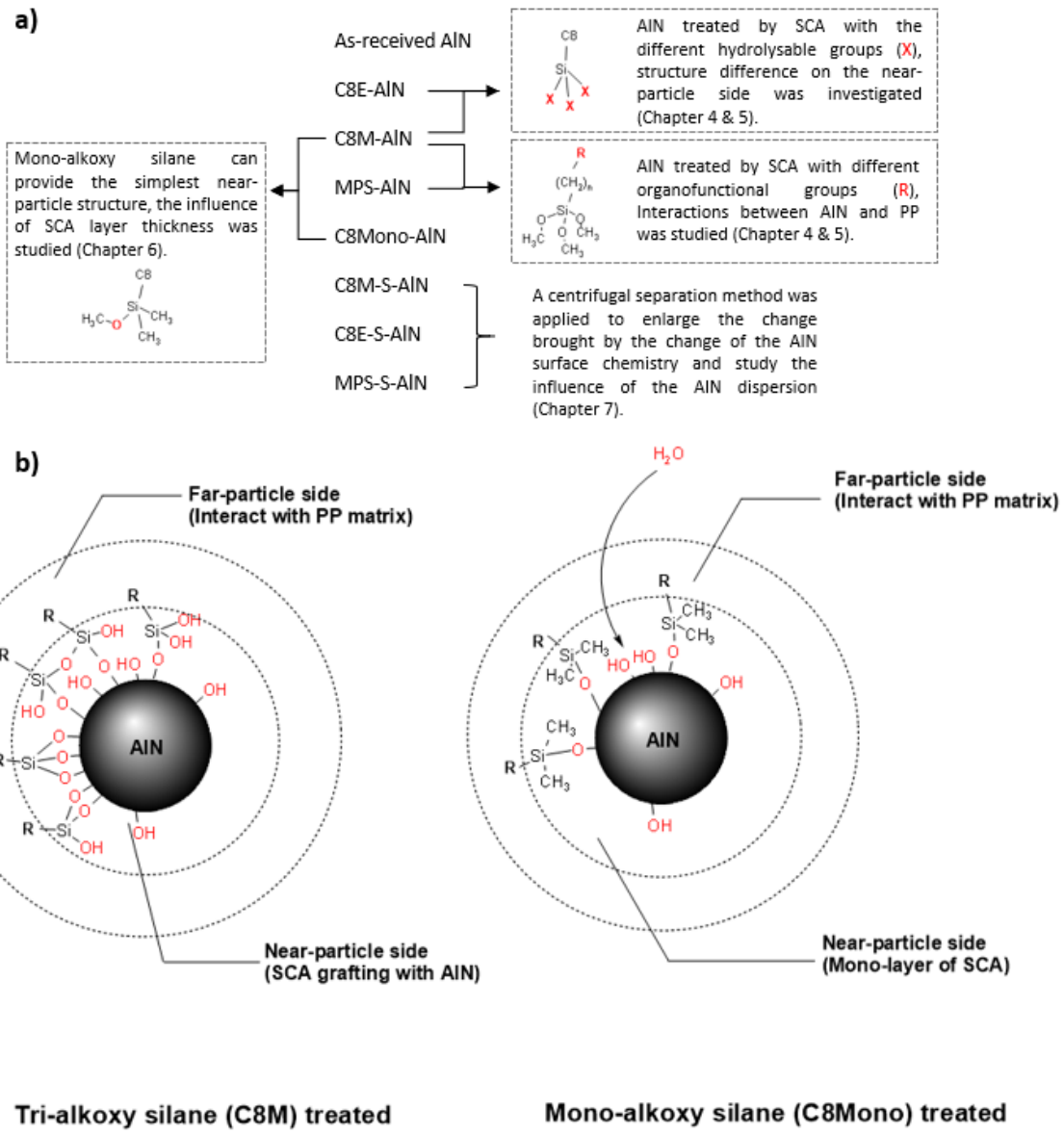

Figure 8.1 a) 8 types of AlN used in this work and their related purpose, b) a proposed two side (near- and far-particles side) model.

Due to the hydrolysis sensitivity of AlN, a thorough investigation of the as-received AlN and the subsequent hydrolysis analysis in water and air has been conducted in Chapter 3. From TEM observation, the as-received AlN is a combination of rod and plate structures with a low aspect ratio, ranging from 20 to 60 nm. However, the powder presents to be composed of entities with irregular shapes and various size distribution under SEM, from dozens of nanometres up to 30 µm, due to the particle agglomeration. FTIR, XRD, and TGA analysis identified a surface layer of amorphous AlOOH and γ-Al2O3, further confirmed by the hydrolysis analysis of AlN in water and air. The above study also proved that most AlN remains non-hydrolysed. The protection method adopted in this work can successfully prevent further reaction with water for more than 26 months (maintain the consistency of the AlN).

An anhydrous SCA treatment method was used to prevent the hydrolysis of AlN. The amount of the grafted SCA is reaching saturation since the condensation of SCA is restricted with this method. Although FTIR can identify the far-particles side regarding different organofunctional groups, the near-particle side structure remains unclear due to the related features overlapping in FTIR spectra.

The morphological structure of PP and its nanocomposites, the nanoparticle dispersion, and the related thermal performance of nanocomposites were presented in Chapter 4. For samples with low AlN loading (1 and 2.5 wt%), the addition of non-treated and MPS treated AlN can significantly change the morphology of PP through a nucleating effect, where smaller crystal size and eliminated inter-spherulites boundaries can be observed from SEM. The nucleating effect is positively related to far-particle properties. C8M and C8E treated AlN only shows minor nucleating effects and a slight decrease in the spherulite size. At high loading ratios (5 and 10 wt%), morphological details were hidden under the particles and agglomerations, but a suppressed formation of spherical structures can be observed in all samples. The higher nucleating effect of non-treated and MPS treated AlN was then confirmed by the higher crystallisation temperature of their nanocomposites. However, all filler surface chemistry shows a weak ability to influence the crystallinity of PP, which is a counterbalanced result of the nucleating and perturbing effects of AlN fillers. This is further supported by the XRD results, where the C8 treated samples show an increased microcrystal size at low filler loading (2.5 wt%) but a decrease at high filler loading (10 wt%). With the increase of the filler loading, the perturbing effect prevails over the weak nucleating effect in samples with C8 treated AlN. All samples, including the neat PP, present α-crystals except a small amount of β-crystals can be found in MPS-10, which is a combined result of the nucleating effect of the MPS treated AlN and the local resistance provided by the large agglomerations during the cooling crystallisation.

All SCA treatments can improve the AlN dispersion, but large agglomerations can still be observed in samples with SCA treated AlN. This suggests the SCA treatments cannot prevent agglomeration,

and SCA layers can form around agglomerations, rather than on the surface of each particle. At high magnifications, C8M and C8E treated AlN show a better dispersion, which indicates C8 groups at the far-particle side have better compatibility with PP than the methacrylate group from MPS. All fillers, including treated and non-treated, improve the thermal conductivity of PP. With the help of the surface treatment, the interfacial thermal resistance between AlN and PP matrix is reduced, thus giving a higher bulk thermal conductivity to the PP with non-treated AlN. The thermal degradation stability of PP is improved by adding AlN since the formation of the AlN barrier during the degradation can restrict oxygen diffusion into the inner material, or the particles have a catalytic effect. Higher thermal stability can be achieved by adding SCA treated AlN, where a denser barrier or increased catalytic effect can be achieved due to better dispersion. The overall picture is that the morphology and the particle dispersions are closely related to the far-particle side, while the near-particle structure shows a negligible effect. Identical behaviours of PP with C8M and C8E treated samples are evident throughout Chapter 4.

The dielectrics spectroscopy measurement, AC breakdown testing and water absorption analysis are presented in Chapter 5. The SCA treatment can effectively reduce the amount of water absorbed in nanocomposites 2 to 3 folds compared to the PP with non-treated AlN. However, both the variation on the near- and far-particle sides show no difference in the water absorption ability of nanocomposites, even though the methacrylate group from MPS has a higher polarity than the C8 group. The formation of the SCA crosslinking layer repels the diffusion of water molecules to the near-particles side. Thus, it could not be able to interact with the surrounding environment.

For dry samples, the introduction of AlN increases the real and imaginary permittivity of the PP. This increase is mitigated with the help of the surface treatment; the displacing of the -OH groups on the AlN will lead to the increased dipole relaxation and interfacial polarization. On the far-particle side, it is reasonable to believe that the interaction with PP has restricted the movement of the methacrylate group from MPS, giving a similar result to the C8 treated samples. However, after the influence of interphase has been enlarged by the absorbed water on the AlN surface, a larger imaginary permittivity of MPS treated samples than the C8 treated samples is evident, which indicates a thicker water layer can be formed surround MPS treated AlN. Meanwhile, a much thicker water layer is formed surrounding the non-treated AlN. The relaxation features from 0.1 Hz to 100 Hz can be observed, which is in line with water absorption results that the application SCA can reduce the thickness of the water shell surrounding AlN.

The introduction of the non-treated AlN will lead to a decreased AC breakdown strength, and the decrease becomes stronger with the filler loading increase. Although SCA treated samples present an improved breakdown strength compared to the PP filled with non-treated AlN, they still have a similar trend, both having a reduced AC breakdown strength to the neat PP. MPS treated samples

show the highest AC breakdown strength among all nanocomposites, resulting from the limited inter-spherulite. Still, this effect can be neutralised in wet conditions where there are thicker water shells within samples. In contrast, C8 treated samples only show a slight decrease after water immersion and provide a higher consistency towards the changing environments.

In the beginning, the near-particle side structure investigation is expected to rely on SCA with different hydrolysable groups. However, it is limited by the anhydrous silane treatment method used where the volume fraction of the SCA layer is restricted. More importantly, the barrier effect of the SCA network on the AlN surface invalidates the water absorption analysis on the near-particle side. Therefore, a mono-alkoxy silane, C8Mmono, with a single bonding site to the nanoparticle surface was applied in Chapter 6. It is expected to bring a near-particle structure which significantly different from that of the AlN treated with C8M. The monolayer with an ordered structure formed on the AlN surface increases AC breakdown strength and decreases dielectric loss compared to C8M treated samples (dry condition). The C8Mono treatment also leads to a morphological structure of PP composites similar to MPS treated samples, where eliminated inter-spherulite boundaries are evident. The increased AC breakdown strength can be seen as the direct consequence of the homogenised structure, rather than the near-particle chemistry itself. The structure change of C8Mono treated samples was confirmed by DSC results, where a stronger nucleating effect and higher crystallinity to the C8M treated samples can be observed. This finding is very different from conventional theories and suggests that the near-particle structure can also determine the interactions with the polymer matrix. Despite the improvement brought by the C8Mono treatment over the use of C8M, the drawbacks of C8Mono are pronounced under wet conditions. The single bonding site leads to decreased stability of the grafted C8Mono, and the “gaps” between grafted silanes (see Figure 8.1b) make the SCA layers unable to prevent the diffusion of water molecules to the near-particle side, reducing the hydrophobicity of the nanocomposites. As a result, the C8Mono treated samples have dramatically increased permittivity and loss, as well as decreased AC breakdown strength under wet conditions.

None of the SCA applied in this work can effectively prevent agglomerations in the as-received AlN, which is limited by selecting the solvent for material processing. A centrifugal separation method was adopted in Chapter 7 to overcome this issue and, in theory, optimise the amount of the interphase. A significantly improved AlN dispersion can be found after separation was applied. The better dispersion leads to a slightly reduced crystallinity of the nanocomposites due to the increased perturbing effect. The increased interfacial area did not lead to increased water absorption. With the better dispersion, PP filled with separated AlN shows an increased AC breakdown to the neat PP, and the highest value was obtained at a medium loading ratio, 2.5 %. When considering the dielectric spectroscopy, all samples show a higher real and imaginary

permittivity to the PP with non-separated AlN due to the increased interfacial polarization result of the better AlN dispersion. However, this insignificant increase does not match the significantly increased interfacial area observed from SEM after the centrifugal separation was applied, suggesting the interfacial area between PP and large agglomerations contributing more polarizations effect than that between PP and better dispersed AlN.

8.2 Conclusions

Conclusions are made based on the aims set in this work (re-presented here from Chapter 1),

- Aim 1: to understand the interactions between nanoparticles and polymer matrix and the role of the surface chemistry on the "far-particle" side of the nanoparticles on the thermal and dielectric properties of nanocomposites.
- Aim 2: to investigate the influence of the "near-particle" side structure on the bulk properties of the nanocomposites.
- Aim 3: to investigate the influence of nanoparticle dispersion and the interphase volume on the thermal and dielectric properties of nanocomposites.
- Aim 4: to obtain a better understanding of interphase properties by using water absorption analysis and formulate an approach to avoid the water absorption issues of the nanocomposites.
- Aim 5: to investigate the potential sources that may cause the inconsistency of the experiment results regarding nanocomposites.

Aim 1 is to answer the questions: what is the interphase looks like? In this work, the idea that the interphase is a distinct layer with different properties to both materials in the composites may not apply. But the introduction of AlN nanoparticles does provide interactions with the PP matrix, then altering the macroscopic crystal structures of the nanocomposites through the nucleating effect. Such interactions are positively related to the far-particle side properties of the nanoparticles. The inter-spherulites free structure induced by the MPS-AlN improves the breakdown strength, while C8-AlN with the less nucleating ability only seen a minor change in the overall structure of their nanocomposites. However, we cannot deny the existence of the microscopic interphase (a distinct interaction layer) since the agglomerations in the samples reduced the interphase volume. These different layers may not be visible with SEM and can only be derived from the dielectric or thermal testing results. These testing results are usually susceptible to nanoparticle agglomerations, thus obscuring our understanding of the microscopic interphase.

Aim 2 is based on the proposed two-side model that emphasizes the influence of the near-particle side. That makes us think, does the near-particle side affect the bulk properties and how? Using tri-

alkoxy silane with different hydrolysable groups with a different reaction rate, C8M and C8E, can form a “network” structure on the near-particles side. However, no significant difference can be found regarding the structural, thermal, and dielectric properties of the corresponding nanocomposites, indicating the minor change on the near-particles side does not affect the bulk properties. The mono-alkoxy silane use allows us to compare the near-particle structure with a greater difference. One noticeable finding is the PP/C8Mono-AlN samples show a similar inter-spherulites free structure like MPS- and non-treated nanocomposites. The single C8Mono layer without interconnections is too thin to minimise the polarity of the AlN surface and showing that in this extreme condition, the near-particle structure can also play an essential role in the interactions between filler and matrix.

Aim 3 directs a common question in nanodielectrics: how the nanoparticle agglomerations affect the bulk properties? SCA can increase the nanoparticle dispersion, but it is insufficient, and large agglomerations up to 30 μm are still visible. The further centrifugal separation process removes large agglomerations successfully. It significantly increases the AC breakdown strength of the nanocomposites, indicating the large agglomerations are the leading cause of structural weakness. However, the increased interfacial area enlarged the interfacial thermal resistance, thus, offset the potentially increased bulk thermal conduction through the percolation pathway formed by the better dispersed AlN. The non-proportional increased interfacial polarization suggests there might have an interaction region where the nanoparticles restrict the chain movements. Still, it could also be that the defects and cavities related to the large agglomerations contribute more dielectric loss.

Aim 4 focuses on using water as a probe to portray a better picture of the nanoparticles surface chemistry. This could allow us to address the barrier of the nanocomposites towards production and application in a humid environment. The application of tri-alkoxy silane provides a barrier effect that restricts the diffusion of the water molecules to the near-particle side and leads to a significantly increased hydrophobicity of the nanocomposites. In contrast, C8Mono treatment is unstable under wet conditions, and de-bonding quickly occurs. Meanwhile, the isolated C8Mono cannot present the barrier effect like tri-alkoxy silane, and the C8Mono treated samples can absorb 3 times more water than the tri-alkoxy silane treated samples. Therefore, the higher stability and hydrophobicity of tri-alkoxy silanes makes them a better option for nanocomposites application.

Aim 5 was achieved by looking through the whole study, start from the material storage, then samples making process and the material characterisation techniques, end at the data processing and presentation; the possible sources of the inconsistent finding are concluded as follow,

1. It is evident for some filler types, like the AlN in this work, the size, shape, surface chemistry, and agglomeration status may vary from the manufacturing and storage method. Even for

researchers to adopt materials from the same supplier, the raw material used for making samples can have a huge difference that will determine the bulk properties of the nanocomposites. A thorough characterisation is usually required to solve this issue. Chapter 3 in this work is an example.

2. The use of C8Mono demonstrate that the near-particle structure also needs to be concerned, but unlike the far-particle structure, it is not easy to be quickly identified through commonly used techniques such as FTIR. Further studies are required regarding this issue.
3. The filler dispersion status is proved to be a crucial factor in the structure, thermal, and dielectric properties of the nanocomposites. Techniques such as TEM and SEM of the cracked or etched surface of the composites are usually used to identify the filler dispersion status. However, there are limitations for researchers about how the filler dispersion status is presented. For example, our pursuing of concise presenting style and page limits of some publication platforms guide us to exhibit the filler dispersion status with minimum results. It will cause a lack of understanding of the overall picture. In this work, the status of large agglomerations has little chance to be characterised if only SEM images with high magnification are presented.
4. From the water absorption analysis, the moisture content and the stability of the SCA treatment determine the bulk properties of nanocomposites. The sample storage and testing environment must be clarified when analysing the results.

8.3 limitations and Future Work

The hydrolysis issue of AlN allows us only to use the anhydrous silane treatment method. The thick layer of SCA and significantly changing the near-particles side structure with tri-alkoxy silane are restricted by this method. It is worth using an alternative filler where the application of the hydrolysis silane functionalisation method (Figure 3.18) can provide a more consistent near-particle structure. The thickness of the silane layer is expected to be controlled by the amount of SCA and water added into the suspension during the surface treatment, thus helping us better understand the effect of the near-particles side on the properties of the nanocomposites.

In this work, the maximum filler loading is 10 wt%. The intention of using higher filler loading is limited by the idea that the best performance of the nanocomposites is usually found at a low loading ratio, and the deteriorated dielectric properties are likely to occur with the increasing filler loading and the agglomerations. However, with the help of the centrifugal separation method and most of the large agglomerations are excluded, the PP with 10 wt% of the separated AlN is still competitive regarding the dielectric properties. This shows a great potential to increase the loading ratio and further improve the thermal conductivity of the nanocomposites. Therefore, investigating

the PP/AlN combination at higher filler loading can give us a better understanding of the prospect and potential of its application.

The mono-alkoxy silane treatment shows a weaker ability to decrease the polarity of the AlN surface. The centrifugal separation method using xylene as the solvent is not suitable for separating due to the low compatibility between xylene and C8Mono treated AlN. Since the study on C8Mono is affected by the large agglomerations in Chapter, it would be beneficial to develop a modified separation method. It is worth trying other solvent-polymer combinations such as DCM-polystyrene, where DCM could be used to adapt the C8Mono treated AlN to the centrifugal separation method.

Appendix A Experimental Techniques

This appendix details the experimental setups in this work; more detailed explanations related to the testing techniques can refer to [65, 92, 146, 177, 194].

A.1 Scanning Electron Microscopy

SEM was used to study the morphological characteristic of nano-fillers, matrix polymers, and nanocomposites. Unlike optical microscopy, it can achieve a higher resolution by break the limitation of the confined wavelength range of visible light. A tungsten filament will emit a beam of electrons with an energy of 1 to 30 eV to the specimen after being demagnified by a condenser lens and an objectives lens. The electron beam has a 2 to 10 nm diameter, and deflector coils drive it to scan across the specimen. A number of secondary emissions and other types of reflected radiations are collected by the detector. Then the computer can plot a beam position image by processing the signal collected by the detector [146, 177].

For the base polymer and nanocomposites, to analyse the morphology and the spherulite structure and the dispersion state of the nanoparticles in the PP matrix, two additional sample treatments are needed before a fine SEM image can be obtained.

The chemical etching procedure is used to separate the amorphous region and the crystalline region of base PP, so the spherulite structure of PP can become visible from the SEM image. The etching procedure can also remove the polymers covering the nano-fillers on the sample surface; thus, the dispersion state can be identified. Also, coating gold on the sample is believed to be an effective way to prevent the charge accumulation on the sample surface so that every sample will be coated with gold before observations.

In this study, a Zeiss Evo50 scanning electron microscope was used. The PP and nanocomposites samples were etched by a permanganate etching method in [157] for 15 to 20 h and were gold coated with an Emitech K550X sputter coater 2 times. For nanoparticles, powders were brushed on conductive tape then coated with cold before the examination.

A.2 Transmission Electron Microscopy

TEM obtain images by shone electron beams transmitted through thin samples. It usually has a higher resolution than SEM and displays more details of the internal composition of the sample, such as nanoparticle morphology and grain structure.

TEM of AlN was performed using a JOEL-2100 TEM operated at 200 kV. The powders were dispersed in isopropyl alcohol in a water sonication bath for 20 min before being transferred onto a standard carbon film-coated Cu TEM grid.

A.3 Fourier Transform Infrared Spectroscopy

FTIR is typically used to analyse the changes in the chemical structure of the nanoparticle surface [111]. ATR-FTIR is suggested in this work as it is more suitable for opaque samples like nanoparticles [146]. The typical diagrammatic drawing of the operating principle of ATR-FTIR is shown in Figure A.1. A parallel-sided diamond crystal with a high relative refractive index is in contact with the sample. The infrared beam is forward into the parallel-sided crystal, followed by the total internal reflection. After interacting with the samples placed on the top side of the parallel-sided crystal, the reflected beams are then be collected and output as infrared spectra [146].

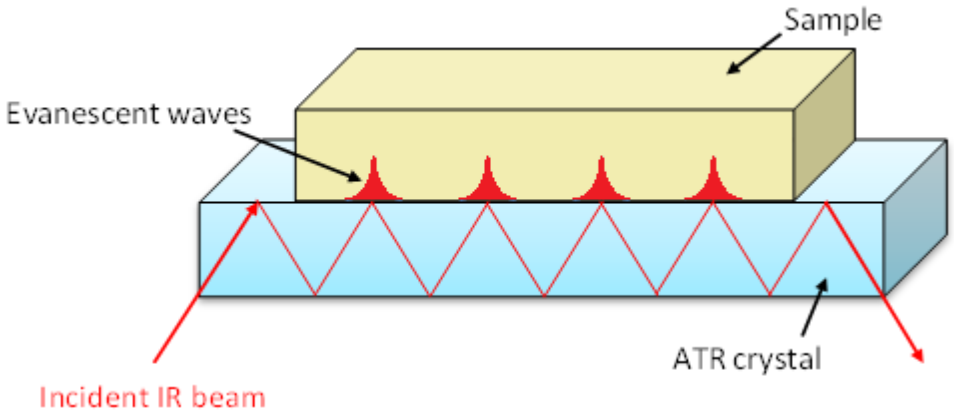

Figure A.1 The typical operating principle of ATR-FTIR [146].

In the present work, ATR-FTIR was performed to examine the surface chemistry of nano-AlN in reflectance mode. A Nicolet iS5 FTIR Spectrometer examined 2 mg of powder with a wavelength ranging from 500 to 4000 cm^{-1}. The ambient air background was measured for calibration before each test.

A.4 Thermogravimetric Analysis

TGA is a technique that can be used to measure the mass change of material in a temperature range or at a specific temperature. The sample from 2 to 5 mg is placed on an aluminium (for the ending temperature less than 600 °C) or a platinum tray hanging on a high-precision scale. Then the scale will be put into a furnace covered by a glass test tube with dry air or nitrogen flow. The temperature scan or the isothermal mode can be set as a function of time or temperature, while the mass of the

sample inside the tray will be measured in real-time. This technique is crucial throughout the sample-making process of the proposed research.

A Perkin-Elmer 1 TGA accompanied by a Perkin-Elmer Pyris user interface was used in this study. It was first used to test the nano-AlN powder to estimate the number of hydroxyl groups contained on the surface, then used to examine the surface state of nanoparticles after the surface functionalisation. Before doing any tests, the loading concentration of nano-filler in nanocomposites will need to be verified by TGA. Also, it can be used to test the boiling point of SCA, which can prove that it is not hydrolysed or polymerised before the surface functionalisation.

A.5 X-Ray Diffraction

XRD is a powerful technique for studying the material structure, predominantly crystalline and semi-crystalline material. XRD pattern is usually generated by collecting the scattered X-ray by samples being tested, where the incoming X-ray interfered by the structures at its wavelength range in samples.

XRD patterns of as-received AlN, PP and their composites were taken by a Bruker D8 Advance diffractometer using a Cu Kα radiation (λ = 1.5406 Å, 40 kV and 40 mA), at a step size of 0.04° over a 2θ range from 10 to 80°. Data in Figure 3.14 was obtained by a Bruker D2 Phaser under 30kV (10 mA, λ = 1.54184 Å, from 10 to 80°).

A.6 Differential Scanning Calorimetry

DSC test was used in the proposed research to analyse the thermal behaviour of PP and PP-based nanocomposites. The sample (2 to 5 mg) was placed in a sealed aluminium pan, and the test cell was placed in a nitrogen atmosphere. The heat flow through the testing sample is measured as a function of temperature.

The Mettler Toledo DSC 820 used in this study can compensate for the temperature difference between the testing sample and reference sample when phase transaction of the testing sample happens. The heat flow as a function of temperature will be plotted. Typical features in the DCS curve of PP can be illustrated in Figure A.2.

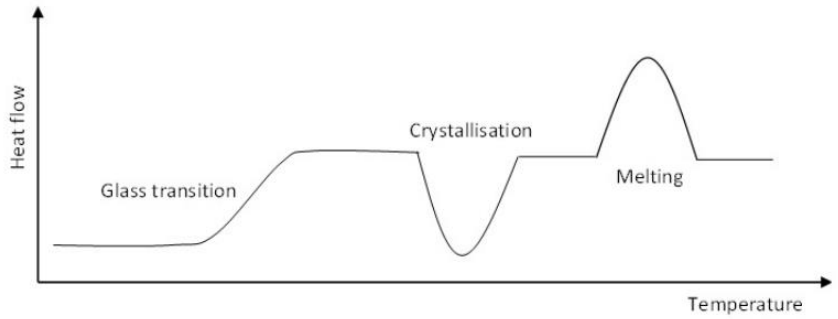

Figure A.2 Typical features in the DCS curve of PP [146].

The glass transition temperature (T_g) and the melting temperature (T_m) of a polymer can be determined by the heating process. In contrast, crystallisation temperature (T_c) can be determined by the cooling process. Before doing any tests, an indium sample with a melting point of 156.6 °C and enthalpy of 28.45J/g was used for the calibration. The temperature scan method was set up for all dielectric systems in the proposed work was as follow: the sample was heated from 20 to 200 °C at 10 °C/min to get the melting curve and kept at 200 °C for 2-5 min to remove the thermal history. Then the sample was cooled to 20 °C to obtain the crystallization curve. From the crystallization curve, the heat flow peak represents the T_c of the testing material. The T_m and the melting enthalpy can be obtained by the melting peak and its peak area.

A.7 Thermal Conductivity Test

The thermal conductivity of each system was performed by a steady-state technique based on the guarded hot plate method in [195]. The testing setup is shown in Figure A.3. A thin film flux sensor from OMEGA Engineering, HFS-4, was placed between the hot plate and sample (3 mm in thickness). One-dimensional heat flux can be obtained by the temperature difference of two brass plates placed at the top (cold) and bottom (hot) sides of the sample. By measuring the heat flux at equilibrium conditions and the temperature difference. The thermal conductivity (k) of samples can be calculated by Equation A.1.

$$\mathrm{k} = -\frac{\Delta x}{\Delta T} \cdot q \tag{A.1}$$

Δx is the thickness of the sample, ΔT is the temperature difference between the top plate and bottom plate, and q is the measured heat flux at the equilibrium condition.

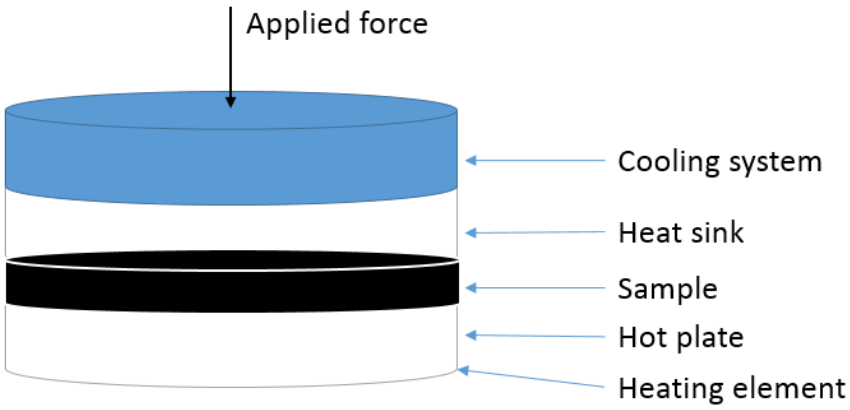

Figure A.3 The thermal conductivity testing setup [195].

A.8 Dielectric Spectroscopy

The dielectric spectroscopy is used to analyse the interaction between the applied electrical field and the dipole moment of a dielectric material at different frequency ranges [177]. That is often expressed by the permittivity, and researchers are usually interested in the complex permittivity (ε^*), which can represent the ability of a material to permit the electric field. The real part of permittivity is termed real permittivity (ε'), representing the energy storage ability. The imaginary permittivity (ε'') is a measure of the losses in the polarization process. The relationship between them can be express in Equation A.2 [146, 177]. The dissipation of energy, $tan\ \delta$, can be calculated as the ratio of energy losses in the polarization and the energy stored by the polarization process (Equation A.3).

$$\varepsilon^* = \varepsilon' - j\varepsilon'' \tag{A.2}$$

$$tan\ \delta = \frac{\varepsilon''}{\varepsilon'} \tag{A.3}$$

The polarization process is sensitive to material changes and acts as a function of both frequency and temperature. The schematic diagram of the polarization mechanism at different frequency ranges is shown in Figure A.4 [65].

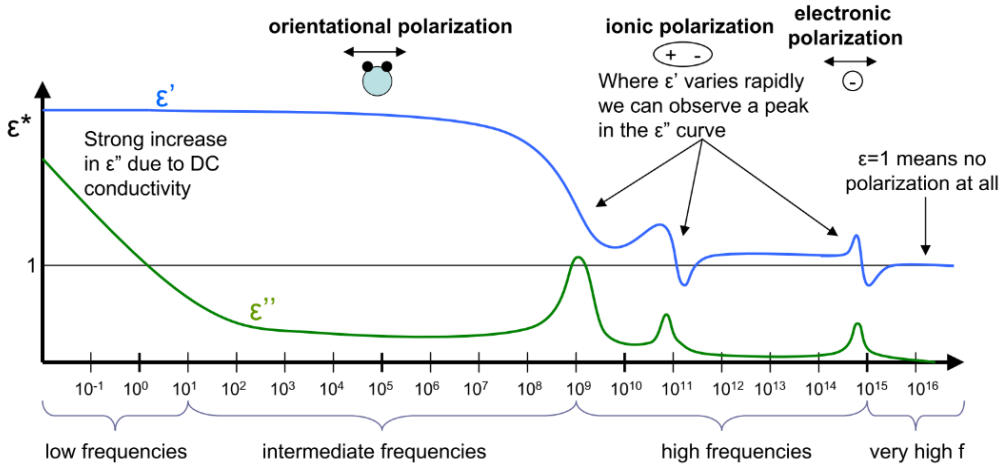

Figure A.4 The schematic diagram of a polarisation mechanism at different frequency range [65].

At the very high-frequency range, even electrons cannot keep up with the changing field; thus, no losses can be measured. The losses of electronic and ionic can be detected at the high-frequency range while the orientational polarization dominates the losses at the intermediate frequency range [65].

At present work, the dielectric response was measured by a SPECTANO 100 Dielectric Material Analyzer and a sample holder with two paralleled 30 mm diameter electrodes. The test was performed based on ASTM standard D150-98. A 50 V AC voltage was applied to the sample (230 µm) during the test with a frequency swap from 5 kHz to 0.1 Hz at room temperature. Both the real permittivity and the imaginary permittivity as a function of frequency were plotted.

A.9 AC Breakdown Strength

The imperfections in insulation systems are inevitable during manufacturing. These imperfections will lead to a dielectric breakdown of insulation material. Many theories try to describe the electrical breakdown mechanism, and the commonly used is the avalanche theory [194, 196]. In avalanche theory, the free charges in the insulation bulk will be accelerated along the mean free path under a high electrical field. The charges will then collide with electrons, and it has chances to drive electrons to exit the electron orbital. The emerging of electron-hole pairs will magnify the above process and lead to the conduction of the material [146].

The AC breakdown test is one of the most significant tests when studying a new insulation material. Although the commonly used transient AC breakdown test used in laboratory research scale cannot provide a trustworthy result for industrial application, the general characteristic about the electric field of insulation material could withstand can be obtained. Besides, the deviation of different results on the same sample can evaluate the quality and the consistency of the sample preparation.

A Faraday cage was used in this work, and the test was performed based on ASTM standard D149-87. The sheet samples (115 µm) were placed between two 6.3 mm ball-bearing electrodes and immersed in silicon oil to prevent surface flashover. The applied electric field will increase until the sample breakdown happens at a ramping rate of 1 kV/s. The layout of the test cage is shown in Figure A.5. The AC breakdown strength value of a single test can be calculated by Equation A.4, where E_b is the breakdown strength with the unit of kV/mm, V_b is the applied field when the breakdown happens, and t is the thickness of the sample [177].

$$E_b = \frac{V_b}{t} \tag{A.4}$$

The two-parameter Weibull analysis was applied to analyse the electrical breakdown data. For each dielectric system, the probability of breakdown can be calculated by Equation A.5, where $P\ (E)$ is the probability of breakdown at the electric field of E. The parameters α and β are the two main parameters of the Weibull distribution. The α parameter represents the electric field, at which 63.2 % of the samples will be subject to breakdown. The β parameter is known as the shape parameter representing the deviation of the breakdown values of an insulation system [177].

$$P(E) = 1 - exp\left[\left(\frac{V}{\alpha}\right)^{\beta}\right] \tag{A.5}$$

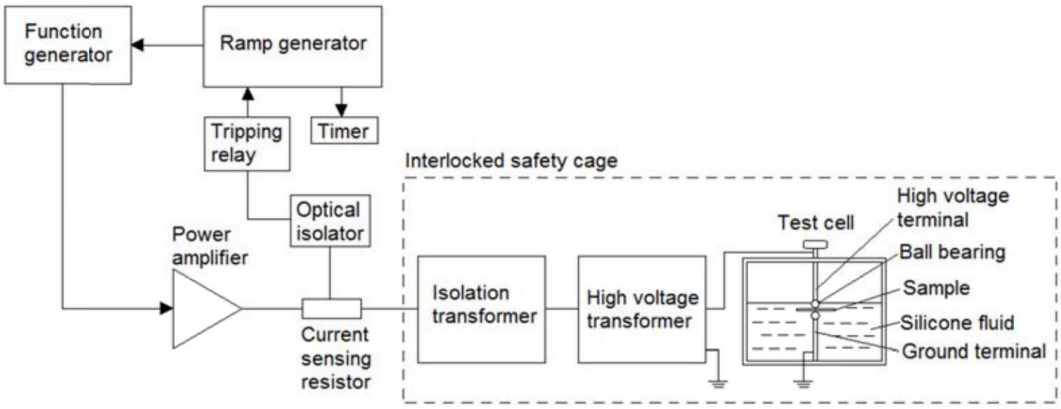

Figure A.5 AC breakdown test diagram [92].

Each data point in the Weibull plot was calculated by Equation A.6, where i is the rank of the tested value, and N is the total number of tests [146, 177].

$$P(E)_{i,N} = \frac{(i-3)}{(N+4)} \tag{A.6}$$

In this study, 20 tests were applied for each sample at room temperature, and the result was plotted with the help of the Origin Plot. Both α and β parameters, as well as 90 % confidence bounds, can be calculated by this software.

Appendix B Morphological Properties of PP Filled with C8Mono Treated AlN

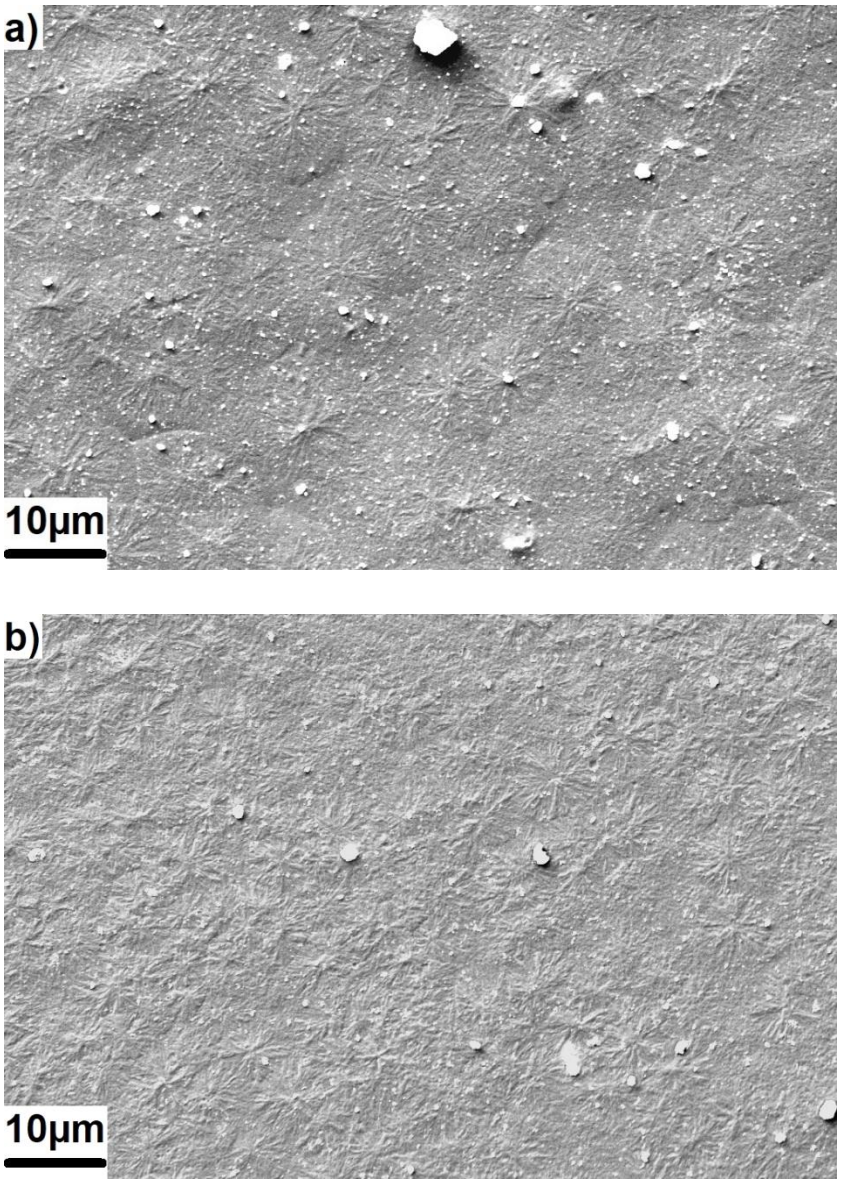

Figure B.1 SEM image of a) C8M-2.5, b) C8Mono-2.5

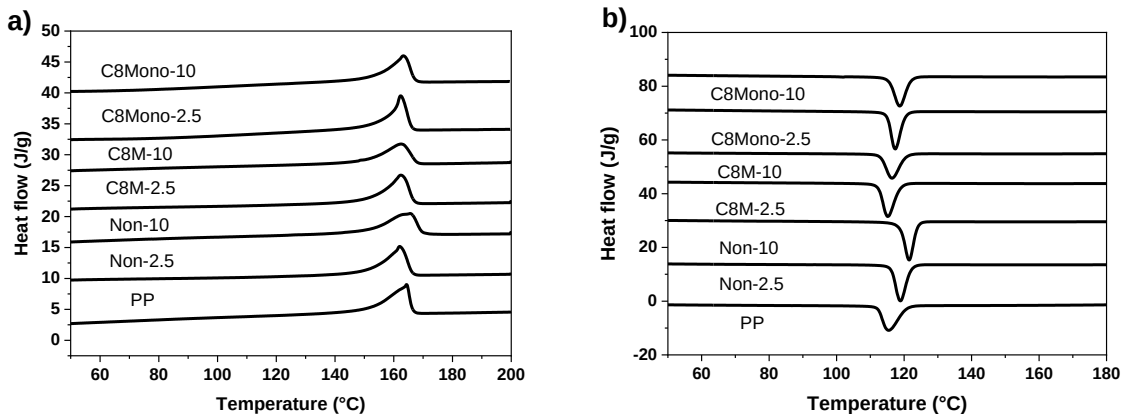

Figure B.2 DSC a) heating and b) crystallisation curve of the selected dielectric systems.

Table B.1 Thermal properties of the selected dielectric systems, ΔH=100% for neat PP is 208 J/g.

	ΔH (J/g)	T_m (°C)	T_c (°C)	χ (%)
PP	49.7	164.3	115.2	23.9
N-2.5	49.9	162.0	119.0	24.6
N-10	48.7	165.5	121.5	26.0
C8M-2.5	47.9	162.5	115.3	23.6
C8M-10	44.4	162.5	116.5	23.7
C8Mono-2.5	47.8	162.3	117.3	23.6
C8Mono-10	44.7	163.3	118.7	23.9

Appendix C Effect of the Amount of the SCA Used in Silane Functionalisation

Table C.1 The amount of C8M used for silane functionalisation, n is the Multiplication factor from Equation 3.14. Weight remains (%) is obtained from Figure C.1; Difference (%) is the additional weight decrease compared to the non-treated AlN after heated to 900 °C

Multiplication factor *n*	C8M for 2 g of AlN (ml)	Weight remain (%)	Difference (%)
0	0	97.0	0
1	0.07	95.4	1.6
7	0.50	93.2	3.8
15	1.08	93.2	3.8
30	2.16	93.1	3.9

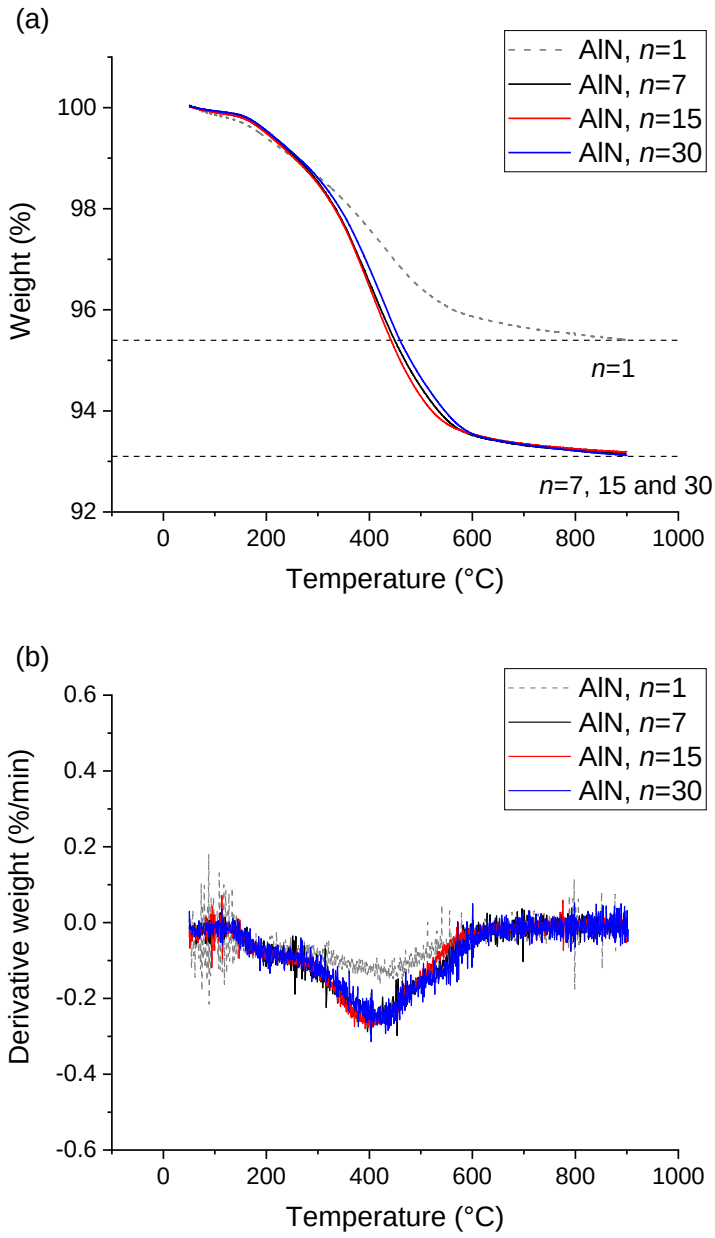

Figure C.1 a)TGA and b) derivative TGA results of AlN treated with different amounts of C8M.

Appendix D Processed TGA Data According to the Mass of PP in the Composite System

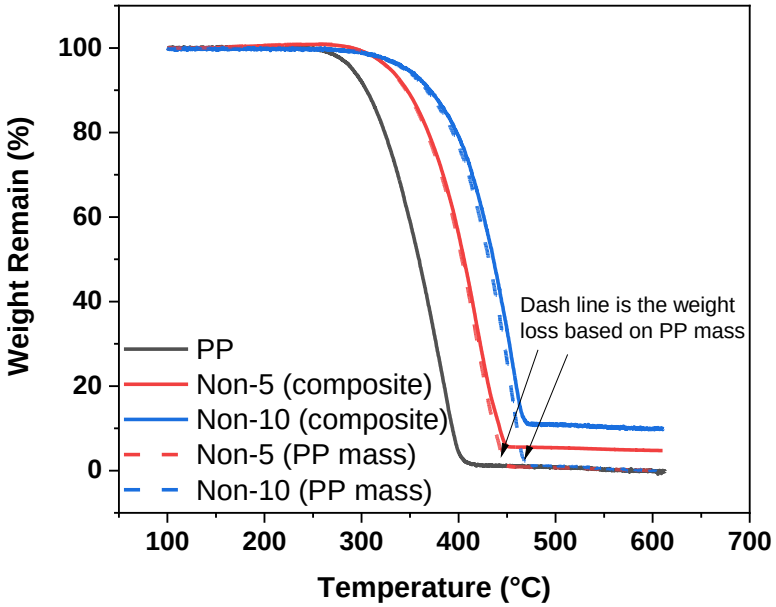

Figure D.1 Processed TGA data according to the mass of PP in the composite system use Non-5 and Non-10 as an example; the dash curves are the processed TGA data based on the PP mass rather than the mass of the composites.

Appendix E Cavities and Defects Related to the Large Agglomerations

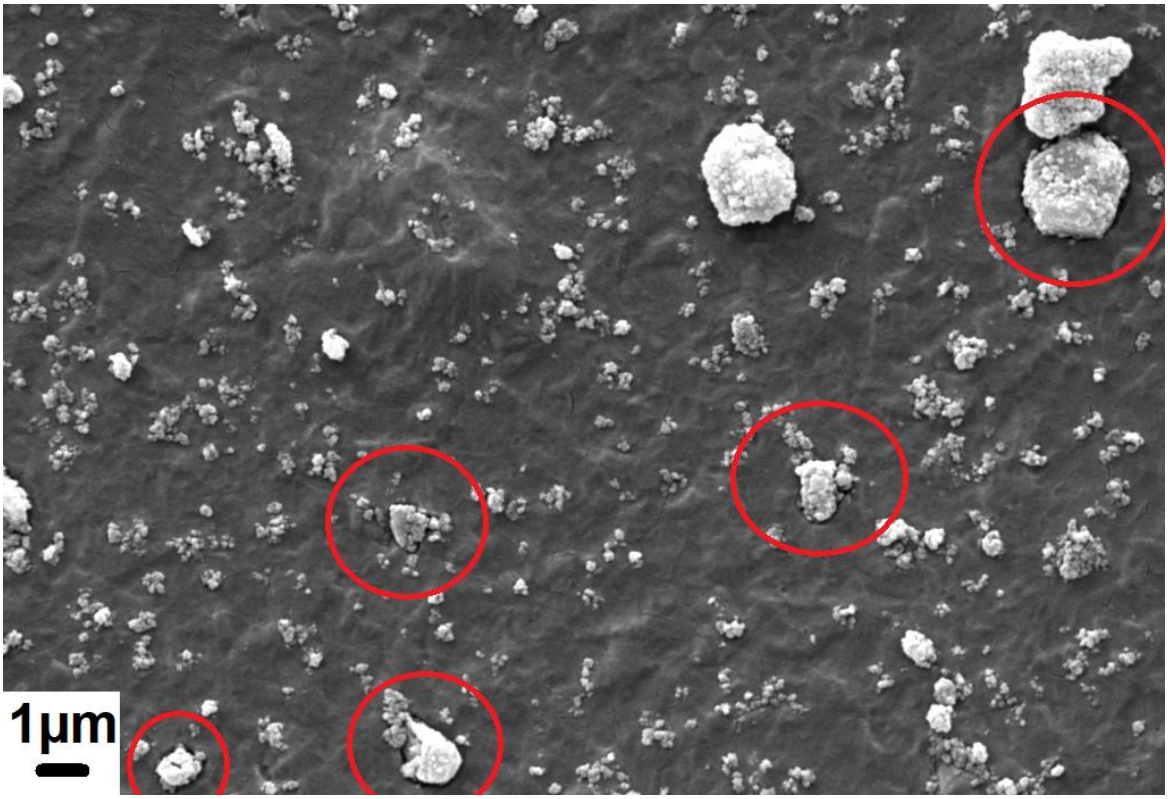

Figure E.1 Evidence of cavities and defects related to large agglomerations founds in N-10.

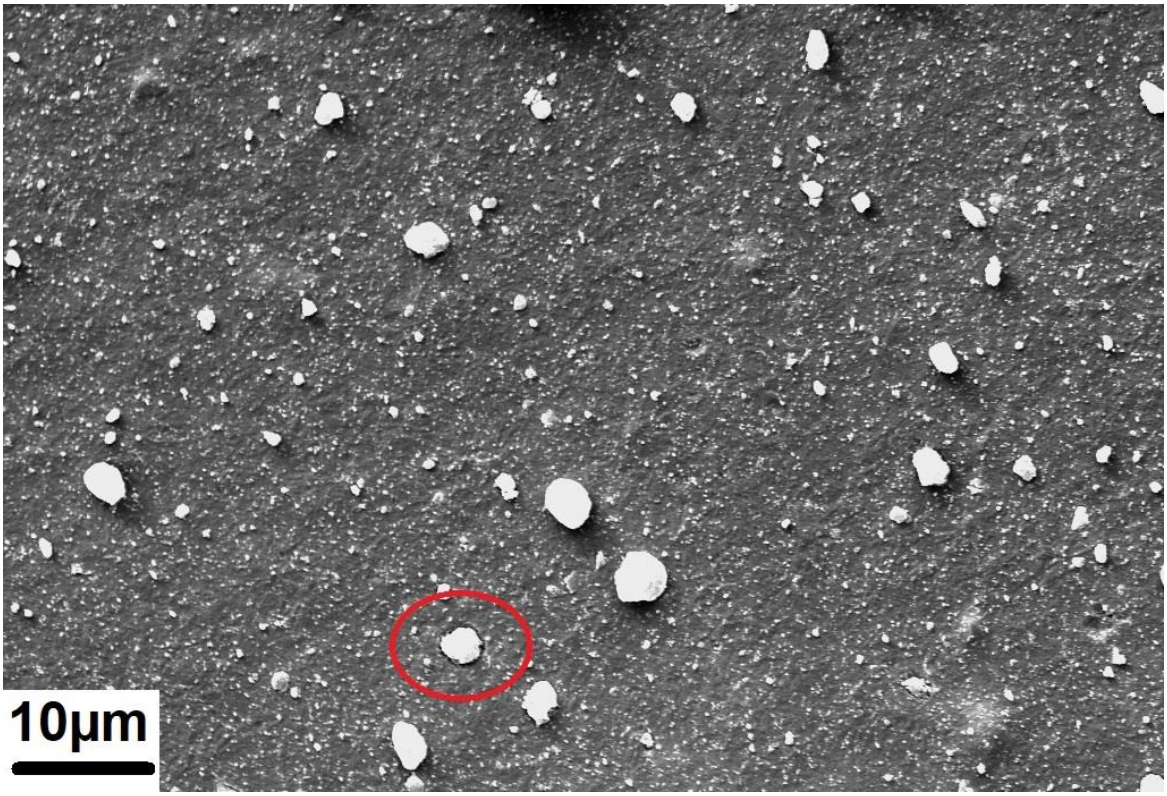

Figure E.2 Evidence of cavities and defects related to large agglomerations found in C8E-10, where fewer said features could be observed than Figure E.1 due to the SCA treatment.

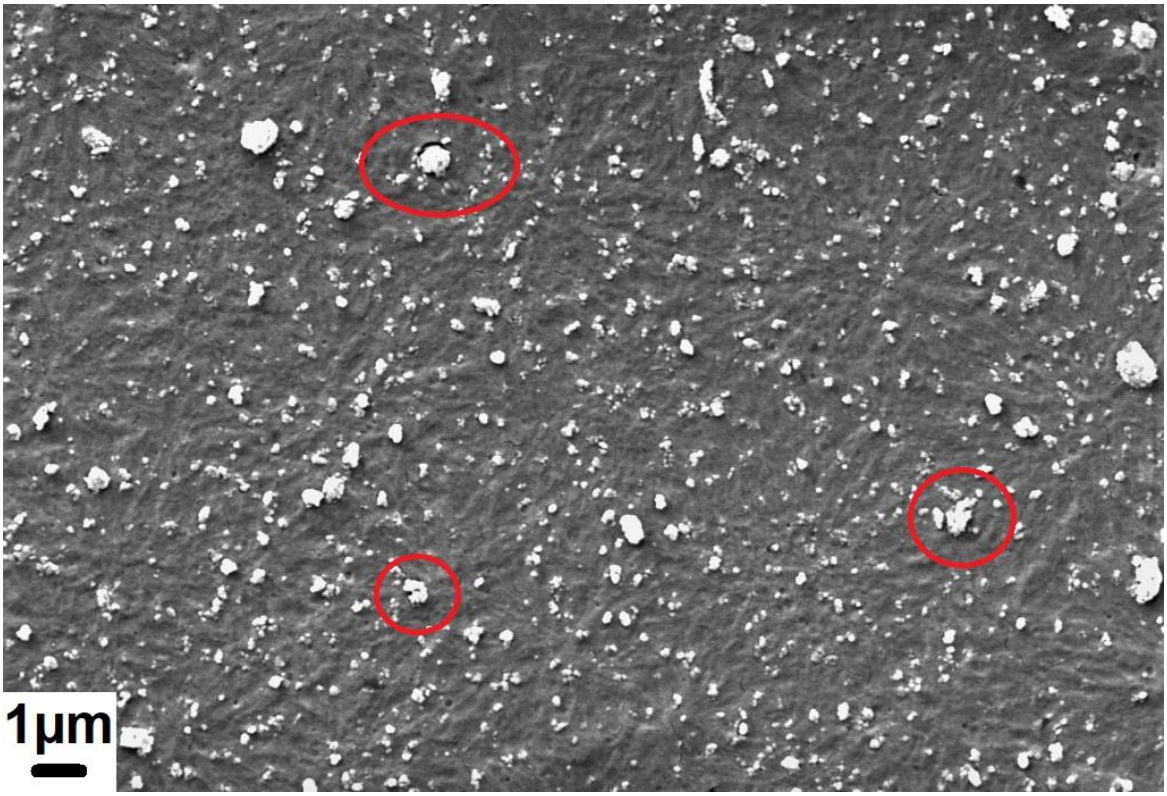

Figure E.3 Evidence of cavities and defects related to large agglomerations found in C8M-10, where fewer said features could be observed than Figure E.1 due to the SCA treatment.

Reference List

[1] G. Chen, M. Hao, Z. Xu, A. Vaughan, J. Cao, and H. Wang, "Review of high voltage direct current cables," *CSEE J. Power Energy Syst.,* vol. 1, no. 2, pp. 9-21, 2015.

[2] A. Alassi, S. Bañales, O. Ellabban, G. Adam, and C. MacIver, "HVDC transmission: technology review, market trends and future outlook," *Renew. Sustain. Energy Rev.,* vol. 112, pp. 530-554, 2019.

[3] M. Wang *et al.*, "Review and outlook of HVDC grids as backbone of the transmission system," *CSEE J. Power Energy Syst.,* vol. 7, no. 4, pp. 797-810, 2020.

[4] I. L. Hosier, A. S. Vaughan, A. Pye, and G. C. Stevens, "High performance polymer blend systems for HVDC applications," *IEEE Trans. Dielectr. Electr. Insul.,* vol. 26, no. 4, pp. 1197-1203, 2019, doi: 10.1109/TDEI.2019.007954.

[5] X. Huang, Y. Fan, J. Zhang, and P. Jiang, "Polypropylene based thermoplastic polymers for potential recyclable HVDC cable insulation applications," *IEEE Trans. Dielectr. Electr. Insul.,* vol. 24, no. 3, pp. 1446-1456, 2017, doi: 10.1109/TDEI.2017.006230.

[6] B. Du, Z. Hou, and J. Li, "A Review of Polypropylene and Polypropylene/Inorganic Nanocomposites for HVDC Cable Insulation," *Chapter in New Trends in High Voltage Engineering,* p. 5, 2018.

[7] P. Meng *et al.*, "Comparisons of different polypropylene copolymers as potential recyclable HVDC cable insulation materials," *IEEE Trans. Dielectr. Electr. Insul.,* vol. 26, no. 3, pp. 674-680, 2019.

[8] T. Andritsch, A. Vaughan, and G. C. Stevens, "Novel insulation materials for high voltage cable systems," *IEEE Electr. Insul. Mag.,* vol. 33, no. 4, pp. 27-33, 2017.

[9] X. Huang, P. Jiang, and T. Tanaka, "A review of dielectric polymer composites with high thermal conductivity," *IEEE Electr. Insul. Mag.,* vol. 27, no. 4, pp. 8-16, 2011, doi: 10.1109/MEI.2011.5954064.

[10] X. Wang, T. Andritsch, G. Chen, and S. Virtanen, "The role of the filler surface chemistry on the dielectric and thermal properties of polypropylene aluminium nitride nanocomposites," *IEEE Trans. Dielectr. Electr. Insul.,* vol. 26, no. 3, pp. 1009-1017, 2019, doi: 10.1109/TDEI.2019.007773.

[11] B. L. Zhu, J. Ma, J. Wu, K. C. Yung, and C. S. Xie, "Study on the properties of the epoxy-matrix composites filled with thermally conductive AlN and BN ceramic particles," *J. Appl. Polym. Sci.,* vol. 118, no. 5, pp. 2754-2764, 2010, doi: 10.1002/app.32673.

[12] J. Gu, Q. Zhang, J. Dang, J. Zhang, and Z. Yang, "Thermal conductivity and mechanical properties of aluminum nitride filled linear low-density polyethylene composites," *Polym. Eng. Sci.,* vol. 49, no. 5, pp. 1030-1034, 2009, doi: 10.1002/pen.21336.

[13] M. G. Danikas and T. Tanaka, "Nanocomposites-a review of electrical treeing and breakdown," *IEEE Electr. Insul. Mag.,* vol. 25, no. 4, pp. 19-25, 2009, doi: 10.1109/MEI.2009.5191413.

[14] J. K. Nelson, J. C. Fothergill, L. A. Dissado, and W. Peasgood, "Towards an understanding of nanometric dielectrics," in *Annual Report Conference on Electrical Insulation and Dielectric Phenomena*, Cancun, Mexico, 2002: IEEE, 2002, pp. 295-298, doi: 10.1109/CEIDP.2002.1048793.

[15] T. Takada, Y. Hayase, Y. Tanaka, and T. Okamoto, "Space charge trapping in electrical potential well caused by permanent and induced dipoles for LDPE/MgO nanocomposite," *IEEE Trans. Dielectr. Electr. Insul.,* vol. 15, no. 1, pp. 152-160, 2008, doi: 10.1109/T-DEI.2008.4446746.

[16] F. Claudio and F. Hanspeter, "ABB Review: Special Report 60 years of HVDC," ABB, 2014.

[17] H. Wang and M. A. Redfern, "The advantages and disadvantages of using HVDC to interconnect AC networks," in *45th International Universities Power Engineering Conference UPEC2010*, Cardiff, UK, 2010: IEEE, pp. 1-5.

[18] Q. Zhao, J. García-González, A. García-Cerrada, J. Renedo, and L. Rouco, "HVDC in the Future Power Systems," in *Transmission Expansion Planning: The Network Challenges of the Energy Transition*: Springer, 2021, pp. 117-151.

[19] T. Andritsch, G. Mazzanti, and J. Castellon, "The Prospects and Challenges for HVDC Cable Technology in a Smart Grid World," *IEEE Smart Grid Newsletter,* 2019.

[20] Z. Li and B. Du, "Polymeric insulation for high-voltage dc extruded cables: challenges and development directions," *IEEE Electr. Insul. Mag.,* vol. 34, no. 6, pp. 30-43, 2018.

[21] R. Stam, "National precautionary policies on magnetic fields from power lines in Belgium, France, Germany, the Netherlands and the United Kingdom," *National Institute for Public Health and the Environment, Netherlands,* 2017.

[22] G. C. Montanari *et al.*, "Criteria influencing the selection and design of HV and UHV DC cables in new network applications," *High Volt.,* vol. 3, no. 2, pp. 90-95, 2018.

[23] Y. Zhou, S. Peng, J. Hu, and J. He, "Polymeric insulation materials for HVDC cables: Development, challenges and future perspective," *IEEE Trans. Dielectr. Electr. Insul.,* vol. 24, no. 3, pp. 1308-1318, 2017.

[24] G. Luoni, E. Occhini, and B. Parmigiani, "Long Term Tests on a ±600 KV DC Cable System," *IEEE Trans. Power App. Syst.,* vol. PAS-100, no. 1, pp. 174-183, 1981.

[25] T. Worzyk, *Submarine power cables: design, installation, repair, environmental aspects*. Springer Science & Business Media, 2009.

[26] H. Ghorbani, M. Jeroense, C.-O. Olsson, and M. Saltzer, "HVDC Cable Systems-Highlighting Extruded Technology," *IEEE Trans. Power Deliv.,* vol. 29, no. 1, pp. 414-421, 2014, doi: 10.1109/tpwrd.2013.2278717.

[27] M. Gilbert, "Plastics materials: Introduction and historical development," in *Brydson's plastics materials*: Elsevier, 2017, pp. 1-18.

[28] G. Chen and M. Kamaruzzaman, "Impact of mechanical deformation on space charge in XLPE," in *2007 IEEE International Conference on Solid Dielectrics*, Winchester, UK, 2007: IEEE, pp. 510-513.

[29] D. J. Youn, J. Li, S. Livazovic, Y. Sun, and S. Sun, "Controlling factors of degassing in crosslinked polyethylene insulated cables," *Polymers,* vol. 11, no. 9, p. 1439, 2019.

[30] C. Fanggao, G. Saunders, R. Hampton, S. Moody, and A. Clark, "The effect of hydrostatic pressure and temperature on the permittivity of crosslinked polyethylene," in *Seventh International Conference on Dielectric Materials, Measurements and Applications (Conf. Publ. No. 430)*, 1996: IET, pp. 267-270.

[31] R. Eichhorn, "A critical comparison of XLPE-and EPR for use as electrical insulation on underground power cables," *IEEE Trans. Dielectr. Electr. Insul.,* no. 6, pp. 469-482, 1981.

[32] C. Martin, A. Vaughan, and S. Sutton, "The thermomechanical behaviour of crosslinked polyethylene cable insulation material," in *2003 Annual Report Conference on Electrical Insulation and Dielectric Phenomena*, Albuquerque, NM, USA, 2003: IEEE, pp. 88-91.

[33] S. Katakai, "Behind the Scenes of the Development of DC XLPE Power Cables," *SEI Tech. Rev.,* no. 91, p. 5, 2020.

[34] J. He and Y. Zhou, "Progress in eco-friendly high voltage cable insulation materials," in *2018 12th International Conference on the Properties and Applications of Dielectric Materials (ICPADM)*, Xi'an, China, 2018: IEEE, pp. 11-16.

[35] Y. Gao, X. Huang, D. Min, S. Li, and P. Jiang, "Recyclable dielectric polymer nanocomposites with voltage stabilizer interface: toward new generation of high voltage direct current cable insulation," *ACS Sustain. Chem. Eng.,* vol. 7, no. 1, pp. 513-525, 2018.

[36] L. Cheng *et al.*, "Polypropylene nanocomposite for power equipment: a review," *IET Nanodielectrics,* vol. 1, no. 2, pp. 92-103, 2018.

[37] D. Tripathi, *Practical guide to polypropylene*. iSmithers Rapra Publishing, 2002.

[38] H. A. Maddah, "Polypropylene as a promising plastic: A review," *Am. J. Polym. Sci,* vol. 6, no. 1, pp. 1-11, 2016.

[39] S. Belli, G. Perego, A. Bareggi, L. Caimi, F. Donazzi, and E. Zaccone, "P-Laser: Breakthrough in power cable systems," in *2010 IEEE International Symposium on Electrical Insulation*, San Diego, CA, USA, 2010: IEEE, pp. 1-5.

[40] L. Castellani, L. Martinotto, C. Scelza, and E. Albizzati, "Cable with recyclable covering," ed: US Patents, 2005.

[41] D. Machl, T. Pham, and K. Klimke, "Cable layer of modified soft polypropylene," ed: US Patents, 2013.

[42] Y. Zhou, J. He, J. Hu, X. Huang, and P. Jiang, "Evaluation of polypropylene/polyolefin elastomer blends for potential recyclable HVDC cable insulation applications," *IEEE Trans. Dielectr. Electr. Insul.,* vol. 22, no. 2, pp. 673-681, 2015.

[43] I. L. Hosier, S. Reaud, A. S. Vaughan, and S. G. Swingler, "Morphology, thermal, mechanical and electrical properties of propylene-based materials for cable applications," in *Conference Record of the 2008 IEEE International Symposium on Electrical Insulation*, Vancouver, BC, Canada, 2008: IEEE, pp. 502-505.

[44] I. L. Hosier, A. S. Vaughan, and S. G. Swingler, "An investigation of the potential of polypropylene and its blends for use in recyclable high voltage cable insulation systems," *J. Mater. Sci.,* vol. 46, no. 11, pp. 4058-4070, 2011, doi: 10.1007/s10853-011-5335-9.

[45] R. Xu *et al.*, "Dielectric properties dependent on crystalline morphology of PP film for HVDC capacitors application," *Polymer,* vol. 213, p. 123204, 2021.

[46] F. Avalos-Belmontes *et al.*, "Effect of different nucleating agents on the crystallization of Ziegler-Natta isotactic polypropylene," *Int. J. Polym. Sci.,* vol. 2016, 2016.

[47] G. Laschet, M. Spekowius, R. Spina, and C. Hopmann, "Multiscale simulation to predict microstructure dependent effective elastic properties of an injection molded polypropylene component," *Mech. Mater.,* vol. 105, pp. 123-137, 2017.

[48] S. Kolesov, "The influence of morphology on the electric strength of polymer insulation," *IEEE Trans. Dielectr. Electr. Insul.,* no. 5, pp. 382-388, 1980.

[49] E. Moghbelli, R. Browning, W.-J. Boo, S. Hahn, L. Feick, and H.-J. Sue, "Effects of molecular weight and thermal history on scratch behavior of polypropylene thin sheets," *Tribol. Int.,* vol. 41, no. 5, pp. 425-433, 2008.

[50] R. Nath and M. Perlman, "Effect of crystallinity on charge storage in polypropylene and polyethylene," *IEEE Trans. Dielectr. Electr. Insul.,* vol. 24, no. 3, pp. 409-412, 1989.

[51] A. Kahouli, O. Gallot‐Lavallée, P. Rain, O. Lesaint, C. Guillermin, and J. M. Lupin, "Dielectric features of two grades of bi‐oriented isotactic polypropylene," *J. Appl. Polym. Sci.,* vol. 132, no. 28, 2015.

[52] B. Krishnakumar, R. Gupta, E. Forster, and J. Laghari, "AC breakdown of melt‐crystallized isotactic polypropylene," *J. Appl. Polym. Sci.,* vol. 35, no. 6, pp. 1459-1472, 1988.

[53] Z. Hui, X. Hengkun, and L. Ziyu, "Morphology and electrical breakdown of polypropylene," in *Proceedings of the 3rd International Conference on Properties and Applications of Dielectric Materials*, Tokyo, Japan, 1991: IEEE, pp. 1161-1164.

[54] B. Ceres and J. Schultz, "Dependence of electrical breakdown on spherulite size in isotactic polypropylene," *J. Appl. Polym. Sci.,* vol. 29, no. 12, pp. 4183-4197, 1984.

[55] P. Wang, G. Liu, H. Ma, Y. Liu, and T. Xu, "Investigation of the ampacity of a prefabricated straight-through joint of high voltage cable," *Energies,* vol. 10, no. 12, p. 2050, 2017.

[56] T. Lewis, "Nanometric dielectrics," *IEEE Trans. on Dielectr. and Electr. Insul.,* vol. 1, no. 5, pp. 812-825, 1994.

[57] Y. Zhou, J. Hu, B. Dang, and J. He, "Effect of different nanoparticles on tuning electrical properties of polypropylene nanocomposites," *IEEE Trans. Dielectr. Electr. Insul.,* vol. 24, no. 3, pp. 1380-1389, 2017.

[58] Y. Zhou, J. He, J. Hu, and B. Dang, "Surface-modified MgO nanoparticle enhances the mechanical and direct-current electrical characteristics of polypropylene/polyolefin elastomer nanodielectrics," *J. Appl. Polym. Sci.,* vol. 133, no. 1, pp. n/a-n/a, 2016, doi: 10.1002/app.42863.

[59] M. Takala *et al.*, "Dielectric properties and partial discharge endurance of polypropylene-silica nanocomposite," *IEEE Trans. Dielectr. Electr. Insul.,* vol. 17, no. 4, pp. 1259-1267, 2010.

[60] Z. Li, W. Cao, G. Sheng, X. Jiang, and M. G. Danikas, "Experimental study on space charge and electrical strength of MgO nano-particles/polypropylene composite," *IEEE Trans. Dielectr. Electr. Insul.,* vol. 23, no. 3, pp. 1812-1819, 2016.

[61] J.-W. Zha, Y. Wang, W.-K. Li, S.-J. Wang, and Z.-M. Dang, "Electrical properties of polypropylene/styrene-ethylene-butylene-styrene block copolymer/MgO nanocomposites," *IEEE Trans. Dielectr. Electr. Insul.,* vol. 24, no. 3, pp. 1457-1464, 2017.

[62] Y. Zhou, J. Hu, and J. He, "Space charge behavior in polypropylene/polyolefin elastomer/MgO nanocomposites under temperature gradient," in *2016 IEEE Conference on Electrical Insulation and Dielectric Phenomena (CEIDP)*, Toronto, ON, Canada, 2016: IEEE, pp. 599-602.

[63] B. Dang, Q. Li, Y. Zhou, J. Hu, and J. He, "Suppression of elevated temperature space charge accumulation in polypropylene/elastomer blends by deep traps induced by surface-modified ZnO nanoparticles," *Compos. Sci. Technol.,* vol. 153, pp. 103-110, 2017.

[64] S. Alapati, J. T. Meledath, and A. Karmarkar, "Effect of morphology on electrical treeing in low density polyethylene nanocomposites," *IET Sci. Meas. Technol.,* vol. 8, no. 2, pp. 60-68, 2014.

[65] T. Andritsch, "Epoxy Based Nanodielectrics for High Voltage DC Applications: Synthesis, Dielectric Properties and Space Charge Dynamics," PhD Thesis, TU Delft, 2010.

[66] A. V. Shaw, P. Ketsamee, T. Andritsch, and A. S. Vaughan, "Effect of organoclay loading on the dielectric properties and charge dynamics of a PP-rubber nanocomposite," *High Volt.,* vol. 5, no. 6, pp. 662-668, 2020.

[67] H. Palza, J. Vera, M. Wilhelm, and P. Zapata, "Spherulite growth rate in polypropylene/silica nanoparticle composites: effect of particle morphology and compatibilizer," *Macromol. Mater. Eng.,* vol. 296, no. 8, pp. 744-751, 2011.

[68] G. B. Olowojoba *et al.*, "A facile way to produce epoxy nanocomposites having excellent thermal conductivity with low contents of reduced graphene oxide," *J. Mater. Sci.,* vol. 52, no. 12, pp. 7323-7344, 2017.

[69] H. Chen, C. Zhao, S. Xu, and X. Yang, "Preparation and properties study of thermally conductive epoxy/modified boron nitride/graphene nanosheets composites," in *IOP conference series: materials science and engineering*, 2017, vol. 274, no. 1: IOP Publishing, p. 012043.

[70] M. Jouni, A. Boudenne, G. Boiteux, V. Massardier, B. Garnier, and A. Serghei, "Electrical and thermal properties of polyethylene/silver nanoparticle composites," *Polym. Compos.,* vol. 34, no. 5, pp. 778-786, 2013.

[71] H. G. Jang, B. Yang, M.-S. Khil, S. Y. Kim, and J. Kim, "Comprehensive study of effects of filler length on mechanical, electrical, and thermal properties of multi-walled carbon nanotube/polyamide 6 composites," *Compos. Part A Appl. Sci. Manuf.,* vol. 125, p. 105542, 2019.

[72] O. Vryonis, T. Andritsch, A. S. Vaughan, and P. L. Lewin, "Effect of surfactant molecular structure on the electrical and thermal performance of epoxy/functionalized‐graphene nanocomposites," *Polym. Compos.,* vol. 41, no. 7, pp. 2753-2767, 2020.

[73] B. Du, X. Kong, B. Cui, and J. Li, "Improved ampacity of buried HVDC cable with high thermal conductivity LDPE/BN insulation," *IEEE Trans. Dielectr. Electr. Insul.,* vol. 24, no. 5, pp. 2667-2676, 2017.

[74] Y. Guo, K. Ruan, X. Shi, X. Yang, and J. Gu, "Factors affecting thermal conductivities of the polymers and polymer composites: A review," *Compos. Sci. Technol.,* vol. 193, p. 108134, 2020.

[75] J. C. Maxwell Garnett, "Colours in metal glasses and in metallic films," *Phil. Trans. R. Soc. Lond, A,* vol. 203, pp. 385-420, 1904.

[76] H. Fricke, "The Maxwell-Wagner dispersion in a suspension of ellipsoids," *J. Phys. Chem.,* vol. 57, no. 9, pp. 934-937, 1953.

[77] D. Hasselman and L. F. Johnson, "Effective thermal conductivity of composites with interfacial thermal barrier resistance," *J. Compos. Mater.,* vol. 21, no. 6, pp. 508-515, 1987.

[78] S. Zhai, P. Zhang, Y. Xian, J. Zeng, and B. Shi, "Effective thermal conductivity of polymer composites: Theoretical models and simulation models," *Int. J. Heat Mass Transf.,* vol. 117, pp. 358-374, 2018.

[79] H. Chen *et al.*, "Thermal conductivity of polymer-based composites: Fundamentals and applications," *Prog. Polym. Sci.,* vol. 59, pp. 41-85, 2016, doi: 10.1016/j.progpolymsci.2016.03.001.

[80] S. Zhang, X. Cao, Y. Ma, Y. Ke, J. Zhang, and F. Wang, "The effects of particle size and content on the thermal conductivity and mechanical properties of Al2O3/high density polyethylene (HDPE) composites," *EXPRESS Polym. Lett.,* vol. 5, no. 7, pp. 581-590, 2011.

[81] K. Pashayi, H. R. Fard, F. Lai, S. Iruvanti, J. Plawsky, and T. Borca-Tasciuc, "High thermal conductivity epoxy-silver composites based on self-constructed nanostructured metallic networks," *J. Appl. Phys.,* vol. 111, no. 10, p. 104310, 2012.

[82] J. Yu *et al.*, "Preparation of hyperbranched aromatic polyamide grafted nanoparticles for thermal properties reinforcement of epoxy composites," *Polymer Chemistry,* vol. 2, no. 6, pp. 1380-1388, 2011.

[83] A. Tessema *et al.*, "Effect of filler loading, geometry, dispersion and temperature on thermal conductivity of polymer nanocomposites," *Polymer Testing,* vol. 57, pp. 101-106, 2017.

[84] L. Zhang, X. Cui, and Y. Zhou, "Surface Ligand Engineering of Polymer Nanodielectrics for HVDC Cables," in *Polymer Insulation Applied for HVDC Transmission*: Springer, 2021, pp. 23-44.

[85] A. Xu, S. Roland, and X. Colin, "Physico-chemical characterization of the blooming of Irganox 1076® antioxidant onto the surface of a silane-crosslinked polyethylene," *Polym. Degrad. Stab.,* vol. 171, p. 109046, 2020.

[86] C. Zhou, H. Yi, and X. Dong, "Review of recent research towards power cable life cycle management," *High volt.,* vol. 2, no. 3, pp. 179-187, 2017.

[87] C. Zou, J. C. Fothergill, and S. W. Rowe, "The effect of water absorption on the dielectric properties of epoxy nanocomposites," *IEEE Trans. Dielectr. Electr. Insul.,* vol. 15, no. 1, pp. 106-117, 2008.

[88] Z. Hashim, K. Y. Lau, C. W. Tan, and K. Y. Ching, "Simulation of nanodielectrics: nanoparticle and interphase effects on electric field distributions," *IET Nanodielectrics,* vol. 3, no. 1, pp. 1-9, 2020.

[89] T. Tanaka, M. Kozako, N. Fuse, and Y. Ohki, "Proposal of a multi-core model for polymer nanocomposite dielectrics," *IEEE Trans. Dielectr. Electr. Insul.,* vol. 12, no. 4, pp. 669-681, 2005.

[90] T. J. Lewis, "Interfaces are the Dominant Feature of Dielectrics at the Nanometric Level," *IEEE Trans. Dielectr. Electr. Insul.,* vol. 11, no. 5, 2004.

[91] S. Raetzke and J. Kindersberger, "The effect of interphase structures in nanodielectrics," *IEEJ Trans. Fundam. Mater.,* vol. 126, no. 11, pp. 1044-1049, 2006.

[92] K. Y. Lau, "Structure and electrical properties of silica-based polyethylene nanocomposites," PhD Thesis, University of Southampton, 2013.

[93] J. K. Nelson, "Overview of nanodielectrics: Insulating materials of the future," in *Electrical Insulation Conference and Electrical Manufacturing Expo, 2007*, 2007: IEEE, pp. 229-235.

[94] X. Chi, W. Liu, S. Li, and X. Zhang, "The Effect of Humidity on Dielectric Properties of PP-Based Nano-Dielectric," *Materials,* vol. 12, no. 9, p. 1378, 2019.

[95] I. L. Hosier, M. Praeger, A. F. Holt, A. S. Vaughan, and S. G. Swingler, "On the effect of functionalizer chain length and water content in polyethylene/silica nanocomposites: Part I—Dielectric properties and breakdown strength," *IEEE Trans. Dielectr. Electr. Insul.,* vol. 24, no. 3, pp. 1698-1707, 2017, doi: 10.1109/TDEI.2017.005788.

[96] I. L. Hosier, M. Praeger, A. S. Vaughan, and S. G. Swingler, "The effects of water on the dielectric properties of aluminum based nanocomposites," *IEEE Trans. on Nanotech.,* vol. 16, no. 4, pp. 667-676, 2017, doi: 10.1109/TNANO.2017.2703982.

[97] I. L. Hosier, M. Praeger, A. S. Vaughan, and S. G. Swingler, "The effects of water on the dielectric properties of silicon-based nanocomposites," *IEEE Trans. on Nanotech.,* vol. 16, no. 2, pp. 169-179, 2017, doi: 10.1109/tnano.2016.2642819.

[98] A. Every, Y. Tzou, D. Hasselman, and R. Raj, "The effect of particle size on the thermal conductivity of ZnS/diamond composites," *Acta. Mater.,* vol. 40, no. 1, pp. 123-129, 1992.

[99] S. Lee, J. Lee, B. Ryu, and S. Ryu, "A micromechanics-based analytical solution for the effective thermal conductivity of composites with orthotropic matrices and interfacial thermal resistance," *Sci. Rep.,* vol. 8, no. 1, pp. 1-11, 2018.

[100] R. Kochetov, A. V. Korobko, T. Andritsch, P. H. F. Morshuis, S. J. Picken, and J. J. Smit, "Modelling of the thermal conductivity in polymer nanocomposites and the impact of the interface between filler and matrix," *J. Phys. D.,* vol. 44, no. 39, p. 395401, 2011, doi: 10.1088/0022-3727/44/39/395401.

[101] I. Jang *et al.*, "Enhancement of thermal conductivity of BN/epoxy composite through surface modification with silane coupling agents," *Colloids Surf. A Physicochem. Eng. Asp.,* vol. 518, pp. 64-72, 2017.

[102] W. Cao, Z. Li, G. Sheng, and X. Jiang, "Insulating property of polypropylene nanocomposites filled with nano-MgO of different concentration," *IEEE Trans. Dielectr. Electr. Insul.,* vol. 24, no. 3, pp. 1430-1437, 2017.

[103] G. Yu, Y. Cheng, and Z. Wu, "Effect of Nano-MgO Particles Doping on Breakdown Characteristics of Polypropylene," *Coatings,* vol. 10, no. 4, p. 312, 2020.

[104] C. Calebrese, L. Hui, L. S. Schadler, and J. K. Nelson, "A review on the importance of nanocomposite processing to enhance electrical insulation," *IEEE Trans. Dielectr. Electr. Insul.,* vol. 18, no. 4, pp. 938-945, 2011.

[105] J. K. Nelson and J. C. Fothergill, "Internal charge behaviour of nanocomposites," *Nanotechnology,* vol. 15, no. 5, p. 586, 2004.

[106] T. Tanaka, "Dielectric nanocomposites with insulating properties," *IEEE Trans. Dielectr. Electr. Insul.,* vol. 12, no. 5, pp. 914-928, 2005.

[107] R. Ayoob, F. N. Alhabill, T. Andritsch, and A. S. Vaughan, "The effect of water absorption on the dielectric properties of polyethylene hexagonal boron nitride nanocomposites," *J. Phys. D: Appl. Phys.,* vol. 51, no. 6, p. 065307, 2018, doi: 10.1088/1361-6463/aaa306.

[108] K. Sato *et al.*, "Thermally conductive composite films of hexagonal boron nitride and polyimide with affinity-enhanced interfaces," *J. Mater. Chem.,* vol. 20, no. 14, pp. 2749-2752, 2010.

[109] D. Golberg *et al.*, "Boron nitride nanotubes and nanosheets," *ACS nano,* vol. 4, no. 6, pp. 2979-2993, 2010.

[110] M. I. Baraton and K. E. Gonsalves, "An IR Spectroscopic Investigation of Nanostructured A1N and GaN Powder Surfaces," *J. Clust. Sci.,* vol. 10, no. 1, 1999.

[111] M.-I. Baraton, X. Chen, and K. Gonsalves, "FTIR study of a nanostructured aluminum nitride powder surface: Determination of the acidic/basic sites by CO, CO2 and acetic acid adsorptions," *Nanostructured materials,* vol. 8, no. 4, pp. 435-445, 1997.

[112] A. Kocjan, "The Hydrolysis of AlN Powder–A Powerful Tool in Advanced Materials Engineering," *Chem. Rec.,* vol. 18, no. 7-8, pp. 1232-1246, 2018.

[113] J. Li, M. Nakamura, T. Shirai, K. Matsumaru, C. Ishizaki, and K. Ishizaki, "Mechanism and kinetics of aluminum nitride powder degradation in moist air," *J. Am. Ceram. Soc.,* vol. 89, no. 3, pp. 937-943, 2006, doi: 10.1111/j.1551-2916.2005.00767.x.

[114] M. Wozniak, P. Rutkowski, and D. Kata, "Rheological properties and thermal conductivity of AlN–poly (propylene glycol) suspensions," *Heat Mass Transf.,* vol. 52, no. 1, pp. 103-112, 2016, doi: 10.1007/s00231-015-1597-0.

[115] C. Liu *et al.*, "The effects of aluminum-nitride nano-fillers on the mechanical, electrical, and thermal properties of high temperature vulcanized silicon rubber for high-voltage outdoor insulator applications," *Mater.,* vol. 12, no. 21, p. 3562, 2019, doi: 10.3390/ma12213562.

[116] J. Li, M. Nakamura, T. Shirai, K. Matsumaru, K. Ishizaki, and C. Ishizaki, "Hydrolysis of aluminum nitride powders in moist air," *Advances in Technology of Materials and Materials Processing Journal,* vol. 7, no. 1, pp. 37-42, 2005.

[117] A. Kocjan, A. Dakskobler, and T. Kosmač, "Evolution of aluminum hydroxides in diluted aqueous aluminum nitride powder suspensions," *Crystal Growth & Design,* vol. 12, no. 3, pp. 1299-1307, 2012.

[118] A. Kocjan, T. Konegger, and A. Dakskobler, "Hierarchical macroporous–mesoporous γ-alumina monolithic green bodies with high strength," *Journal of Materials Science,* vol. 52, no. 19, pp. 11168-11178, 2017.

[119] M. Oliveira, S. Olhero, J. Rocha, and J. Ferreira, "Controlling hydrolysis and dispersion of AlN powders in aqueous media," *J. Colloid Interface Sci.,* vol. 261, no. 2, pp. 456-463, 2003.

[120] I. Ganesh, S. M. Olhero, A. B. Araújo, M. R. Correia, G. Sundararajan, and J. M. Ferreira, "Chemisorption of phosphoric acid and surface characterization of as passivated AlN powder against hydrolysis," *Langmuir,* vol. 24, no. 10, pp. 5359-5365, 2008.

[121] L. Zhou, W. Zhuang, X. Wang, K. Yu, S. Yang, and S. Xia, "Potential acute effects of suspended aluminum nitride (AlN) nanoparticles on soluble microbial products (SMP) of activated sludge," *J. Environ. Sci.,* vol. 57, pp. 284-292, 2017, doi: 10.1016/j.jes.2017.02.001.

[122] H. H. Nersisyan, J. H. Lee, H. Y. Kim, S. Ryu, and B. U. Yoo, "Morphological diversity of AlN nano-and microstructures: synthesis, growth orientations and theoretical modelling," *Int. Mater. Rev.,* vol. 65, no. 6, pp. 323-355, 2020.

[123] S.-C. Shi, S. Chattopadhyay, C.-F. Chen, K.-H. Chen, and L.-C. Chen, "Structural evolution of AlN nano-structures: Nanotips and nanorods," *Chem. Phys. Lett.,* vol. 418, no. 1-3, pp. 152-157, 2006.

[124] S. Kazantsev *et al.*, "Preparation of aluminum hydroxide and oxide nanostructures with controllable morphology by wet oxidation of AlN/Al nanoparticles," *Mater. Res. Bull.,* vol. 104, pp. 97-103, 2018.

[125] W. Sinkler, S. A. Bradley, U. Ziese, and K. P. de Jong, "3D-TEM study of gamma alumina catalyst supports," *Microsc. Microanal.,* vol. 12, no. S02, pp. 52-53, 2006.

[126] N. V. Usoltseva, V. V. Korobochkin, M. A. Balmashnov, and A. S. Dolinina, "Solution transformation of the products of AC electrochemical metal oxidation," *Procedia Chem.,* vol. 15, pp. 84-89, 2015.

[127] H. d. S. Costa, M. M. Pereira, G. I. Andrade, E. F. B. Stancioli, and H. S. Mansur, "Characterization of calcium phosphate coating and zinc incorporation on the porous alumina scaffolds," *Mater. Res.,* vol. 10, no. 1, pp. 27-29, 2007.

[128] Y. Zhang and J. Binner, "Hydrolysis process of a surface treated aluminum nitride powder—a FTIR study," *J. Mater. Sci. Lett.,* vol. 21, no. 10, pp. 803-805, 2002.

[129] T. Sindhu, S. Chakravarthi, R. Jayaganthan, and R. Sarathi, "Studies on generation and characterization of nano aluminium nitride using wire explosion technique," *Synthesis and Reactivity in Inorganic, Metal-Organic and Nano-Metal Chemistry,* vol. 36, no. 1, pp. 53-58, 2006.

[130] S. Angappan, R. A. Jeneafer, A. Visuvasam, and L. J. Berchmans, "Synthesis of AlN-presence and absence of additive," *Int. J. Eng.,* vol. 19, no. 3, p. 239, 2013.

[131] Y. Zhou, J. Hu, X. Chen, F. Yu, and J. He, "Thermoplastic polypropylene/aluminum nitride nanocomposites with enhanced thermal conductivity and low dielectric loss," *IEEE Trans. on Dielectr. and Electr. Insul.,* vol. 23, no. 5, pp. 2768-2776, 2016, doi: 10.1109/TDEI.2016.7736836.

[132] G. Paglia, E. S. Božin, and S. J. L. Billinge, "Fine-scale nanostructure in γ-Al2O3," *Chem. Mater.,* vol. 18, no. 14, pp. 3242-3248, 2006, doi: 10.1021/cm060277j.

[133] Y. Q. Li, T. Qiu, and J. Xu, "Effect of thermal oxidation treatment in air on the hydrolysis of AlN powder," *Mater. Res. Bull.,* vol. 32, no. 9, pp. 1173-1179, 1997, doi: 10.1016/S0025-5408(97)00093-7.

[134] S. Olhero, S. Novak, M. Oliveira, K. Krnel, T. Kosmac, and J. Ferreira, "A thermo-chemical surface treatment of AlN powder for the aqueous processing of AlN ceramics," *J. Mater. Res.,* vol. 19, no. 3, pp. 746-751, 2004.

[135] A. A. Elagin, A. R. Beketov, M. V. Baranov, and R. A. Shishkin, "Aluminum nitride. Preparation methods," *Refract. Ind. Ceram.,* vol. 53, no. 6, pp. 395-403, 2013, doi: 10.1007/s11148-013-9546-2.

[136] C. Sweegers, H. De Coninck, H. Meekes, W. Van Enckevort, I. Hiralal, and A. Rijkeboer, "Morphology, evolution and other characteristics of gibbsite crystals grown from pure and impure aqueous sodium aluminate solutions," *J. Cryst. Growth,* vol. 233, no. 3, pp. 567-582, 2001.

[137] A. Kocjan, A. Dakskobler, K. Krnel, and T. Kosmač, "The course of the hydrolysis and the reaction kinetics of AlN powder in diluted aqueous suspensions," *J. Eur. Ceram. Soc.,* vol. 31, no. 5, pp. 815-823, 2011.

[138] X. Zhang *et al.*, "Fast synthesis of gibbsite nanoplates and process optimization using Box-Behnken experimental design," *Cryst. Growth Des.,* vol. 17, no. 12, pp. 6801-6808, 2017.

[139] K. Krnel, G. Dražič, and T. Kosmač, "Degradation of AlN powder in aqueous environments," *J. Mater. Res.,* vol. 19, no. 4, pp. 1157-1163, 2004.

[140] D. G. Syarif, M. Yamin, and Y. I. Pratiwi, "Self combustion synthesis of Al2O3 nanoparticles from bauxite utilizing sugar as fuel for nanofluids with enhanced CHF," *J. Phys. Conf. Ser.,* vol. 1153, no. 1, p. 012068, 2019.

[141] S. Q. Su, J. Yang, H. W. Ma, F. Jiang, Y. Q. Liu, and G. Li, "Preparation of ultrafine aluminum hydroxide from coal fly ash by alkali dissolution process," *Integr. Ferroelectr.,* vol. 128, no. 1, pp. 155-162, 2011.

[142] Y. Xie, C. A. S. Hill, Z. Xiao, H. Militz, and C. Mai, "Silane coupling agents used for natural fiber/polymer composites: A review," *Compos. Part A-Appl. Sci. Manuf.,* vol. 41, no. 7, pp. 806-819, 2010, doi: 10.1016/j.compositesa.2010.03.005.

[143] S. Kango, S. Kalia, A. Celli, J. Njuguna, Y. Habibi, and R. Kumar, "Surface modification of inorganic nanoparticles for development of organic–inorganic nanocomposites—a review," *Prog. Polym. Sci.,* vol. 38, no. 8, pp. 1232-1261, 2013.

[144] B. Arkles, *Silane coupling agents: connecting across boundaries V3.0* (Gelest). 2014.

[145] E. P. Plueddemann, *Silane coupling agents*. Springer Boston MA, 1991.

[146] C. Yeung, "Spectroscopic Analysis of Nanodielectric Interfaces," PhD Thesis, University of Southampton, 2013.

[147] T. Andritsch, R. Kochetov, Y. T. Gebrekiros, P. H. Morshuis, and J. J. Smit, "Short term DC breakdown strength in epoxy based BN nano-and microcomposites," in *2010 10th IEEE International Conference on Solid Dielectrics*, Potsdam, Germany, 2010, 2010, pp. 1-4, doi: 10.1109/ICSD.2010.5568098.

[148] C. Yeung and A. S. Vaughan, "On the effect of nanoparticle surface chemistry on the electrical characteristics of epoxy-based nanocomposites," *Polym.,* vol. 8, no. 4, p. 126, 2016, doi: 10.3390/polym8040126.

[149] S. Zhao *et al.*, "Synergistic enhancement of glass fiber and tetrapod-shaped ZnO whisker on the mechanical and thermal behavior of isotactic polypropylene," *J. Appl. Polym. Sci.,* vol. 133, no. 46, p. 44217, 2016, doi: 10.1002/app.44217.

[150] R. Metselaar, R. Reenis, M. Chen, H. Gorter, and H. Hintzen, "Surface characterization of chemically treated aluminium nitride powders," *J. Eur. Ceram. Soc.,* vol. 15, no. 11, pp. 1079-1085, 1995.

[151] C. Y. Lung and J. P. Matinlinna, "Resin Bonding to Silicatized Zirconia with Two Isocyanatosilanes and a Cross-linking Silane. Part II: Mechanistic Approach," *Silicon,* vol. 2, no. 3, pp. 163-169, 2010.

[152] J. Li, K. Matsumaru, C. Ishizaki, and K. Ishizaki, "Diffuse reflectance infrared Fourier transform spectroscopy of commercial AlN powders in vacuum up to 700 C," *J. Am. Ceram. Soc.,* vol. 89, no. 8, pp. 2537-2541, 2006.

[153] M. Abdelmouleh, S. Boufi, M. N. Belgacem, and A. Dufresne, "Short natural-fibre reinforced polyethylene and natural rubber composites: effect of silane coupling agents and fibres loading," *Compos. sci. and technol.,* vol. 67, no. 7, pp. 1627-1639, 2007.

[154] C. Bressy, V. G. Ngo, F. Ziarelli, and A. Margaillan, "New insights into the adsorption of 3-(trimethoxysilyl) propylmethacrylate on hydroxylated ZnO nanopowders," *Langmuir,* vol. 28, no. 6, pp. 3290-3297, 2012.

[155] K. Linehan and H. Doyle, "Size controlled synthesis of silicon nanocrystals within inverse micelles," *MRS Online Proceedings Library,* vol. 1546, no. 1, pp. 1-6, 2013.

[156] J. Brandrup, E. H. Immergut, E. A. Grulke, A. Abe, and D. R. Bloch, *Polymer handbook*. Wiley New York etc, 1989.

[157] R. Olley and D. Bassett, "An improved permanganic etchant for polyolefines," *Polym.,* vol. 23, no. 12, pp. 1707-1710, 1982, doi: 10.1016/0032-3861(82)90110-0.

[158] M. Gómez, H. Palza, and R. Quijada, "Influence of organically-modified montmorillonite and synthesized layered silica nanoparticles on the properties of polypropylene and polyamide-6 nanocomposites," *Polymers,* vol. 8, no. 11, p. 386, 2016.

[159] Y. Lin, H. Chen, C.-M. Chan, and J. Wu, "Nucleating effect of calcium stearate coated CaCO3 nanoparticles on polypropylene," *J. Colloid Interface Sci.,* vol. 354, no. 2, pp. 570-576, 2011.

[160] M. Sarkar, K. Dana, S. Ghatak, and A. Banerjee, "Polypropylene-clay composite prepared from Indian bentonite," *Bull. Mater. Sci.,* vol. 31, no. 1, pp. 23-28, 2008, doi: 10.1007/s12034-008-0005-5.

[161] Y. Liang, S. Wen, Y. Ren, and L. Liu, "Fabrication of nanoprotrusion surface structured silica nanofibers for the improvement of the toughening of polypropylene," *RSC Adv.,* vol. 5, no. 40, pp. 31547-31553, 2015, doi: 10.1039/C5RA01510C.

[162] F. Orellana, J. Lisperguer, and C. Nuñez, "Synthesis and characterization of polypropylene-silica, alumina and titania nanoparticles, prepared by melting," *J. Chil. Chem. Soc.,* vol. 59, no. 1, pp. 2389-2393, 2014.

[163] E. Franco-Urquiza, J. May-Crespo, C. Escalante Velázquez, R. Pérez Mora, and P. González García, "Thermal Degradation Kinetics of ZnO/polyester Nanocomposites," *Polymers,* vol. 12, no. 8, p. 1753, 2020.

[164] K. Król-Morkisz and K. Pielichowska, "Thermal decomposition of polymer nanocomposites with functionalized nanoparticles," in *Polymer Composites with Functionalized Nanoparticles*: Elsevier, 2019, pp. 405-435.

[165] F. Bertini, M. Canetti, G. Audisio, G. Costa, and L. Falqui, "Characterization and thermal degradation of polypropylene–montmorillonite nanocomposites," *Polym. Degrad. Stab.,* vol. 91, no. 3, pp. 600-605, 2006.

[166] M. Yourdkhani, T. Mousavand, N. Chapleau, and P. Hubert, "Thermal, oxygen barrier and mechanical properties of polylactide–organoclay nanocomposites," *Compos. Sci. Technol.,* vol. 82, pp. 47-53, 2013.

[167] P. Rajeshwari and T. Dey, "Finite element modelling and experimental investigation on effective thermal conductivity of AlN (nano) particles reinforced HDPE polymer nanocomposites," *Thermochim. Acta,* vol. 638, pp. 103-112, 2016.

[168] R. Kochetov, T. Andritsch, U. Lafont, P. Morshuis, S. Picken, and J. Smit, "Thermal behaviour of epoxy resin filled with high thermal conductivity nanopowders," in *2009 IEEE Electrical Insulation Conference*, Montreal, QC, Canada, 2009: IEEE, pp. 524-528.

[169] W. Peng, X. Huang, J. Yu, P. Jiang, and W. Liu, "Electrical and thermophysical properties of epoxy/aluminum nitride nanocomposites: Effects of nanoparticle surface modification," *Compos. Part A-Appl. Sci. Manuf.,* vol. 41, no. 9, pp. 1201-1209, 2010, doi: 10.1016/j.compositesa.2010.05.002.

[170] T. S. English, J. C. Duda, J. L. Smoyer, D. A. Jordan, P. M. Norris, and L. V. Zhigilei, "Enhancing and tuning phonon transport at vibrationally mismatched solid-solid interfaces," *Phys. Rev. B,* vol. 85, no. 3, p. 035438, 2012.

[171] D. Qiang, Y. Wang, G. Chen, and T. Andritsch, "Dielectric properties of epoxy silica and boron nitride nanocomposites and moisture/temperature influences," *IET Nanodielectrics,* vol. 1, no. 1, pp. 48-59, 2018, doi: 10.1049/iet-nde.2017.0002.

[172] K. Lau, A. Vaughan, and G. Chen, "Nanodielectrics: opportunities and challenges," *IEEE Electr. Insul. Mag.,* vol. 31, no. 4, pp. 45-54, 2015.

[173] K. Y. Lau, A. S. Vaughan, G. Chen, I. L. Hosier, and A. F. Holt, "On the dielectric response of silica-based polyethylene nanocomposites," *J. Phys. D: Appl. Phys.,* vol. 46, no. 9, p. 095303, 2013, doi: 10.1088/0022-3727/46/9/095303.

[174] A. V. Shaw, A. S. Vaughan, and T. Andritsch, "The dielectric effect of xylene on an organoclay-containing composite," *IEEE Trans. Dielectr. Electr. Insul.,* vol. 26, no. 3, pp. 890-897, 2019, doi: 10.1109/TDEI.2019.007854.

[175] K. Y. Lau, A. S. Vaughan, G. Chen, and I. L. Hosier, "Dielectric response of polyethylene nanocomposites: The effect of surface treatment and water absorption," in *2012 Annual Report Conference on Electrical Insulation and Dielectric Phenomena*, Montreal, Canada, 2012: IEEE, 2012, pp. 275-278, doi: 10.1109/CEIDP.2012.6378774.

[176] P. Steeman and F. Maurer, "An interlayer model for the complex dielectric constant of composites," *Colloid Polym. Sci.,* vol. 268, no. 4, pp. 315-325, 1990.

[177] R. Ayoob, "Dielectric properties of hexagonal boron nitride polymer nanocomposites," PhD Thesis, University of Southampton, 2017.

[178] M.-I. Baraton, X. Chen, and K. E. Gonsalves, "FTIR analysis of the surface of nanostructured aluminium nitride powder prepared via chemical synthesis," *J. Mater. Chem.,* vol. 6, no. 8, pp. 1407-1412, 1996, doi: 10.1039/JM9960601407

[179] C. Zhang, J.-W. Zha, H.-D. Yan, W.-K. Li, and Z.-M. Dang, "High improvement in trap level density and direct current breakdown strength of block polypropylene by doping with a β-nucleating agent," *Appl. Phys. Lett.,* vol. 112, no. 9, p. 091902, 2018, doi: 10.1063/1.5020736.

[180] Y. Tong, L. Li, J. Liu, K. Zhang, and Y. Jiang, "Influence of coupling agent on the microstructure and dielectric properties of free-standing ceramic-polymer composites," *Mater. Res. Express,* vol. 6, no. 9, p. 095322, 2019.

[181] Q. Zhang *et al.*, "Enhanced dielectric tunability of Ba0. 6Sr0. 4TiO3/Poly (vinylidene fluoride) composites via interface modification by silane coupling agent," *Compos. Sci. Technol.,* vol. 129, pp. 93-100, 2016.

[182] K. Lau, A. Vaughan, G. Chen, and I. Hosier, "Space charge dynamics in silica-based polyethylene nanocomposites," in *2013 IEEE International Conference on Solid Dielectrics (ICSD)*, Bologna, Italy, 2013: IEEE, pp. 880-883.

[183] C. Zou, J. C. Fothergill, and S. W. Rowe, "A" water shell" model for the dielectric properties of hydrated silica-filled epoxy nano-composites," in *2007 IEEE International Conference on Solid Dielectrics*, Winchester, UK, 2007: IEEE, 2007, pp. 389-392, doi: 10.1109/ICSD.2007.4290834.

[184] H. W. Carvalho, C. V. Santilli, V. Briois, and S. H. Pulcinelli, "Polymer–clay nanocomposites thermal stability: experimental evidence of the radical trapping effect," *RSC Adv.,* vol. 3, no. 45, pp. 22830-22833, 2013.

[185] R. Wang, C. Xie, L. Zeng, and H. Xu, "Thermal decomposition behavior and kinetics of nanocomposites at low-modified ZnO content," *RSC Adv.,* vol. 9, no. 2, pp. 790-800, 2019.

[186] S. Marcinko and A. Y. Fadeev, "Hydrolytic stability of organic monolayers supported on TiO2 and ZrO2," *Langmuir,* vol. 20, no. 6, pp. 2270-2273, 2004.

[187] O. Vryonis, S. Riarh, T. Andritsch, and A. S. Vaughan, "Stoichiometry and molecular dynamics of anhydride-cured epoxy resin incorporating octa-glycidyl POSS co-monomer," *Polymer,* vol. 213, p. 123312, 2021.

[188] I. Ganesh, S. Olhero, and J. Ferreira, "Phosphoric acid treated AlN powder for aqueous processing of net-shape dense AlN and β-SiAlON parts," *Adv. Appl. Ceram.,* vol. 108, no. 2, pp. 111-117, 2009.

[189] M. Longhi *et al.*, "Effect of tetraethoxy-silane (TEOS) amounts on the corrosion prevention properties of siloxane-PMMA hybrid coatings on galvanized steel substrates," *Mater. Res.,* vol. 18, no. 6, pp. 1140-1155, 2015.

[190] A. S. Khan *et al.*, "Vibrational spectroscopy of selective dental restorative materials," *Appl. Spectrosc. Rev.,* vol. 52, no. 6, pp. 507-540, 2017.

[191] C. Yu, Y. Ke, X. Hu, Y. Zhao, Q. Deng, and S. Lu, "Effect of bifunctional montmorillonite on the thermal and tribological properties of polystyrene/montmorillonite nanocomposites," *Polymers,* vol. 11, no. 5, p. 834, 2019.

[192] M. Spoerk *et al.*, "Polypropylene filled with glass spheres in extrusion-based additive manufacturing: effect of filler size and printing chamber temperature," *Macromol. Mater. Eng.,* vol. 303, no. 7, p. 1800179, 2018.

[193] T. Lozano, J. Laria, P. Lafleur, S. Sánchez-Valdés, F. Rodríguez-González, and A. Morales-Cepeda, "Beta phase in polypropylene induced by shear in a single-screw extruder," *Polym. Eng. Sci.,* vol. 52, no. 8, pp. 1672-1677, 2012.

[194] M. Reading, "An investigation into the structure and properties of polyethylene oxide nanocomposites," PhD Thesis, University of Southampton, 2010.

[195] E. Senis, I. O. Golosnoy, O. Thomsen, J. Barton, and S. Madsen, "Characterization of through-thickness thermal conductivity of wind turbine blade CFRP materials using a steady-state technique," in *21st International Conference on Composite Materials*, Xi'an, China, 2017.

[196] P. Barber *et al.*, "Polymer composite and nanocomposite dielectric materials for pulse power energy storage," *Materials,* vol. 2, no. 4, pp. 1697-1733, 2009.